Title

The EGS Collab Project — Summaries of Experiments 2 and 3: Experiments at 1.25 km depth at the Sanford Underground Research Facility

Authors

Kneafsey, Timothy
Johnson, Timothy
Burghardt, Jeff
et al.

Publication Date

2024-01-09

The EGS Collab Project – Summaries of Experiments 2 and 3: Experiments at 1.25 km depth at the Sanford Underground Research Facility

The EGS Collab Team

J. Ajo-Franklin, T. Artz, T. Baumgartner, K. Beckers, G. Bettin, D. Blankenship, A. Bonneville, B. Borames, L. Boyd, S. Brown, J.A. Burghardt, C. Chai, A. Chakravarty, T. Chen, Y. Chen, B. Chi, K. Condon, P.J. Cook, D. Crandall, N. Creasy, R. DeBoer, P.F. Dobson, K. Dobler, T. Doe, C.A. Doughty, D. Elsworth, J. Feldman, Z. Feng, A. Foris, L.P. Frash, Z. Frone, P. Fu, K. Gao, A. Ghassemi, Y. Guglielmi, B. Haimson, A. Hawkins, J. Heise, C. Hopp, M. Horn, R.N. Horne, J. Horner, M. Hu, H. Huang, L. Huang, K.J. Im, M. Ingraham, E. Jafarov, R.S. Jayne, T.C. Johnson, S.E. Johnson, B. Johnston, S. Karra, K. Kim, D.K. King, T. Kneafsey, J. Knight, H. Knox, J. Knox, E. Krantz, D. Kumar, K. Kutun, M. Lee, D. Li, J. Li, K. Li, Z. Li, M. Maceira, P. Mackey, N. Makedonska, C.J. Marone, E. Mattson, M.W. McClure, J. McLennan, T. McLing, C. Medler, R.J. Mellors, E. Metcalfe, J. Miskimins, J. Moore, C.E. Morency, J.P. Morris, T. Myers, S. Nakagawa, G. Neupane, G. Newman, A. Nieto, T. Paronish, R Pawar, P. Petrov, B. Pietzyk, M. Plummer, R. Podgorney, Y. Polsky, J. Pope, S. Porse, J.C. Primo, T. Pyatina, J. Quintanar, C. Reimers, B.Q. Roberts, M. Robertson, V. Rodríguez Tribaldos, W. Roggenthen, J. Rutqvist, D. Rynders, M. Schoenball, P. Schwering, V. Sesetty, C.S. Sherman, A. Singh, D. Sirota, M.M. Smith, H. Sone, E.L. Sonnenthal, F.A. Soom, D.P. Sprinkle, S. Sprinkle, J. St. Clair, C.E. Strickland, J. Su, Y. Tanaka, N. Taverna, D. Templeton, J.N. Thomle, C. Ulrich, N. Uzunlar, A. Vachaparampil, C.A. Valladao, W. Vandermeer, G. Vandine, D. Vardiman, V.R. Vermeul, J.L. Wagoner, H.F. Wang, J. Weers, N. Welch, J. White, M.D. White, P. Winterfeld, T. Wood, S. Workman, H. Wu, Y.S. Wu, E.C. Yildirim, Y. Zhang, Y.Q. Zhang, Q. Zhou, M.D. Zoback

Project PI: Tim Kneafsey (2017-2022), Michelle Robertson (2022-2023)

coPI: Doug Blankenship

Lead Authors: Tim Kneafsey, Tim Johnson, Jeff Burghardt, Paul Schwering, Luke Frash, Bill Roggenthen, Chet Hopp, Ghanashyam Neupane, Earl Mattson, Craig Ulrich, Florian Soom, Tom Doe, Jon Weers, Tyler Artz, Michelle Robertson

Table of Contents

KEY CONTRIBUTORS

Experiment Design	Joe Morris Doug Blankenship Hunter Knox Paul Schwering Jeff Burghardt Vince Vermeul Chris Strickland Mark White Pat Dobson Luke Frash Bill Roggenthen Thomas Doe Pengcheng Fu Jonathan Ajo-Franklin Tim Kneafsey
Site Characterization	Paul Schwering Bill Roggenthen Pat Dobson Craig Ulrich Megan Smith Tyler Artz Nuri Uzunlar Mark White Jeff Burghardt Earl Mattson Ghanashyam Neupane J.C. Primo
Stress Modeling	Jeff Burghardt Ankush Singh Thomas Doe Herb Wang Pat Dobson Yves Guglielmi Mark Zoback
Testbed Design/Construction	Joe Morris Paul Schwering Mathew Ingraham Vince Vermeul Hunter Knox Chris Strickland Pat Dobson

	Dana Sirota Lianjie Huang Chet Hopp Verónica Rodríguez Tribaldos Todd Wood Tim Johnson George Vandine Jonathan Ajo-Franklin Mark White Thomas Doe Bill Roggenthen Luke Frash Earl Mattson Joe Pope Tatiana Pyatina Ben Roberts Craig Ulrich Doug Blankenship Tim Kneafsey
Thermal Modeling	Mark White Luke Frash Thomas Doe
Geophysical Monitoring System Design and Monitoring	Chet Hopp Verónica Rodríguez Tribaldos Chris Strickland Tim Johnson Jonathan Ajo-Franklin Todd Wood Dana Sirota Ben Roberts Lianjie Huang Yves Guglielmi Florian Soom Paul Cook
Data Management	Jon Weers Nicole Taverna Pengcheng Fu Jonathan Ajo-Franklin Jay Huggins Jeff Burghardt Chet Hopp Chris Strickland Lianjie Huang

Analysis	Denise Templeton Mark White Hui Wu Doug Blankenship Jeff Burghardt Chet Hopp Verónica Rodríguez Tribaldos Bill Rogenthen Lianjie Huang Tim Johnson Neala Creasy Pat Dobson Thomas Doe Christine Doughty Luke Frash Pengcheng Fu Ankush Singh Yves Guglielmi Tim Kneafsey Earl Mattson Mark McClure Joe Morris Paul Schwering Hiroki Sone
Data Interpretation and Integration	Ghanashyam Neupane Thomas Doe Bill Roggenthen Pat Dobson Pengcheng Fu Craig Ulrich
Project Coordination	Paul Schwering Hunter Knox Tim Kneafsey George Vandine Jaret Heise Markus Horn Susan Sprinkle Michelle Robertson Jeff Burghardt Doug Blankenship Pat Dobson
Tracer Testing and Water Balance	Ghanashyam Neupane Earl Mattson

	Dana Sirota Tim Johnson Chris Strickland Tyler Artz Reghan DeBoer
Experiment Execution	Jeff Burghardt Mark White Vince Vermeul Chet Hopp Verónica Rodríguez Tribaldos Chris Strickland Tim Johnson Matthew Ingraham Florian Soom Paul Cook Todd Wood Dana Sirota Ben Roberts J. Carlo Primo George Vandine Hunter Knox Paul Schwering
Grout formulation and injection for monitoring wells	Tatiana Pyatina Tim Johnson Lance Sollohub Daniel Bour Joe Pope Tim Kneafsey Doug Blankenship Hunter Knox Paul Schwering Chris Strickland
Executive Committee	John McLennan Doug Blankenship Zach Frone Joe Morris Alain Bonneville Hunter Knox Giorgia Bettin Travis McLing Lianjie Huang Tim Kneafsey Roland Horne

	Bill Roggenthen Ahmad Ghassemi Michelle Robertson
SURF Coordination, Logistics, and Safety-related activities	Paul Schwering Pat Dobson Tim Kneafsey Vince Vermeul Chris Strickland Jaret Heise Markus Horn George Vandine Tim Baumgartner Paul Bauer David Rynders Shane Heydon Jason Connot Timm Comer Craig Ulrich Bill Roggenthen Mathew Ingraham Jeff Burghardt Hunter Knox Earl Mattson Megan Smith Michelle Robertson

ABSTRACT

The EGS Collab project performed well-monitored rock stimulation and flow tests at the 10-m scale in an underground research laboratory to inform challenges in implementing enhanced geothermal system (EGS) technology. This project, supported by the US Department of Energy, gathered data and observations from the field tests and compared these to simulation results to understand processes and to build confidence in numerical modeling of the processes. The project consisted of 3 Experiments, each comprising test and testbed design, many individual tests, numerical simulation, and analysis. The Experiments were performed in two deep underground testbeds at the Sanford Underground Research Facility (SURF) in Lead, South Dakota. Field experiments are now complete, significant data sets have been collected and analyzed, and some analysis continues.

Experiments using underground test facilities have many advantages in that they allow:

- Three-dimensional characterization of the stimulated volume by complementary geophysical methods surrounding the experiment
- Using techniques that are currently not applicable under geothermal condition to provide processes insight
- Comprehensive tracer testing and detailed characterization of complex fluid movements
- Understanding the geometry of the stimulated network at the meso-scale and its implications for effective fracture surface area, rock block size, and heat exchange.

Underground testing has its own set of complications, however, which affect the ability to perform tests as desired and affect the experiment results. Included here are the inability to flow at desired injection rates due to stress gradients caused by drift cooling, and the need to strongly limit induced seismicity because the distance to people and equipment.

Experiment 1 examined hydraulic fracturing at a depth of 1.5 km in a well-characterized phyllite. Eight subhorizontal boreholes were used in this Experiment. Geophysical monitoring instrumentation was deployed in six boreholes to monitor stimulation events and flow tests. The other two boreholes were used to perform and carefully measure water injection and production. More than a dozen stimulations and nearly one year of flow tests in the testbed were performed. Detailed observations of processes occurring during stimulation and dynamic flow tests were collected and analyzed. Flow tests using ambient-temperature and chilled water were performed with intermittent tracer tests to examine system behavior. We achieved adaptive control of the tests using close monitoring of rapidly disseminated data and near-real-time simulation. Numerical simulation was critical in answering key experimental design questions, forecasting fracture behavior, and analyzing results. We were successful in performing many simulations in near-real-time in conjunction with the field experiments, with more detailed simulations performed later.

Experiment 2 was intended to examine hydraulic shearing of natural fractures at a depth of 1.25 km in amphibolite. The stresses, rock type, and fracture conditions are different than in Experiment 1. The testbed consists of 9 boreholes, in addition to 2 exploratory characterization boreholes. Four boreholes drilled as two fans of 2 monitoring holes contained grouted-in monitoring sensors. The remaining five open boreholes drilled in a five-spot pattern were adaptively used for injection, production, and monitoring. Approximately five fracture set orientations were encountered in the

testbed along with a low-stress rhyolite sill at 35 m below the access drift in exploratory well TV4100. The testbed was designed to optimize the potential for shear stimulation while also avoiding the low-stress rhyolite. Experiment 2 focused on stimulating a fracture in the most likely orientation to shear, however shear stimulation did not occur probably due to cementation from natural secondary mineralization. Other fracture sets encountered were also cemented and had orientations less likely to shear.

Experiment 3 consisted of several stimulations in the same testbed as Experiment 2 allowing different stimulation approaches including ramped-rate injection, rapid injection, and oscillating-pressure injection. Ultimately these methods created hydraulic fractures, one of which was used for a medium-duration cold water injection test.

The major findings of the EGS Collab Project include:

1. Significant shear stimulation did not occur during our stimulation attempts. Shear stimulation may occur but under a limited set of conditions not encountered.
2. Our stimulations resulted in hydraulic fractures that required hydraulic propping. Pumping at pressures exceeding the minimum principal stress may not be feasible in an enhanced geothermal system.
3. The systems we generated were complex hydraulic fracture/natural fracture systems, and these systems changed over time in response to applied pressures and flowrates and to unknown stimuli.
4. The project attempted alternative stimulation methods, which did not provide significant flow improvement.
5. Thermal breakthrough was not achieved as designed, most likely because flow to production boreholes was not adequate.
6. The combination of geophysical tools used provided excellent understanding of many important processes.
7. Microearthquakes (MEQs) didn't necessarily identify flow paths.
8. Engineering tools bounding expected seismicity are needed.

This report provides a summary of tests and analyses performed for EGS Collab Experiment 2 (Shear Stimulation in Testbed 2) and Experiment 3 (Alternative Stimulation methods). Much of the EGS Collab work has been published in journals and conference papers, presented in conferences, included in written reports, and submitted in data sets to the Geothermal Data Repository (GDR). The entirety of these written works is included as an appendix to this report, and this report serves as a summary and framework pointing to these published papers, presentations, and reports.

1 INTRODUCTION

Enhanced or engineered geothermal system (EGS) technology offers tremendous potential as an energy resource supporting the energy security of the United States, and implementation is being examined worldwide. Estimates exceed 500 GWe for the western US, surpassing the resource base hosted by conventional hydrothermal systems (Williams et al., 2008), and up to an order of magnitude larger including the entire United States (Augustine, 2016). Implementation of an EGS will typically require stimulation to generate appropriate in-situ conditions allowing communication among multiple wells. Techniques to perform these stimulations require greater understanding for implementation. Additional improvements needed for implementing EGS technology include improving imaging and monitoring techniques for permeability enhancement and evolution, understanding and managing associated seismicity, improving technologies for zonal isolation for multistage stimulations under elevated temperatures, developing technologies to isolate zones for controlling fast flow paths within the reservoir to reduce early thermal breakthrough, and developing scientifically-based long-term EGS reservoir sustainability and management techniques.

The approach of the EGS Collab project was to refine our understanding of rock mass response to stimulation using accessible deep rock. We performed 10-m spatial scale experiments under stresses relevant to a full-scale EGS (at 1.25 and 1.5 km depth) in crystalline rock. Experiments using underground test facilities have many advantages in that they allow: 1) three-dimensional characterization of the stimulated volume by complementary geophysical methods surrounding the experiment, 2) using techniques that are currently not applicable under geothermal condition to provide processes insight, 3) comprehensive tracer testing and detailed characterization of complex fluid movements, and 4) understanding the geometry of the stimulated network at the meso-scale and its implications for effective fracture surface area, rock block size, and heat exchange. Underground testing has its own set of complications, however, which affect the ability to perform tests as desired and affect the experiment results. Included here are the inability to flow at desired injection rates due to stress gradients caused by drift cooling, and the need to strongly limit seismicity because the distance to people and equipment.

Our tests and analyses were performed to support validation of thermal-hydrological-mechanical-chemical (THMC) modeling approaches. In addition, the EGS Collab project tested and improved novel and conventional field monitoring tools. By observing system behavior during our experiments, we gained insight into permeability enhancement and evolution in crystalline rock. These observations and interpretations provide understanding of creating sustained and distributed permeability for heat extraction in an EGS reservoir by generating new fractures that complement existing fractures.

The project consisted of three multi-test experiments to increase understanding of 1) hydraulic fracturing (Experiment 1), 2) shear stimulation (Experiment 2), and 3) other stimulation methods in Experiment 3. Modeling supported experiment design and observation interpretation. Post-test modeling and analysis were performed to examine the effectiveness of our modeling and monitoring tools and approaches. This is to allow building confidence in and improving the array of modeling and monitoring tools and approaches.

The EGS Collab experiments were conducted at the Sanford Underground Research Facility (SURF) in Lead, South Dakota (Heise, 2015). SURF maintains and upgrades underground

facilities at multiple depths in a variety of rock types remaining from the former Homestake gold mine for scientific investigation. SURF hosts a number of scientific projects ranging from collection and analysis of rock and water samples for biological investigation, to enormous infrastructure-intense multibillion dollar physics experiments. EGS Collab Experiment 1 was performed at 1.5 km depth (the 4850-foot depth level) as shown in Figure 1.1. Experiment 1 tests established a fracture network using hydraulic fracturing that connects an injection well and a production well (Kneafsey et al., 2021a; Kneafsey et al., 2021b; Kneafsey et al., 2021c; Morris et al., 2018). More than a dozen stimulations were performed and the injection and production boreholes were connected (White et al., 2019). Flow tests using initially ambient-temperature water and then chilled water (as an EGS analog) were conducted over the course of a year (Kneafsey et al., 2021a), and tracer tests were intermittently performed to understand flow conditions (Mattson et al., 2019a; Mattson et al., 2019b; Neupane et al., 2020; Wu et al., 2019a; Wu et al., 2019b). Details of Experiment 1 have been extensively covered in previous publications. Please see ***Appendix A - Project Bibliography*** for references to this experiment.

Experiment 2 was intended to investigate shear stimulation. The testbed for this experiment (Testbed 2) is at 1.25 km depth (4100-foot depth) (Figure 1.2). This testbed is in the Yates amphibolite (a blocky, low permeability rock) with subsurface stress conditions different from those of Experiment 1 (Ingraham et al., 2020). Based on information available at the time, several sets of analyses showed a reasonable probability of shearing if a sufficiently weak fracture with an appropriate orientation relative to the stress field were intercepted at the site (Burghardt et al., 2020; Dobson et al., 2018; Singh et al., 2019). Fractures and features observed at the drift wall were mapped, and a 10 m horizontal borehole (TH4100) and a 50 m vertical borehole (TV4100) were drilled. TV4100 penetrated an unexpected ~10m thick rhyolite layer within the amphibolite that is likely to be continuous and present beneath our testbed (Figure 1.2). Eighteen stress tests were performed in TV4100, eight of which used the Step-Rate Injection Method for Fracture In-Situ Properties (SIMFIP) tool (Guglielmi et al., 2015; Guglielmi et al., 2021; Guglielmi et al., 2014) to quantify three-dimensional displacement during testing. These stress tests showed significant stress heterogeneity and lower than expected stress anisotropy (Ingraham et al., 2020). Instantaneous shut-in pressures (ISIP – providing an estimate of minimum principal stress) in the deeper amphibolite below the thick rhyolite layer were ~ 27.6 MPa (4000 psi), ~ 18.6 MPa (2700 psi) in the rhyolite, and ~ 21.4 MPa (3100 psi) in the upper amphibolite (Kneafsey et al., 2021a). A sleeve fracture reopening test conducted above the rhyolite layer, together with the absence of borehole breakouts suggests that the most probable magnitude of the intermediate principal stress, which is subhorizontal, is between 30 and 40 MPa (Burghardt et al., 2022). Since the lithostatic stress at the site is approximately 35 MPa, this places the stress state as transitional between a normal faulting and strike-slip regime. Because of the low stress in the rhyolite and the complexity that it introduced, Experiment 2 was designed to be entirely *above* the rhyolite layer.

Experiment 3 was also performed in Testbed 2. The tests performed in Experiment 3 include a slow ramped increase in stimulation flow rate in an attempt to create a fracture that was more likely to follow natural fractures, and shear at a later time in the stimulation. The second test of Experiment 3 injected water with a cyclic pressure profile. The rationale for this method was that in the presence of stresses that could shear the resulting fracture, cyclic stimulation may create scalloped fracture faces which may be more prone to self-propping. The third method tested was hydraulic fracturing providing a baseline for comparison. Ultimately these methods created hydraulic fractures, one of which was used for a weeks-long cold-water injection test.

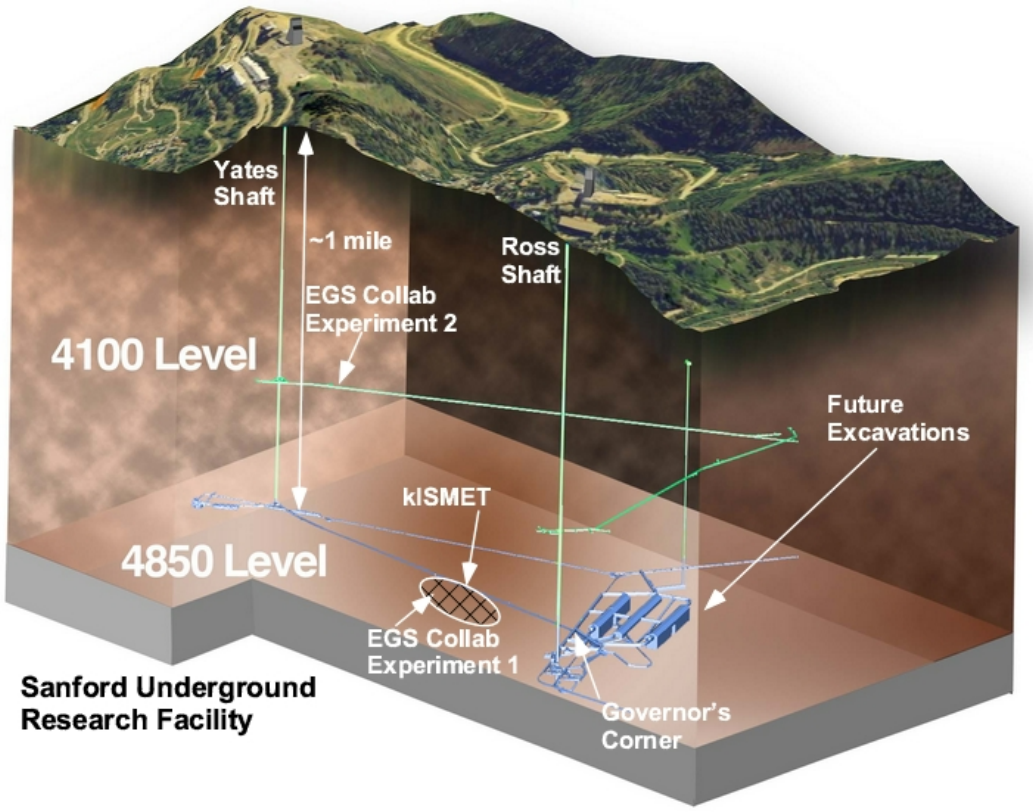

Figure 1.1: Schematic view of the Sanford Underground Research Facility (SURF), depicting a small fraction of the underground facilities including the Yates (left) and Ross (right) shafts, the 4850 level, the location of the kISMET experiment, Experiment 1, and EGS Collab Experiment 2 on the 4100 level.

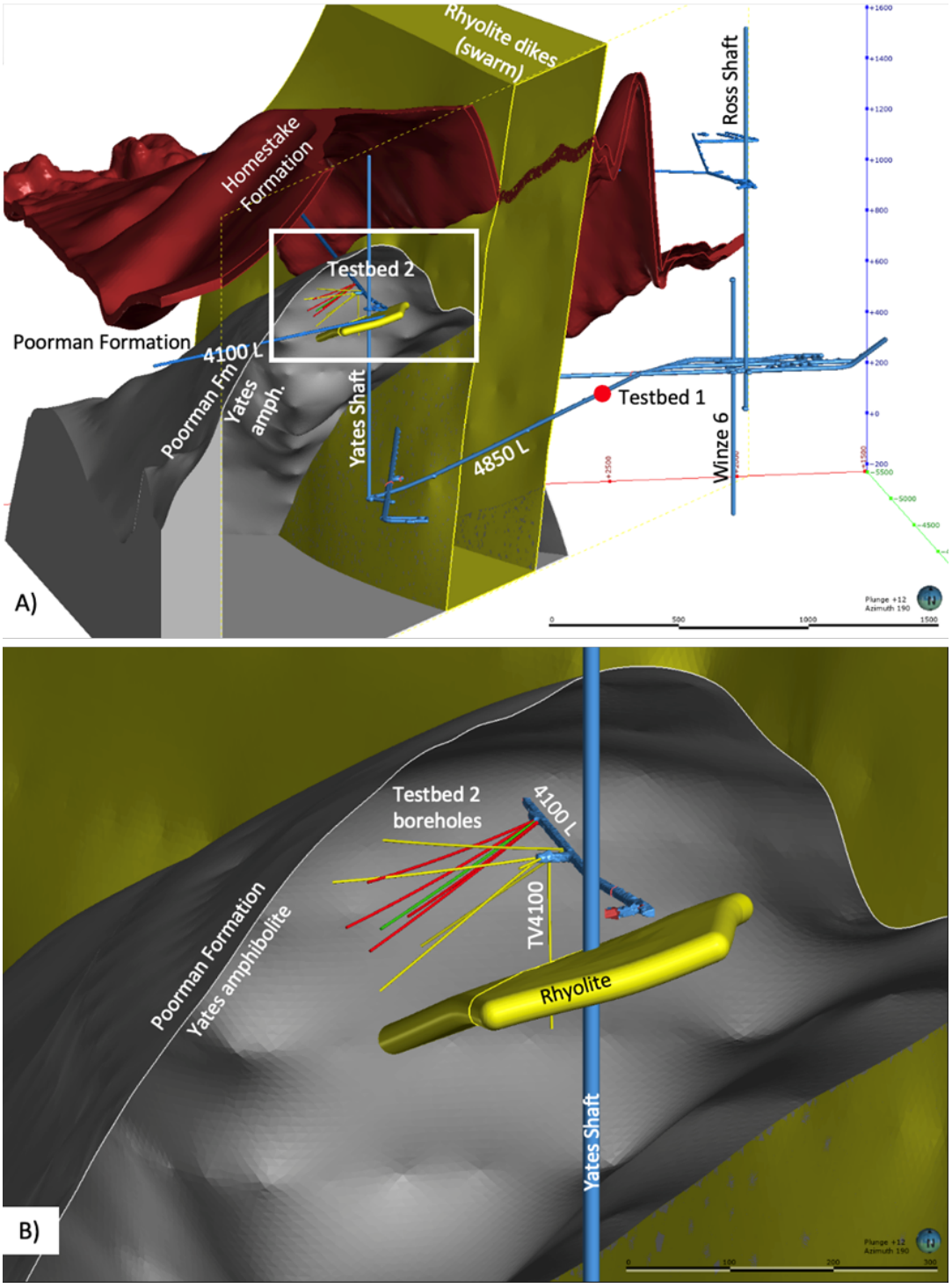

Figure 1.2. Location of EGS Collab testbeds. A) Testbed 1 is located entirely within metasediments of the Poorman Formation on the western limb of Lead Anticline, and Testbed 2 is located in the metabasalt (amphibolite) of Yates unit of the Poorman Formation on the eastern limb of the anticline. Scale bar length 1,500 m. B) Enlarged region showing Testbed 2, the host rock, and location of the rhyolite encountered in an exploratory hole (TV4100). The grouted-monitoring wells are yellow and open test wells are red and green. Scale bar length 300 m.

This report provides a summary of tests and analyses performed for EGS Collab Experiment 2 (Shear Stimulation in Testbed 2) and Experiment 3 (Alternative Stimulation methods). Much of the EGS Collab work has been published in journals and conference papers, presented in conferences, included in written reports, and submitted in data sets to the Geothermal Data Repository (GDR). A bibliography and the entirety of these written works is included as ***Appendix A - Project Bibliography*** to this report. This report serves as a summary and framework pointing to these published papers, presentations, and reports. Most of the EGS Collab works are indexed by Google Scholar (https://scholar.google.com/citations?hl=en&user=h-rd4hkAAAAJ&view_op=list_works&authuser=1&sortby=pubdate) and can be found easily from that site. Additionally, many data sets have been submitted to the Geothermal Data Repository (***Appendix B - Data Submissions***).

The major findings of the EGS Collab project include:

- Shear stimulation was not achieved, and testbeds were created with hydraulic fractures that were hydraulically propped. Pumping at pressures exceeding the minimum principal stress to hydraulically prop fractures may not be feasible in an enhanced geothermal system.
- Hydraulic fractures propagated towards the drifts as a result of stress gradients caused by temperature gradients as expected.
- Thermal breakthrough was not definitively achieved in any experiment.
- Microearthquakes (MEQs) didn't necessarily identify flow paths.
- The systems we generated were complex hydraulic fracture/natural fracture systems, and these systems changed over time in response to applied pressures and flowrates and to unknown stimuli.
- Simple testbeds (field sites) provide significant complexity.
- The project attempted alternative stimulation methods, which did not provide significant flow improvement.
- Tracer dispersion in tubing exceeded dispersion in rock limiting interpretation of tracer tests.
- Engineering tools bounding expected seismicity are needed.

2 DATA MANAGEMENT

The EGS Collab project generated substantial amounts of research data, over 6.7 TB of which are available on the Geothermal Data Repository (GDR) at https://gdr.openei.org/egs_collab. (***See Appendix B Data Submissions***) A project overview, shift reports, core logs, experiment summaries, and additional project metadata are available on the EGS Collab Wiki at https://openei.org/wiki/EGS_Collab_Project_Overview.

A guiding principle of the EGS Collab project was to enable research and scientific discovery through the timely dissemination of information. This proved challenging given the source of experiment data (located underground in the SURF) and the size of the EGS Collab team. The project team consisted of numerous researchers from ten US DOE National Laboratories, eight universities, and several industry partners. An organized, collaborative, and cloud-based data management system (DMS) was developed in order to facilitate timely access to project data for the many organizations involved. The EGS Collab DMS provided project partners with a universally accessible, central access point to project data (Weers et al., 2018). The centralized access model helped ensure project partners had easy access to the latest version of the data, reducing the potential for errors resulting from different versions of source data, while also reducing the time and effort needed to transfer large datasets to team members. The timely dissemination of EGS Collab data to the diverse array of project participants, which included modelers, geophysicists, hydrologists, senior scientists, graduate students, and industry professionals, allowed for a multitude of perspectives to be considered. Important insights were often discovered by broader team members and were made possible by the EGS Collab project's devotion to centralized, universally accessible data (Fu et al., 2021b).

Over the course of the project, the EGS Collab DMS evolved into the Data Foundry, a tool developed to overcome institutional barriers to data access and address the limitations of other data management tools not inherently designed for large, collaborative projects. (Weers et al., 2020). The Data Foundry was used to share both raw and processed data with project team members throughout the project and functioned as a secure, cloud-based sandbox for the team to collaborate on the organization, processing, and analysis of data, as well as the development of models and visualizations. This also allowed the team to refine the data, attribute metadata, and ensure quality prior to publication.

Whenever possible EGS Collab project data were made available to the public on either the Geothermal Data Repository or the EGS Collab Wiki. Datasets too large for traditional download were made available in a universally accessible, cloud-based data lake through the GDR's integration with the Open Energy Data Initiative (OEDI). The EGS Collab project has made over 5 terabytes (TB) of Continuous Active-Source Seismic Monitoring (CASSM) data available in a data lake on Amazon Web Services (AWS), accessible for free via AWS command line tools, native cloud services, or any cloud-enabled compute system (Weers et al., 2021). To facilitate the easy publication of project data, the Data Foundry was integrated with the GDR to allow the team to publish datasets by simply selecting them and clicking a "Send to GDR" button – Figure 2.1 (Weers et al., 2020). This helped to streamline data submission and further reduce data transfer times, freeing up more project resources for research activities.

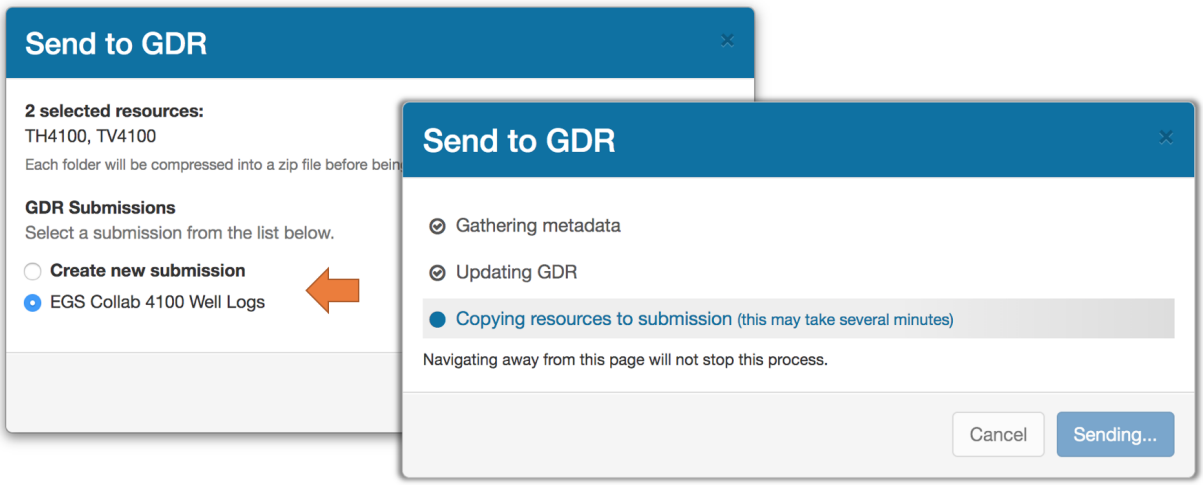

Figure 2.1: Screenshots showing the "Send to GDR" functionality in the Data Foundry

Analytics on digital impact metrics including downloads of EGS Collab project data were collected through the GDR and made available to project stakeholders in monthly and quarterly reports. As of this paper, EGS Collab data have been downloaded over 13,600 times.

3 TESTBED DESCRIPTION

Nine ~10 cm diameter (HQ wireline) subhorizontal boreholes from 55 to 80 m deep were drilled for this experiment (Figure 3.1). Two sets of 2 monitoring wells containing grouted sensors fan out from a location in the Battery Alcove (AMU and AML) and a location in the drift (DMU and DML). An injection well (TC) surrounded by four open production/monitoring wells (TU, TL, TN, TS) extend from Site B. Five joint sets were considered in the analyses of hydraulic shearing (Burghardt et al., 2022). Well TC was oriented to optimally intersect shear-oriented fractures while also avoiding the sub-horizontal rhyolite zone below the testbed (Kneafsey et al., 2022). Two earlier boreholes (TV4100 and TH4100) were drilled to better characterize the geology and fracture orientations of this area and to conduct stress measurements used to design the geometry of the testbed layout (e.g., Ingraham et al. (2020)).

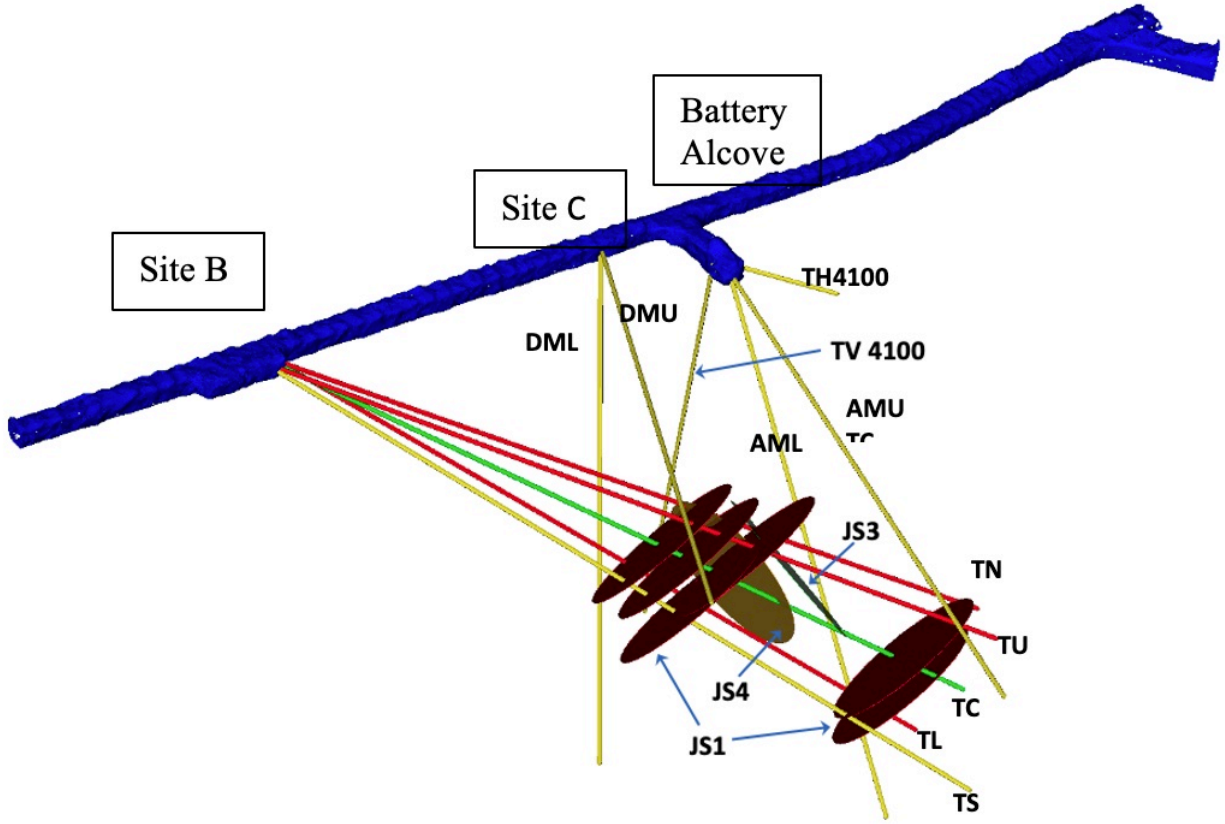

Figure 3.1. Borehole orientations for Experiment 2, oblique view. The thick blue object represents the drift (mine tunnel), the green line represents the injection well, red lines represent production wells, and yellow lines represent monitoring wells. Other than the vertical well TV4100, all wells are subhorizontal. Disks indicate natural fracture orientations that connect the injection and production wells and hotter colors indicate greater slip tendency. JS1 has a higher slip tendency than other fracture set orientations.

The EGS Collab Testbed 2 was constructed entirely within the Yates Unit of the Poorman Formation. The Yates unit consists of amphibolite that shows strong textural (grain-size) as well as compositional layering (hornblende and plagioclase). The amphibolite is cross-cut by calcite veins (Caddey et al., 1991). Along with these calcite veins, local oxidized sulfide layers define the

zones of weakness in the rock. At the testbed site, the host rock consists of amphibole, plagioclase, and chlorite with minor amounts of sulfides. Structurally, the testbed is located on the eastern limb of a southerly plunging Lead Anticline (Figure 1.2). Over the geologic history, the host rock was subject to multi-deformation phases and igneous intrusions. Some of the noted deformation occurred during the Precambrian (Paleoproterozoic) time that created fractures which were subsequently folded and filled with minerals consisting primarily of calcite and quartz. During the Tertiary (Paleogene) time, rhyolitic intrusions occurred that resulted in a series of fractures and shear zones. Tertiary rhyolite dikes, mostly striking along NW-SE direction, intersect several geologic units in the area including Yates amphibolite. Most of the rhyolite dikes in the vicinity of testbed are located to the western side; however, one of the exploratory holes (e.g., Borehole TV4100) encountered a thick rhyolite dike that was correlated with an exposure in the 4100 drift near the Yates Shaft, and it is expected that this rhyolite body extends to the area underneath the stimulated volume of rock in the Testbed 2 (Figure 1.2).

Figure 3.2 is a geologic map showing a portion of the 4100 Level where EGS Testbed 2 was constructed. These data were derived from the Homestake/SDSTA geologic database that was developed over the long history of mining in the facility, and three units were mapped on this level. The Poorman Formation consists of the two informal units including the Yates Unit (purple) defined as the lower part of the Poorman Formation and the upper part of the Poorman which is a metasedimentary carbonate mica phyllite (Caddey and others, 1991). Other formations in this figure include the Homestake Formation (brown), and the Ellison Formation (blue).

Only two geologic units were encountered during the drilling and site characterization of Testbed 2. These were the rocks of the Yates Unit, a Precambrian amphibolite, and a Tertiary rhyolite intrusive that was encountered in Borehole TV4100. The amphibolite in the testbed consists of an assemblage of amphibole, chlorite, and plagioclase that is generally massive although a weak foliation can be recognized where the rock is freshly exposed. The rock faces usually are not well-exposed because dust and surface alteration have accumulated over the extended time since it was mined. Work in the testbed was confined to the amphibolite, and the testbed was designed to avoid the rhyolite.

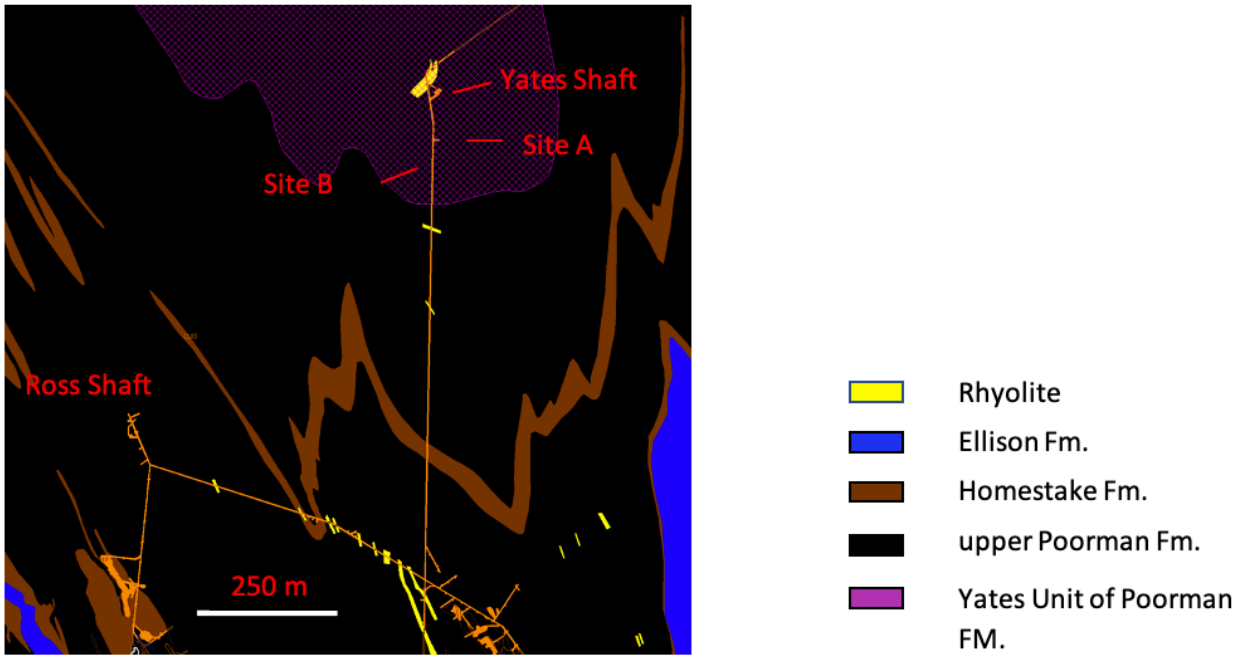

Figure 3.2. Geologic map of the 4100 Level. The map units are all Paleoproterozoic (Precambrian) in age with the exception of the rhyolite which was intruded during the Paleogene (early Tertiary). The rhyolite is only mapped where encountered in drifts and drill holes.

In addition to this description of Testbed 2 and those presented in Dobson et al. (2018); Johnson et al. (2022); Kneafsey et al. (2022); Ulrich et al. (2022), detailed descriptions of mineralogy, fractures (e.g. Figures 3.3 and 3.4), foliation, and fracture-filling minerals observed both in the drift and in boreholes are presented in ***Appendix C - EGS Collab Testbed 2 Fractures and Visualizations***, and ***Appendix D - Mineralogic and Petrologic Characterization of the 4100 Test Bed***.

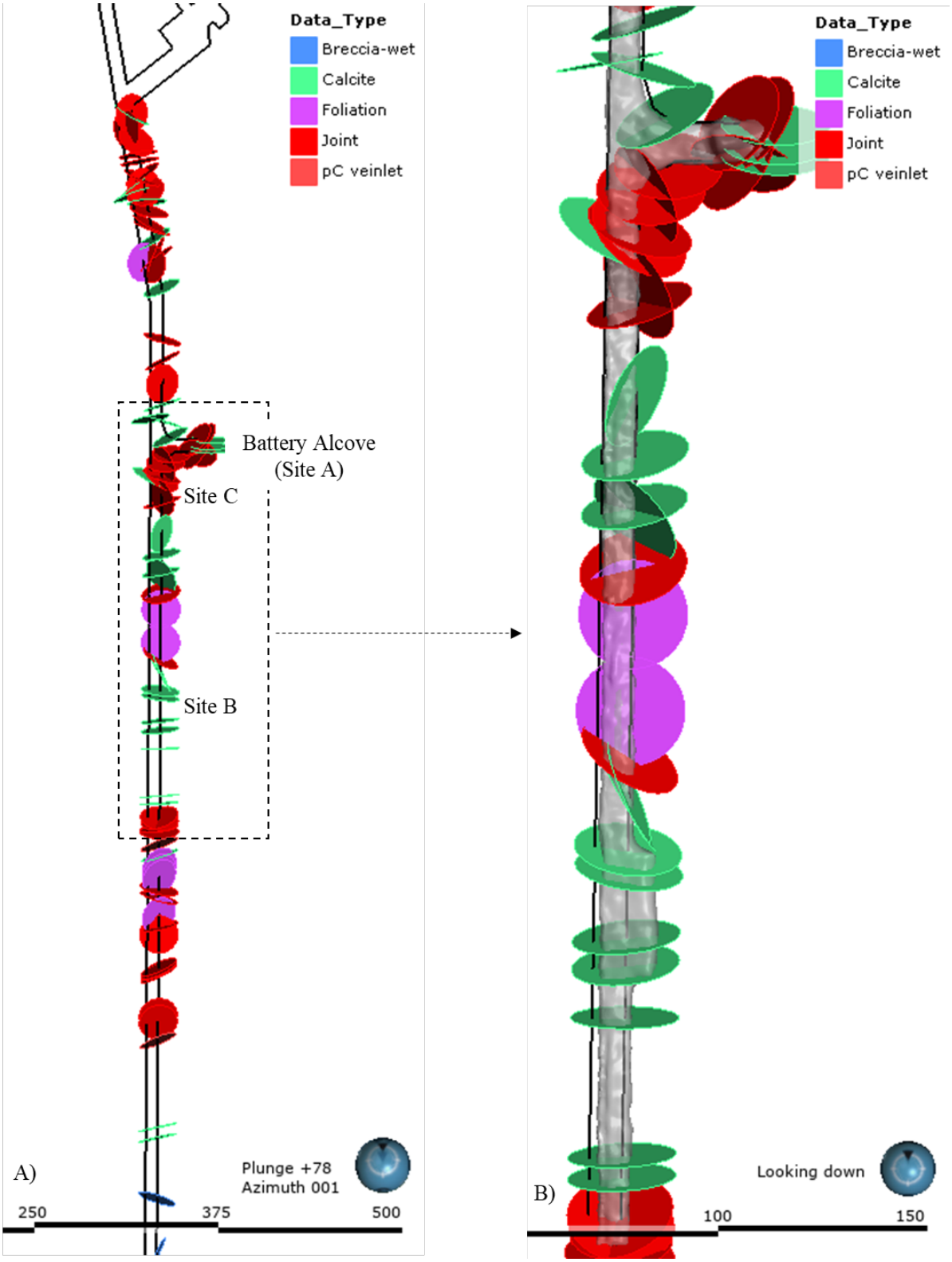

Figure 3.3. (A) Map showing various fractures identified along the 4100-level drift south from Yates Shaft. (B) Enlarged portion of the map showing fractures at Testbed 2 location. Fracture mapping was conducted on 9/18/2018 and 3/27/2019.

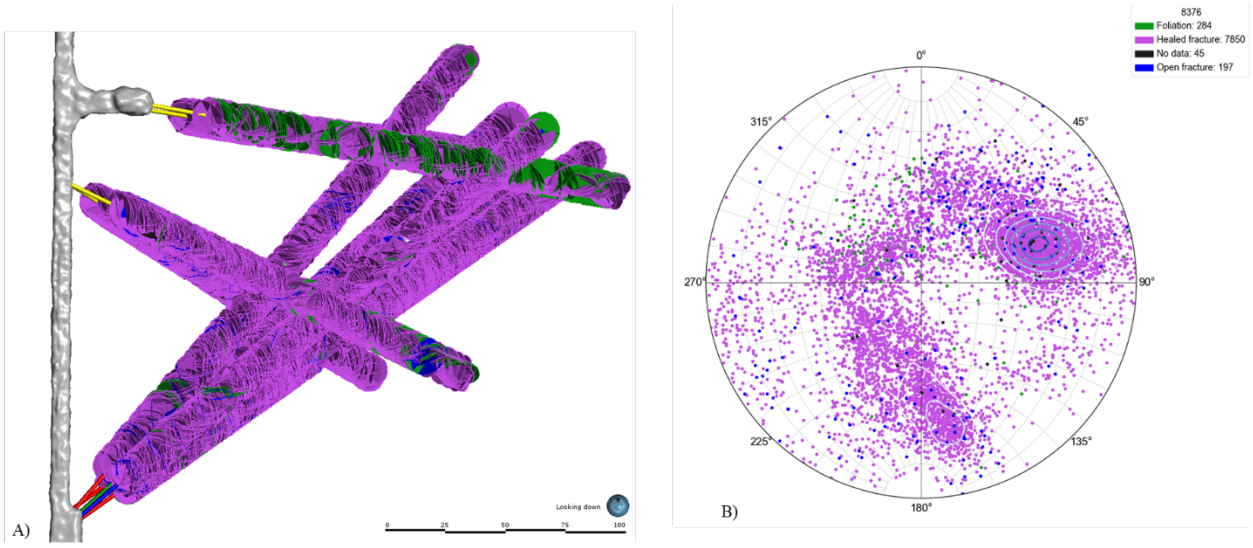

Figure 3.4. Discontinuity features identified after optical televiewer image interpretation for all Testbed 2 boreholes. (A) Discontinuity features plotted as circular disks along the boreholes, and (B) stereonet pole plots (equal angle, lower hemisphere) of the discontinuity features. Foliations are green disks and points, healed fractures are purple disks and points, open fractures are blue disks and points, and unidentified (no data) are black disks and points.

4 TESTBED CHARACTERIZATION

4.1 Core Logging

Of the nine boreholes, four holes were used as monitoring wells which were drilled from Sites A and C (Figure 3.1). An injection well and four production/monitoring wells were drilled from Site B. The EGS Collab and supporting RESPEC Company LLC teams oversaw the drilling operation and logged the lithographic and geotechnical characteristics of the core. During drilling, the core was retrieved in 5-foot runs and transferred to photography stations.

Two photography stations were set up to capture images of all sides (360-degrees) around the core. One photography station included two digital cameras mounted on a sliding rail that snapped close-up pictures of segments of the core (Figure 4.1 A. and B.). The other photography station consisted of a high-resolution phone camera attached to a sliding rail that took panoramic photos of the entire run of core in one single image (Figure 4.1 C.). Photos were taken of the core both wet and dry and the core was rotated to capture its entire circumference. Photos were uploaded after every core run to a central drive location and this allowed viewers to analyze digital copies of the core remotely with very little time lag (Figure 4.2).

Along with photographs, the core was logged and sketched on log documents (Figure 4.1 D.). Natural fractures, healed fractures, mechanical breaks caused by drilling, and also depth and orientation of fractures were noted. Additionally, core recovery was noted along with Rock Quality Designation (RQD), lithology, general geology such as foliation, induration, intrusions of other minerals, and any other unique features. Details of the core were annotated along the log that provided descriptions of the teams' observations.

Once the core was logged and photographed, it was placed in sturdy wooden core boxes (Figure 4.1 E.) and labeled with the hole identification name, the run it was taken from, recovery, RQD, and the depth it was drilled at. The core boxes were brought to the surface and transferred to an onsite long-term core storage facility.

A.

B.

C.

D.

E.

Figure 4.1. A. Core photography station, B. Photographing core, C. Panoramic photo station, D. Examining and logging core, E. Core in core boxes.

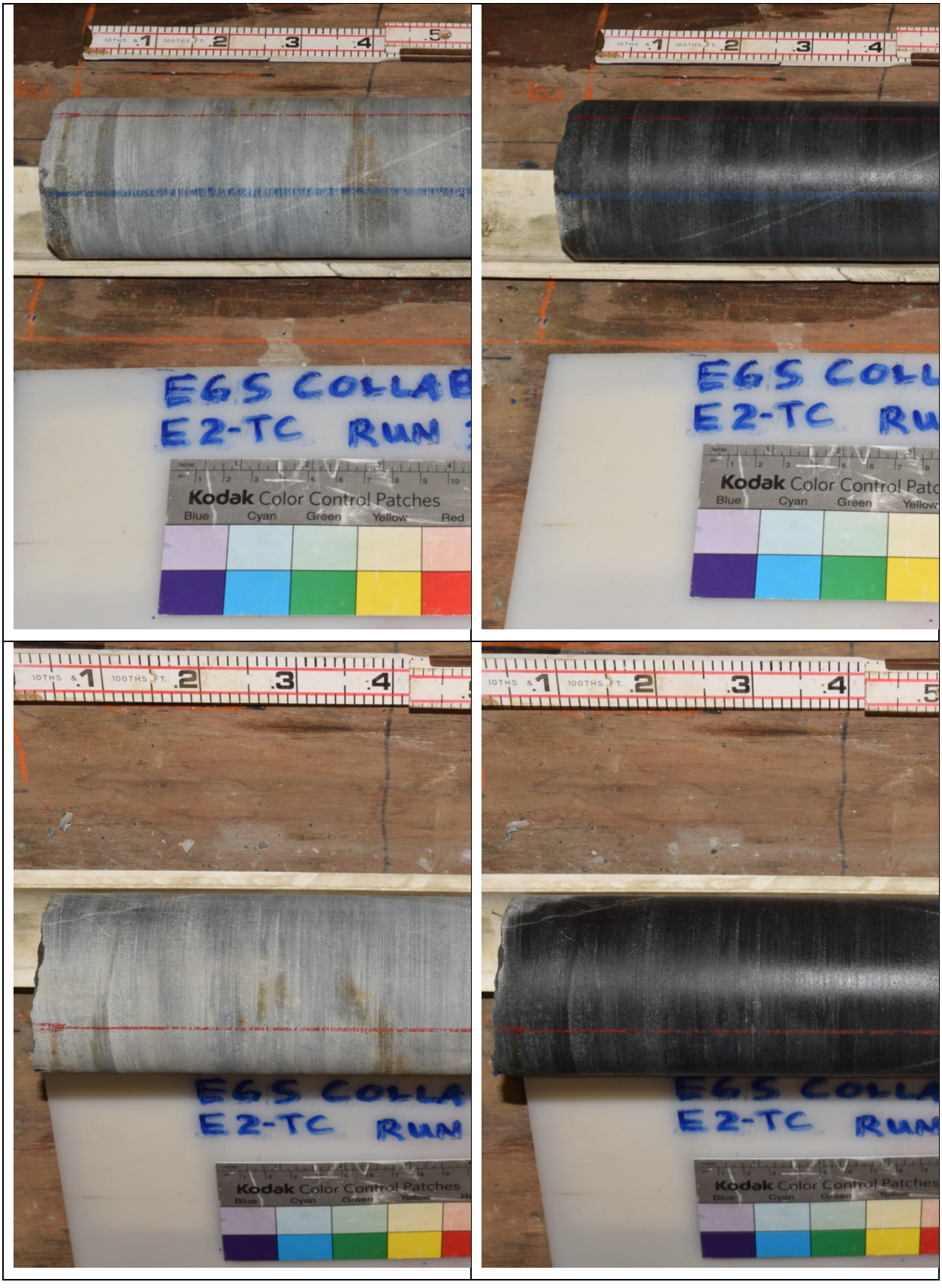
EGS COLLAB
E2-TC RUN
Kodak Color Control Patches
Blue Cyan Green Yellow Red
EGS COLL
E2-TC RU
Kodak Color Control Patc
Blue Cyan Green Yellow
EGS COLLA
E2-TC RUN
Kodak Color Control Patches
EGS COLLA
E2-TC RUN
Kodak Color Control Patches

A.

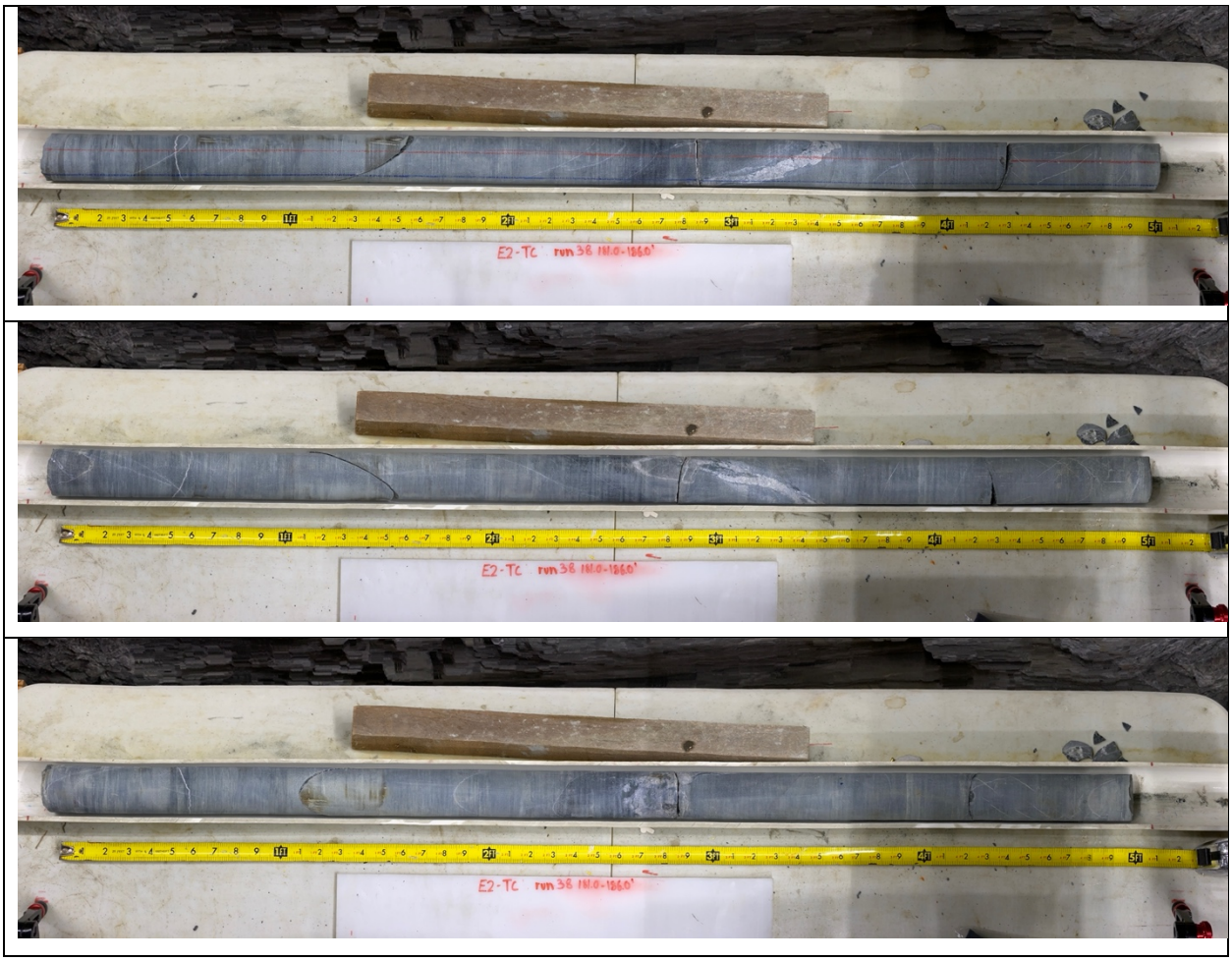

B.

Figure 4.2. Example A. wet and dry core photos and B. panoramic core photos.

4.2 Geophysical Wireline Logging

Characterization of Testbed 2 was in part completed with a suite of wireline geophysical tools. These included True North Gyro, Fluid Temperature Conductivity (FTC), Optical (OTV) and Acoustic (ATV) televiewer, Electrical Resistivity + Gamma (ELOG + Gamma), and Full Waveform Sonic (FWS). These tools provided information about in-flowing fractures (e.g. FTC), thermal gradient from the drift (e.g. FTC), fracture orientation-opening-breakouts (e.g. OTV/ATV), borehole diameter (e.g. ATV), zones of fluid-filled fractures (e.g. ELOG/FWS), fracture fill material (e.g. Gamma/OTV), and rock seismic velocities and elastic properties (e.g. FWS) that are further discussed in Ulrich et al. (2022). Each borehole had single to multiple data collections of each geophysical tool to capture initial testbed state and changes to the testbed from stimulation or inflow of fluids into a borehole.

To better understand the testbed conceptually, different logs were plotted together since all of the tools use a different physics and are sensitive to different rock and hydrologic properties. For

example, Figure 4.4 shows FTC where there is a drastic increase in borehole fluid conductivity that is associated with an open fracture also observed in the OTV log at the contact between amphibolite and a quartz vein. This indicates that fluids are moving from the formation into the borehole and this fracture set could be connected to other fractures within the testbed. Results from the FTC logs indicated only two inflowing (to the borehole) fractures within the testbed: one in E2-AML (Figure 4.4) and the other in E2-DMU. The temperature logs from the FTC were later used to model the temperature distribution from the drift out into the testbed (***See Section 10.1 Thermal Breakthrough Prediction*** below). Rock resistivity data along with natural gamma were collected with the ELOG tool and were used to assess the changing in rock properties throughout the testbed. The resistivity data were also used to model the desired grout formulation to ensure the maximum amount of applied current from the ERT monitoring system would transfer into the formation instead of traveling in the grout along the borehole. An example of compiled logs is shown in Figure 4.5 and highlights a resistivity decrease is associated with a mineralogy change in the amphibolite (red hachured zone of darker rock in OTV, Figure 4.5), where the resistivity decrease is associated with an increase in the gamma response associated with an increase in clay minerals.

Other logs such as the FWS were used to characterize the rock acoustic velocities at different orientations to the testbed. The wave velocities were used in models to predict rock behavior during future stimulation. An example of using FWS to estimate rock modulus is shown in Figure 4.4. In order to understand, predict and select the best locations to stimulate within the testbed a thorough discrete fracture network (DFN) was required attempting to incorporate all data available (See ***Appendix C - EGS Collab Testbed 2 Fractures and Visualizations***). The OTV logs were used to pick all of the features (fractures, veins, foliation, etc.) within each borehole in order to get the orientations for plotting within a 3D geological modeling software package. Given this testbed is located within a former gold mine it was expected that the OTV and ATV logs would contain magnetic interference in their respective orientation data because they use sensed magnetic information to determine their location. Therefore, a north seeking gyro log was collected to substitute for the magnetic orientation data collected by each tool. The gyro data were also used to plot the borehole trajectories within the 3D model. Within the eleven boreholes drilled at Experiment 2 there were a total of 8711 features picked from the OTV logs. Figure 4.6 shows an example of the types of features picked within the testbed. The majority of the picked features were healed or sealed veins and fractures. For simplicity any feature observed in the OTV that had apparent porosity (openings at the borehole wall) was called “open”. This does not mean that the feature is continuously open throughout the testbed. Calling these features open ensured that they were distinguished within the 8711 picked features and could be investigated further during the hydrologic characterization phase.

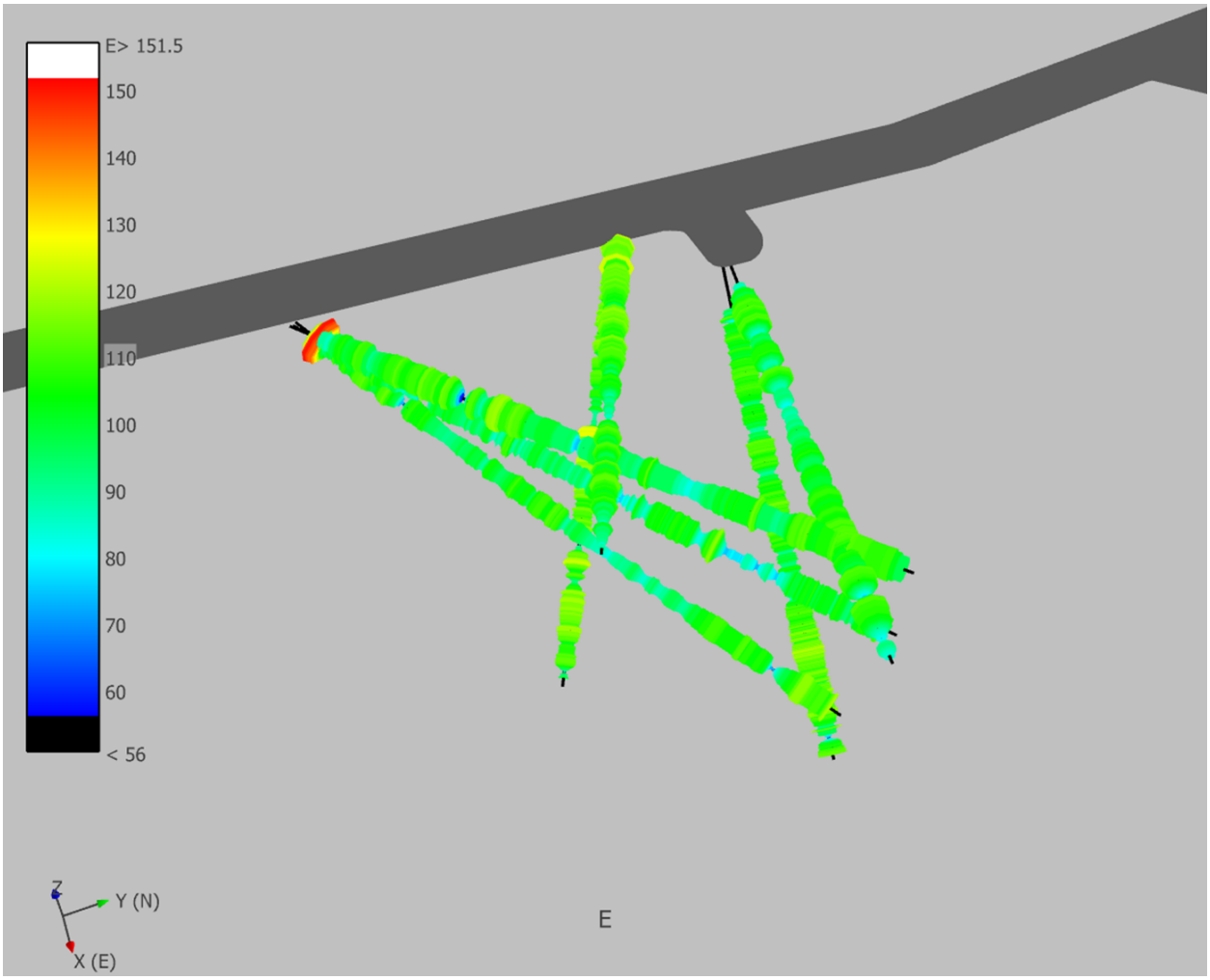

Figure 4.3. Modulus values estimated from FWS data to look for testbed scale structure.

The ATV log was collected in each well during the initial characterization phase. Because the majority of the rock is black, identifying stimulated fractures from the OTV proved impossible, so post stimulation ATV logs were collected to compare against pre-stimulation logs to identify generated fractures and pick their orientations. In cases where the stimulated fracture was an existing fracture a sinusoid could be fit to the fracture to get the orientation. In most cases, the fractures from stimulation were not on existing fractures but instead linked almost orthogonally to existing fractures and were almost in-line with the borehole axis in E2-TC. Since a sinusoid could not be fitted to these very short features a lineation picker (another picking tool) was used to get the orientation of those features as they intersect the boreholes (Figure 4.7).

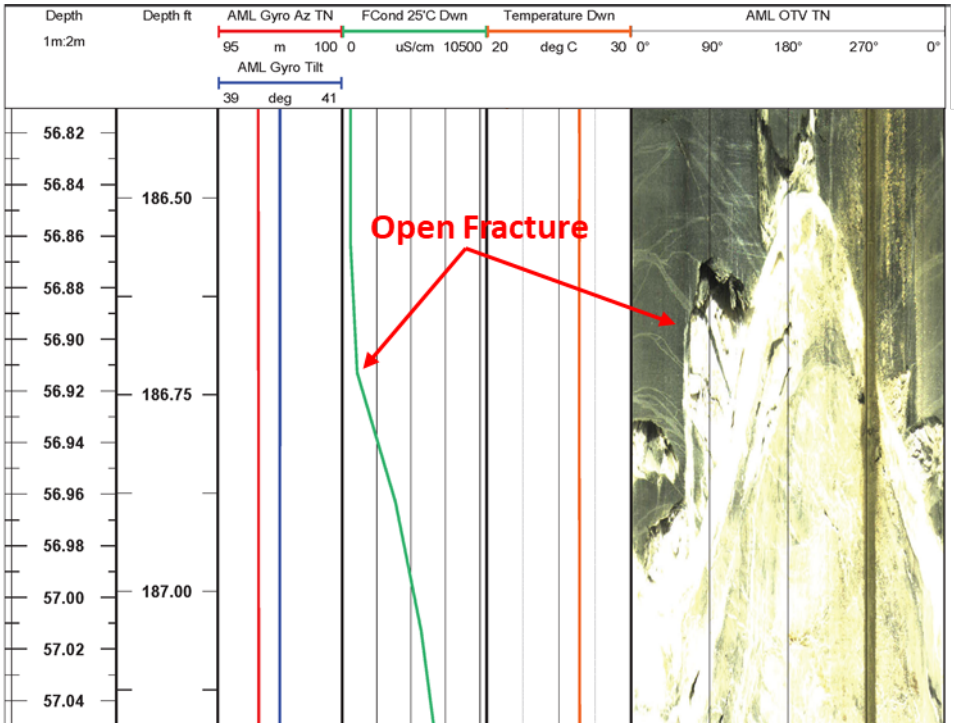

Figure 4.4. The FTC data show a constant temp (orange line) and a conductivity increase (green line) at approximately 186.7 ft along E2-AML that is associated with open fractures at the amphibolite-quartz vein contact.

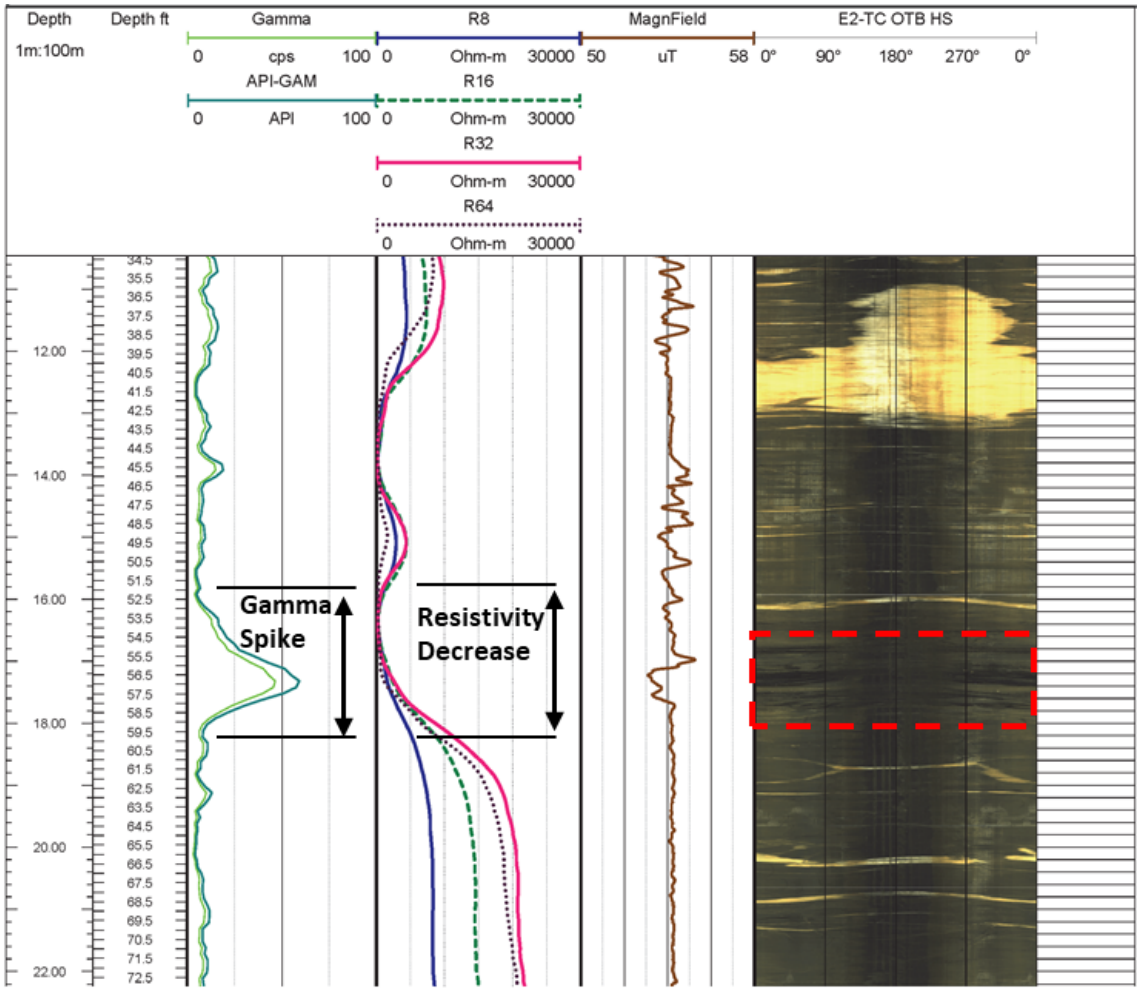

Figure 4.5: Resistivity – Gamma log with Optical Televiewer that shows a gamma spike associated with a change in rock type (red hachured area OTV) and a resulting decrease in resistivity (Borehole E2-TC injection well).

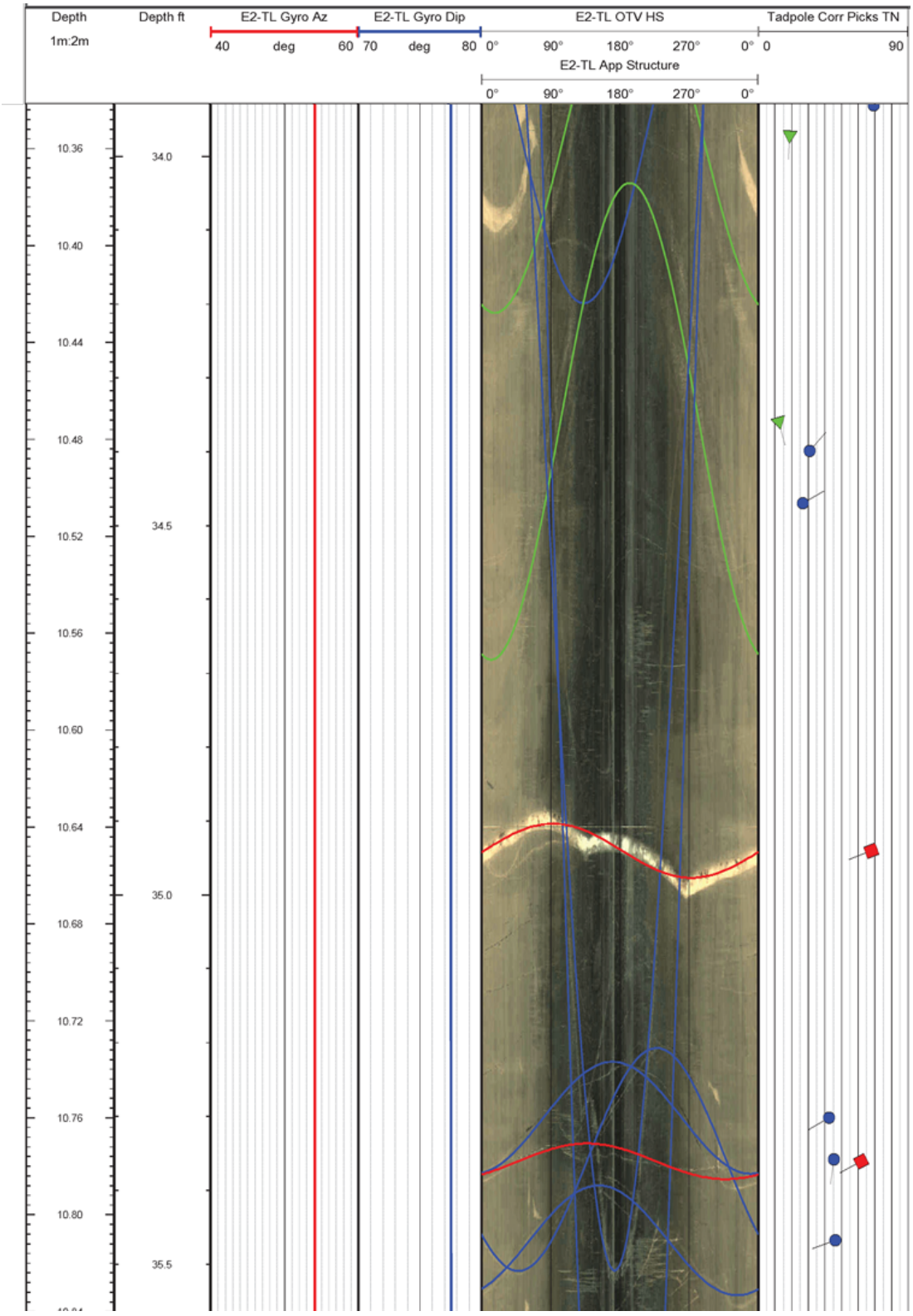

Figure 4.6: Optical borehole image log showing different types of features (green – foliation, blue – healed fractures/veins, and red – open fractures) (Borehole E2-TL, located beneath the injection well).

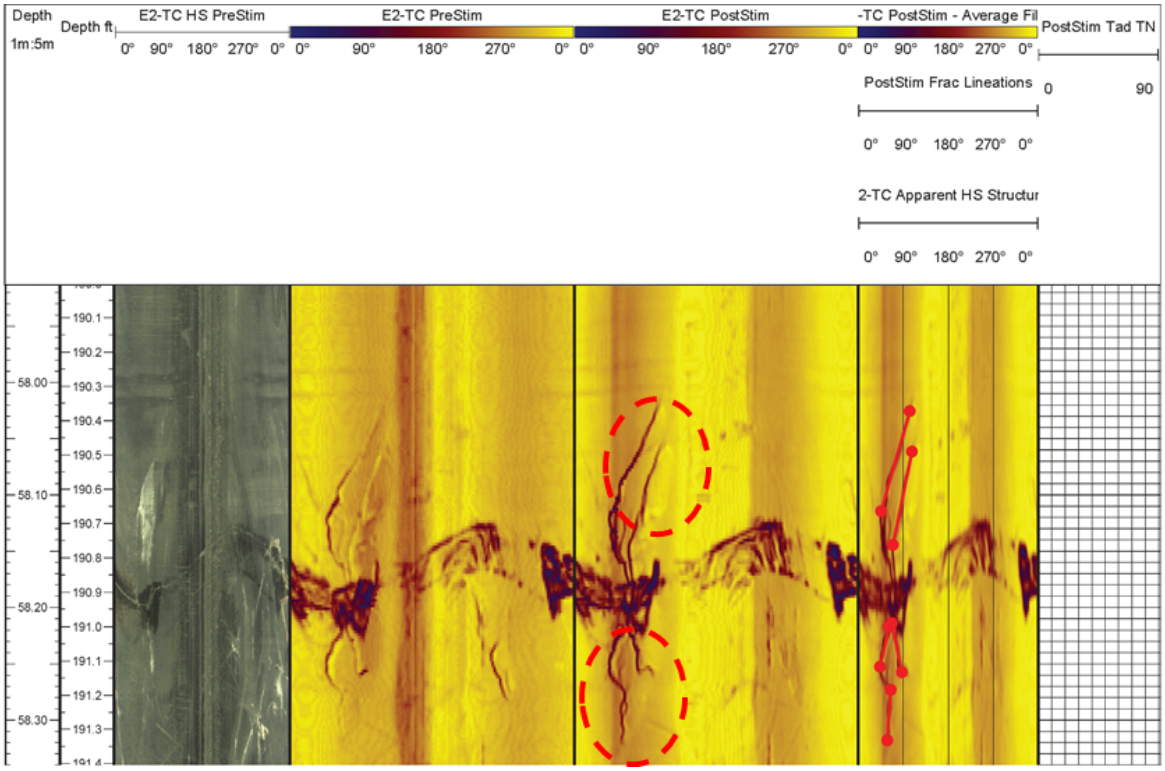

Figure 4.7: PreStim (left gold) and post (middle gold) ATV images in E2-TC show the generated fractures extending the existing borehole fractures. The lineation picks (right gold) are shown on the E2-TC PostStim image.

Surveyed locations of the tops of boreholes, registration of core to optical televiewer log, and seismic calibration locations are contained in ***Appendix E – Hole Locations, Registration of Core to Geophysical Logs, and Seismic Calibration Locations***.

4.3 Core Examination

A physical review of the Testbed 2 core was conducted on Oct 5-6, 2021 to look for fractures to stimulate, features that might influence the experiments, and other interesting testbed features. The example shown in Figure 4.8 compares the physical examination of an observed fracture in the core to its corresponding borehole log. The borehole log does not indicate that the fracture is open, however the core separated at the fracture. This may be from drilling, or it may indicate that larger aperture healed fractures may not necessarily be as strong as the matrix rock. Meng et al. (2022) concluded that the healed fractures can be as strong or stronger than the matrix. Additional insights from the core examination are included in ***Appendix F - EGS Collab 4100' borehole core review***. Measured and literature values for rock and site parameters are contained in ***Appendix G - EGS Collab Experiment 2 Parameter Table***.

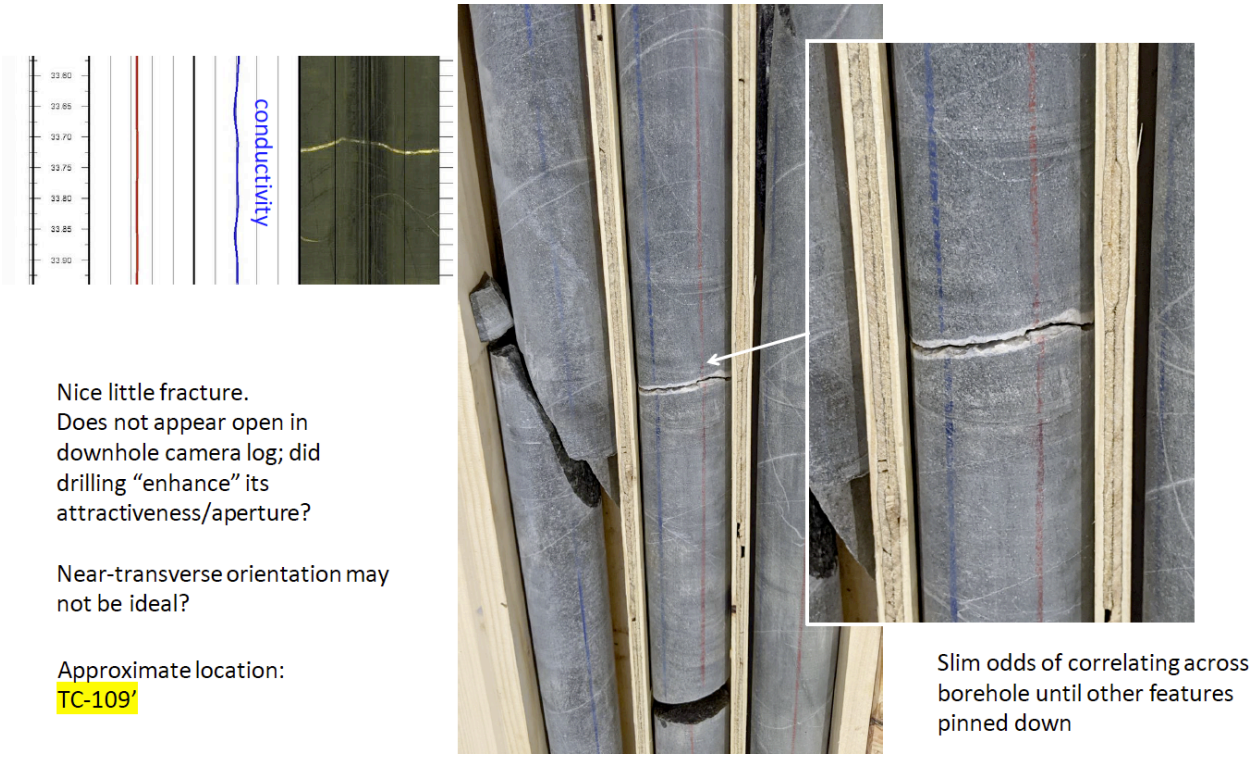

Figure 4.8. Field core examination notes and thoughts compared to wireline logging observations.

4.4 Hydrogeology of the Experiment 2 Testbed

This section summarizes the hydrologic characterization work described further in ***Appendix H - Hydrogeology of the Experiment 2 Testbed***. The hydrologic activities included the following:

- Flow and shut-in tests on TV-4100
- Integration of observations including core and geophysical logging to identify key fractures in the testbed.
- Monitoring water inflow and outflow from borehole during drilling Testbed 2
- Single packer pulse tests to determine the permeability of the testbed rocks

Groundwater flow in the regions of the SURF facility where the COLLAB experiments were carried out is typified by widely-spaced conductive fracture zones with minor seepage and local fracture networks that are isolated or poorly connected to groundwater sources or mine sinks. (Stetler, 2015) compiled data from the DUSEL characterization work of the late 2000's that describes a flow system with few connected fractures with variable pore pressures ranging from 15% to 60% of the hydrostatic gradient from the surface.

Testbed 1 intersected one of these weakly-flowing fracture zones (the "weep" zone) and multiple hydraulically isolated fractures (for example, the OT-P connector). Testbed 2 on the 4100-foot level is in a dry section of the mine, the nearest seeps being ~100 m south of the testbed near the Poorman-Yates contact. Mapping of the drift identified an open fracture near the Battery Alcove that was non-flowing and hydraulically isolated.

Monitoring of water flows to the Testbed 2 boreholes during drilling revealed water losses to the rock rather than water production with the exception of two flowing zones, one in the rhyolite of TV4100 and the other at 49.8 m measured depth in E2-DMU. The TV4100 flowing fracture produced <0.1 liters/min and recovered to approximately 100 psi (0.7 MPa) when shut in. The DMU flowed at about 500 ml/day (0.3 ml/min) and was not shut in for a pressure measurement. An open fracture like the one mapped in the drift at the Battery Alcove was encountered in E2-AML at about 56.2 m measured depth. Like the Battery Alcove fracture, it appears to be isolated hydraulically. None of these fractures projects into the portions of Testbed 2 where stimulation and circulation tests occurred.

The measured water losses and production are given in Table 4.1. Water data were collected during each drilling shift and into September 2021. The loss of water in all boreholes except E2-DMU indicate flow to a sink at lower elevation than the 4100 level, possibly the nearby Yates shaft. The water losses and the shut-in test on TV4100 indicate the initial pore pressures in the testbed are very low compared to the stimulation and circulation pressures.

Single-packer tests were run over the open lengths of all boreholes along with three additional tests at various depths in E2-TC, the planned stimulation hole. The test procedure had three steps (Figure 4.9). The first step was pressuring the test interval to mine-water pressure (~70 psi or 500 kPa) while monitoring the flow rate. For the second step, the test zone was then shut-in to allow the pressure to decay for 30 minutes. Given the low conductivity of the rock the pulses decayed by only about 10% over the 30-minute durations. The third step was a two-minute injection at 25 ml/min using an ISCO syringe pump. For this duration in tight rock, the linear pressure buildup reflects primarily the total compressibility of the test zone and the equipment. Knowing the total compressibility allows calculating the water loss to the borehole during the pulse decay period. Dividing this loss by the time-duration of the pulse gives a flow rate for calculation of transmissivity and hydraulic conductivity assuming a steady state flow, which is reasonable approximation for the relatively small pulse drops. The flowing borehole, E2-DMU was too conductive for the pulse methods. Instead, the flow rate at constant mine-water pressure achieved a steady value of 180 ml/min, which was used for the hydraulic property calculations. Test results presented in Table 4.2 affirm the overall low permeability of Testbed 2.

Table 4.1. Water loss rates to boreholes during drilling and after drilling (September 2021). Gains (outflow from hole) in red.

Borehole	During Drilling		Post Drilling (Sept. 2021)	
	Flow Rate			
	ml/day	m^3/s	ml/day	m^3/s
E2-AMU	90	1.0E-09	23	2.6E-10
E2-AML	107	1.2E-09	114	1.3E-09
E2-DMU	Not Measured		**521**	**6.0E-09**

E2-DML			44	5.1E-10
E2-TU	31	3.6E-10	-	-
E2-TS	21	2.4E-10	-	-
E2-TC	177	2.0E-09	-	-
E2-TN	52	6.0E-10	87.5	1.0E-09
E2-TL	28	3.2E-10	-	-

Table 4.2. Hydraulic test results.

Borehole	Packer Set Depth m	Zone Length m	Head m	Transmissivity m^2/s	Hydraulic Conductivity m/s	Permeability m^2	Test Type
E2-TC	9.1	68.0	47.1	1.9E-09	2.8E-11	2.9E-18	Pressure-Pulse
E2-TU	9.1	67.4	49.3	4.7E-10	6.9E-12	7.1E-19	Pressure-Pulse
E2-TL	9.1	67.4	47.3	2.0E-09	2.9E-11	3.0E-18	Pressure-Pulse
E2-TN	9.1	67.4	47.2	3.1E-09	4.6E-11	4.7E-18	Pressure-Pulse
E2-TS	9.1	71.9	48.0	1.5E-09	2.1E-11	2.2E-18	Pressure-Pulse
E2-DML	9.1	46.0	47.2	1.5E-09	3.3E-11	3.3E-18	Pressure-Pulse
E2-DMU	9.1	45.7	45.8	6.8E-08	1.5E-09	1.5E-16	Steady Outflow
E2-AML	9.1	51.2	47.2	4.0E-09	7.9E-11	8.0E-18	Pressure-Pulse
E2-AMU	9.1	51.2	47.0	1.3E-09	2.5E-11	2.6E-18	Pressure-Pulse
E2-TC	30.5	46.6	47.4	1.5E-09	3.3E-11	3.3E-18	Pressure-Pulse
E2-TC	45.7	31.4	47.3	2.0E-09	6.5E-11	6.6E-18	Pressure-Pulse
E2-TC	61.0	16.2	47.0	2.2E-09	1.3E-10	1.4E-17	Pressure-Pulse

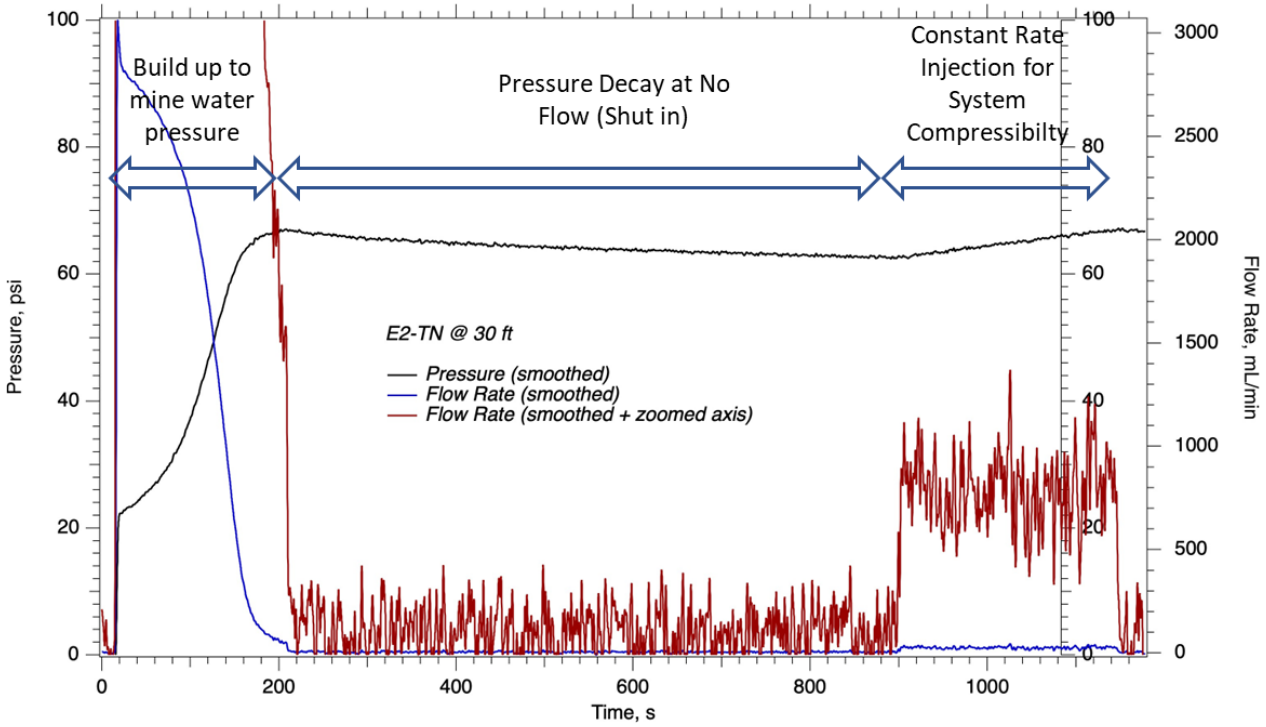

Figure 4.9 Pressure pulse test. The test starts by setting the packer and building up test zone to mine water pressure (~0.5 MPa, 70 psi). Then the zone is "shut in" and the pressure decays as water flows into the rock. After 30 minutes of pressure decay, the injection resumes at 25 ml/min. The pressure buildup indicates the compressibility of the test zone. The water loss volume and the rate of flow are computed from the compressibility and pressure decay. Assuming approximate steady flow, the transmissivity can be determined from the flow rate and the pressure change (converted to hydraulic head).

5 INSTRUMENTATION

5.1 Instrumentation Description

Instrumentation for the experiment includes active seismic sources and sensors for Continuous Active Source Seismic Monitoring (CASSM) and passive seismic monitoring, a hybrid fiber-optic cable with single mode (strain – DSS, acoustic – DAS) and multi-mode fiber (temperature – DTS,), electrical resistivity tomography (ERT), and thermistors. These were deployed and grouted in AMU, AML, DMU, and DML (Figures 3.1, 5.1). CASSM sources, an array of hydrophones, ERT electrodes and multi-mode fiber-optic cable for DTS were also deployed in TS. ERT and multi-mode fiber were deployed in TU, TL, and TN as allowed by experiment constraints. A new Downhole Robotic Strain Analysis (DORSA) tool was also constructed and co-deployed with ERT sensors in well TN (Figures 5.1, 5.2). Stimulations could be performed in any of the wells emanating from Site B, with initial stimulations targeted for the central borehole TC. Initial stimulations used the SIMFIP tool to quantify multidirectional strain during stimulation, and subsequent stimulations were performed with other straddle packer sets.

All told, the multi-physics geophysical monitoring array was housed in four grouted monitoring wells and 1 open "wet" monitoring well (E2-TS). The passive seismic array contained four three-component (3C) accelerometers in each grouted monitoring well on tubing encapsulated cable (TEC) (16 total 3C accelerometers, 48 channels). These were recorded at 100 kHz on a 64-channel Data Translations ViBBox. Four channels were used to record signals from the active-source (CASSM) system. This left 12 available channels for the hydrophone array in the "wet" well (every other hydrophone was recorded). The CASSM system comprised 20 CASSM sources. Four were placed in each of the four grouted monitoring wells on TEC, and four were deployed in the wet monitoring well (for tube wave profiling). The 24-channel hydrophone array in the wet monitoring well, 48 channels of accelerometers, and 4 aux. channels (76 total) were recorded on four Geometrics Geode dataloggers. Details of the sensors used for passive seismic monitoring and sources and sensors for CASSM including calibration and real-time processing are included in ***Appendix I - EGS Collab Experiment 2: Passive seismic monitoring system***.

Fiber optic sensing was accomplished using a custom, TEC cable containing 2 multi-mode and 4 single mode fibers. This high-density polyethylene-coated package was installed as a continuous loop (run down each well and back up). We used a Silixa XT-DTS for temperature measurements and an Omnisens DITEST for strain. We used the following three separate DAS units, each interrogating its own fiber: Silixa iDAS v3, Terra15 Treble, Optasense ODH-4 with a strain-temperature correction unit. Details on the DTS system are contained in ***Appendix J - EGS Collab Experiment 2: Distributed temperature (DTS) system***.

ERT electrodes were constructed of stainless steel mesh attached to the outside of the PVC shroud. Each monitoring well had 16 electrodes with 3 m spacing between electrodes. To prevent high pressure fluid migration along muli-conductor electrode cables, each electrode was connected to an individual 18 guage Teflon (PTFE) coated wire. All 16 wires extended to the surface, along with the multi-mode fiber, through the narrow annulus between the shroud and the formation (Figures 5.2 and 5.3A). Electrical coupling between the formation and electrodes was accomplished through the annular grout in the grouted wells (AMU, AML, DMU, DML) and

through water in the annulus in TS (and TN, TU, and TL when deployed). Complete 3D Pole-Pole type ERT surveys were collected continuously for the duration of the experiments using an 8-channel data collection system, with one survey collected every 40 minutes. We used the galvanized steel wire mesh that was rock-bolted to the back of the drift (for rock fall protection) as both the potential reference electrode and the current sink electrode for all measurements. Further details on the ERT array may be found in Johnson et al. (2022).

The DORSA was deployed in E2-TN to measure strains at a distance from the stimulation borehole. Prior to deployment it was integrated into an ERT string (Figure 5.2).

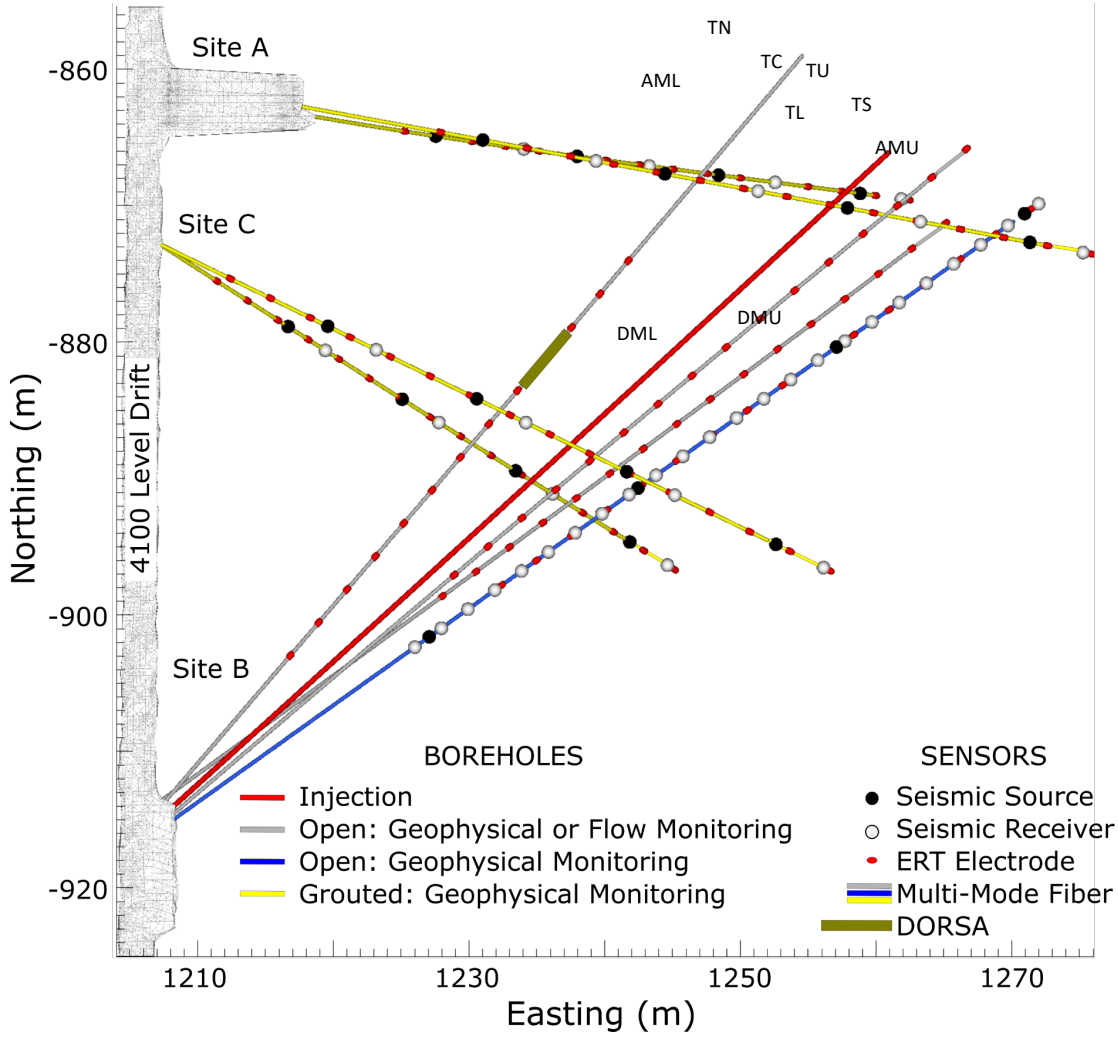

Figure 5.1. Plan view of geophysical monitoring borehole layout and sensor locations for Experiment 2. Coordinates are based on the Homestake coordinate grid system.

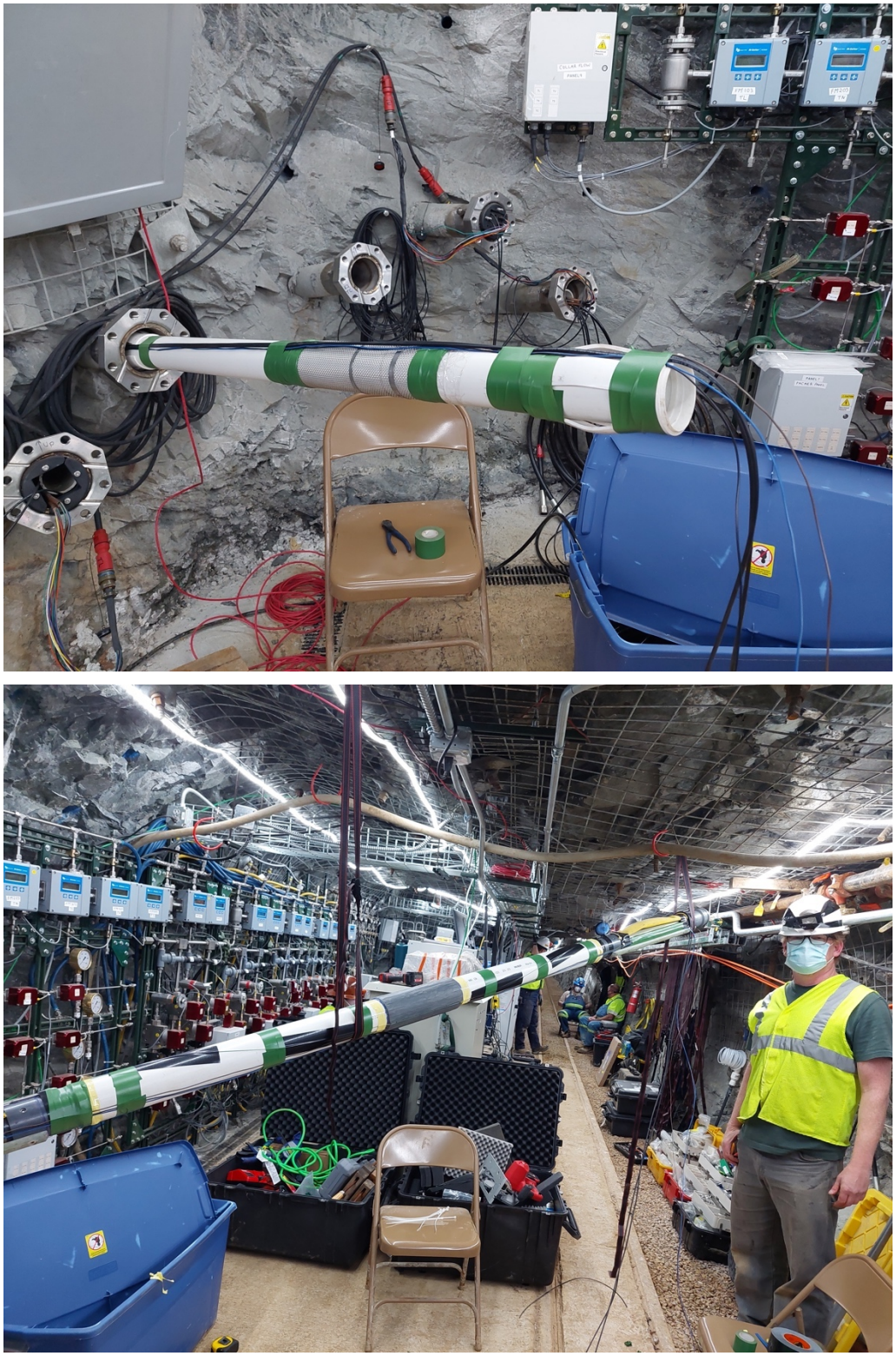

Figure 5.2. ERT/DORSA tools. Top: ERT electrode on PVC Shroud. Bottom: DORSA added to ERT shroud.

In addition, broadband seismometers from the University of California at San Diego were installed in the drift near the Spearfish weather station on a concrete pad.

Installation of the monitoring equipment was performed by starting with a PVC centralizer to provide the largest radius bend in the fiber optic fibers. Lengths of PVC shroud were sequentially installed and ERT electrodes attached per design spacing. Wires and fibers were attached to the PVC shroud such that the grout would flow around each and not be continuously occluded anywhere (Figure 5.3). When the PVC shroud with the fiber and ERT sensors were fully installed, the seismic sensors and CASSM sources were installed inside the shroud attached at the appropriate spacing to a fiberglass conveyance rod. The conveyance rod was as stiff as possible, however it had to bend for assembly. Once all the monitoring equipment was installed, a custom wellhead (Figure 5.4) was installed allowing the grout which was specifically designed and tested for these wells to be flowed down the outside of the shroud and back up the inside of the shroud. Sufficient grout was injected such that the grout exuded from the well met the grout design criteria.

Grouted Wells (AMU, AML, DMU, DML)

Per well:
- 4 accelerometers
- 4 Sources

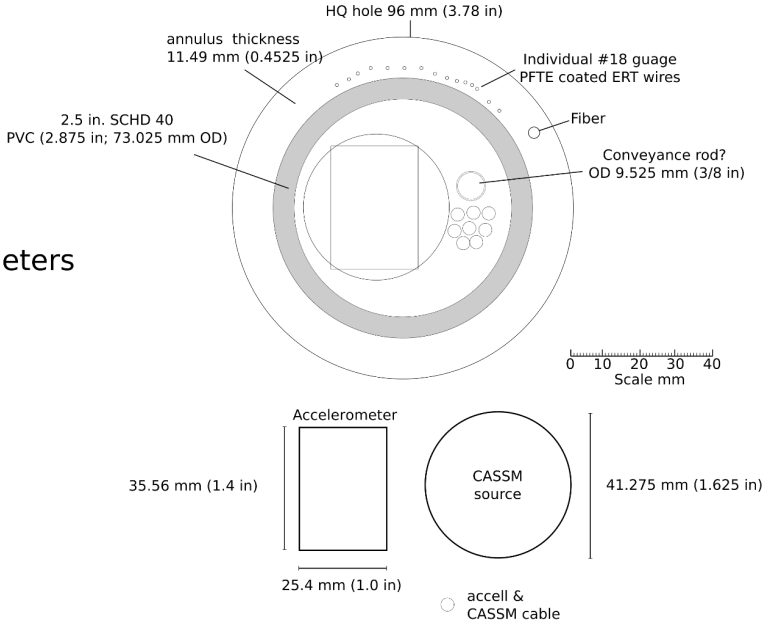

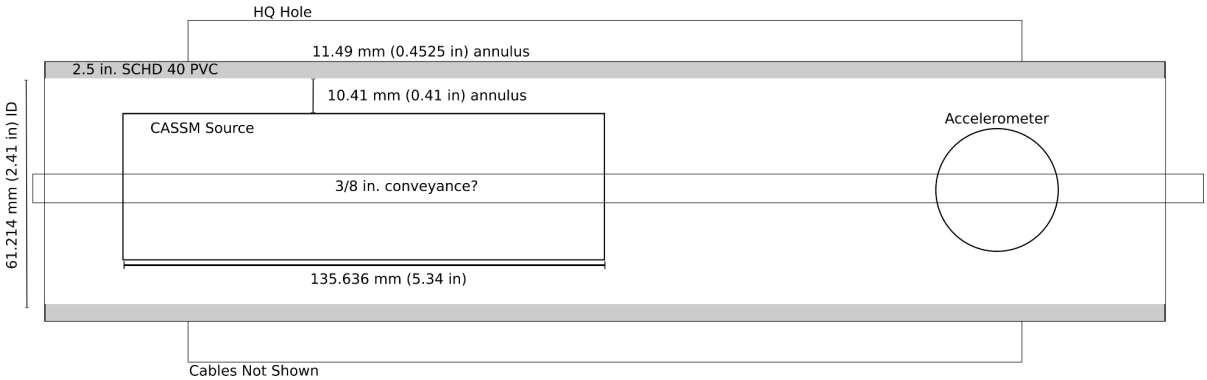

A.

Wet Well (TS)

Per well:
- 24 hydrophones
(2.5 m spacing)
- 4 CASSM sources

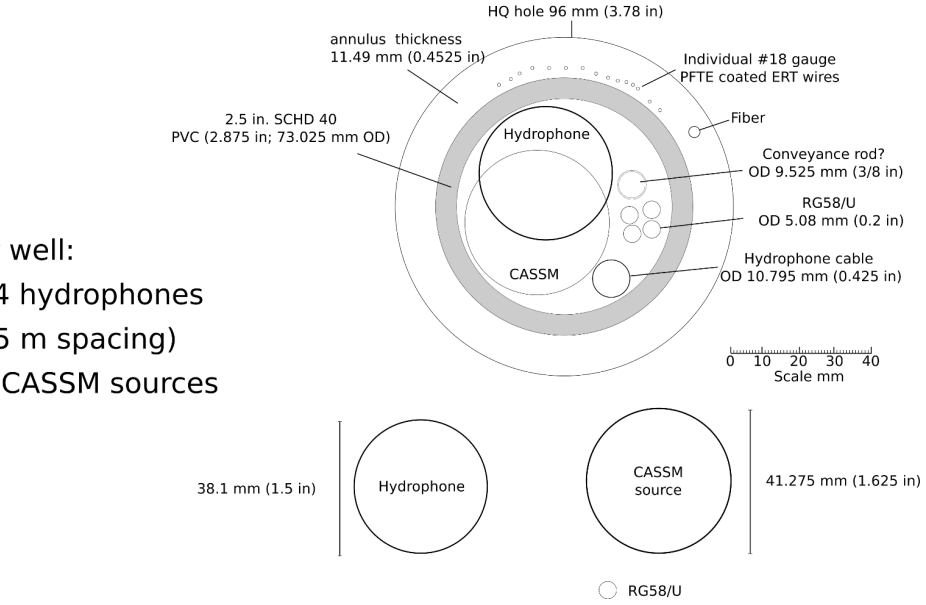

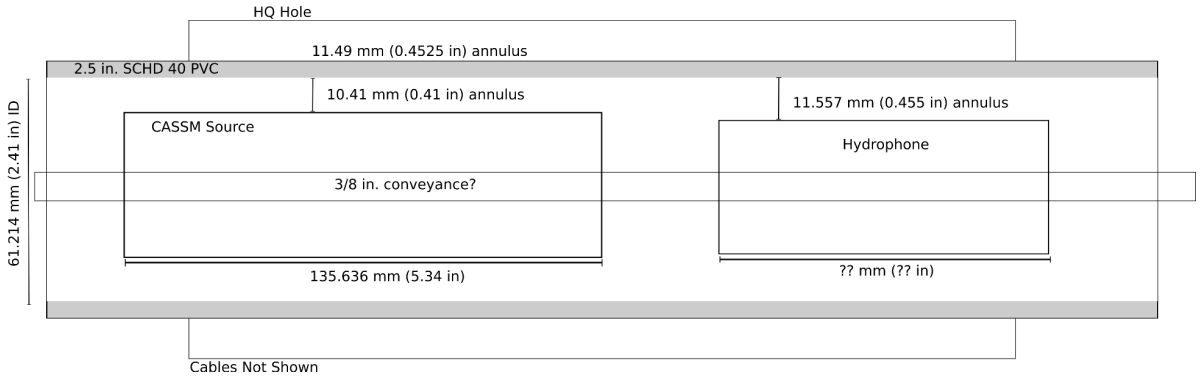

B.

Figure 5.3. Layout of the instrumentation in the shroud and borehole for A. the grouted wells, and B. the open well.

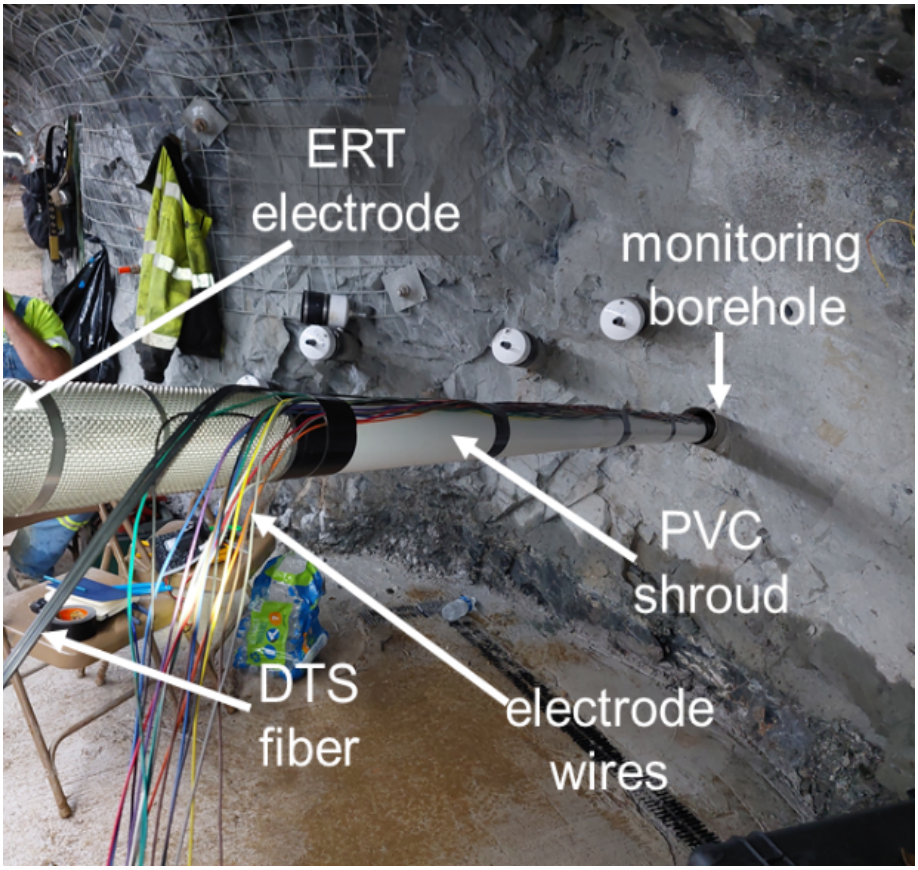
ERT
electrode
monitoring
borehole
PVC
shroud
DTS
fiber
electrode
wires

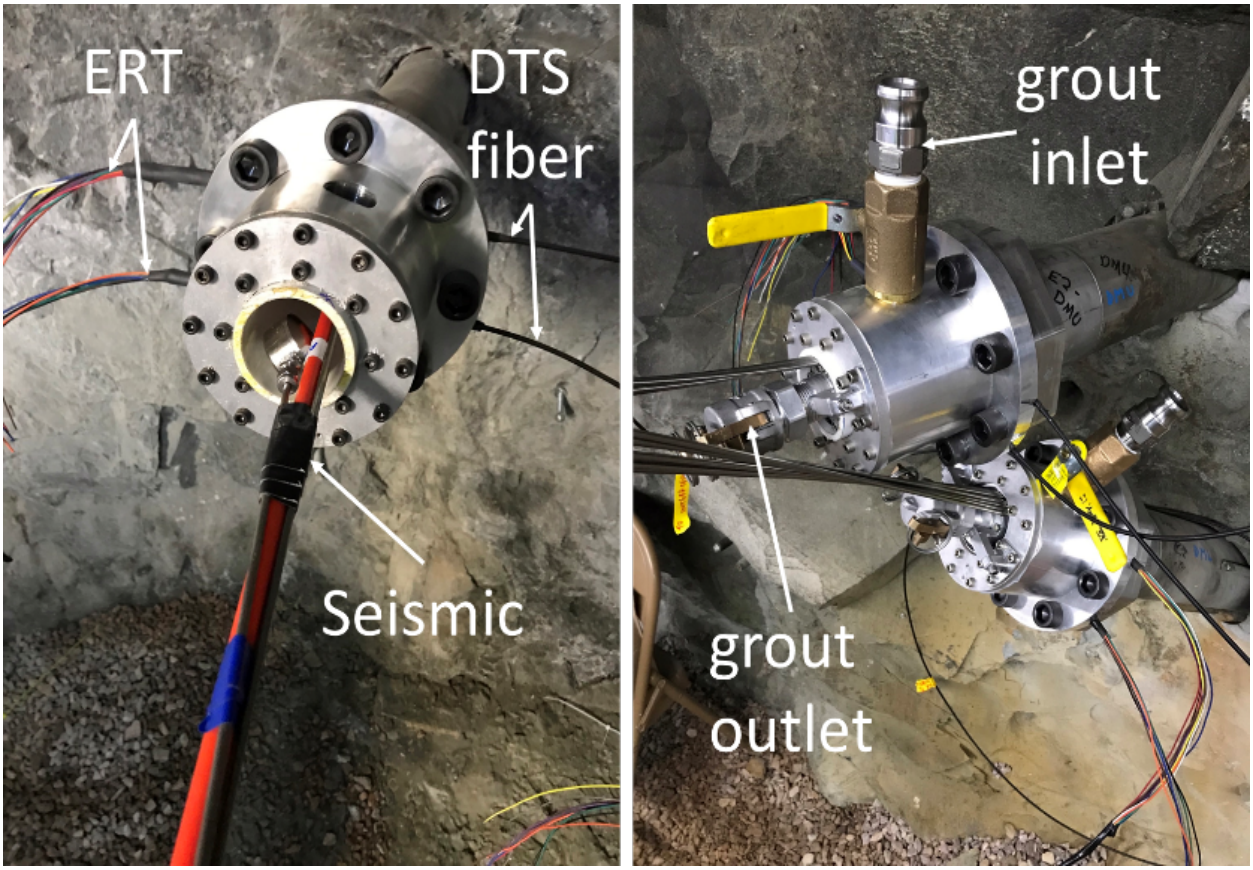

Figure 5.4. top - Installation of PVC shroud with showing ERT electrode, wires, and fiber optic cable. middle - Wellhead after shroud and instrument installation prior to grouting. bottom - Wellhead awaiting grouting.

5.2 Borehole Grouting

Cement was needed to secure the suite of instruments in the nearly horizontal monitoring holes and to seal them preventing the movement of fluids along the length of the wells. Design criteria included an electrically resistive cement, with the resistivity of no less than 1000 Ohm-m, and cement heat of hydration temperature not exceeding the temperatures allowed by the installed instruments and their cable insulation, set to be below 75°C. Additionally, cement was to have low rheological parameters to easily flow into tight spaces between the cables and the equipment (on the order of 5 mm) while still being stable and able to provide a tight seal against the cable insulation and a PVC pipe (no shrinkage). The requirement of high electrical resistivity did not allow slurry modifications with common cementing additives, which are for the most part, ionic compounds strongly increasing conductivity of cement. A combination of latex and silica fume provided desirable rheological properties, including high slurry stability, low viscosity, and yield stress. Latex also provided more than 4 times improvement of cement toughness. A combination of slag, silica fume and gypsum allowed increase of electrical resistivity to above 2000 Ohm-m. An important role in this was attributed to the formation of ettringite molecules by slag and OPC in reactions with gypsum, which immobilized both calcium ions and water molecules transporting ionic species. Additionally, controlled slurry expansion improved bonding properties of the slurry. The drawback of high latex concentrations was a slow set at room temperature that could

potentially be accelerated by the addition of non-ionic accelerators. Introduction of calcium chloride accelerator would compromise the resistivity of the cement even at low concentrations, so was abandoned. Nevertheless, the slurry remained stable even through the long setting time (Sollohub et al., 2022).

6 EXPERIMENT 2 STIMULATIONS

A major thrust of the EGS Collab project was to stimulate two different types of rock under different stress and fracture conditions. Additionally, the project was to examine hydraulic fracturing, hydraulic shearing, and alternative methods of stimulation. In Experiment 1, the project hydraulically stimulated Testbed 1, with some resultant shear in the rock mass. Experiment 2 was to attempt to primarily hydraulically shear stimulate Testbed 2. Experiment 3 was to examine alternative stimulation methods.

Shear stimulation can occur under conditions where fractures are oriented such that the stress field will cause the opposing rock faces to move laterally relative to each other when a fracture is inflated at a pressure *below* the minimum principal stress. Key to this occurring is the ability to apply pressure in the fracture over an area large enough to allow displacement of the opposing rock faces. These fractures need to be permeable enough to provide an adequate hydraulic connection to the well, but not so permeable that the hydraulic pressure can't be sufficiently increased.

6.1 Experiment 2 - Shear Stimulation Attempt

6.1.1 Predictions of Shear Stimulation

Initial calculations indicated that shear stimulation would occur along some fractures in the rock in Testbed 2 (Singh et al., 2019). These calculations were performed based on the best available information, which at the time was the stimulations performed on the 4850 level. The stress magnitudes were estimated by interpolation based on the depths of both testbeds. To improve upon the initial shear stimulation calculations a series of mini-frac and SIMFIP mini-frac tests were conducted in well TV4100 to develop a site-specific stress model. The stress measurements indicated significant differences in the stress field above, within, and below the rhyolite dike (Figure 6.1). Table 6.1, modified from (Burghardt et al., 2022), summarizes the results of the stress measurements made in zones in well TV4100 above the rhyolite dike. In addition to these calculations, hydraulic fracturing simulations were performed (Fu et al., 2021a). These simulations considered the effect of the temperature gradient in the rock upon the stress gradient, and the measured stresses from TV4100. The results indicated that stimulations performed near the underlying lower-stress rhyolite layer would likely be drawn into the rhyolite layer. Based on this result, it was decided that all the wells being used for the stimulation and flow experiments in Testbed 2 would be above the rhyolite dike. Because of this, the stress model used to design the stimulation tests focused only on the measurements above the rhyolite dike. From the mini-frac measurements made in TV4100, the smallest indicator for the fracture closure pressure in this region (which is an indication of the magnitude of the least compressive principal stress) is 18.3 MPa (2654 psi). This value was observed on the flowback test data at a nominal depth of 19.7 m (64 ft). A similar value was observed in the flowback test at 25.9 m (85 ft), where an instantaneous shut-in pressure (ISIP) of 20 MPa (2900 psi) and a shut-in closure pressure of 19.5 MPa (2828 psi) were observed. Using these data it is suggested that for shear stimulation - if tensile opening of a fracture (hydraulic fracturing) is to be avoided - the fluid pressure during stimulation should be maintained below 18.3 MPa (2654 psi).

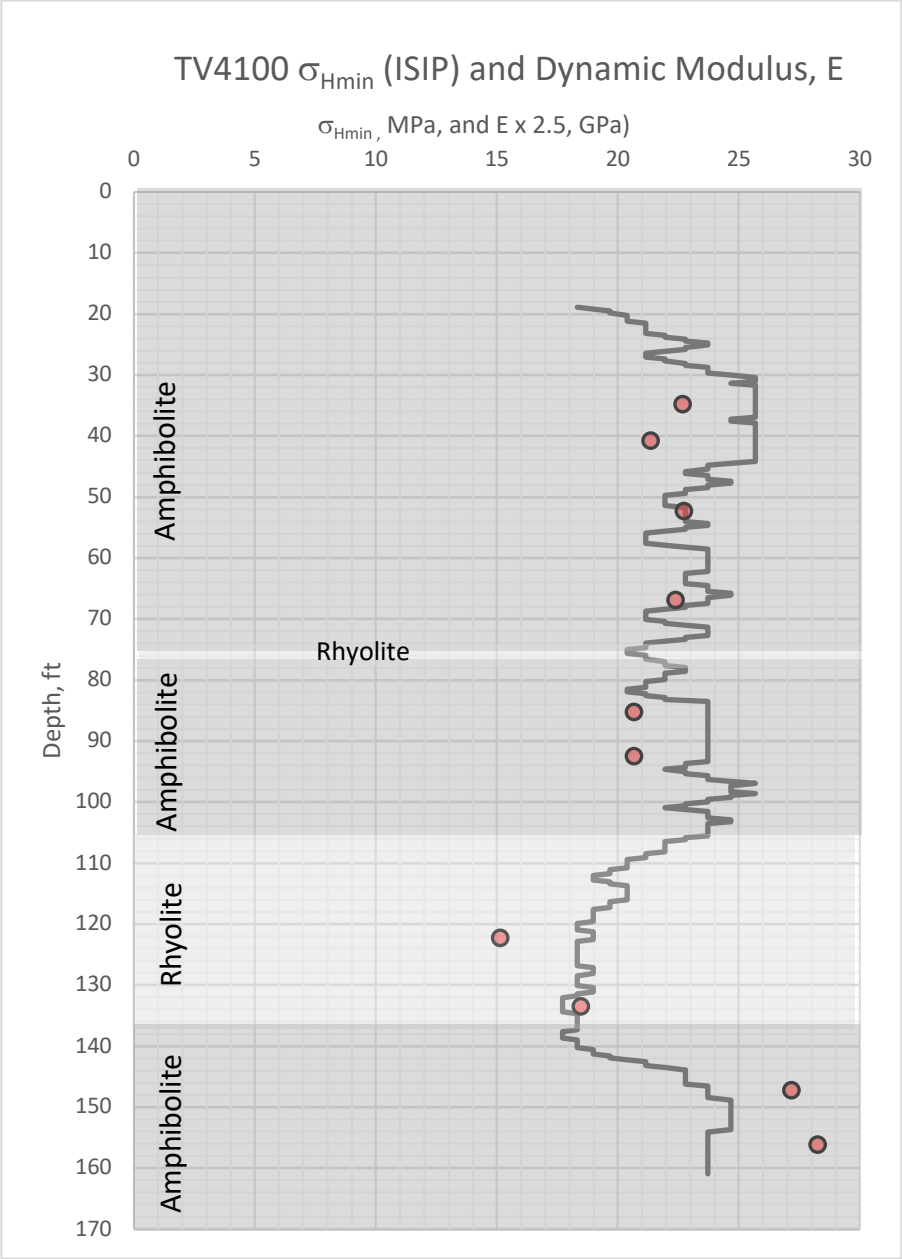

Figure 6.1. Measured instantaneous shut-in pressure (ISIP - indicating minimum principal stress) and estimated dynamic modulus from wellbore geophysical measurements.

Table 6.1. Measured stress indicators in well TV4100 for zones above the rhyolite dike; NT = not tested; AMB = ambiguous test results

Depth (m)	Initiation Pressure (MPa)	Hydraulic Reopening Pressure (MPa)	Sleeve Opening Pressure (MPa)	ISIP (MPa)	Flowback Closure Pressure (MPa)	Shut-in Closure Pressure (MPa)

9.6	25.1	23.8	NT	22.3	AMB	20.9
11.9	23.8	20.4	**20.1**	21.5	AMB	AMB
16.1	21.8	22.5	NT	22.7	AMB	21.5
19.7	22.4	18.6	NT	21.7	18.3	AMB
25.9	23.4	18.6	NT	20.0	18.4	19.5
28.4	22.1	18.3	NT	21.5	AMB	AMB

The best constraint on the magnitude of the maximum horizontal stress is the sleeve reopening test conducted at 11.9 m depth in TV4100. This test uses a packer to reopen the fracture which avoids any loading of the fracture faces themselves as occurs with a hydraulic reopening test when there is residual conductivity in the fracture. The induced hydraulic fractures in TV4100 were approximately 20-30 degrees deviated from vertical. This led to two possible interpretations of the stress orientation and magnitudes at the site. One hypothesis is that the principal stresses are in a vertical/horizontal alignment but that the inclined fractures were caused by a pervasive and consistently-oriented plane of weakness in the rock. This is referred to as the rock fabric-driven hypothesis. The other hypothesis is that the inclined fractures are the result of stresses that are rotated from vertical/horizontal (Burghardt et al., 2022). This is referred to as the stress-driven hypothesis.

Both hypotheses were integrated into a stochastic Markov Chain Monte Carlo analysis for the principal stresses and their directions. Interpretation of the sleeve reopening test based on the rock fabric driven hypothesis results in a maximum horizontal stress value of 35-60 MPa with a vertically oriented lithostatic stress. A similar interpretation under the stress-driven hypothesis resulted in a maximum sub-horizontal stress magnitude of 25-40 MPa, with the lithostatic stress deviating from vertical by 10-20 degrees. See (Burghardt et al., 2022) for full details of this analysis.

Using these two stress state interpretations the shear and normal stress probability distributions were calculated for each fracture identified in E2-TC. Figure 6.2 (Burghardt et al., 2022) shows the mean shear-to-normal stress ratio for each fracture for both stress hypotheses. These results indicated that the rock was not likely to shear, as maximum shear-to-normal stress ratios were between 0.26 and 0.35, depending on the assumptions used to interpret the stress characterization data. This is significantly less than the desired value of 0.6. Meng et al. (2022) conducted a series of laboratory tests on actual core samples from the 4100 level, and found that most of the tested sealed fractures did *not* fail under shear conditions. Additionally, for shear stimulation, the selected fracture set would need to be in pressure communication with the well and able to take water at a rate adequate to open the fracture. These fractures did not take sufficient water to enable pressure communication with the well.

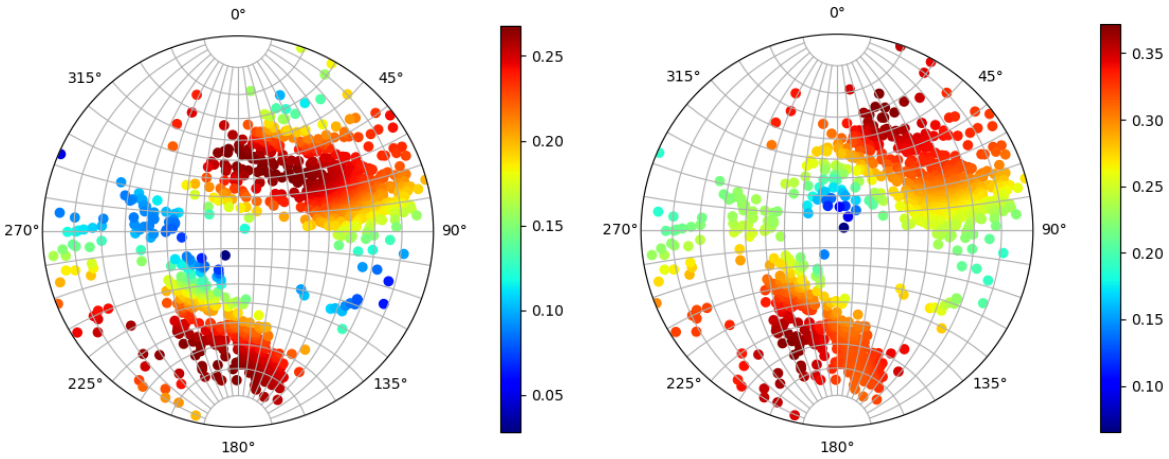

Figure 6.2. Left - Equal angle lower hemisphere projection of poles of identified fractures in E2-TC, colored according to the mean shear-to-normal stress ratio under the hypothesis that the principal stresses are rotated from vertical/horizontal. Right - Equal angle lower hemisphere projection of poles of identified fractures in E2-TC under the assumption that the principal stresses are vertical/horizontal. Both plots are colored according to the mean critical shear-to-normal stress ratio (i.e., maximum friction coefficient that permits slip with zero cohesion).

6.1.2 GeoDT Simulations

Geomechanical analyses were performed (Figure 6.3) informed by in-situ stress tests (Burghardt et al., 2022; Ingraham et al., 2020), borehole fracture mapping (Ulrich et al., 2022), and laboratory tests (Meng et al., 2021a; Meng et al., 2021b; Meng et al., 2022). These show an evolution of understanding from the initial conditional for Experiments 1 and 2 to the more informed understanding based upon applying more data. Results of these analyses show the initially expected and updated shear slip predictions for the Testbeds 1 and 2 as a function of fracture orientation and critical slip pressure. In these analyses, cohesion (c) was initially assumed to be zero until laboratory tests demonstrated much greater values in the range of 2.0 to 20.0 MPa. The friction coefficient (μ) was initially assumed at the typical value of 0.6 for faults, but laboratory testing revealed some fractures with friction as low as 0.3 (i.e., sample PS01-11) for Experiment 1 or closer to 0.83 (i.e., sample YA02-05) for Experiment 2 (Meng et al., 2022). These analyses show that shear was more probable at Experiment 1 than what was initially expected, and less probable at Experiment 2 than what was initially expected.

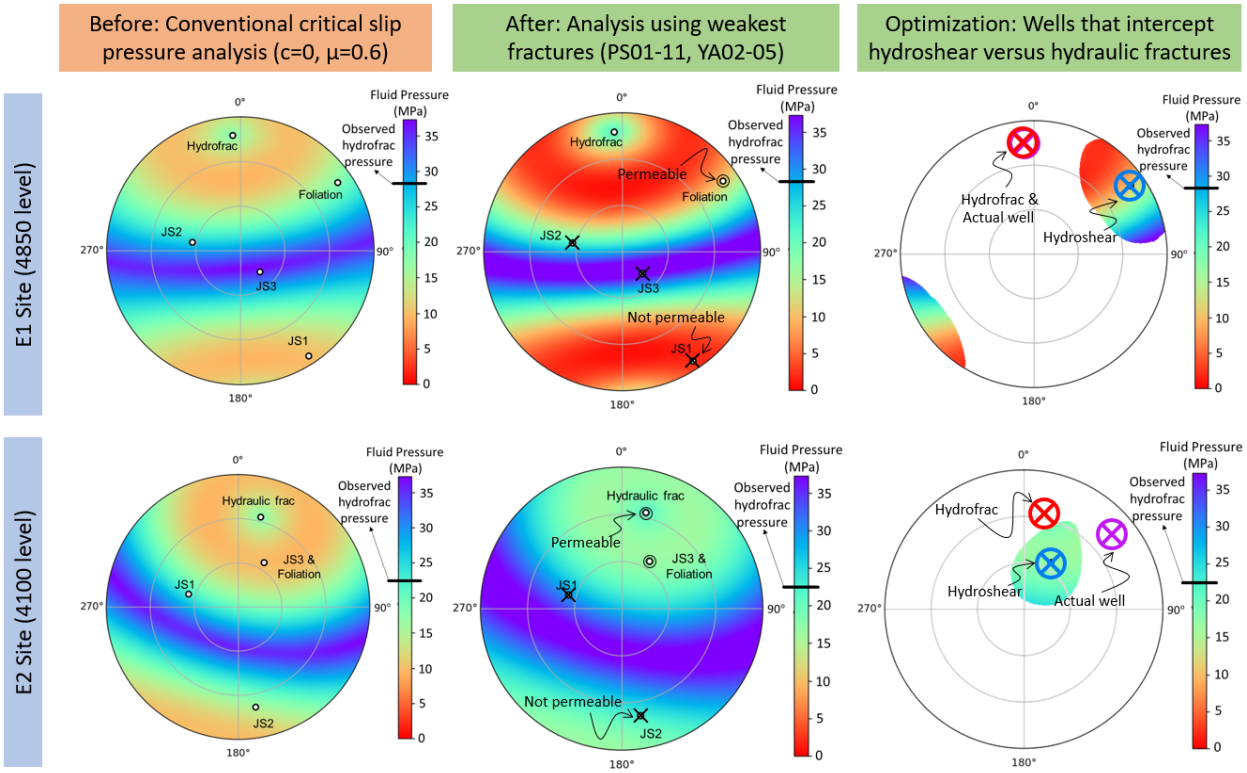

*Fractures from a joint set must be permeable, oriented for shear, and sufficiently weak to be suitable for hydroshearing.

Figure 6.3. Geomechanical analysis informed by in-situ stress tests (Burghardt et al., 2022; Ingraham et al., 2020), borehole fracture mapping (Ulrich et al., 2018), and laboratory tests (Meng et al., 2021a; Meng et al., 2021b; Meng et al., 2022), showing the initially expected (left column) and updated shear slip predictions (center column) at the Experiment 1 and Experiment 2 sites as a function of fracture orientation and critical slip pressure. Cohesion (c) was initially assumed to be zero until laboratory tests demonstrated much greater values in the range of 2.0 to 20.0 MPa. Friction coefficient (μ) was initially assumed at the typical value of 0.6 for faults, but laboratory testing revealed some fractures with friction as low as 0.3 (i.e., PS01-11) for Experiment 1 or closer to 0.83 (i.e., YA02-05) for Experiment 2.

In an additional set of simulations using the updated in-situ stress and fracture data from the exploratory boreholes (TH4100 and TV4100), an ensemble of 16,000 simple discrete fracture network stimulation, circulation, and heat recovery models were completed (Frash, 2022). These models used our open-source Geothermal Design Tool (GeoDT: Frash et al. (2021); (Frash et al., 2022), the development of which was motivated in part by the questions facing the EGS Collab experiments. All of these models assumed injection into the center borehole (E2-TC) with a randomly selected distance between 35 m and 66 m into the borehole and an injection interval length of 0.65 m (Figure 6.4). The injection rate was randomly selected from the range of 0.100 to 10,000 L/min, with the modeled maximum rate greatly exceeding our actual pumping capacity to help identify and quantify safe operating limits for the experiment. Known natural fractures from logs for TC that were thought to potentially support fluid flow were included in all of the models with the goal of finding the optimal location to attempt hydraulic shearing. Fracture tensile and shear stimulation, injection pressures, production rates, and produced fluid temperature were all predicted outputs from each of the 16,000 models. All these models were completed and analyzed

in less than 1 week. The key outputs from this modeling effort are summarized in Table 6.2. At injection at rates slower than 2 L/min, predictions using GeoDT indicate that the fracture system could be diffusion dominated with flow distributed through the fracture network into the drift and various monitoring wells. At injection rates faster than this limit, the model predicts that the relative proportion of flow into the production wells would favor TN, TL, TU, TS, other intervals of TC, and then other locations, in order from highest to lowest production rate. At injection rates faster than 40 L/min, the model predicts that the production wells would be overwhelmed and flow would predominantly occur from the mine drift. The circulation rate recommendations were estimated with the goal of achieving at least 10% thermal drawdown in the fastest flowing production well within 180 six months. This work is presented in more detail by (Frash et al., 2022).

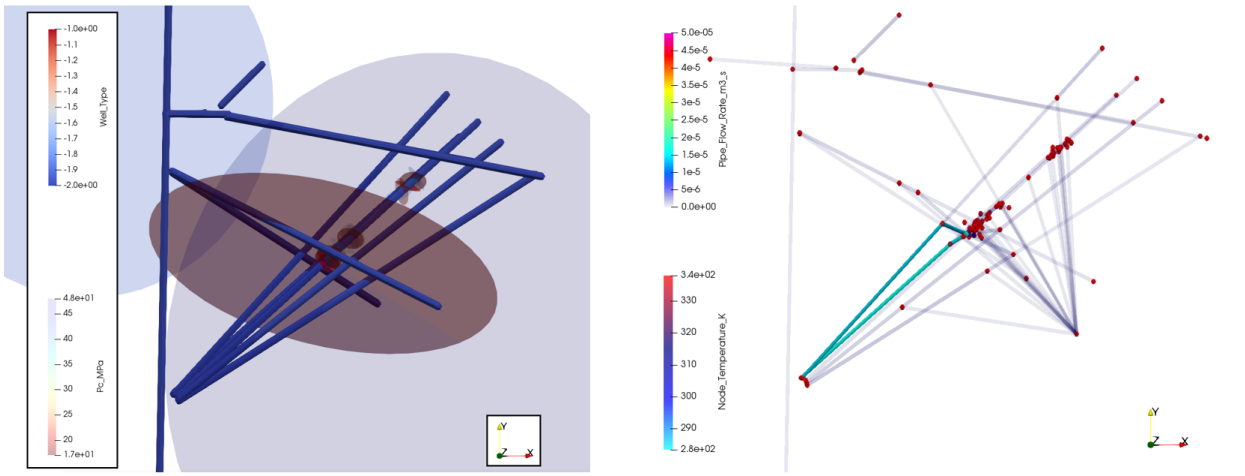

Figure 6.4. (Left) Example output from GeoDT with injection onto a zone near monitoring wells DMU and DML that predicts a hydraulic fracture that intercepts the two monitoring wells and the drift. (Right) View from the GeoDT flow and heat solver for this scenario showing a fast flow path from well TC to TN in addition to flow from nearly every other well and the drift due to interactions with natural fractures.

Table 6.2. Summary of key results from GeoDT modeling to predict the operational envelope.

Parameter	Unit	Minimum	Nominal	Maximum
Stimulation Injection Rate	mL/min	2,000	15,000	40,000
Circulation Injection Rate	mL/min	3,000	15,000	22,000
Fastest Production Rate	mL/min	2,400	4,200	5,600
Stimulation Net Injected Volume	L	80	800	2,000
Diffusive Low Flow Limit	mL/min	4.3	125	123.7
Best Location to Inject for Shear in TC	m	58.5	60.0	62.3
Best Location to Inject for Containment in TC	m	47.5	50.0	54.0

6.1.3 Preliminary Stimulations and Tests

The first stimulations were made at shallow depths in E2-TC to test the system and gain an understanding of the rock (Table 6.3). The preliminary tests included a small hydraulic fracturing test with the straddle centered at a depth of 30.9 feet. At this depth the core indicated there was a natural fracture oriented for high slip tendency. The tests were performed to 1) characterize the initial permeability of the formation in this interval, 2) test if the SIMFIP is well-seated in these wells, and 3) to estimate the stiffness of the probe-chamber system. This test indicated that fracturing occurred between 3500 and 4000 psi (24.13 MPa to 27.6 MPa), which is similar to values obtained in TV4100.

Low-pressure hydraulic tests were then performed over several more intervals in the borehole (Table 6.3). These tested intervals were selected from within seven zones having characteristics of interest including few fractures, fractures more likely to shear, and fractures less likely to shear. Ultimately stimulation tests were largely performed in Zones 1, 4, and 7 where Zone 7 had the most suitable fracture for shear, and Zones 1 and 4 had a comparable frequency of fractures that were not likely to shear. Monitored water levels in the wells indicated that some water could imbibe into the rock, but the rates were small and the locations of the inlets were unclear. To shear stimulate a fracture, the fracture must be in good hydraulic communication with the well. These tests confirmed that water uptake in selected fractures was not significant enough for shear stimulation. Rather, the rock matrix and the natural fractures have a very low permeability and there was no evidence of significant shearing along the natural fractures or increases in permeability.

6.1.4 Shear Stimulation Attempt

To establish hydraulic communication between the fracture and well, the SIMFIP was placed with packers straddling the highest slip probability fracture (referred to as Zone 7, at depths of 192.4-200.3 ft), and the zone was pressurized to 2340 psi for two weeks (below the minimum principal stress but greater than 90% of the minimum principal stress). Over the two weeks, the rock and fractures did not take a significant quantity of water (only tens of mL/day) thus good hydraulic communication was not able to be established reducing the chances of shear. This result indicates that hydraulic shearing as a mechanism for fracture stimulation was unsuccessful in Experiment 2. Based on our experience, we can expect similar, but amplified, difficulties when planning hydraulic shear stimulation at field sites where much less datawill be available during the planning stages, compared to what we had available. This attempt may have been complicated by the observation that nearly all of the fractures in Testbed 2 were mineralized. The mineralization resulted in fracture cementation inhibiting flow into the fracture and strengthening the fractures, limiting hydraulic reactivation. In the absence of any detectable shear stimulation, the Experiment 2 series was concluded and the EGS Collab team proceeded to the Experiment 3 series of stimulations.

Table 6.3. Timeline and summary of Experiment 2 stimulation activities. All simulations were conducted in well TC using SIMFIP. (Schwering et al., 2023)

Start Time (UTC)	End Time (UTC)	Interval Top (m)	Interval Bottom (m)	Notes

3/23/22 14:21	3/23/22 19:28	8.23	10.64	Tensile hydraulic fracture at shallow depth outside of monitoring zone to verify fracture pressure. Hydraulic test was done on 24 March 2022 in the same zone. This test indicated that fracturing may occur between 3500 and 4000 psi (24.13 MPa to 27.6 MPa).
3/23/22 21:38	3/24/22 14:38	58.64 (Zone 7)	61.05	Overnight pressure held at 15.2 MPa (2200 psi).
3/24/22 14:38	3/24/22 17:11	63.46	65.87	60-minute pressure held at 15.2 MPa (2200 psi).
3/24/22 17:12	3/24/22 19:10	53.83	56.24	60-minute pressure held at 15.2 MPa (2200 psi).
3/24/22 19:10	3/24/22 21:04	49.01	51.42	Pressure held at 15.2 MPa (2200 psi). Subsequent injections into TU on 05 May 2022 fractured into this zone and on 06 May 2022 injections were made into the fracture that was created from TU. Additional high-rate injections were made on 18 May 2022. These later injections are documented as part of Experiment 3.
3/24/22 21:04	3/24/22 22:08	44.20	46.61	Pressure held at 15.2 MPa (2200 psi). Subsequent injections in this zone were made on 13 April 2022 and are documented as part of Experiment 3.
3/24/22 22:08	3/24/22 22:42	8.23	10.64	Held pressure at 15.2 MPa (2200 psi) to evaluate post-fracture hydraulic conductivity. The fracture was generated on 23 March 2022 as a tensile fracture.
3/25/22 0:00	3/25/22 0:00	61.05	63.46	Pressure held at 16.1 MPa (2340 psi). Test was shortened to less than 60 minutes due to time constraints.
3/25/22 15:23	3/25/22 17:52	46.60	49.01	Pressure held at 16.1 MPa (2340 psi). There was a Quizix pump communication problem that resulted in a premature depressurization of the interval. The test was resumed but was shortened from the planned 60-minute hold.
3/25/22 17:52	3/25/22 19:21	51.42	53.83	Pressure held at 16.1 MPa (2340 psi). Test was shortened to less than 60 minutes due to time constraints. On 14 April 2022 a stimulation was made in this zone by cycling the injection pressure above/below the fracture opening pressure repeatedly. This later injection is documented as part of Experiment 3.
3/25/22 19:23	3/25/22 20:50	56.23	58.64	Pressure held at 16.1 MPa (2340 psi). Test was shortened to less than 60 minutes due to time constraints.
3/25/22 22:08	4/11/22 17:02	58.64 (Zone 7)	61.05	Pressure held at 16.1 MPa (2340 psi) from 25 March 2022 until 11 April 2022 to give as much time as possible for pressure to diffuse into natural fractures and promote shear slip/stimulation. On 11 April 2022, after no indication of shear stimulation had occurred, a constant rate injection at 3 mL/min was started. This is considered as the transition to Experiment 3 since the pressure was intentionally allowed to exceed the least compressive principal stress.

7 EXPERIMENT 3 –STIMULATIONS AND FLOW TEST

Experiment 3 tests were performed to investigate alternate stimulation methods. The tests included a slow ramped increase in stimulation flow rate in an attempt to create a fracture that was more likely to follow natural fractures, and shear at a later time in the stimulation. Another test injected water with a cyclic pressure profile. The rationale for this method was that in the presence of stresses that could shear the resulting fracture, cyclic stimulation may create scalloped fracture faces which may be more prone to self-propping. The third method tested was hydraulic fracturing providing a baseline for comparison. Ultimately these methods all are thought to have created hydraulic fractures, one of which was used for a weeks-long cold-water injection test.

Results from the four major Experiment 3 stimulations in Testbed 2 are presented below. The stimulations were performed in three intervals in well TC working from the bottom of the hole upwards: Zone 7; 192.4 – 200.3 ft (58.64 - 61.05 m), Zone 4; 168.7-176.6 ft (58.64 - 61.05m), and Zone 1; 145.0-152.9 ft (44.20 - 46.61 m), and one in TU 177.4-179.5 ft (54.07 - 54.74 m) (Figure 7.1). The Zone 7 stimulation was performed at low flow rates ramping up from 3 mL/min to 400 mL/min with a total injected volume of 300 L. The Zone 4 stimulation was performed by cycling the pressure about the minimum principal stress (40 L total volume). The Zone 1 stimulation was performed by breaking the rock down at 1 L/min and extending the fracture at 5 L/min with a total injected volume of about 400 L. Similarly, the stimulation in "Zone 4" of TU was initiated at 1 L/min and extended at 5 L/min by injecting 1200 L of water (Table 7.1). Selected observations from these stimulations are presented in detail below.

Table 7.1. Experiment 3 stimulations (Schwering et al., 2023).

Time (UTC)	Stimulated Well/ Interval	Method	Volume	Connects to/ Interferences	Breakdown (psi)	Notes
4/11/22 17:02 - 4/12/22 19:50	TC 58.64 61.05 /SIMFIP (Zone 7)	Increasing flow from 0.003 L/min to 0.4 L/min	300 L	TN, TS (dripping), AMU	3650	Constant rate injection at increasing rates, then shut-in when fracture was detected in monitoring well AMU via DTS anomaly and dripping from well head. Subsequent flow test, observed with a downhole camera, was conducted on 20 April 2022.
4/12/22 19:52 - 4/13/22 21:51	TC 44.20 46.61 /SIMFIP (Zone 1)	-	-	-	-	Pressure held at 13.8 MPa (2000 psi) overnight. On 14 April 2022 a high-rate injection was conducted and stopped when outflow was observed in the drift.
4/13/22 21:52 - 4/14/22 15:44	TC 58.64 61.05 /SIMFIP (Zone 7)	1 L/min, 5 L/min	400 L	TN, TL, TS, and TV4100	~3400 psi	Hydraulic test of fracture created with constant-rate injections on 11-12 April 2022.

4/14/22 15:46 - 4/14/22 18:15	TC 44.20 46.61 /SIMFIP (Zone 1)	-	-	-	-	Hydraulic test of fracture created on 13 April 2022.
4/14/22 18:16 – 4/14/22 21:30	TC 51.42 53.83 /SIMFIP (Zone 4)	Cyclic (2800 < P < 4500 psi)	40 L	TN, TL, and TS (a little)	Not clear	Cyclical injection above/below fracture pressure until 40 L had been injected and flow from production wells was observed. Following this stimulation, the well was held under 16.1 MPa (2340 psi) constant pressure for several days to observe flowback. Subsequently an injection was made on 21 April 2022 into this zone with the downhole camera deployed in TN and TL to observe outflow locations.
5/5/22 18:39 - 5/7/22 0:00	TU 54.07 - 54.74 26" straddle	1 L/min, 5 L/min	1200 L	TC, TN, and TL	5500 psi	Initial stimulation of this zone.
5/17/22 20:45 5/18/22 01:45	TC 45.93 46.60, 26 straddle	5 L/min	1,500 L	TN, TL,	DML	Stimulation at 5 L/min in Zone 1. Less than 20% recovery in TL & TN, and DTS indicated intersection with DML. Aborted after 5 hours to try stim/flow of Zone 3. This stim/flow test was accidentally overlooked in the table presented by Schwering et al. (2023).
5/18/22 14:24 - 5/19/22 13:52	TC 50.44 - 51.11 26" straddle	5 L/min	3600L	TL, Batter Alcove, DML	-	Stimulation at 5 L/min. Outflow was mostly from TL with about 20-25% recovery. Weeps in the drift near the Battery Alcove were observed. Flow was stopped on the evening of 19 May 2022 3:44:55 after an intersection with DML was observed with the DTS.
5/19/22 13:42 - 5/19/22 13:52	TU 50.44- - 51.11 26" straddle	-	-	-	-	Stimulation of this zone, leakage observed at DML.

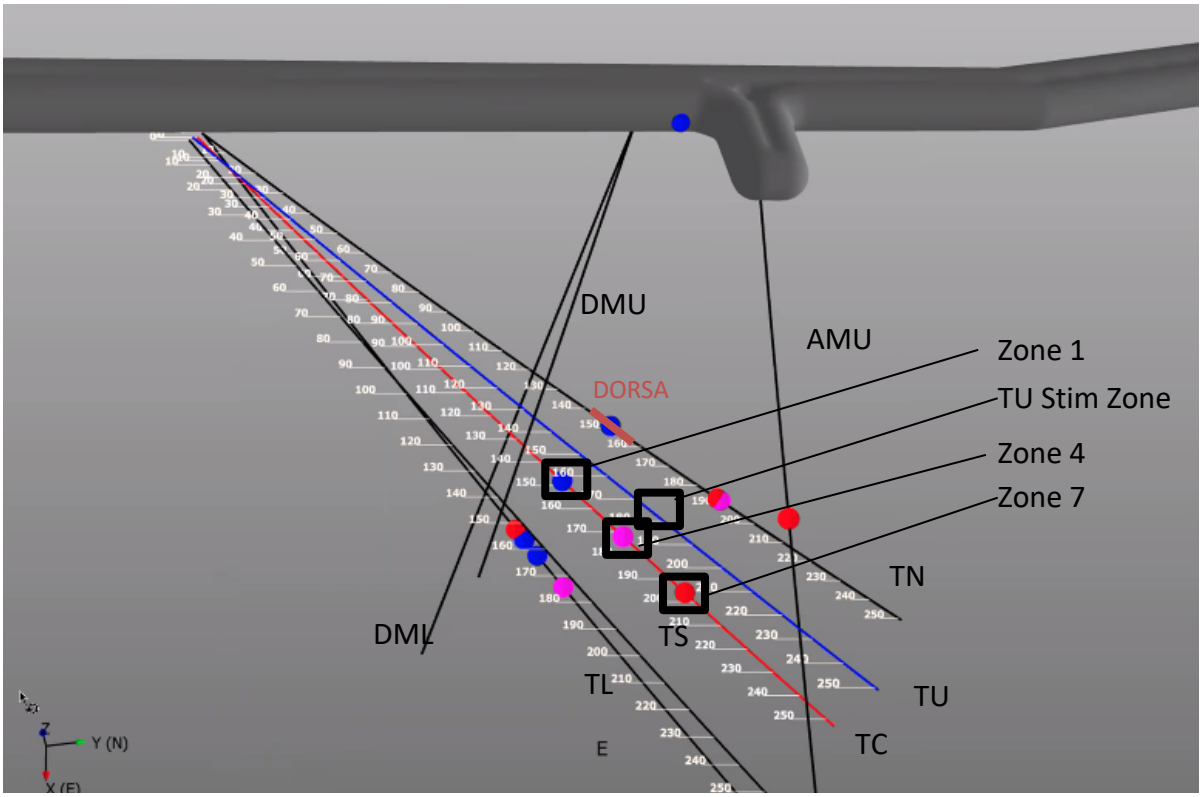

Figure 7.1. Stimulation locations in TC and TU and early fracture intersections from TC stimulations indicated by colored dots. Red - Zone 7, pink - Zone 4, blue - Zone 1.

7.1 Stimulation 1 – TC Zone 7 (192.4-200.3 ft, 58.64 - 61.05m) – Slow Flow (Attempt to activate natural fractures)

Following Experiment 2, the SIMFIP tool was left at the location in TC where it had held a pressure just below the minimum principal stress for two weeks. This stimulation was initiated by pumping water at 3 mL/min into the packed interval on April 11, 2022 at around 17:00 UTC. Following breakdown, the rate was stepwise increased each ~80 minutes or more until a maximum flow rate of 400 mL/min was reached (Figure 7.2). The rationale for this approach was to propagate the fracture with as low of a flow rate as was practically possible so as to maximize the potential for activation of natural fractures. After several hours of pumping at 400 mL/min, breakthrough into the production wells (primarily TN with a drip observed from TS) was observed. Flows as high as 250 mL/min were recovered from TN (63% of the inflow rate). An elevated temperature spike in the DTS data in well AMU indicated that the stimulation intersected with well AMU at ~ 5:23 UTC on April 12 (Figure 7.3).

Spikes in strain can also be observed in some of the DAS monitoring systems at the same time and location, however changes in strain around the breakthrough region in AMU began at least 6 hours *prior* to breakthrough (Figure 7.4). The initial strain signal was somewhat diffuse within a larger zone, just below the location of the fracture, showing compressive strain. The breakthrough is evidenced by a more defined extensional signal (see arrows in Figure 7.4 center). A slow drip of water from the AMU wellhead was also observed.

The ERT data are consistent with the strain and temperature data (Figure 7.5). Figure 7.5 shows a decrease in electrical conductivity near the injection site. This decrease is likely caused by pressure in the packers squeezing water out of rock pores from the increased compressive stress adjacent to the borehole and fracture (Johnson et al., 2021). A decrease in conductivity is also observed near the breakthrough location in AMU. This may also be caused by compression of the rock as shown by the DAS strain data prior to breakthrough. Additionally, water in well AMU increased conductivity and that is clearly observed in Figure 7.5. When it was determined that the fracture intersected the monitoring well, the injection was stopped, and outflows from production wells and E2-AMU decreased slowly with time.

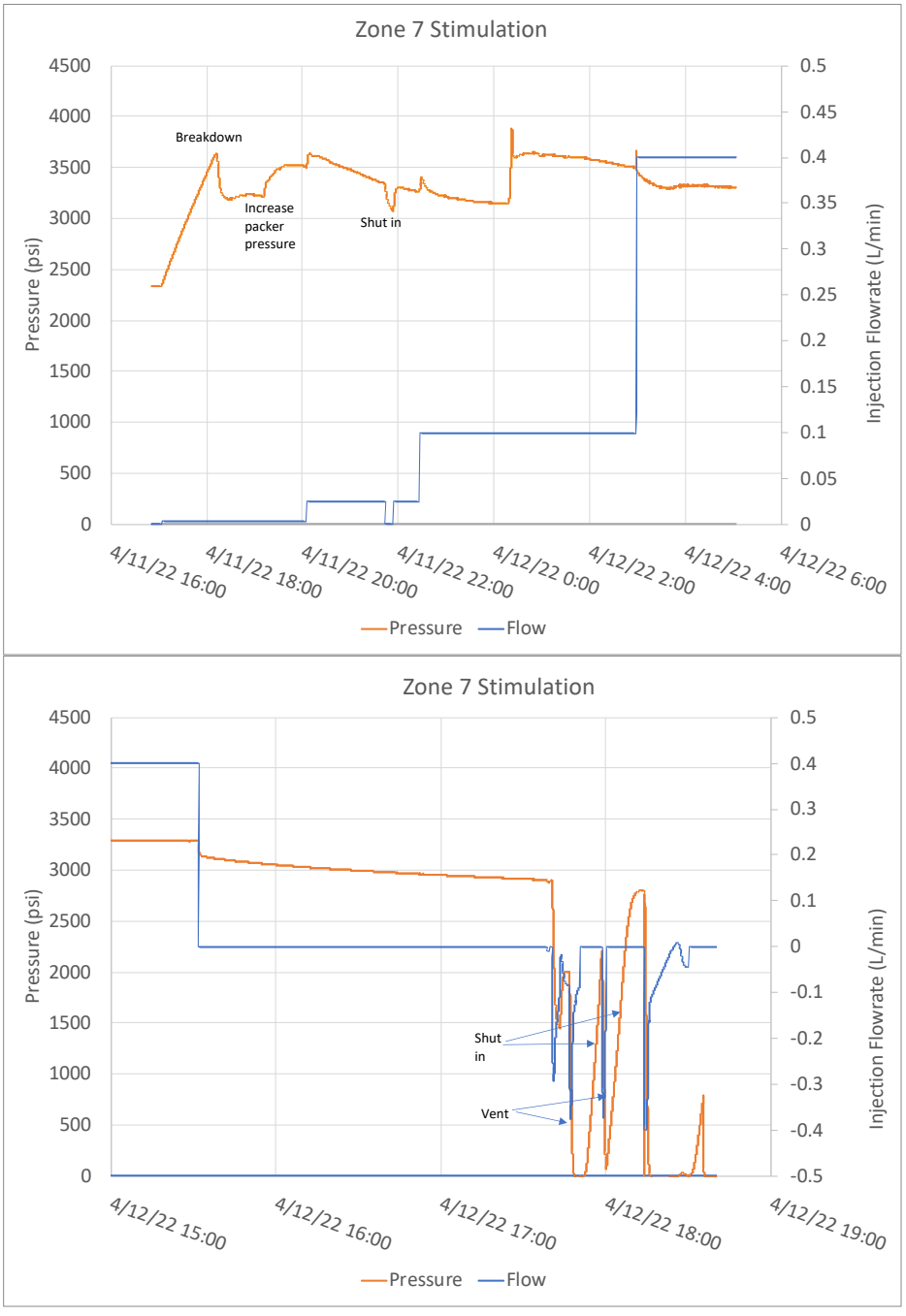

Figure 7.2. Pressure and flow for Stimulation 1 at Zone 7. Left, breakdown and initial fracture extension. Note: breakdown occurred with an injection flow rate of 3 mL/min. Right, continued extension, shut-in, and alternating episodes of shut-in and well venting.

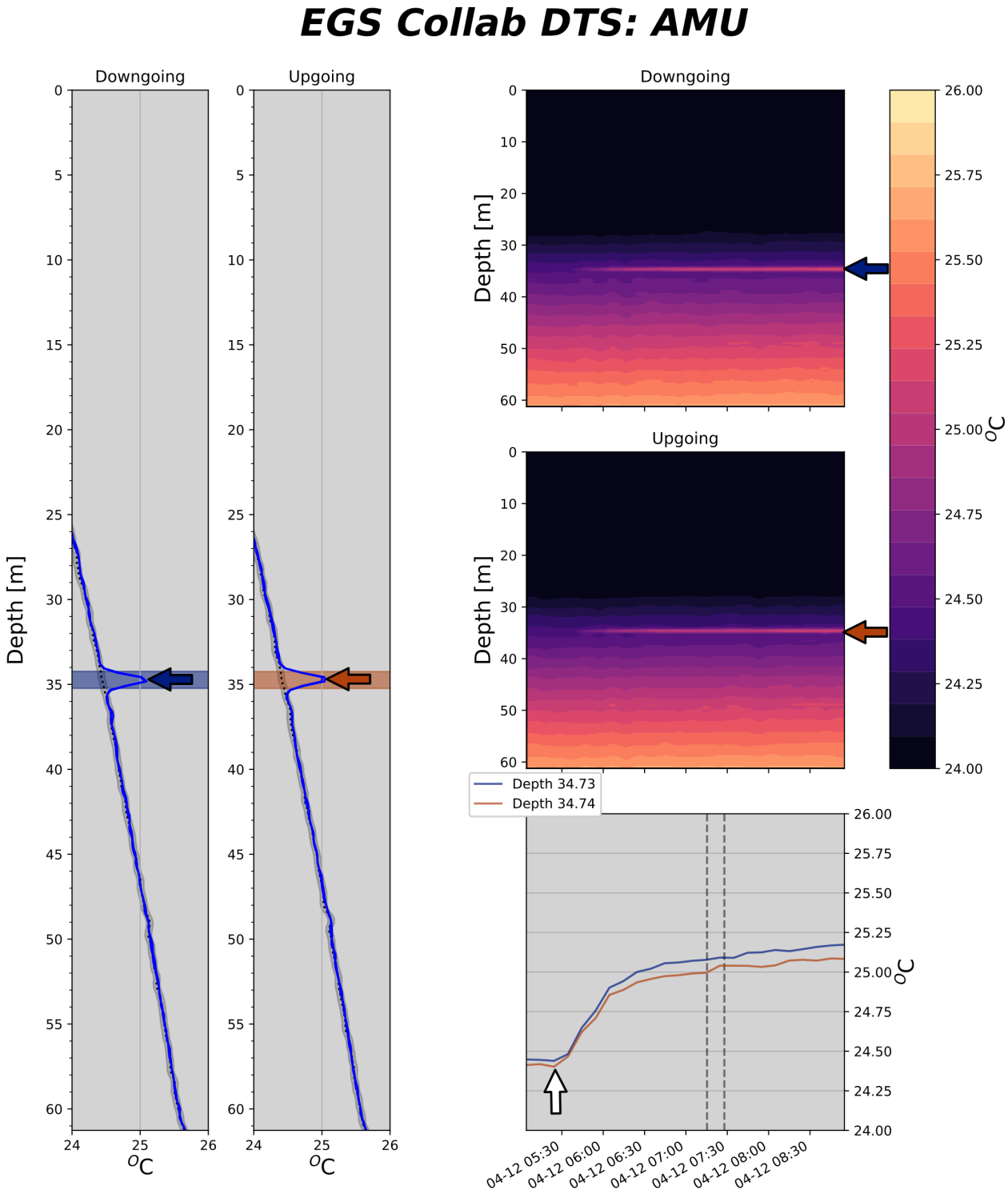

Figure 7.3. Temperature signal from the distributed temperature sensing (DTS) in monitoring well AMU showing a peak at a depth of about 35 m starting at about 5:30 UTC (white arrows). Blue and

red arrows indicate the depth of the fracture on the downgoing and upgoing section of fiber, respectively. These colors correspond to the blue and red timeseries traces shown in the bottom right.

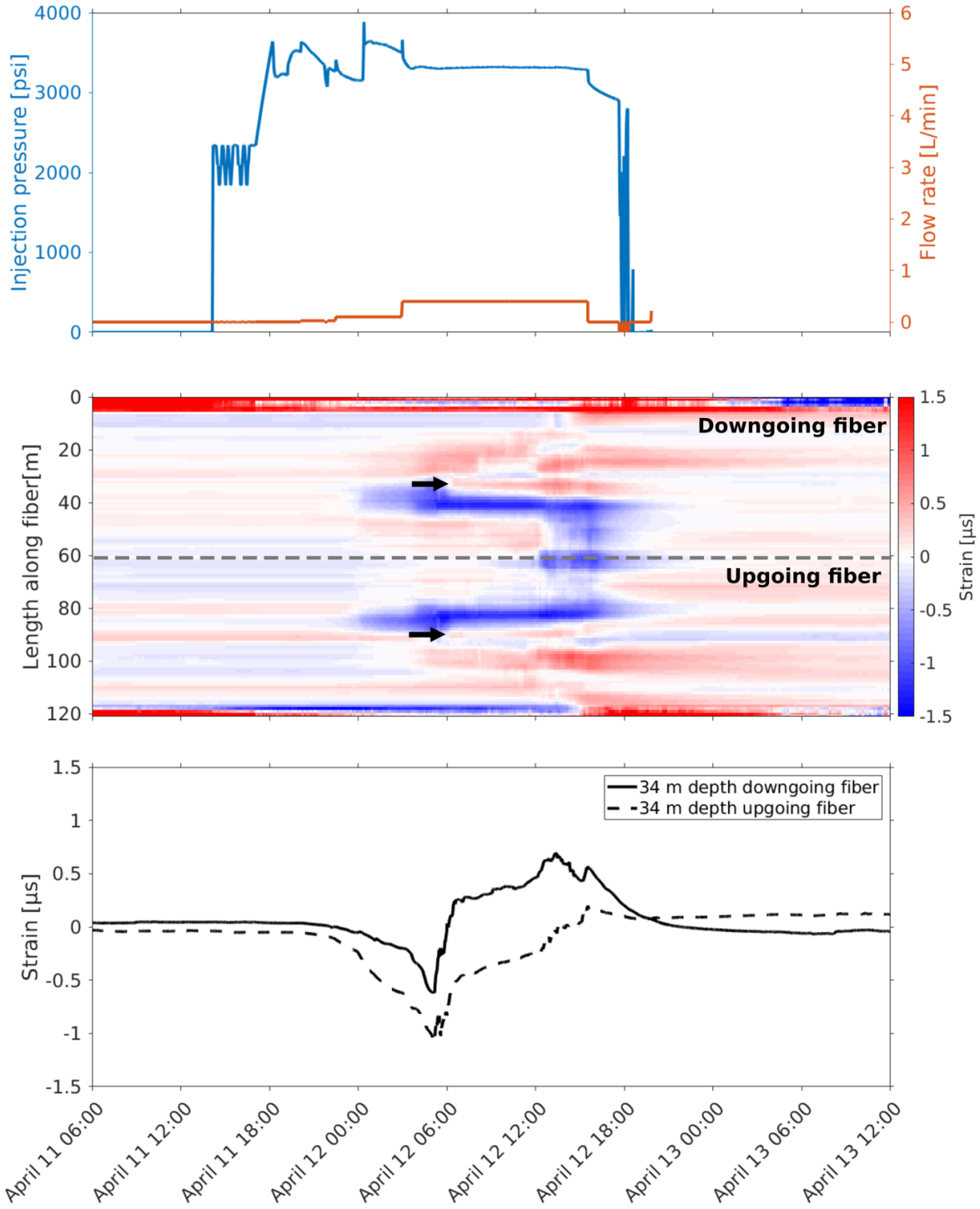

Figure 7.4. Low-frequency DAS strain recorded along borehole AMU during Stimulation 1 in Zone 7. (Top) Injection pressure and flow rate; (Center) Low-frequency DAS strain recorded along the

length of the fiber deployed in borehole AMU. Note the expected symmetry with respect to the bottom of the well. Arrows indicate extensional signals indicating fracture hits at a depth of ~34 m, recorded on both sections of the fiber. (Bottom) Strain at ~34 m depth over the time of the observed DTS spike (5:23 am UTC) for both sections of the fiber.

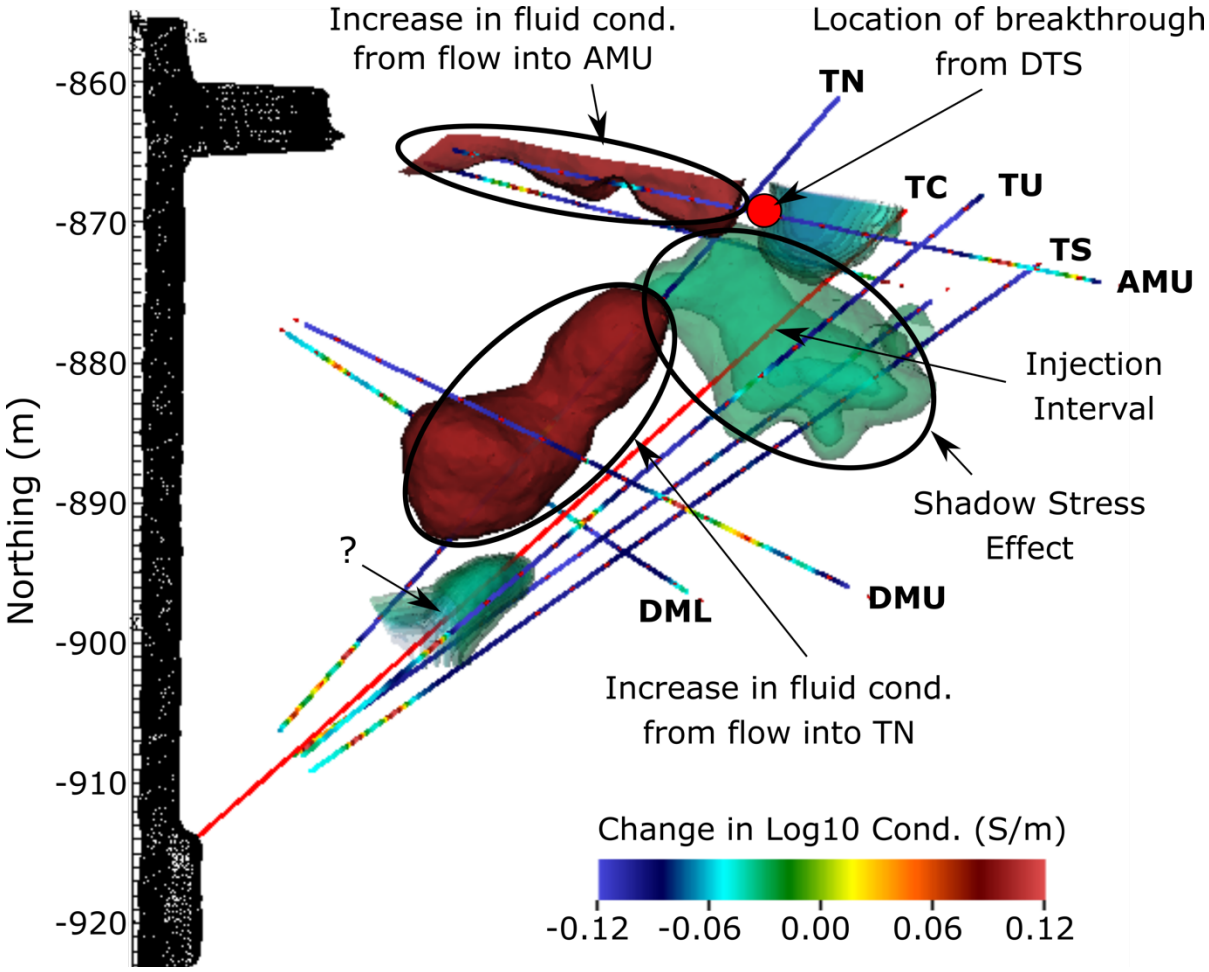

Figure 7.5. Electrical resistance tomography image of the testbed during Stimulation 1. Several things are notable: near the injection interval, a shadow stress feature is observed (green). Increases in conductivity are observed near well TN carrying produced water, and AMU, which the stimulated fracture penetrated.

Early on during this stimulation while the flowrate was very low (3 mL/min), the SIMFIP tool measured a consistent, mostly vertically downward displacement in short steps of few micrometers totaling about 20 micrometers starting at pressures between 2500 – 3000 psi, which is well below the breakdown pressure of ~3650 psi. At the breakdown at a pressure of ~3650 psi, an abrupt change in the direction of the displacement of almost 90 degrees from mostly vertical down to north and slightly upwards occurred totaling about 5 micrometers. This was accompanied by a drop in pressure (with flow kept at a constant flow rate of 3 mL/min) indicating that fracturing occurred. This displacement was subsequently partially reversed, however an irreversible component in the direction of the initial step-wise displacements remained (Figure 7.6). The

pattern of the displacements observed in combination with the initial pressure build up and subsequent drop could be an indication of the activation of a pre-existing fracture in a stick-slip-like shear mode preceding opening at breakdown and partial closing when pressure starts to drop again. The same step-wise displacement was not observed during later stages of the test.

The initial movement of the rock during stimulation was not indicated by the DORSA probe located in the TN borehole several tens of meters away. However, after flow was increased to 400 mL/min the DORSA started to exhibit a very linear but polyaxial contraction. This trend started to reverse after the injection was stopped (Figure 7.6). The DORSA was placed far away from where fractures intersected TN, therefore only measuring secondary effects of the stimulation. The contraction on the DORSA is in agreement with the negative strain measured by the DAS below the fracture intersection at 34m in AMU, indicating a compression of the rock mass outside the area where a fracture/fracture network intersects the borehole. A repeated injection in Zone 7 with a borehole camera in TN instead of the DORSA confirmed fractures intersecting at 172' and177' in TN.

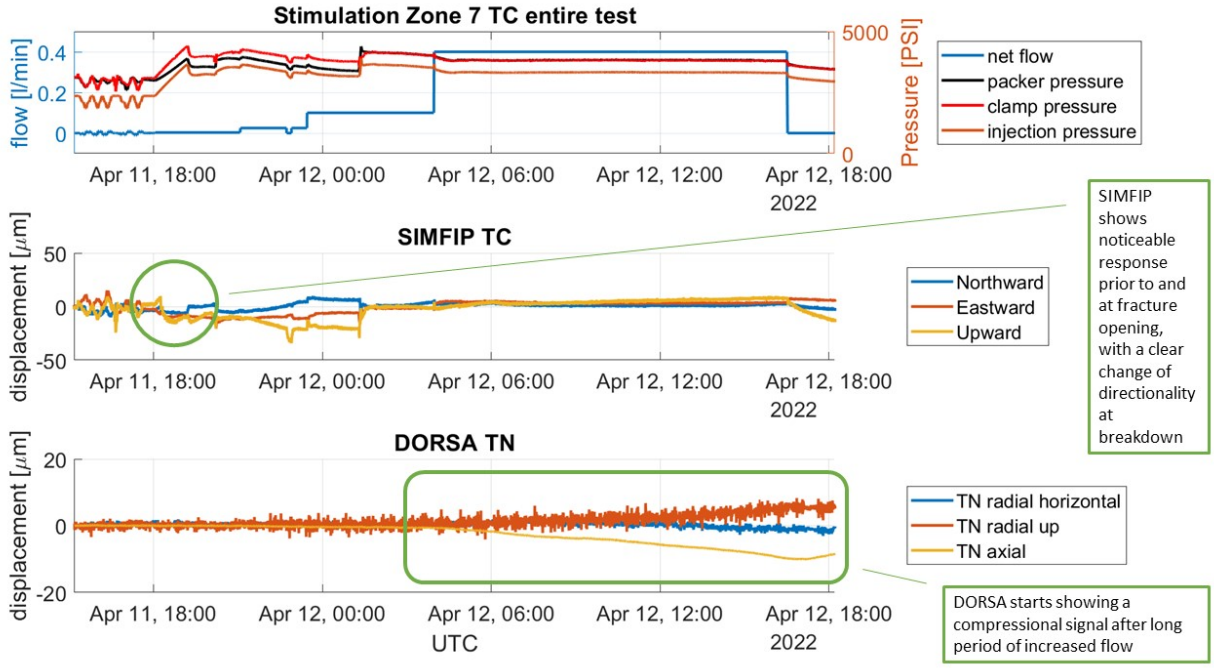

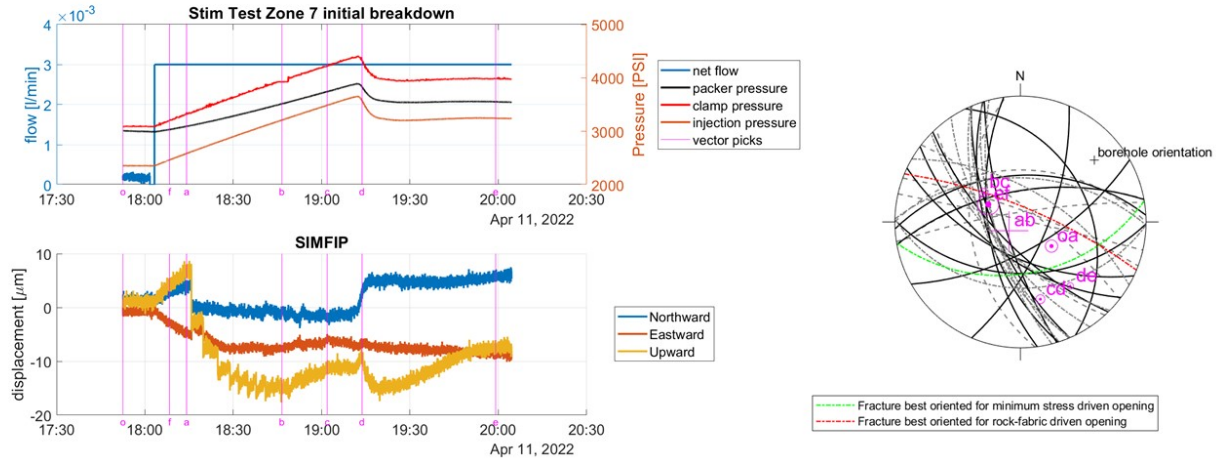

Figure 7.6. Top: Displacements measured in TC and TN by the SIMFIP and DORSA probes during Zone 7 stimulation. Bottom: Displacements measured with the SIMFIP probe at the injection point prior to, at, and after initial breakdown in North, East and vertical direction - showing in which direction the bottom of the interval was moved relative to the top - as well as injection pressure and flowrate. The displacements between selected points in time (depicted by magenta lines) are also plotted in a lower hemisphere stereoplot together with pre-existing fractures as identified by the borehole logging campaign, showing in which direction the displacements occurred relative to the natural fractures affecting the test interval.

P-wave arrival time changes from the CASSM data also correlate well with the ERT results. Up to Stimulation 1, most of the P-wave arrivals for all raypaths to the single-component hydrophones decreased gradually, indicating a velocity decrease (Figure 7.7). However, after Stimulation 1, the arrival times of P-waves abruptly changed. Raypaths that intersect the stimulation region along the injection well show a marked decrease in arrival times of the P-wave, correlating to a velocity decrease along the injection region (Figure 7.8). Velocity decreases are expected when fluids are injected, temperatures increase, and fractures open. The time-lapse arrival times of the P-wave also illustrate that some raypaths undergo a velocity increase, which could be due to a temperature decrease, fracture closing, or a movement of fluids away from those regions.

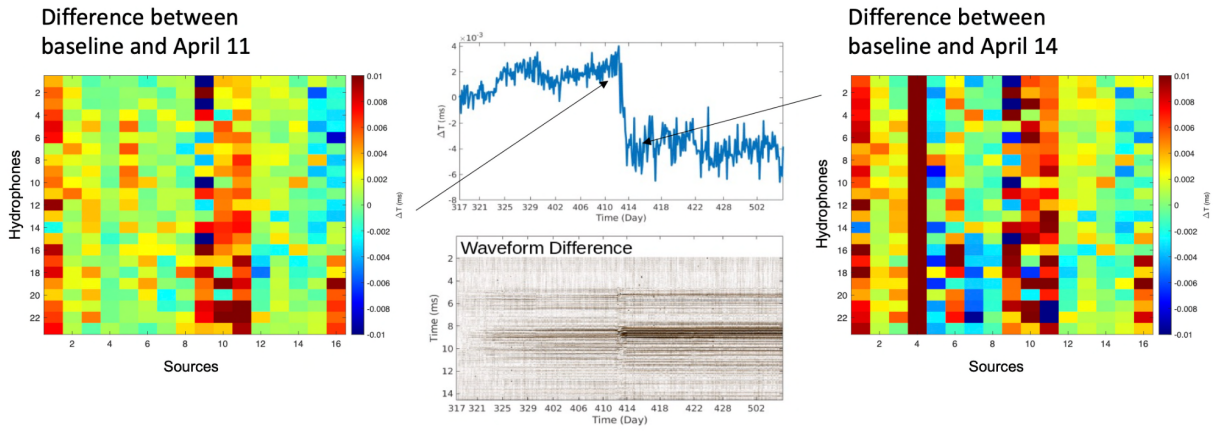

Figure 7.7. left - Arrival time changes of the P-wave arrival between baseline and CASSM hydrophone data collected on April 11, 2022, before Stimulation 1. middle - Arrival time changes of the P-wave relative to the baseline of one selected raypath, marking the sharp change in P-wave arrival time and waveform difference. X-axis represents dates where the first number is month and second number is day. right - Arrival time changes of P-wave between baseline and CASSM hydrophone data collected on April 14 after the stimulation period. Source 4 did not initiate in this period. Red colors indicate a velocity decrease and blue indicates a velocity increase.

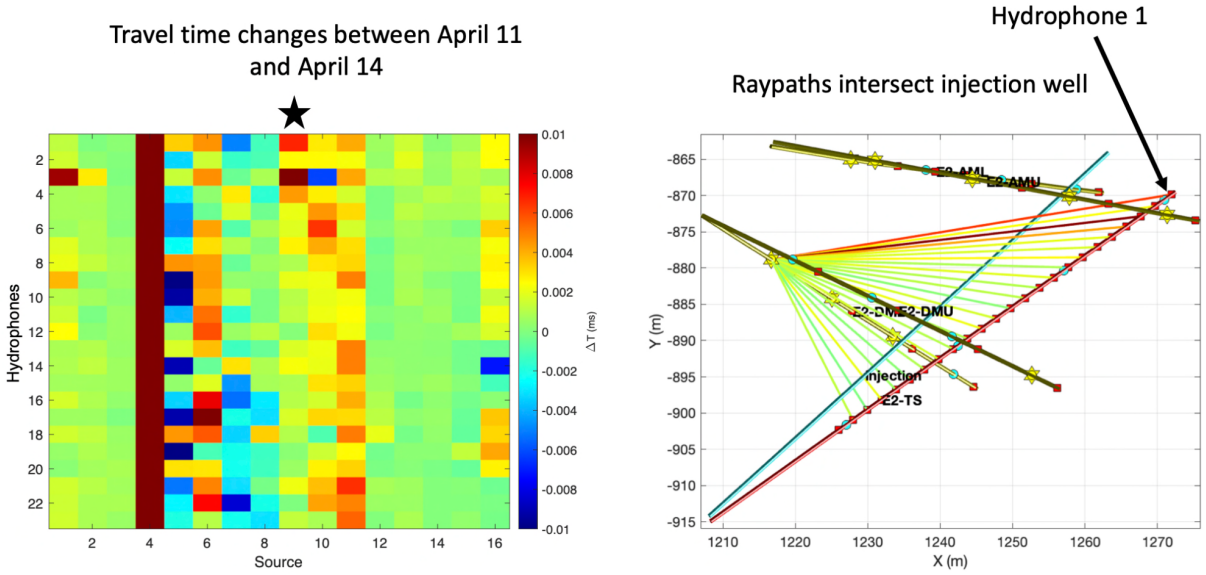

Figure 7.8. left- Arrival time changes of the P-wave arrival between April 11 and April 14, 2022, data in Figure 7.7 on CASSM hydrophone data (left image). Right - One set of raypaths that intersect the injection well for one source is shown (marked with black star in the left image). Raypaths are colored based on travel time change from April 11 to April 14 for all hydrophone data. Source 4 did not initiate in this period. Red colors indicate a velocity decrease and blue indicates a velocity increase.

7.2 Stimulation 2 - TC Zone 4 (168.7-176.6 ft, 51.42 - 53.83m) - Cyclic Injection

Stimulation in Zone 4 was performed by cycling the injection pressure about the fracture opening pressure repeatedly in an effort to create a scalloped fracture (Figure 7.9). The fracture initiation pressure on this zone was higher than the other zones. Because of that, pressures on the high and low part of the cyclic injection were gradually increased until it was evident that a fracture had been formed. The pressure continued to be cycled until a net volume of 40 L was injected. During this time a small amount of effluent flow was observed from wells TN, TL, and TS, though the production rate from TS was considerably smaller than from the other two wells. No production was observed from well TU. This stimulation did not intersect any grouted monitoring wells or the drift, but the total injection volume was small. Following this stimulation, the injection interval in the TC well was held at 2340 psi for several days to observe flowback.

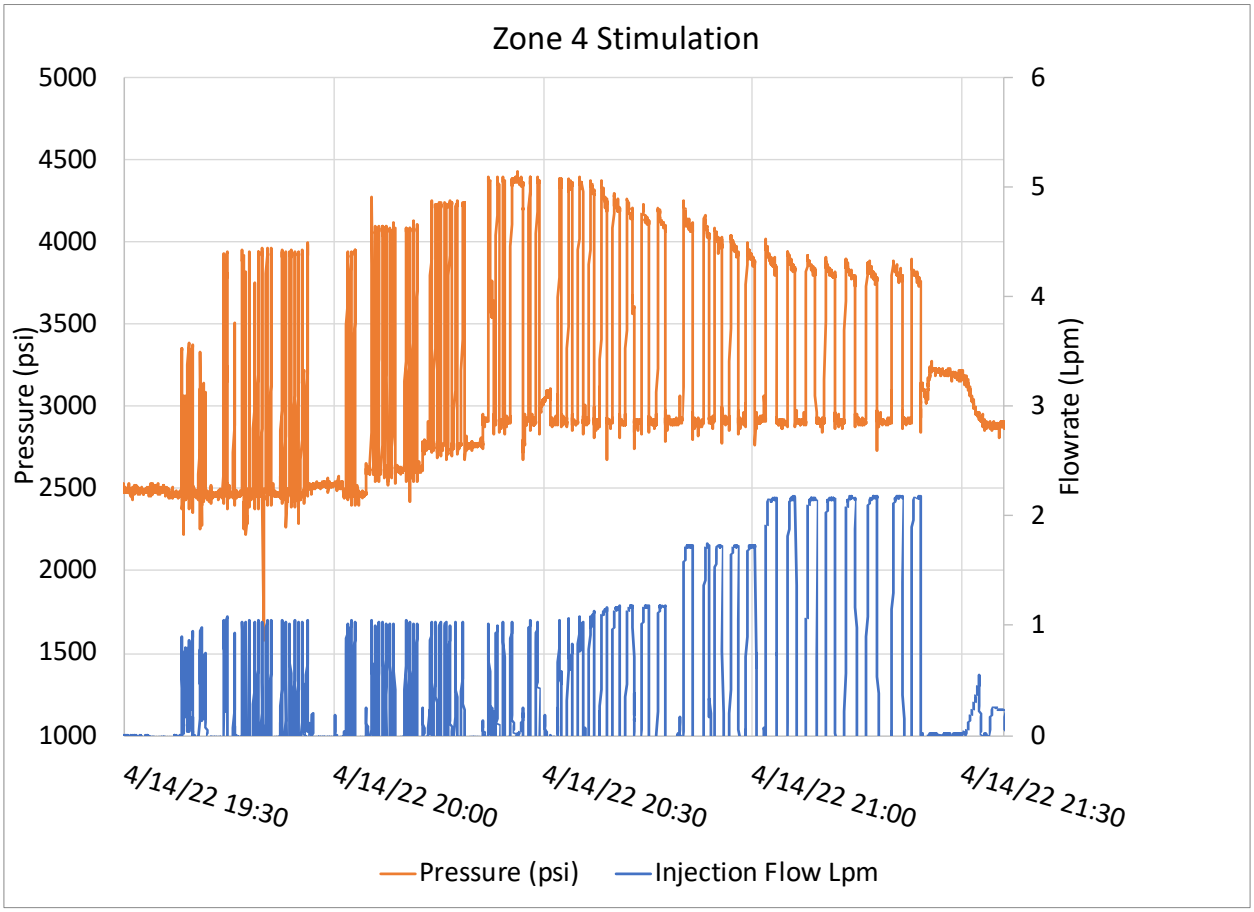

Figure 7.9. Injection pressure and flow for the cyclic pressure stimulation at Zone 4.

The displacement signal measured by the SIMFIP during Zone 4 stimulation was masked by the effects from the rapid pressure cycles from the stimulation itself (Figure 7.9). The DORSA probe exhibited a very linear mostly axial elongation (third panel in Figure 7.10), which started to reverse into an axial contraction after the injections ended. This shows that a small extensional deformation of less than 10 micrometers started happening in the area at around 140' feet down in TN where the DORSA was situated, without a clear fracture breakthrough event. This is consistent with what was observed during a repeated injection one week later, with a borehole camera in TN in lieu of the DORSA. While weak inflow could be observed, likely from several locations between 140' and 180', no flowing fracture or fracture network could be identified. In the DAS low-frequency strain data, a similar pattern of concentration of extensional deformation along an entire section of a borehole without one clear point of inflow could be observed in neighboring boreholes during several stimulations, as described below (Figure 7.15). The DTS confirms an inflow of warmer water somewhere in the lower section of the borehole at the same time as the deformation is recorded on the DORSA (fourth panel in Figure 7.10).

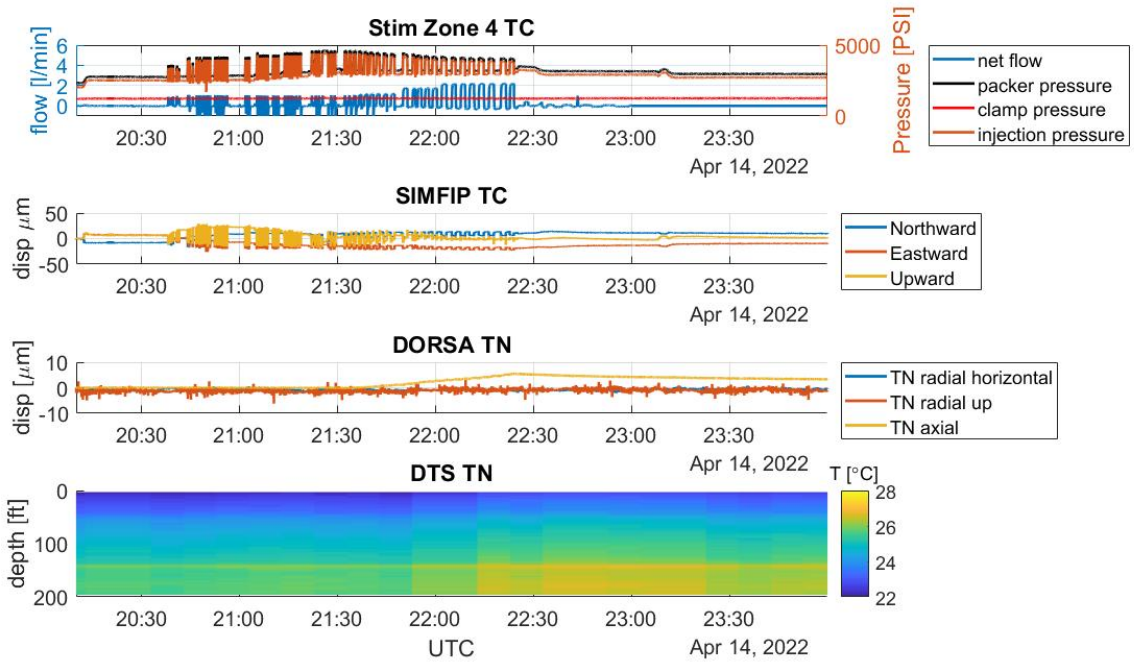

Figure 7.10: Injection pressure and flow for the cyclic pressure stimulation at Zone 4 (Panel 1) and corresponding displacements measured in TC and TN by the SIMFIP and DORSA probes (Panels 2 and 3) during Zone 4 stimulation, as well as temperature along borehole TN from DTS (Panel 4). Whereas the SIMFIP signal is hidden by the strong cyclic pressure variations of the stimulation in TC, DORSA and DTS show a weak but clear extensional deformation accompanied by warming in the lower section of TN.

Faint, small magnitude strain signals were observed in monitoring boreholes AML, DMU and DML, although they are most likely related to poroelastic deformation being transferred through the volume being stimulated.

7.3 Stimulation 3 - TC Zone 1 (145.0-152.9 ft, 44.20 - 46.61 m) - High Flow

To compare with the low rate (Zone 7) and cyclical (Zone 4) injections, a higher-rate stimulation was performed in Zone 1 (Figure 7.11). The fracture was initiated by injecting at 1 L/min for approximately 2 minutes, then the well was shut-in for approximately 1 hour. Following the shut-in, the well was flowed back at a controlled rate of 250 mL/min followed by shutting in the well when the pressure declined to atmospheric pressure. This shut-in resulted in a significant pressure increase in the packed off interval, indicating that pressurized water remained trapped in the fracture. The fracture was reopened by pumping at 1 L/min and pumping continued for approximately 2 minutes. We followed the reopening by a controlled flowback at 100 mL/min. This slower rate was selected to minimize the near-wellbore fracture pinching that trapped pressurized water inside the rock. Again, the pressure rebounded significantly but at a smaller rate and to a smaller magnitude. We opened the fracture again by injecting at 1 L/min, then propagated the fracture by injection at 5 L/min. A short time later breakthrough into TN, TL, and the wall of the drift near Site A was observed. The peak production rate from the production wells was approximately 1.3 L/min. Typical flows from TL were ~0.640 L/min, TN ~ 0.55L/m, and TS was dripping. No production was observed from well TU. Although the Zone 1 stimulation did not

intersect any grouted monitoring wells as no temperature spikes were observed in the DTS data, it did intersect the drift and appears to also result in low-rate water production from well TV4100 (located in Alcove A). In spite of not indicating intersection of the fracture and any grouted monitoring wells, a significant strain signal was observed in DML at depths that correspond to DTS hits during tests in May (described below). It is not clear whether this strain signal means that there was a fracture hit with no flow, or deformation transferred along weaker zones without actually breaking and intersecting the borehole. Strain signals were also observed in AML and DMU, but the magnitude is much smaller. This might suggest poroelastic deformation in the testbed. The intersection of the fracture with TV4100 is hypothesized to occur through a path within or along the contact with the rhyolite dike that underlies the stimulation wells and connects to TV4100.

On 4/21/2022 a flow test was performed using a sewer camera deployed in TL and TN while injecting into TC. Water jetted vigorously into TN at 148.9 ft (Figure 7.12). After shut-in, the jetting declined. Reinitiating injection at 2 L/min resulted in a time lag of about 2 minutes for the jets to reappear. Jets were also observed at 154.5 ft in TL, and another inflow point was observed in TL at 160 ft. DTS data from TN during this stimulation show a clear temperature signal from the inlet water at about the same location identified using the visual observations in Figure 7.12.

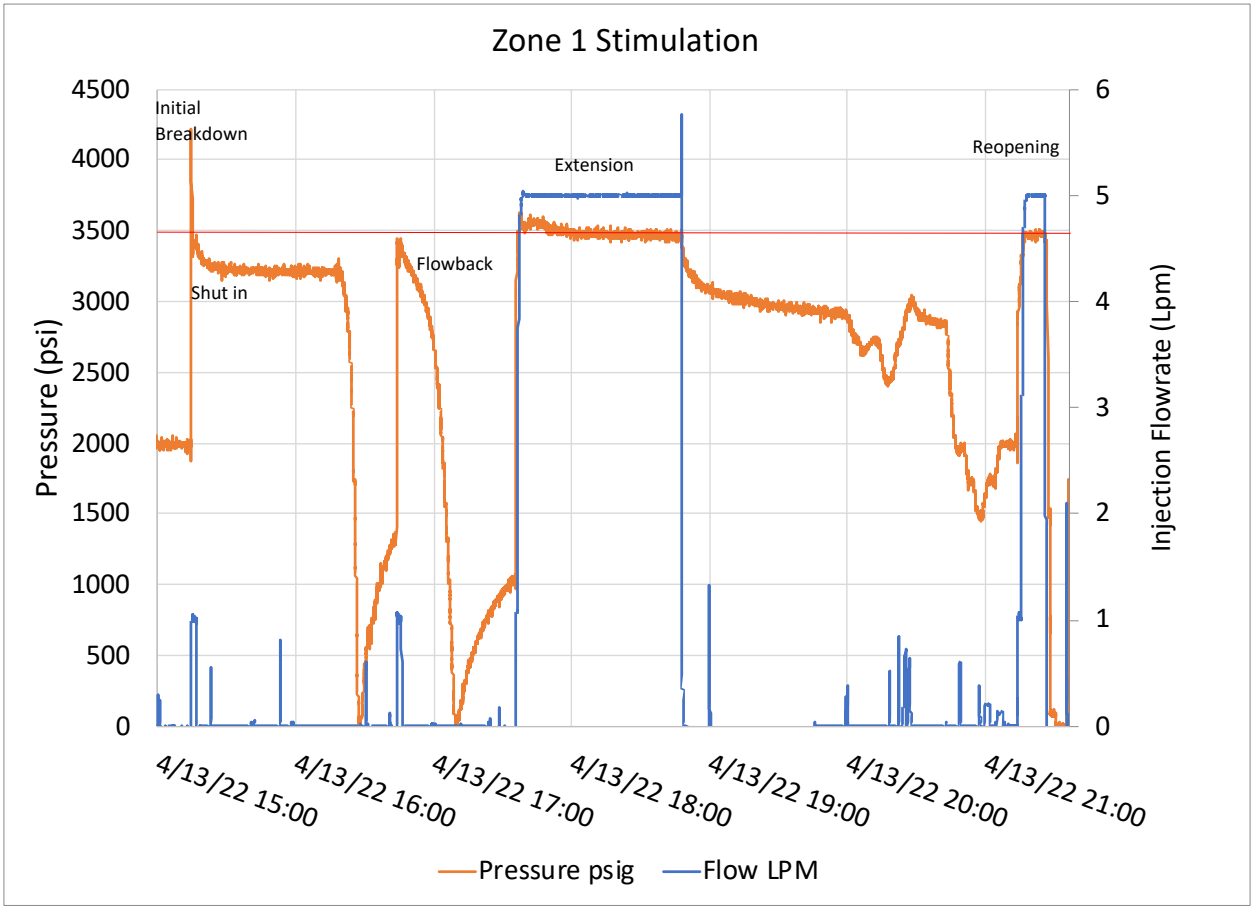

Figure 7.11. Injection pressure and flowrate for high-rate injection. The horizontal red line at 3,500 psi was added to allow easy comparison of the initial breakdown pressure, fracture extension pressure, and reopening pressure.

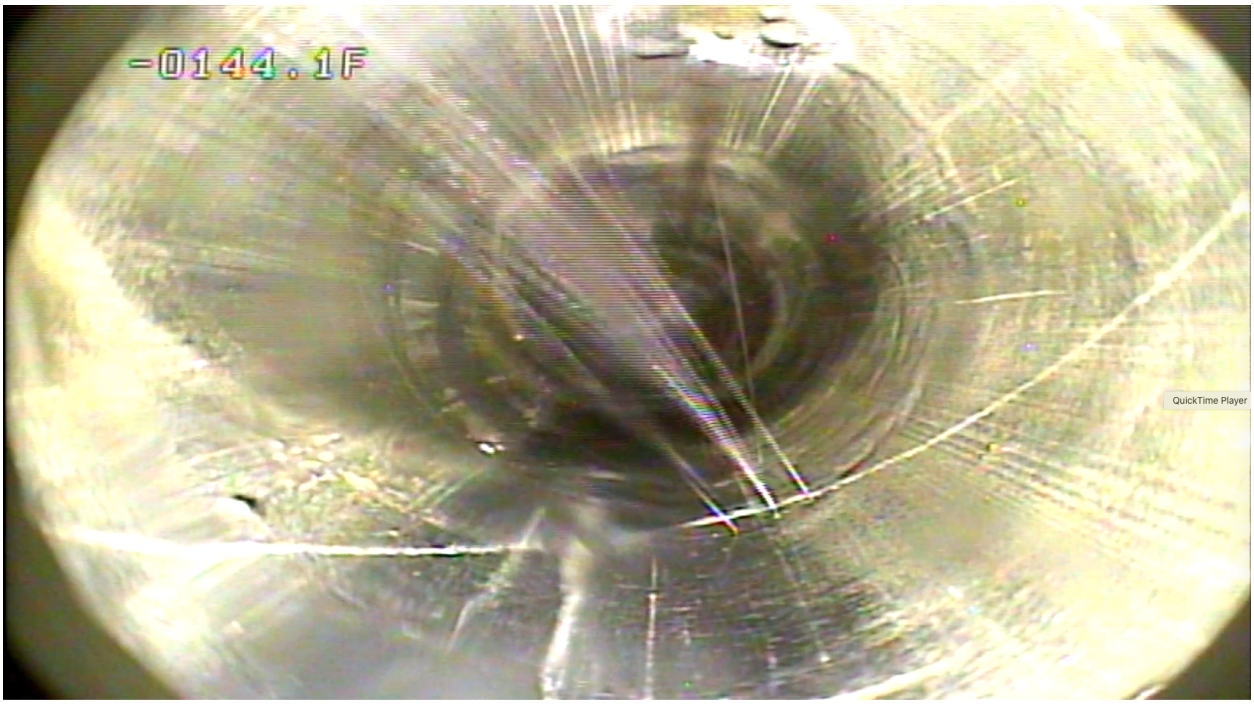

Figure 7.12. Water jetting into well TN at 149.8 ft (depth notation on image is incorrect) when pumping into Zone 1 in TC.

During the stimulation of Zone 1, the pressure control of the system anchoring the SIMFIP probe to the rock was overpowered by the rapid rise in zone pressure, resulting in a declamping of the tool and loss of data during the breakdown phase of the test. During later cycles of the test, clear and mostly reversible displacements of up to 200 micrometers (not corrected for potential tool-pressure effects) were observed (Figure 7.13).

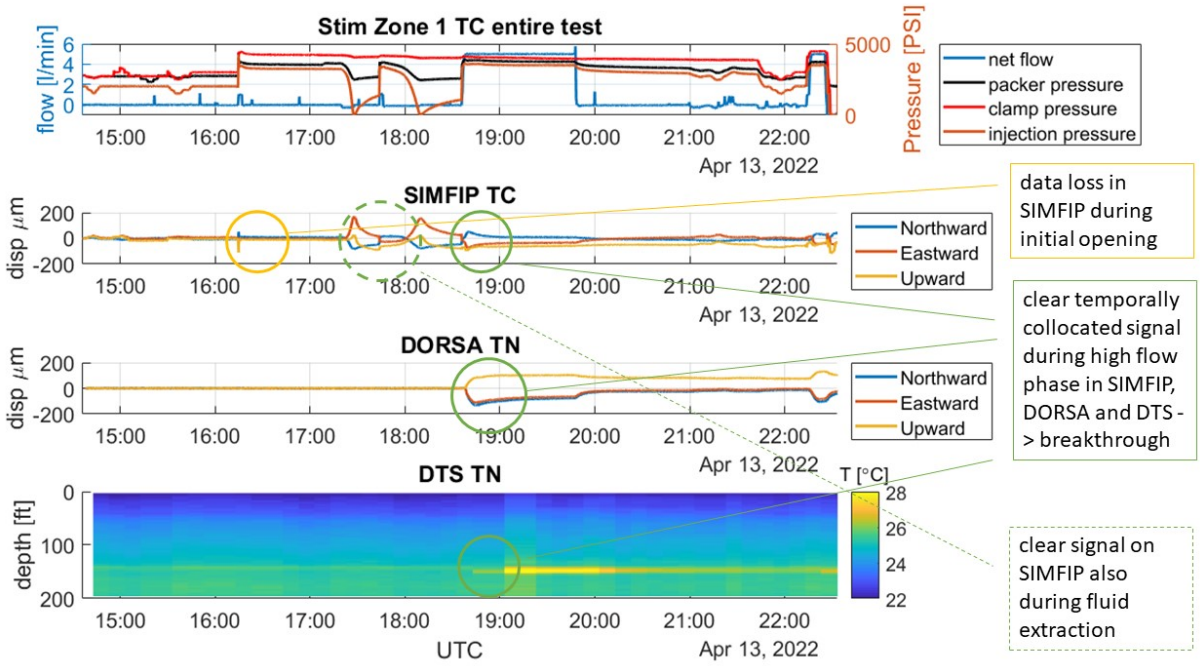

Figure 7.13. Displacements measured in TC and TN by the SIMFIP and DORSA probes during Zone 1 stimulation, as well as injection pressure and flowrate in TC and DTS in TN.

During the last cycle of this stimulation with flow increased to 5 L/min, the DORSA indicated a clear displacement of the rock in TN of several hundred micrometers where the DORSA probe was positioned (Figure 7.13 Panel 3). This displacement is spatiotemporally synchronized with a peak in temperature observed on the DTS in TN, indicating a breakthrough of fluid right at the DORSA location. This was later confirmed with a downhole camera during a repeat-injection into Zone 1 (Figure 7.12). Before the large displacement corresponding to the hydraulic TC-TN connection, the DORSA recorded a clear micrometer scale signal, distinguishable only in the lower-noise axial measurement (Figure 7.14 Panel 3). This rapid DORSA response is likely a poroelastic deformation pre-dating the fracture propagation to TN.

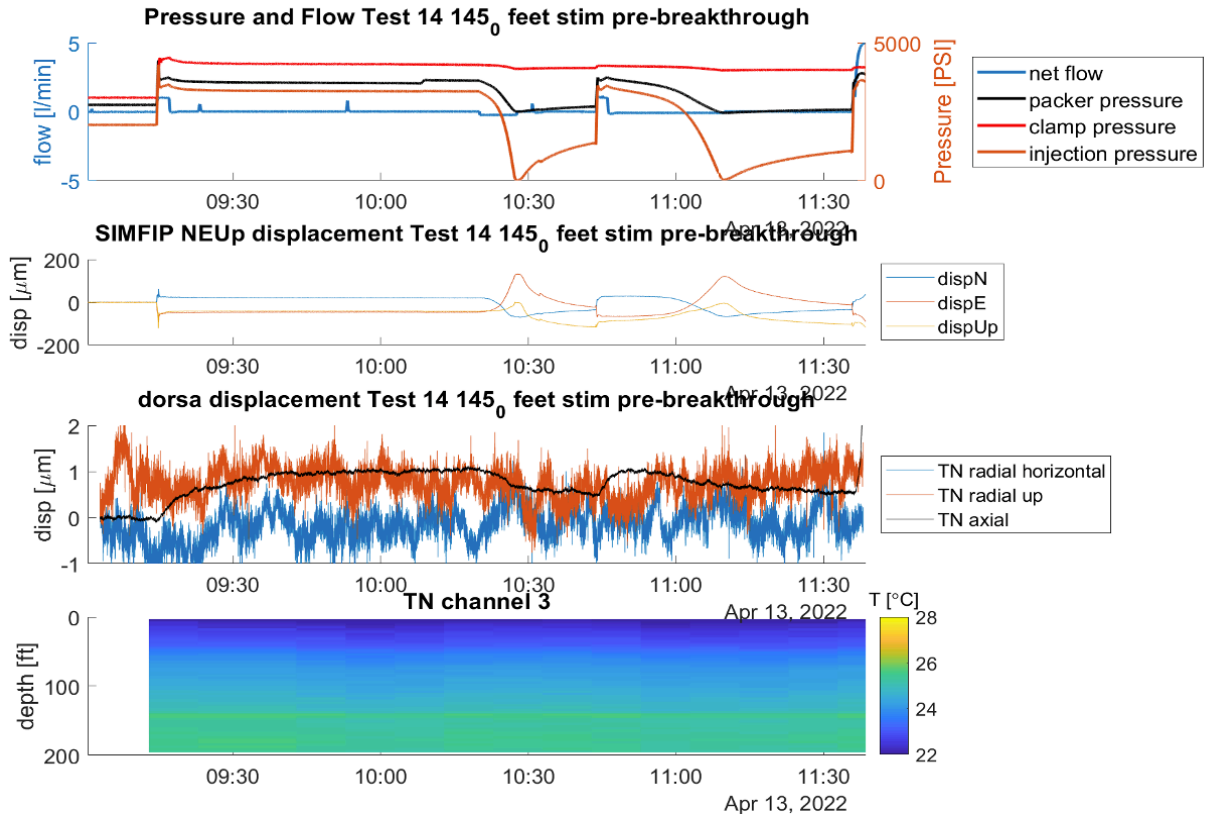

Figure 7.14. Displacement measured by the DORSA in TN and SIMFIP in TC before the fluid-breakthrough into TN (note no indication of increased temperature in the DTS data - bottom panel). These are plotted in parallel with injection pressure and flow and SIMFIP measurements.

DAS data suggest strain responses in wells AMU, AML and DMU. Low-frequency (1Hz) DAS strain data (Figure 7.15) recorded a strain peak in borehole DML at depths of ~15 m (black arrows in the center panel) and ~43 m (blue arrows in the center panel) shortly after flow rate was increased to 5 L/min (top panel). These strain signals do not correlate with DTS peaks during this stimulation, but extensional signals are an indication of concentration of deformation around these areas. Interestingly, fracture intersections at these exact depths are observed in DTS measurements during flow tests conducted a month later. These observations could be linked to areas of pre-existing weakening that did not carry flow during this first round of tests but ended up opening and conducting water into the monitoring boreholes after repeated stimulation. Minor strain signals are observed in boreholes AML and DMU during stimulation of Zone 1 at depths of 20-30 m and 25-35 m, respectively. These less localized, smaller magnitude extensional signals are most likely related to poroelastic deformation transferred across the rock volume.

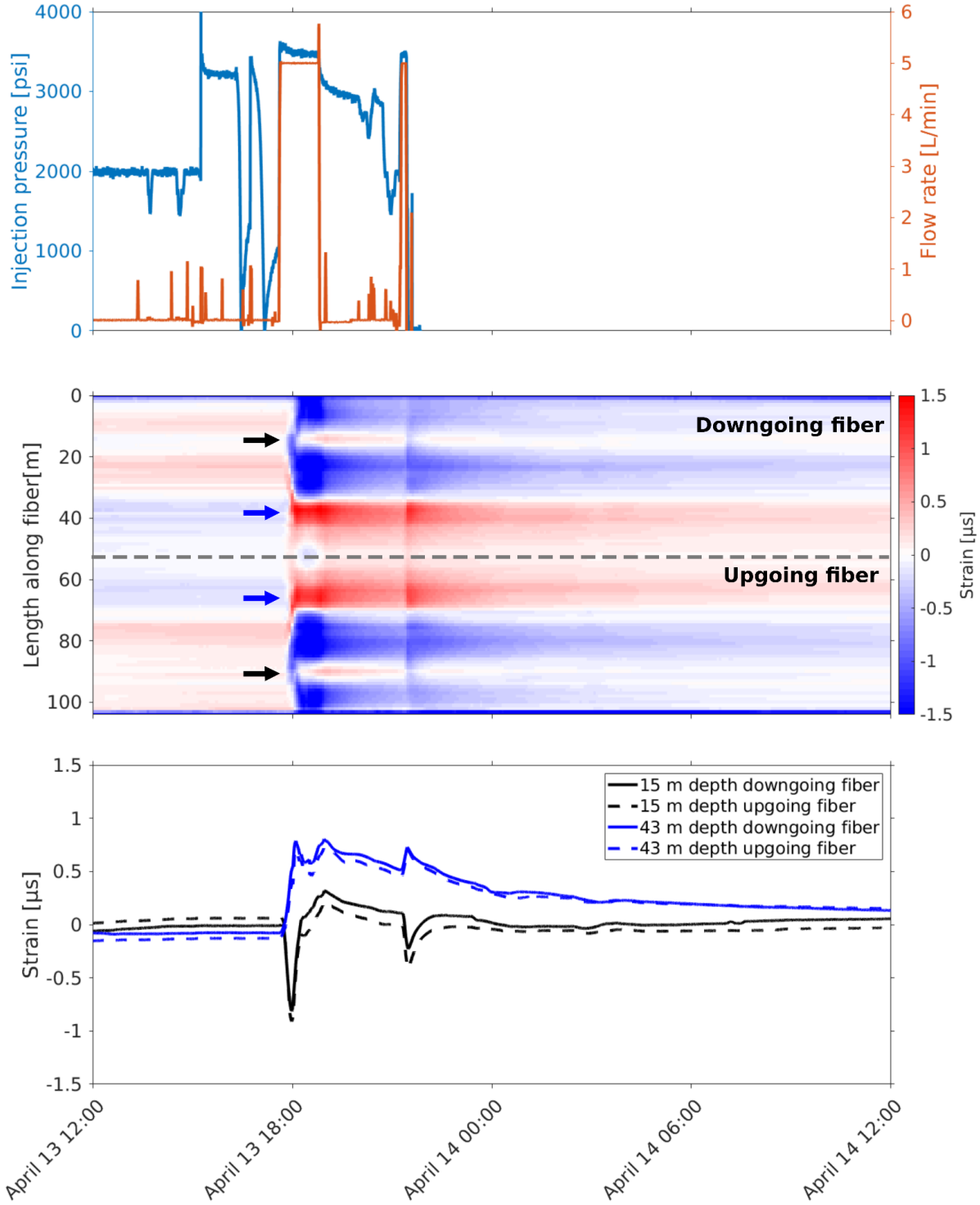

Figure 7.15. Low-frequency DAS strain recorded along borehole DML during stimulation in Zone 1. (Top) Injection pressure and flow rate; (Center) Low-frequency DAS strain recorded along the length of the fiber deployed in borehole DML. Arrows indicate extensional signals of ~34 m recorded on both legs of the fiber-optic cable at 15 m and 43 m depth. (Bottom) Strain at 15 m and 43 m depth for both legs of the cable.

7.4 Stimulation 4 - TU 177.4 - 179.6 ft. (54.07 - 54.74m) - High Flow (54.07 - 54.74m)

Simulations indicated that injection of fluid from TC would not be sufficient to observe a thermal breakthrough. Consequently, an attempt was made to stimulate a zone of borehole TU. TU was targeted for stimulation because it was the only well from which no significant production flow had been observed in previous tests and it had a number of wells below it to possibly cage flow (Frash et al., 2018a; Frash et al., 2018b; Frash et al., 2021; Frash et al., 2020). On May 5, 2022, a stimulation was performed in TU (Figure 7.16) at a depth approximately aligned with Zone 4 of TC using a straddle packer without the SIMFIP tool. Injection commenced at 1 L/min until breakdown was observed approximately 1 min later. A peak pressure of ~5500 psi was reached and flow was subsequently increased to 5 L/min and held for roughly 4 hrs. During this time, pressure approached a steady state value of 4500 psi. The resulting fracture intersected TC, TN, and TL and outflow from these boreholes totaled approximately 25% of the injected volume.

7.4.1 TU Flow Test

On May 6, 2022, injection into TU resumed at 5 L/min. While flowing into TU, the packer installed in TC was moved slightly because it appeared that a fracture from TC was impinging on the packer. The final installed depths were as follows:

- TC: 167 ft (straddle interval centerline from flow metadata)
- TN: 176.7 ft (straddle interval centerline from flow metadata)
- TL: 172.0 ft (straddle interval centerline from flow metadata)

7.4.2 TC Flow Tests

Injection was then switched to TC at 2 L/min to identify whether flow from TC would be captured at TU. Outflow was measured from the packer intervals in TN and TU totaling ~35% of injection, representing a significant improvement in fluid recovery from previous TC injections.

During this phase of stimulation, no intersections were observed with the grouted monitoring boreholes via DTS. DAS recorded small magnitude, broad strain signals, specifically in boreholes AMU, AML and DMU. These signals are most likely related to the bulk deformation of the testbed as fluid is injected. This phase of injection did produce the first detectable seismic events beginning with the restart of injection at 5 L/min on May 6 (Figure 7.17). Due to the low signal-to-noise ratio of the seismic events, automatic processing during the entire experiment did not produce reliable locations. We therefore manually revised all phase arrival picks, added S-wave arrivals which were not included in the automatic workflow and relocated the seismicity before interpreting the results. Figure 7.17 shows the timing and location of seismicity during this time period. Only nine events were detected and were located generally above and towards the drift from the injection point. This is consistent with the observations of flow at the grouted wells and drift during previous tests.

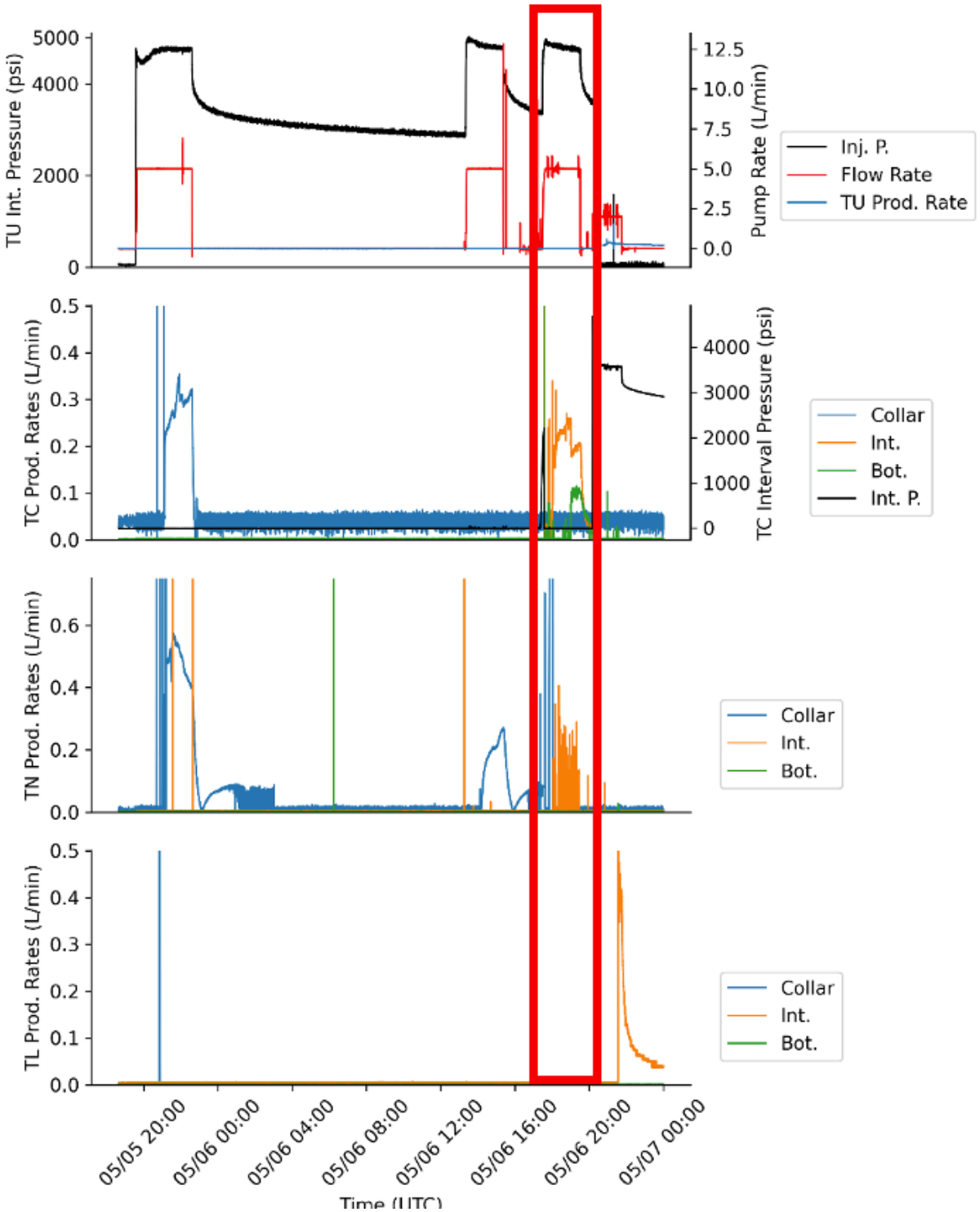

Figure 7.16. Plot of the stimulation data for the 177.4-179.6ft interval in well E2-TU on May 5 and May 6. Upper plot is the pump rate and interval pressure in well E2-TU. Note that for the last injection cycle the flow was directed into the interval of well E2-TC while water was produced from well E2-TU (red box). The bottom three plots show the recorded flow rates from the packed-off interval, zone below the interval (Bot.), and from the well collar for wells TC, TL, TN.

A plan view of the change in bulk electrical conductivity caused by the TU-TC stimulations is shown in Figure 7.18. A positive conductivity anomaly (pink zone in Figure 7.18) is likely associated with an increase in porosity (i.e., fractures opening). This appeared shortly after the TU injection on May 5th, with no further changes after the TC stimulation on May 6th. Alignment of the anomaly generally corresponds with the alignment of the microseismic events shown in Figure 7.17. Although the injection intervals in TC and TU were depressurized by May 7th, the positive conductivity anomaly persisted through to the next stimulation events in TC starting on May 17th.

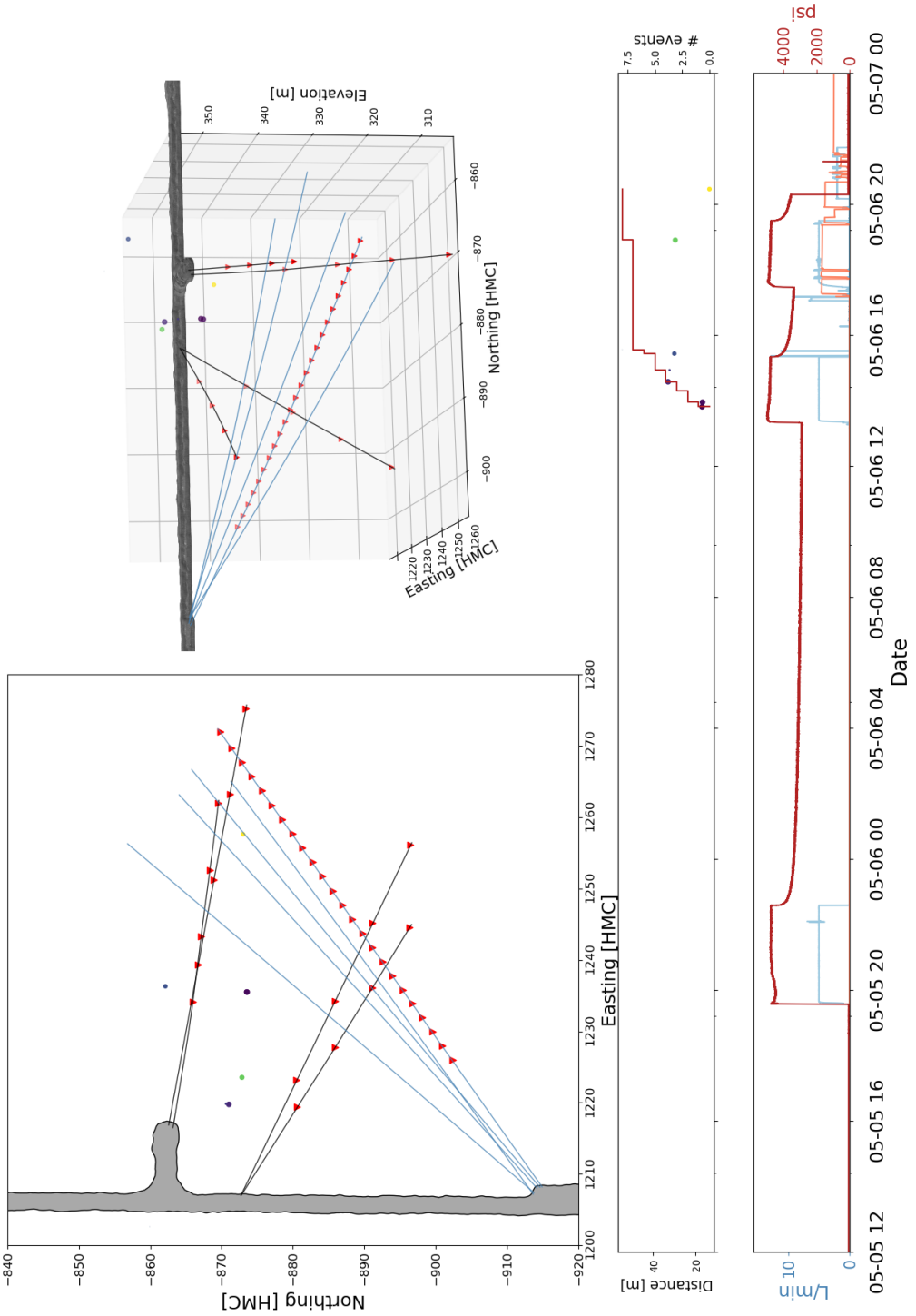

Figure 7.17. Microearthquakes detected during stimulation of the 177.4 - 179.6 ft interval of TU. The top two panels show the location of each event. The uppermost time series plot shows the cumulative number of events and their distance from the injection point, with dot color changing with time. The bottom timeseries plot shows the injection pressure and flow rate in psi and L/min, respectively. The time axis is in UTC.

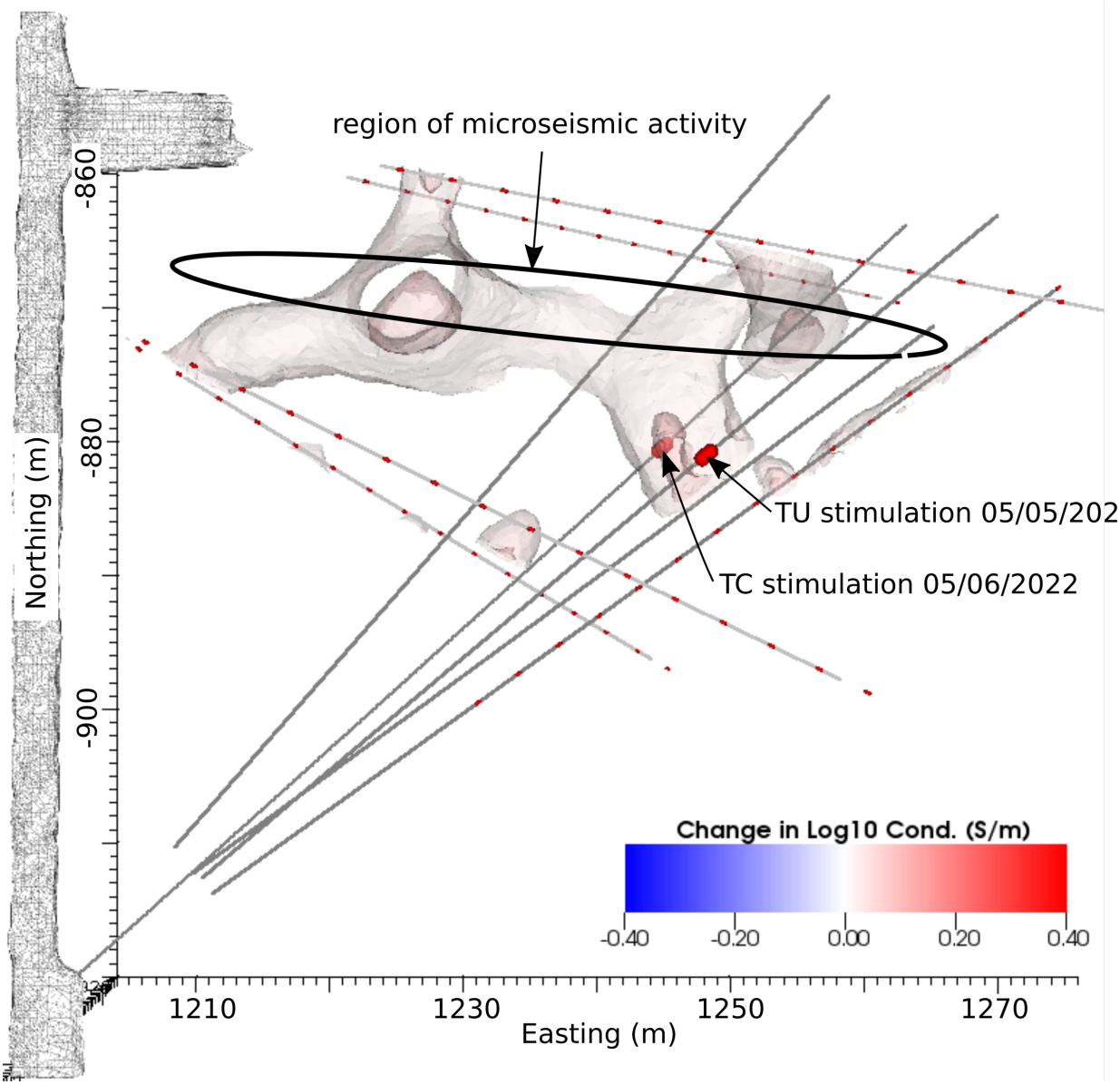

Figure 7.18. ERT-based change in bulk electrical conductivity from pre-stimulation on May 05 12:00, to post stimulation on May 7 00:00 (TU Injection). Increases in conductivity are likely caused by increases in porosity (e.g., fractures opening), and generally align with microseismic event locations shown in Figure 7.17. Negative changes in conductivity associated with compressive porosity reduction adjacent to the positive anomaly are not shown.

Stimulation and flow tests were conducted in TC 45.9-46.6 m and TC 50.44 – 51.11m on May 17 and May 18 respectively. The TC 45.9-46.6 m injection occurred at a nominal flowrate of 5 L/min for ~5 hrs, followed by the TC 50.44 – 51.11m injection at a nominal flowrate of 5 L/min for ~24 hrs. During the latter injection in particular, significant changes in bulk conductivity developed within the testbed. Figure 7.19 shows the change in bulk conductivity from 5 hrs before the 177.4

- 179.6 ft interval TU stimulation on May 5, to 2 hrs after the TC Zone 3 injection and shut-in test (including the changes shown in Figure 7.18) on May 19. Positive changes in conductivity, which are indicative of increases in porosity (i.e., fracture aperture dilation), originate near the TU Injection Zone injection point and extend north-northwest to connect to a nearly east-west trending anomaly that appears to extend to the drift outside of the ERT imaging zone. This general pattern of changes in conductivity is maintained for the remainder of the flow testing in TU as described below, including the saline tracer imaging and the final high-rate flow test. Negative changes in conductivity adjacent to the positive changes are thought to be caused by compressive stresses that squeeze native pore water out of the rock and reduce pore space, thereby reducing bulk conductivity (Johnson et al., 2021).

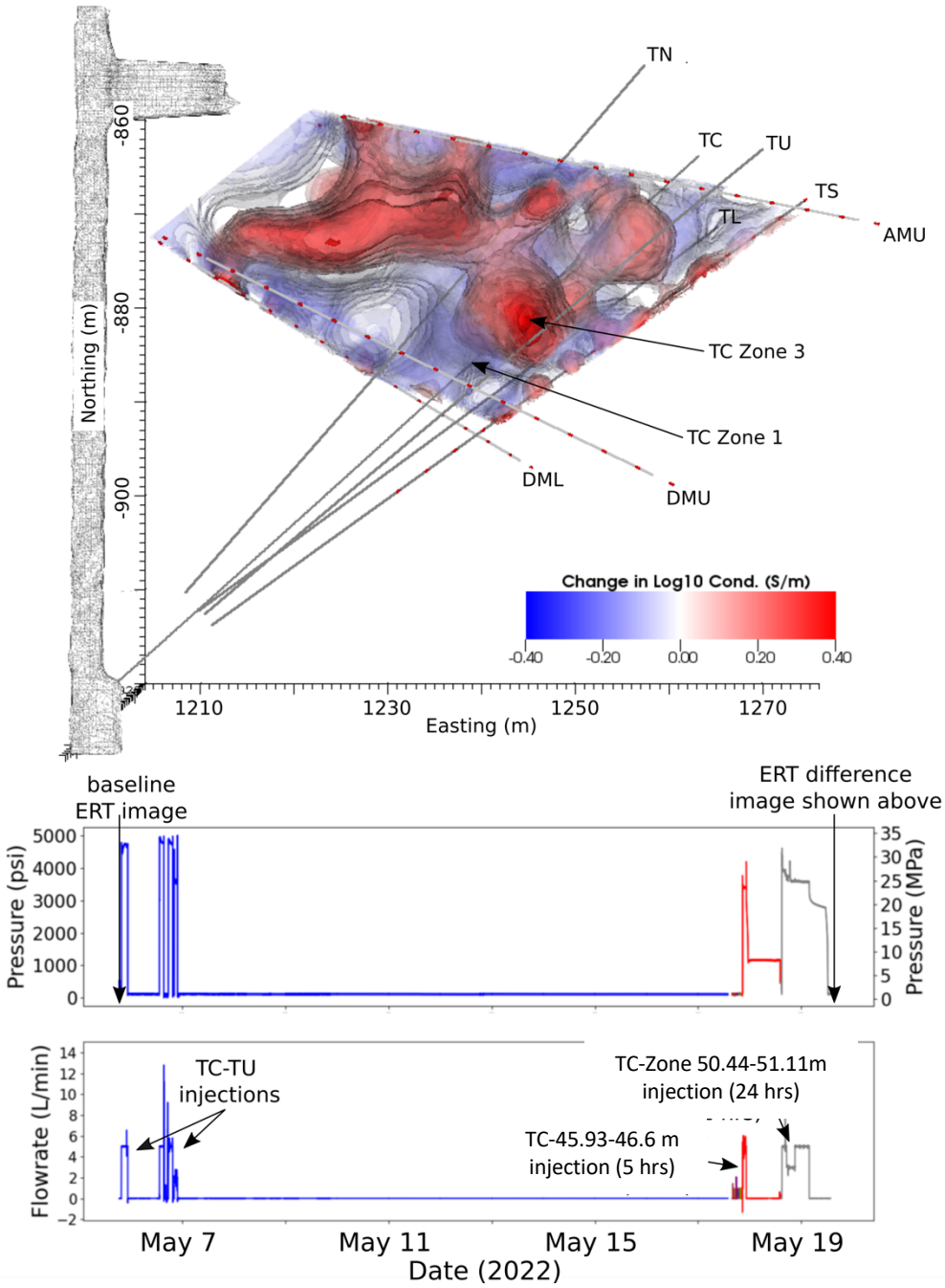

Figure 7.19. ERT-based change in bulk electrical conductivity from pre-stimulation on May 05 12:00, to final TC simulation in TC Zone 3 on May 19. Increases in conductivity are likely caused by increases in porosity (e.g. fractures opening). Negative changes in conductivity are associated with compressive porosity reduction (i.e. water squeezing out of pore spaces in regions of injection-induced compression).

During these flow tests, a fracture intersected with grouted monitoring borehole DML at depths of 42.9 m and 43.9 m. Low-frequency DAS also reveals several areas of localized strain, most significantly in boreholes AMU and DML (Figure 7.20). Extension at a depth of 43 m in borehole

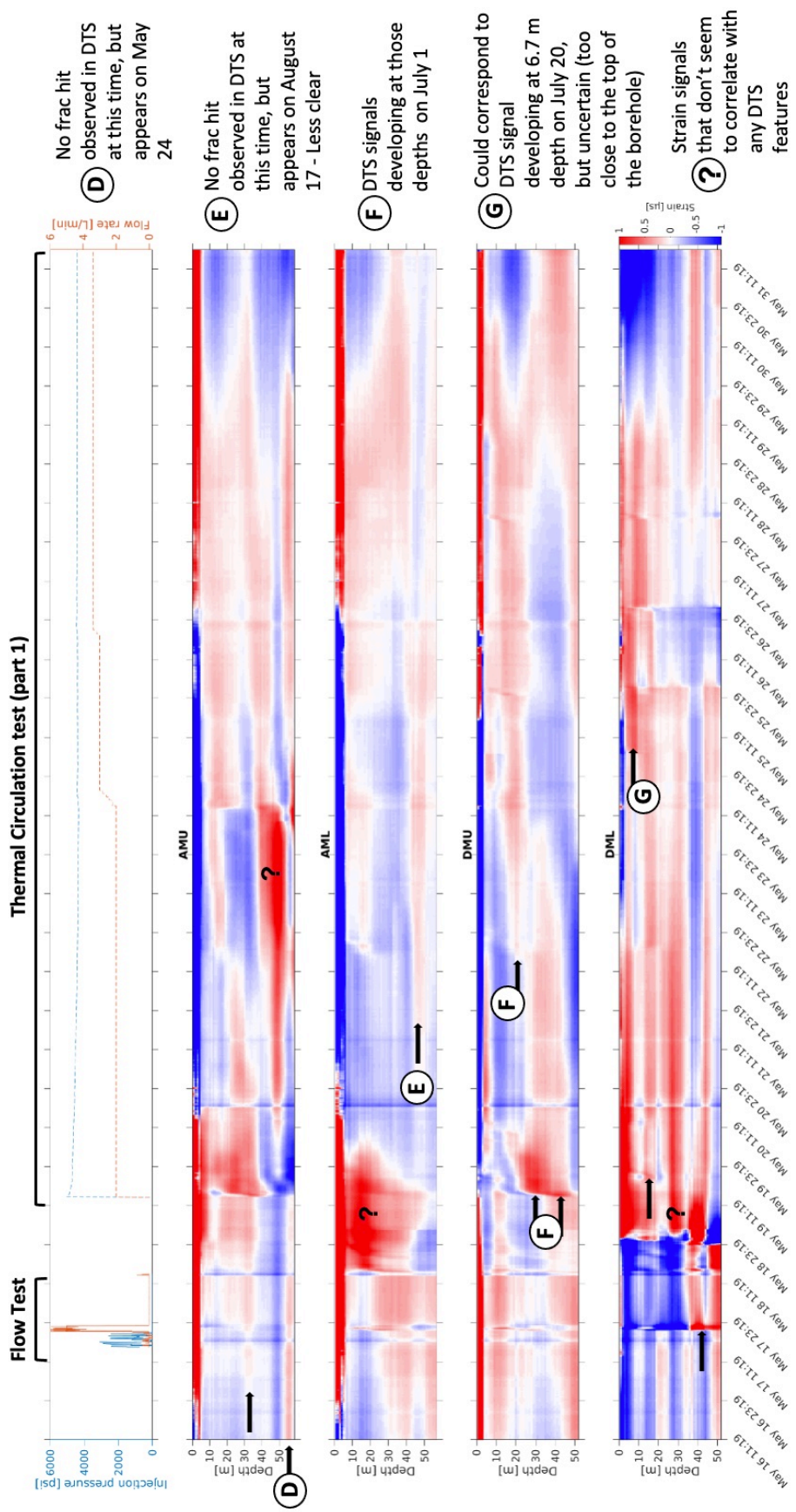

DML corresponds to the signal observed during stimulation of TC Zone 1, and agrees with the DTS intersection. The first localized extension zone in monitoring well AMU corresponds to the fracture intersection developed during stimulation of TC Zone 1 at a depth of 34 m, which appears a few hours before the flow-test starts. A second signal is observed at a depth of 55 m, although it seems to have been developed during the stimulation of the TU 177.4 - 179.6 ft interval.

Figure 7.20. Low-frequency DAS data recorded during flow tests and the first phase of thermal circulation.

8 FLOW, TRACER, AND THERMAL CIRCULATION TESTING: 177.4 - 179.6 FT INTERVAL OF TU

Following the flow tests in TC Zones 1 and 3, the 177.4–179.6 ft interval in TU was selected as the injection zone for a flow test, tracer testing, and then a thermal circulation test consisting of injection of chilled water due to its relatively optimal connectivity with other test (i.e., production) wells. Injection began on May 19, 2022 at 2 L/min before being increased to 3 L/min on May 24 and then 3.4 L/min on May 26 (Table 8.1.). On May 19 and May 20 while flowing, packers installed in TC, TN, and TL were incrementally placed at various depths to better isolate and capture flow. A failure in the flow system occurred on June 4, which resulted in a two-week hiatus in testing before the system was brought back online for an additional month of circulation testing (Figure 8.1).

Figure 8.1 presents notable parameters over the duration of the flow test allowing direct comparison between injection pressure, injection rate and two indications of the injection temperature, the rate of water production from the interval, bottom (below the interval), and collar regions (above the interval) of well TN, temperatures in well TN at two locations (U and L refer to upper and lower thermocouples) within the packer interval and two below the packer, the rates of water production from the interval, bottom, and collar of well TC, temperatures within and below the interval in well TC, and electrical conductivity of the injected water and produced water from the interval, bottom, and collar of well TN, and the interval and bottom of well TC. U and L mean upper and lower thermocouples that are at the top and bottom of the interval.

Panels C and E show variable rates of water collection from specific locations over the duration of the flow test. At times the reason for the rate change is obvious (e.g. lack of inflow June 4 - June 15, or change in packer location July 28), however some changes are not correlated with changes in flow, pressure, or packer location. Temperatures of collected water (Panels D and F) also varies over time, and sometimes in nonintuitive ways. For a system where chilled water is being injected, the natural expectation would be that temperatures would likely stay the same (no thermal breakthrough) or decline (thermal breakthrough). However, the temperatures of the produced water exceed the temperature of the ambient temperature injection water, and the monitored temperatures decline when the chilled water is not flowed (June 4 to June 15). An explanation for this is provided in ***Section 10 Temperature Tests*** below. A brief discussion of the test using electrical conductivity as a tracer (Panel G) is presented in the ***Section 9 Tracer Tests*** below.

Table 8.1. TU injection test information. From Mattson (2023).

Date	Flow Rate	Notes
5/19/22 13:53 - 8/26/22 20:38		**TU 54.07 - 54.74 /26" straddle, Thermal circulation with injection into TU. Both the injection location in TU and the production packer locations in TN, TL, and TU were adjusted to optimize fluid recovery.**
5/19/22	2 L/min	Weeps in drift

5/24/22	Increased from 2 to 3 L/min in 0.25 L/min increments	TN interval recovery more than doubled increasing from 223 to 505 mL/min. TC interval had a slight increase from 101 to 113 mL/min. Overall recovery increased from 31% to ~39%. Walls of the drift seem to become more wet.
5/26/22	Increased injection rate from 3 to 3.4 L/min in 0.2 L/min increments.	TN interval recovery increased from 550 to ~630 mL/min (14.5%) TC had a slight increase from 119 to 133 mL/min (11.7%).
6/4/22 to 6/15/22	Flow stopped, pump failure	Approximately 10 days without injection while pump was being repaired
7/18/22	Brief injection interruption	Power outage for a few hours
8/17/22	Injection stopped	Production wells were shut-in, water production in the drift decreased.

8.1 Microseismicity

Detectable seismicity was again absent during the flow testing while injecting into TC, but resumed when injection was switched back to TU. Figure 8.2 shows the location and timing of the detected seismic events. From the start of the flow testing into TU until the flow system failure, more than 150 events were detected. Until May 26, these events loosely defined a structure striking ENE and dipping SSW, broadly consistent with a sigma-3-normal fracture or series of fractures that intersect the drift near the entry to the battery alcove. However, it is important to note that the majority of the detected seismicity occurred above the depths of the testbed. It is unclear why seismicity was mostly detected outside of the monitoring array, but hammer shots conducted in the drift as well as full waveform sonic logging in boreholes TN and TC were detected and correctly located by the realtime seismic system, indicating that the system was indeed sensitive to signals inside the array. Therefore, if seismicity occurred inside the seismic network, it was of a smaller magnitude than the FWS logging shots, the hammer shots in the drift, and then the seismicity outside of the array, all of which generated signals sufficient to trigger the seismic detection thresholds of the system. Such a stark spatial variation in the magnitude distribution of seismicity is difficult to explain. Multiple fractures were driven towards the drift within the volume of rock bound by the geophysical monitoring arrays and it is impossible for these to have propagated in the absence of seismicity. So we have to conclude that the seismicity was just too small to detect. Why, then, did the injection into TU result in more energetic seismicity? Did this injection connect with natural fractures large enough to produce bigger events, while the injections into the other boreholes did not?

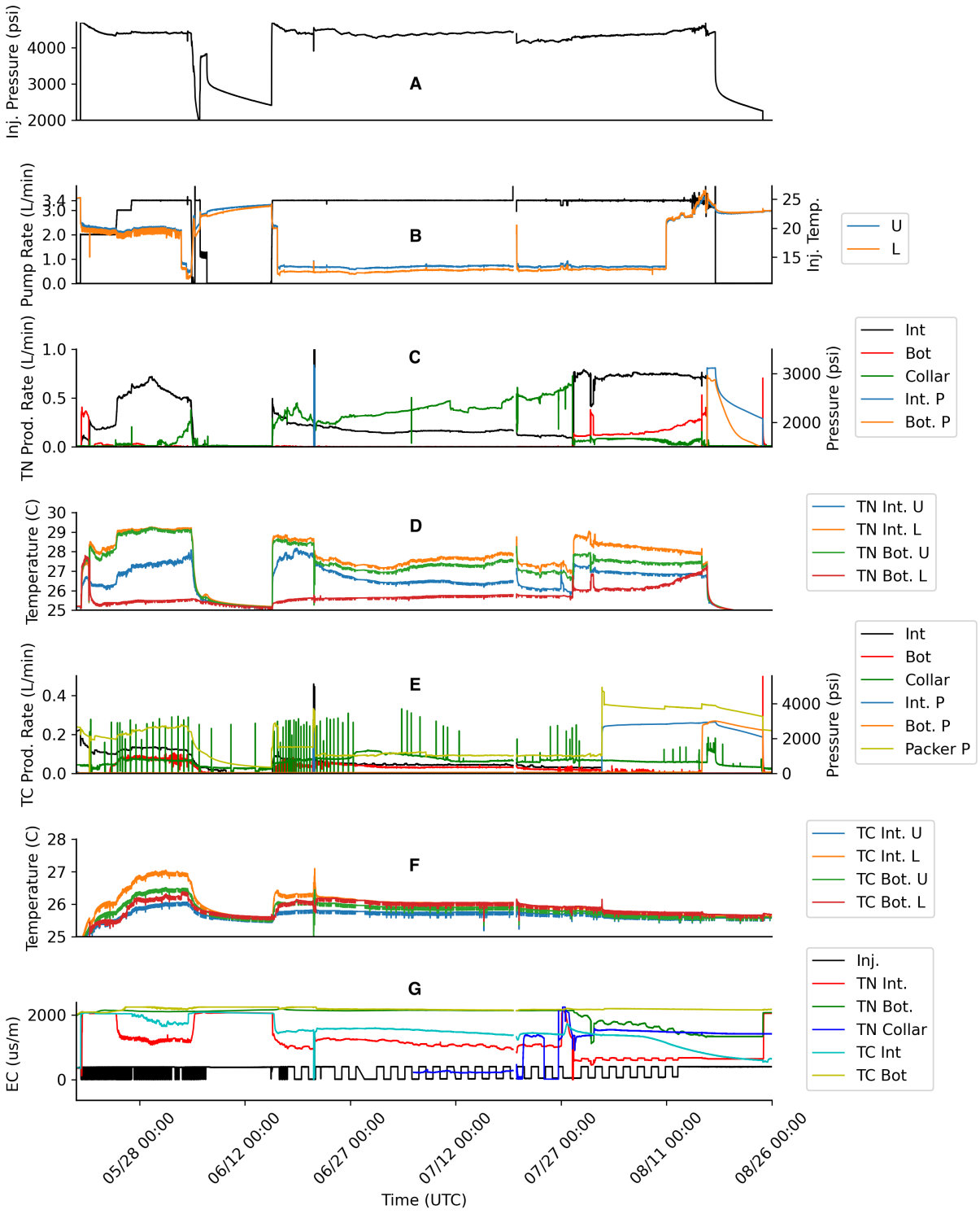

Figure 8.1. Top-tier parameters logged over the flow test. A - injection pressure, B – pump rate and two indications of the injection temperature, C – water production rates for the interval, bottom (below the interval), and collar regions of well TN, D – Temperatures in well TN in the packer interval and bottom, E – Water production rates from well TC from the interval, bottom, and collar, F – Temperatures in well TC in the interval and bottom, G – electrical conductivity of the injected water and produced water from the interval, bottom, and collar of well TN, and the interval and bottom of

well TC. U and L mean upper and lower thermocouples that are at the top and bottom of the interval. P means pressure.

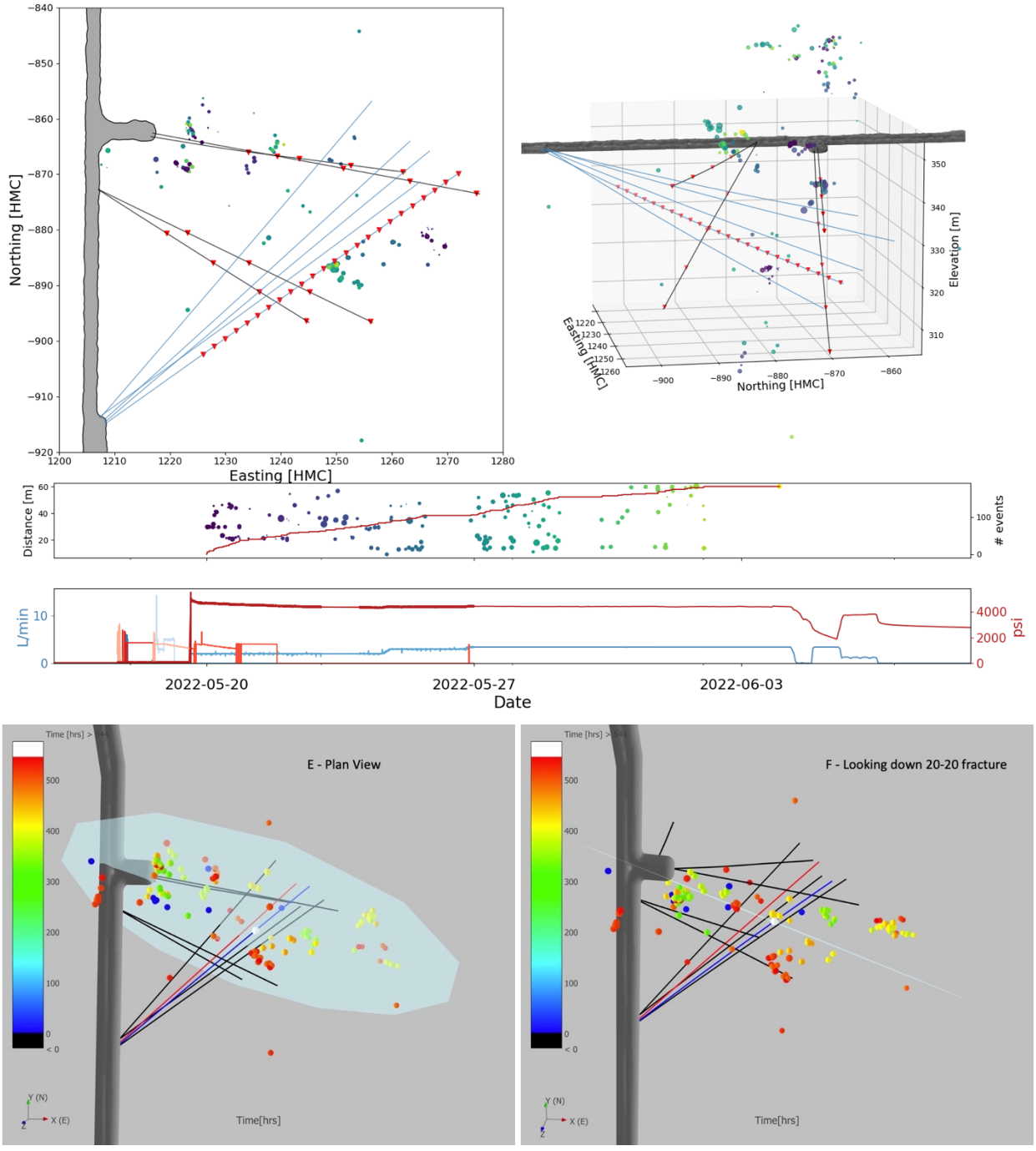

Figure 8.2. Microearthquakes detected during flow testing into the 177.4 - 179.6 ft interval of TU. A and B show the location of each event. C shows the cumulative number of events and their distance from the injection point. D shows the injection pressure and flow rate in psi and L/min, respectively. The time axis is in UTC. E shows a plan view of a fracture plane fitted to the MEQs, and F provides a view parallel to the fitted fracture plane.

The start of flow testing in TU also produced a complex pattern of fracture intersections with the grouted monitoring boreholes, as shown by temperature measured on the DTS system and strain recorded on the DAS systems. Figure 8.3 shows the change in temperature at all four grouted boreholes relative to the temperatures measured on May 18, before the flow testing in TU began. Changes in temperature indicate inflows into or past a well. Increases in temperature are the result of the Joule-Thomson effect, where water temperature increases upon depressurization. These flowing fracture intersections are most abundant in DML, which is consistent with generally SSW dipping fracture trends.

In addition to temperature increases, long-term temperature decreases are observed in DMU (~22m, and ~35m) and AMU (~43m). These locations are not initially coincidental with Joule-Thomson heating events. The simplest explanation for these cooler zones is that cooler injected water flows past these zones. Each zone becomes broader and cooler over time, which would be consistent with rock cooling surrounding a fracture. It is not clear whether these zones are consistent with ERT or strain measurements. Many of the measurements shown here are difference measurements, thus they might ignore features initially present. Since no Joule-Thomson effect was seen, some initially present feature that is not significantly altered by the stimulation could be responsible for conveying the cooler water. This is discussed further in the ***Section 10 Temperature Test*** section below.

Difference ERT relative to just prior to injection on May 19 (Figure 7.18) shows a significant increase in conductivity, particularly along the fracture plane identified by microseismic activity in Figure 8.2. Figure 8.4 presents a series of ERT data sets showing only the change in conductivity due to the previous injection. Figure 8.4 (panels A through C -early times) shows TS is filling with formation water. Over this time period conductivity increases in the same location shown in Figure 8.2. Even though the time increment is small, the conductivity increases significantly from panels C to D when the flowrate is increased from 2-3 L/min. There is relatively little change that occurs over the two-week period of no flow. These changes are slow to dissipate and could suggest that much of the system remained pressurized during the outage. Regions of decreasing conductivity adjacent to the regions of increased conductivity are thought to be caused by compressive stresses.

These data are also consistent with observations of seeps in the drift (Figure 8.8). At the beginning of the flow test, seeps into the drift were primarily in the area near the battery alcove. In general, ceiling drips appear in groups of multiple dripping points within ~10 square feet. These were subsequently collected (See ***Section 8.2 Water Production*** below) and quantified. As the test continued, seeps developed at locations south of the initial locations, and that trend continued over the duration of the flow test.

When the flow test was completed, shut-in testing was performed. The shut-in test data are analyzed and interpreted in Schwering et al. (2023). Briefly, however, this work concluded that ISIP values generally are consistent with minimum stress estimates obtained from a nearby borehole (TV4100). Upon shut-in, the immediate drop in pressure in the TU injection interval indicates that there is significant (i.e., 3-10 MPa) near-borehole impedance to flow. This suggests that the injection interval pressure was considerably higher than the pressure in the stimulated fracture network. Additionally, the bottom zone of TU, below the injection interval, is well-connected to the injection interval. The longer duration pressure decline of other zones reflects connectivity to pressure sinks. In particular, the TN bottom interval has the strongest pressure decline. That interval is interpreted to have strong connections to the mine openings from

observations of water outflow in the 4100L drift as well as rapid arrival of tracers during transport experiments. The lack of significant circulation between injection and production wells, at pressures below the minimum stress value suggests that the initial circulation and the establishment of connections from TU to the main producing intervals in TC and TN did not benefit from shear stimulation below the minimum stress value.

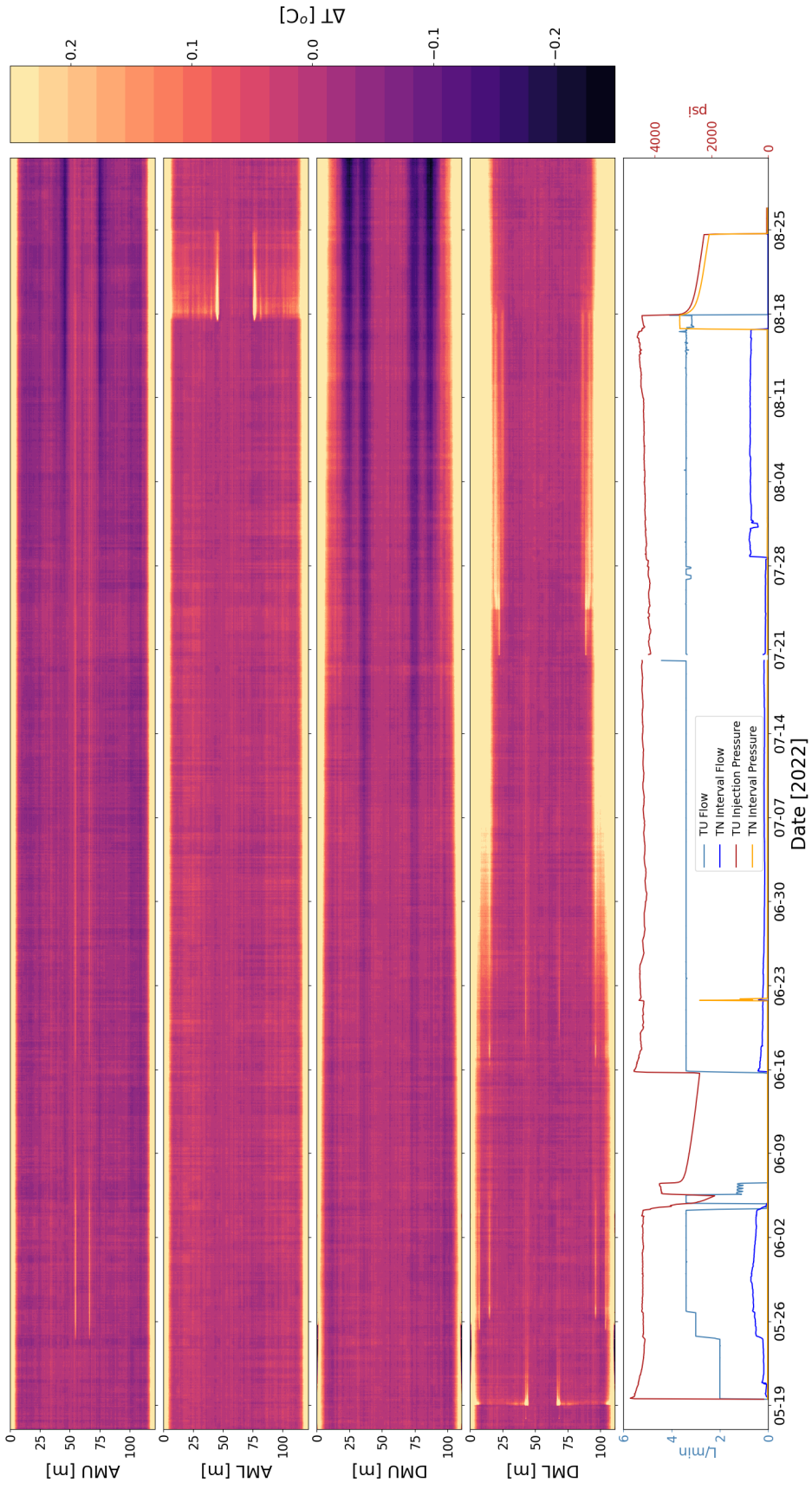

Figure 8.3. Change in temperature in each grouted borehole during the circulation test in TU. Each borehole is represented by a waterfall plot with hot colors representing temperature increases up to 0.25°C and dark colors decreases. The fiber package is installed as a loop going into and then back out of each borehole, so the y-axes represent distance along the fiber from the point where it enters until the point where it exits each borehole, thus the top half and bottom half of each panel are near mirror images of each other. The injection parameters are shown in the bottom panel for reference.

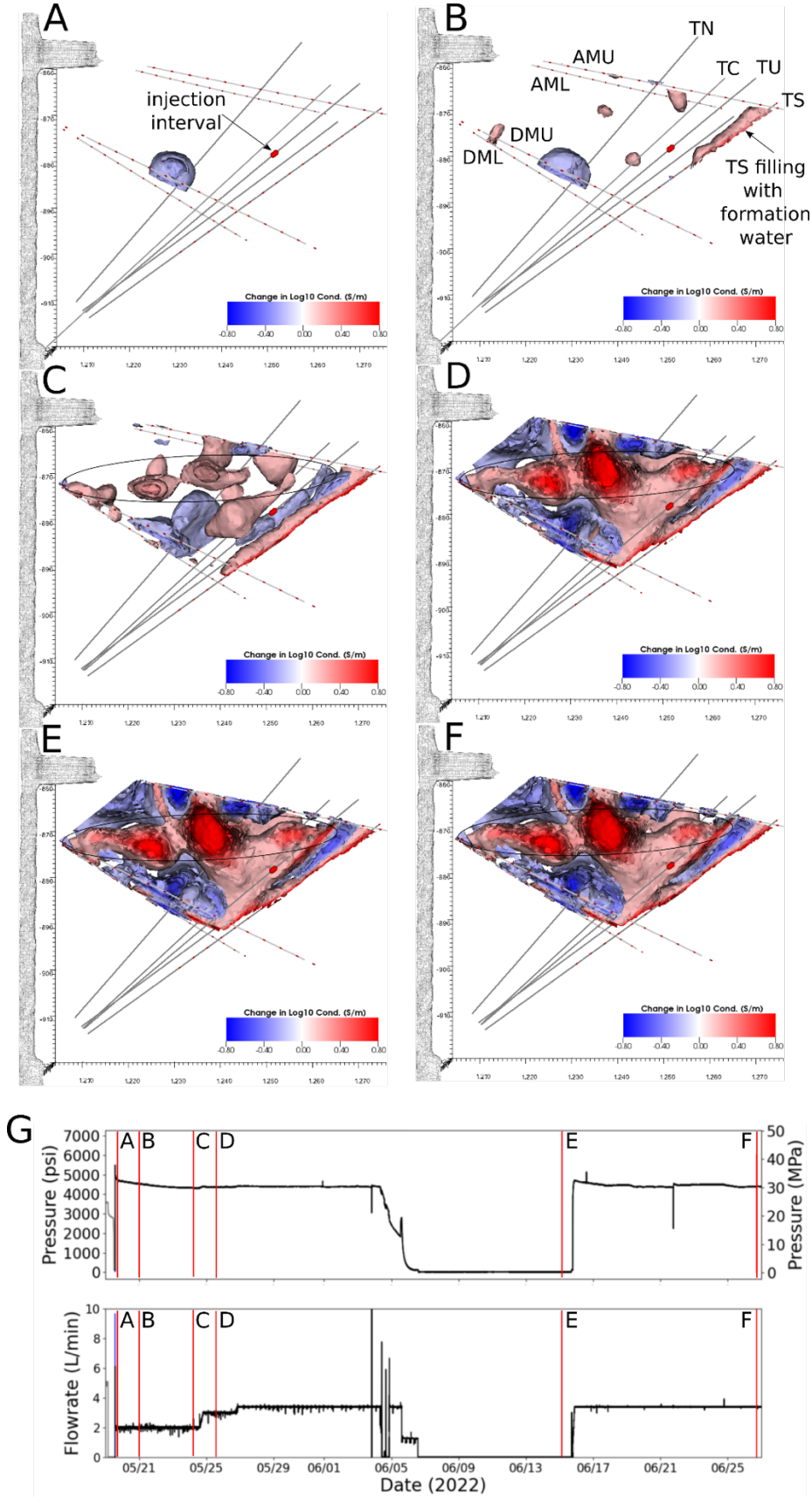

Figure 8.4. ERT imaging sequence showing changes in bulk conductivity during the TU 177.4 - 179.6 ft injection. Baseline ERT is just prior to injection on May 19, so these results do not show the total change in conductivity, only the changes caused by this flow test. A-F show the change in bulk conductivity at the times indicated by red lines in G. Over the time from A-C, it is apparent that TS is filling with formation water, and the same anomaly from the TC injections shown in Figure 8.2 is developing. A large increase in conductivity occurs from times C to D when the flowrate is increased from 2-3 L/min. Changes during the two-week flow outage are small (compare D and E), suggesting much of the system remained pressurized during the outage. Note that TS is the only borehole that did not contain a packer: the increases in conductivity around TS are likely caused by infilling of TS with formation water. Negative anomalies adjacent to the positive anomalies are presumably caused by

compressive stresses. TC may also be infilling as suggested by the elongated positive anomaly along TC in C-F.

8.2 Water Production

Measurements of the production well discharge over the 2.5-month constant rate injection suggest that the major injected water flow pathway shifted from the battery alcove/drift intersection towards Site B over time. Measurements in the drift from the ceiling and walls suggest a dynamic flow of water in secondary flowing fractures from the northern part of the drift towards the south. It also appears that disruptions in the continuous injection of water had a relatively larger effect on these secondary discharges compared to the higher flowing production wells. Analysis of the water flow rates from the two drift sumps suggest that most of the injected water bypassed the production wells and was discharged to the base of the drift near the alcove/drift intersection.

8.2.1 Production Wells

A straddle packer was placed in each production well to isolate flow into each production well into three separate zones; the collar (the drift to the upper packer), the interval (the zone between the upper and lower packer) and the bottom (from the bottom of the lower packer to the tip of the borehole). Since the packer straddle interval could most precisely isolate a flowing fracture, it was typically positioned over the highest flowing fracture if possible.

Figure 8.5 depicts the flow rate from production wells TS, TC and TN for the three isolated zones in the wells. TL exhibited very little discharge. The injection into TU was fairly continuous with the exception of a ten-day hiatus near the beginning of the long-term flow test and a brief shutdown in July due to a power issue. Flow rates in TS decreased from 200 mL/min at the beginning of the test to nearly zero in early July (Figure 8.5 top). This decrease is generally correlated with a similar decrease in the TN interval flow and an increasing TN collar flow which continued throughout July. On July 28, the TN packer interval was moved 10.5 feet closer to the drift to capture this high-flow pathway (as noted by the last three orange data points in Figure 8.5 bottom).

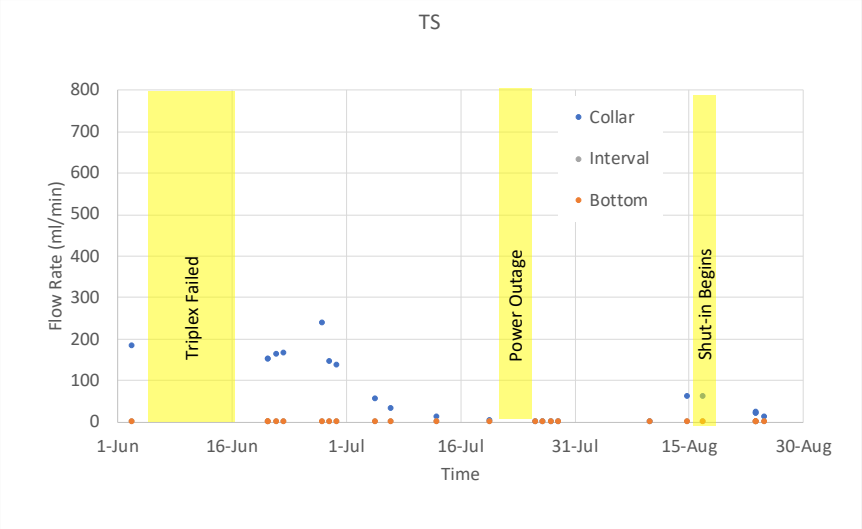

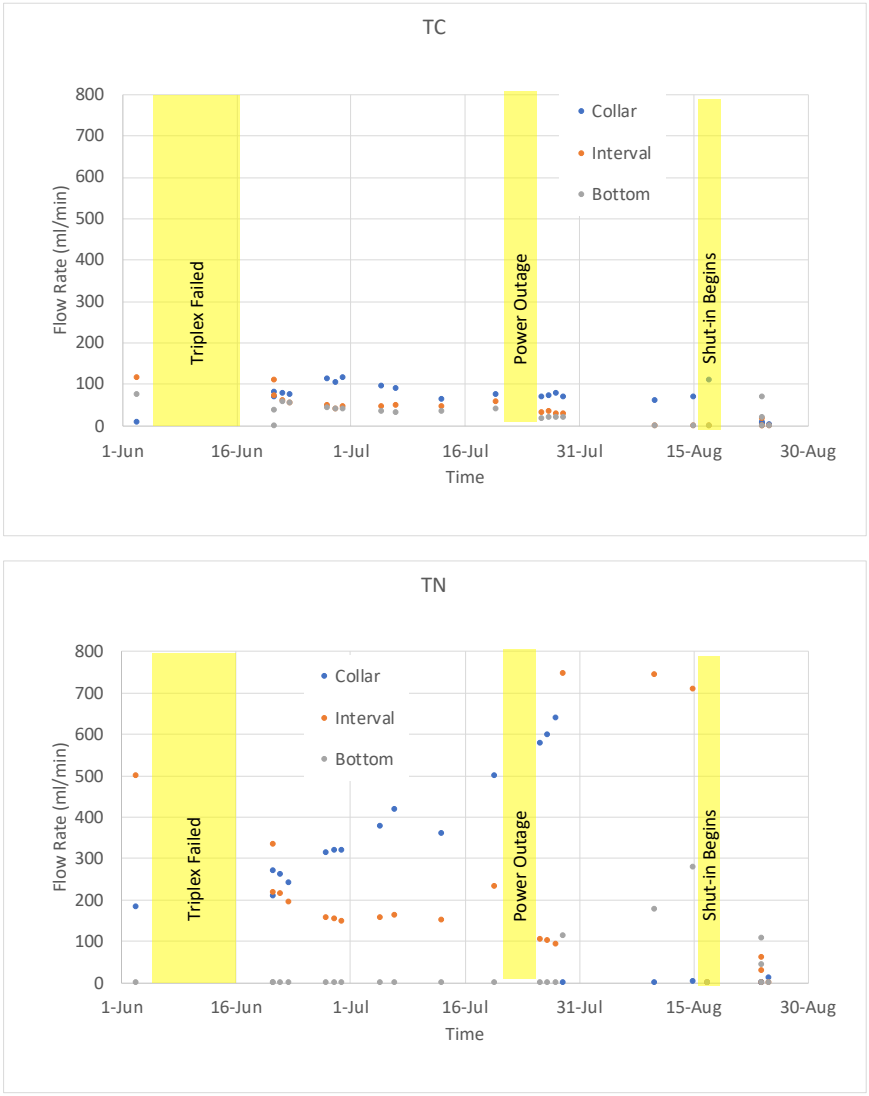

Figure 8.5. Production wells flow rates as a function of time for production well TS, production well TC, and production well TN. Note on July 28, the TN packer interval was moved 10.5 feet closer to the drift to capture this high-flow pathway.

8.2.2 Measurements in the Drift

Water inflow measurements were manually measured from various drips from the ceiling, wall weeps, and grouted monitoring wells. In general, ceiling drips appear to be in groups of multiple dripping points within ~10 square feet and were subsequently collected by hanging tarps from the ceiling draining to a common collection point. Wall weeps were collected using tissue paper as a wick to produce localized dripping points. Monitoring well samples were collected at leaking conduit seals. Although we were able to collect the water sample in the drift, the location and flow pathway through the grouted well has some uncertainty. Other wall weeps/ceiling drips existed in addition to those shown in Figure 8.6, but these were generally at such low flow rates that measurement was difficult.

In general, the flow rates were fairly steady, however there was a shift of water fluxes from the Site A, AMU, the Corner tarp (Figure 8.7), and Site C (all at the northern extent of the test site) to

the south (Sites 6, 7 and 7.5) in late June and July. The Site C tarp, (a ceiling tarp adjacent to the DMU/DML monitoring well collars) was the highest flowing ceiling/wall weep with a flow rate of ~60 mL/min (Figure 8.6 top). This flow steadily decreased to approximately 30 mL/min throughout July, then remained steady to the end of the injection test. At the Site A ceiling AMU, the corner tarp also exhibited a slight decrease in flows. In late June, new water flow drips in the drift ceiling appeared south of Site C (Figure 8.6 middle) along with a spike of water in DMU in late July after a brief power outage.

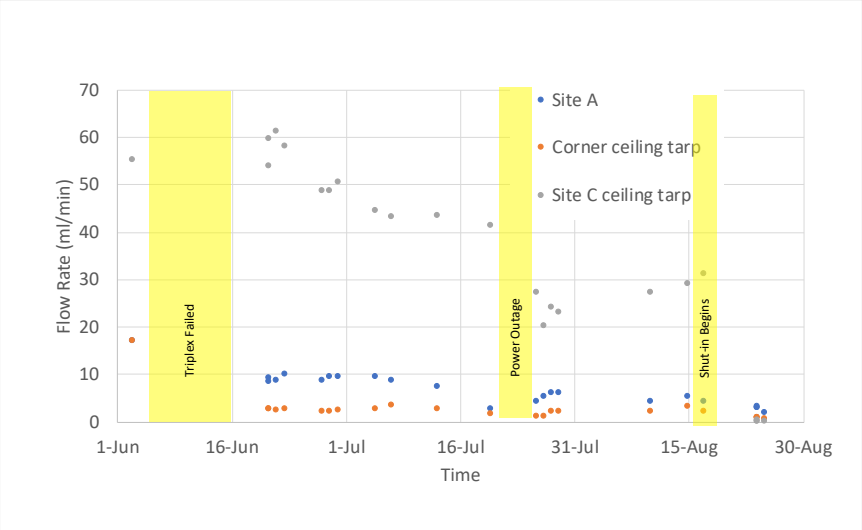

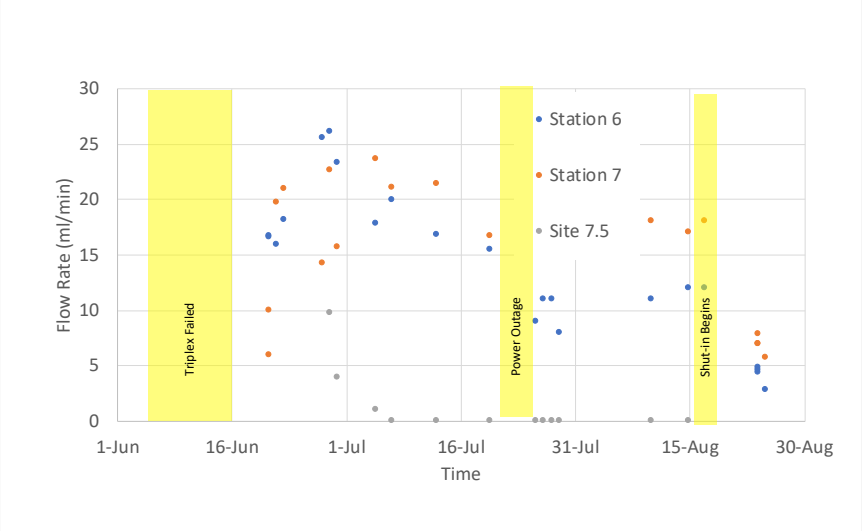

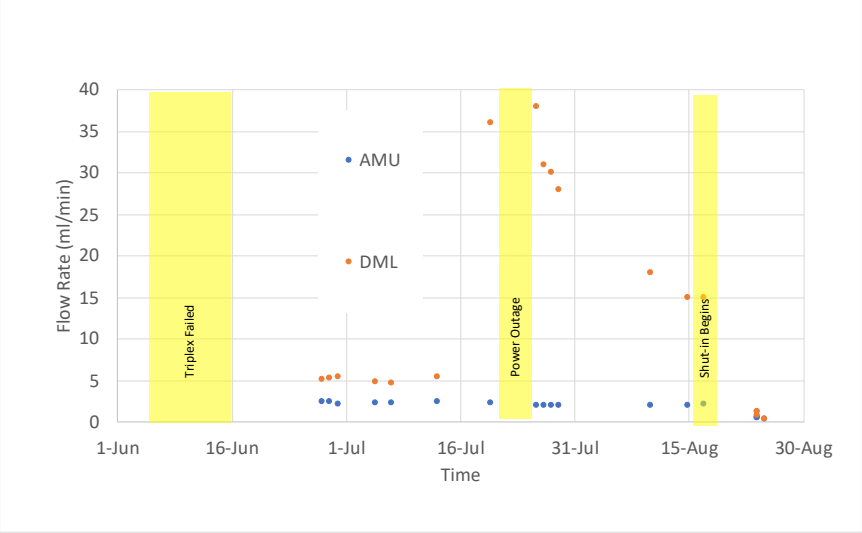

Figure 8.6. Drift ceiling drips and monitoring wells flow rates as a function of time.

Disruption in the injection conditions may change flow pathway dynamics at locations some distance from the injection point. As seen in Figure 8.6, the injection (triplex) pump failure in early June and the brief power outage may be correlated with changing discharge rates in these secondary discharge locations. Figure 8.6 top illustrates a discharge rate drop from ~20 mL/min before the triplex pump failure to ~4 mL/min after injection was reestablished. The initiation of water dripping in the southern part of the drift (Figure 8.6 middle) also started close to this time. Flow from the grouted monitoring well DML substantially increased after a brief power outage in July (Figure 8.6 bottom). Changes in the production well closer to the injection point did not exhibit a similar effect, albeit the discharge rate was much higher than those in the drift ceiling/wall weeps.

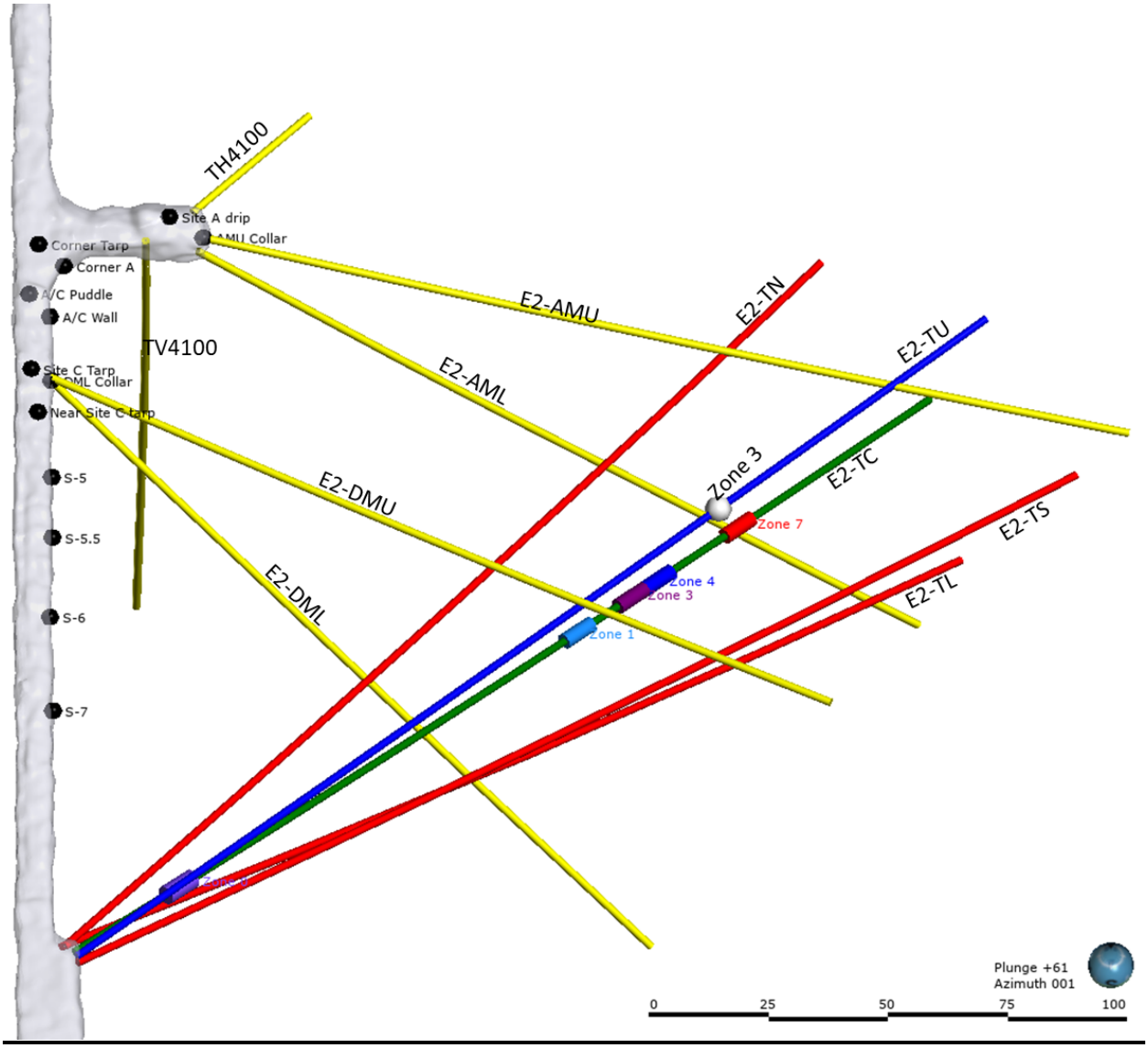

Figure 8.7. Stimulation zones along TC, TU, and leak points along the drift.

Water discharge from ceiling drips and wall weeps in the drift were dynamically changing during the flow test. Figure 8.8 illustrates the spatial change of the water discharge locations. Soon after a 2 L/min injection was established on May 19th in TUI, water weeps from the walls and ceiling drips were noted. On May 24th, the locations of these water discharges were located from the Site C ceiling tarp to wall weeps and ceiling drips in the Site A alcove. Despite the injection rate being raised from 2 L/min to 3.4 L/min during May 24-26th, water discharge at the corner tarp and Site A appears to have decreased. The injection pump failed on June 4th and flow was re-established on June 15. The June 22nd water discharge observations suggest a near steady state in the northern area of the drift but with new flow locations to the south at Sites 6 and 7. The injection in TU remained constant with the exception of a brief hiatus on July 18th. The July 5th and 26th observations suggest a shift of the drift water discharge towards Site C. By August 15th, the ceiling drips had reached a near steady state discharge.

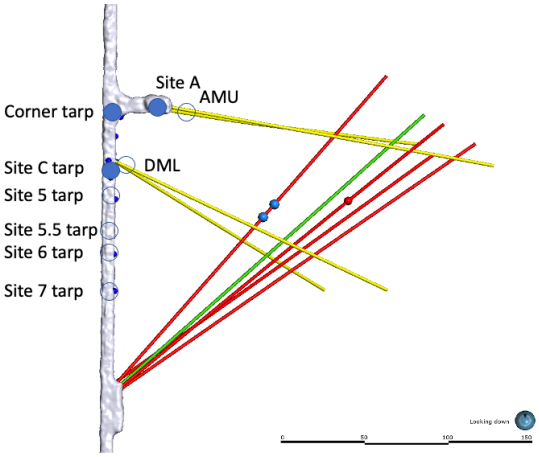

May 24, 2022

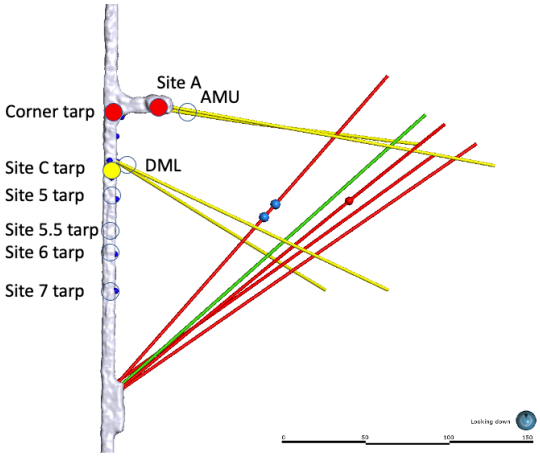

June 1, 2022

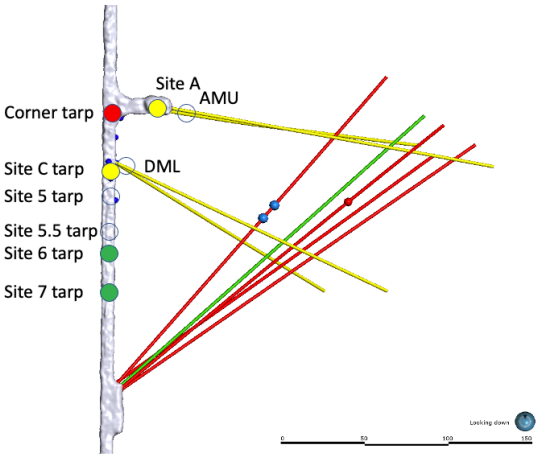

June 22, 2022

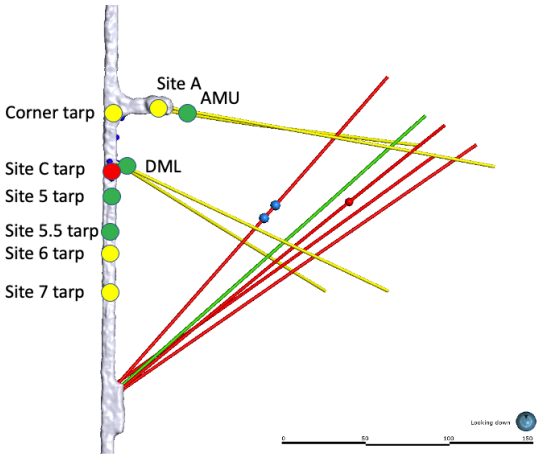

July 5, 2022

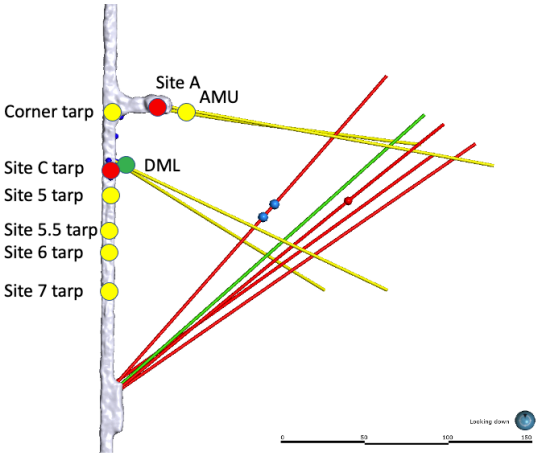

July 26, 2022

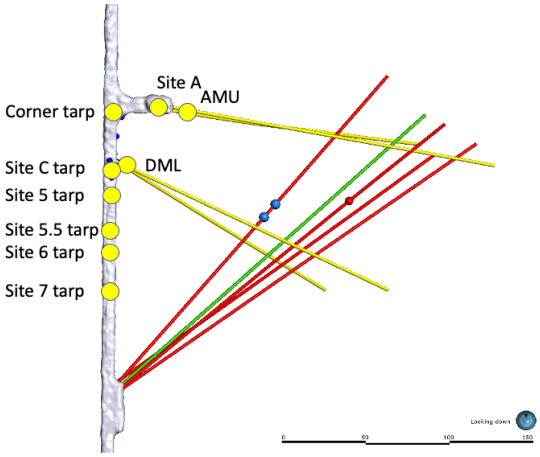

August 15, 2022

Figure 8.8. Subjective observations of dripping from the drift ceiling over time. Empty circles represent non-flowing collection locations, blue dots are initial collection locations, green dots represent increasing discharge over the previous observation, yellow - staying steady, and red - reduced discharge.

8.3 Water Balance Quantification

Prior to termination of the TU injection, the water discharge rate from sumps in the main drift and the production wells were measured and compared to the TU injection rate. As the steady state injection into TU continued, a free water surface developed along the main drift, south of Site A. In some locations the water surface was above the drift floor gravel surface whereas in other places a hole was dug in the drift gravel ballast (floor) to find the water surface. A laser level was used to map the free water surface elevation along the drift revealing that the water formed a "mound" just south of the Site A intersection (Figure 8.9). From this mound, water flowed to the north to a ditch in the ballast and the water level in this ditch was controlled by a sump pump with a mechanical float. On the other side of the mound, the water that flowed to the south terminated in a sump constructed in Site B. The Site B sump also was the disposal of any water produced in the production wells.

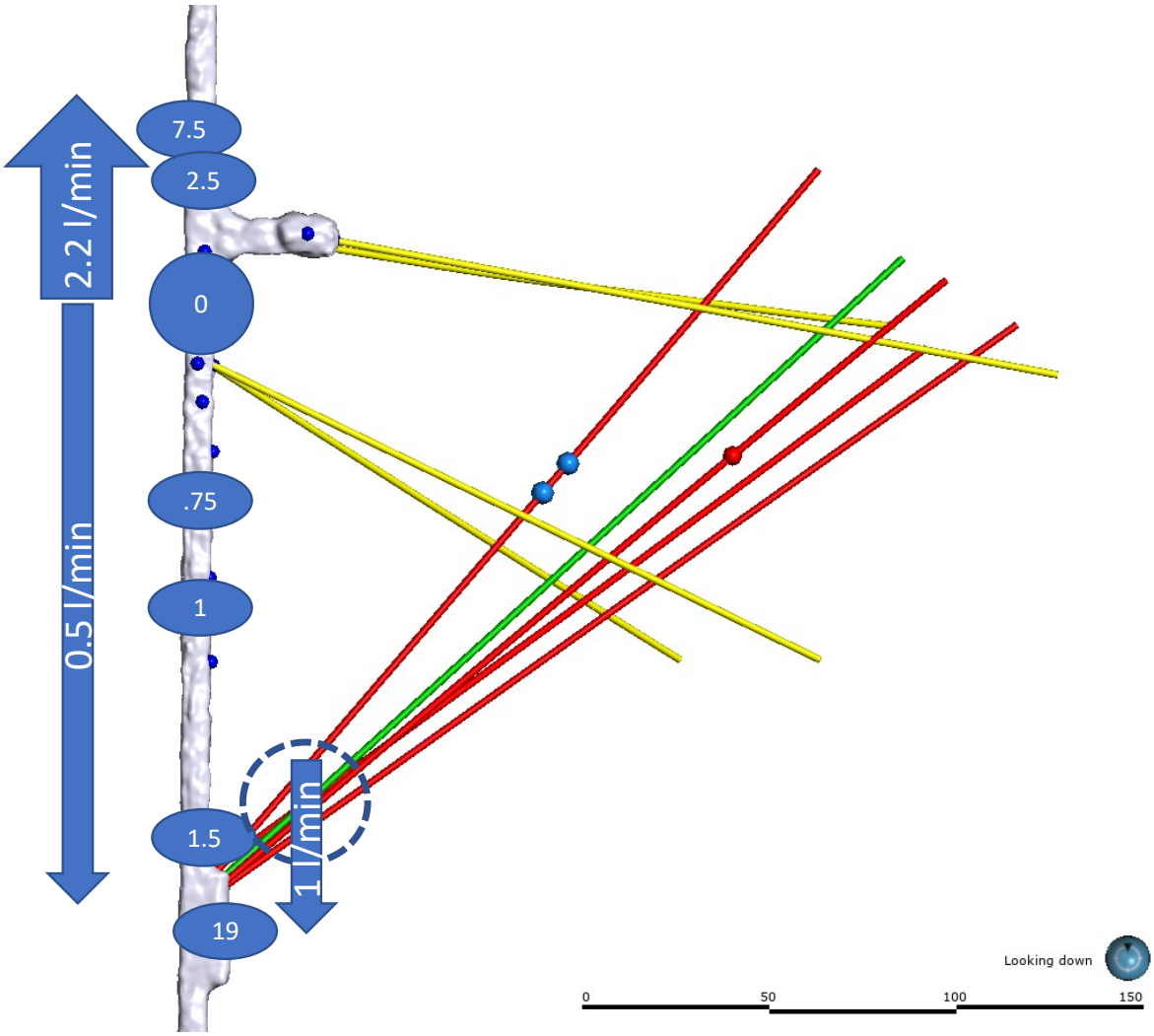

Figure 8.9. Free water surface elevation (in inches) below the laser level datum along the main drift, flow direction determined by gradient, and rates determined from the sump pump discharges.

Total water recovery from the production wells, ceiling and wall weeps, and flow through the ballast was estimated from two sump discharge rates. The northern ditch produced 2.2 L/min whereas the southern sump produced 1.5 L/min, totaling 3.7 L/min. This value is slightly higher (< 10%) than the TU injection rate of 3.4 L/min. This slight overestimate may be due to manual operation of the North ditch pump which would have released some water stored in the drift ballast. Figure 8.9 illustrates the location of the surface water divide (indicated by "0") and the calculated water flows through the ballast of the main drift and the water recovery from the production wells. *The production wells capture approximately 30% of the flow whereas the drift (ceiling drips, wall weeps, and water egress through the drift floor into the ballast) account for the remaining ~70%.* Based on measurements of the major ceiling and wall weeps (~3%), most of the water entered the drift ballast through the drift floor (~67%). The water flow (~2.5 L/min) coming through the drift floor was the termination region of the major flow pathway from the TU injection well. Based on the location of the surface water mound and tracer detection in the ballast, this fracture enters the drift floor just south of the Site A alcove intersection with the main 4100 drift (~20 feet south of the midline of Site A alcove).

8.4 Water Production Summary and Experiment Impacts

As discussed above, the partition of water production between the drift and the production boreholes was about 70% to the drift and 30% to the production boreholes. In terms of the chilled-water circulation tests, most of the water was flowing to the drift, where temperature could not be monitored rather than the production boreholes, where it could. The inflows to each production borehole were further partitioned between flow to a short, straddle-packer interval and flows above and below the straddle packer assemblies. The straddle packer assemblies were positioned in the production wells to capture the largest inflow points and produce the highest quality temperature-breakthrough signatures. Of the production boreholes, most of the flow was to E2-TN, where the location of the highest inflow migrated over time from the interval to above the interval. This migration necessitated relocation of the packers to a slightly shallower depth.

A major goal of the circulation experiment was achieving a chilled-water breakthrough within the experiment's 3-month (shortened due to time constraints from the planned 6 months) time period. The experiment was predicated on most of the ultimate 3.4 liter/min injection flow rate moving along stimulated fracture pathways to a small number of production points intersections in the boreholes. Of the 30% of the flow captured by the production boreholes approximately 64% was going to E2-TN in early July and 86% (~1 liter/min) in August before test shut in. Of the flow produced from E2-TN approximately 700 ml/min was being captured by the straddle packer interval, or about 20% of the total injected flow rate.

The low recovery of the production well intervals had a significant impact on the ability of the experiment to observe a thermal breakthrough. Rather than the ~3 liter/minute design rate, the highest production interval rate was only 0.7 liters/minute. The analytical solutions for thermal breakthrough (Gringarten et al, 1975; Doe et al, 2022) suggest that breakthrough time depends on the inverse square of rate, thus a circulation rate that is only 25% of expected would increase the time the thermal breakthrough time by a factor of approximately 16, thus stretching the breakthrough on the order of months stretch to a year or more.

9 TRACER TESTS

Fluorescein - a nonsorbing tracer, rhodamine B - a sorbing tracer, and both sodium chloride and purified water (reverse osmosis) - nonsorbing electrical conductivity tracers were applied in these tests. Tracers were detected at a number of locations within the production wells, two grouted monitoring wells, ceiling drips, wall weeps, and the floor. Based on the tracers and bulk water measurements, (Section 8 and Mattson et al. (2023)) conclude that most of the injected water was collected, however a large fraction of the water entered the drift through the floor, where the ability to collect, quantify, and analyze water was limited to crude bulk measurements. Water measurements over time from ceiling drips and wall weeps suggest a dynamic flow system where drift outflows shifted location with time. Fluorescein tracer breakthrough curves were used to determine travel time to the production wells and various parts of the drift. These results suggest a main fast flow pathway from the injection point in TU to the alcove/drift intersection with a series of secondary fractures with slower transport.

Fluorescein injection tests are listed in ***Appendix K - Tracer Tests***. Two tracer tests were conducted to quantify the effects of the equipment (no flow in the rock) with fluorescein or sodium chloride. Additional tracer tests include two injections of rhodamine B, one sodium chloride injection for which the BTC was monitored using the inline electrical conductivity probes, and an 8-hour duration sodium chloride injection for electrical resistivity tomography analysis. Additional detail on tracer testing including preliminary sodium chloride testing, tracer testing and analysis methods, system and rock dispersion analysis, and behavior of sorbing rhodamine B relative to fluorescein are presented in ***Appendix K - Tracer Tests***.

9.1 Automated Electrical Conductivity Tracers

The stimulation-flow-tracer system (SFTS) was designed to control and measure injection/production flow rates, pressures, temperature, and electrical conductivity (EC) in each of the 15 zones created within the five open boreholes present in the 4100L testbed. The shallowest zone in each borehole was bounded below by the top of a straddle packer and above by the wellhead assembly located at the top of the borehole. The middle zone was located between the packer bladders and the lower zone consisted of the volume below the deepest packer bladder (Figure 9.1). Any of the two deeper zones could be selected for injection and all of the remaining zones could simultaneously serve as monitored producers. In addition to point measurements in each of the three zones, temperature was recorded along the length of the upper zone using a distributed temperature sensing cable.

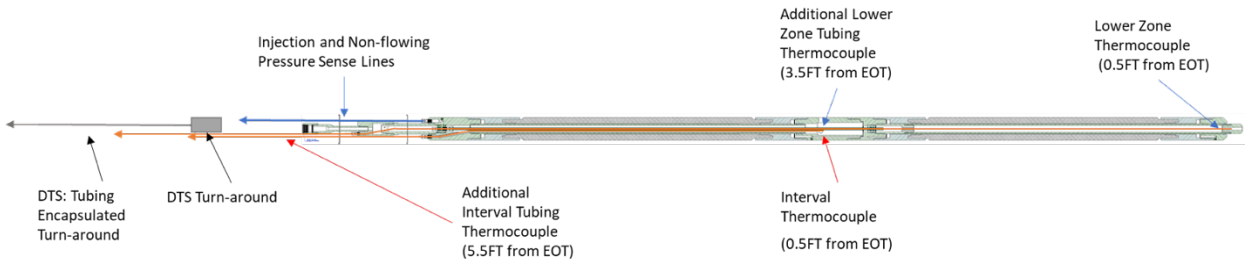

Figure 9.1. Packer for Stimulation-Flow-Tracer System

Most of the control and monitoring systems were located in Site B that was newly mined for the project to house the SFTS (Figure 9.2). Major subsystem elements consisted of: 1) packer sensors and control, 2) injection-production pressure-flow-EC monitoring and control valving, 3) temperature control, 4) high flow pump, 5) precise low flow syringe pump, 6) DTS, 7) reverse osmosis, and 8) data acquisition.

Figure 9.2. Drift Stimulation-Flow-Tracer System components.

The injection system was configured such that the local mine water (~400 uS/cm) and mine water treated by reverse osmosis (<100 uS/cm) could be automatically cycled to create a series of varying EC pulses throughout the long-term constant injection. A time series of the RO/mine-water cycling throughout the duration of Experiment 3 was shown in Section 8. A select period of time is shown in Figure 9.3.

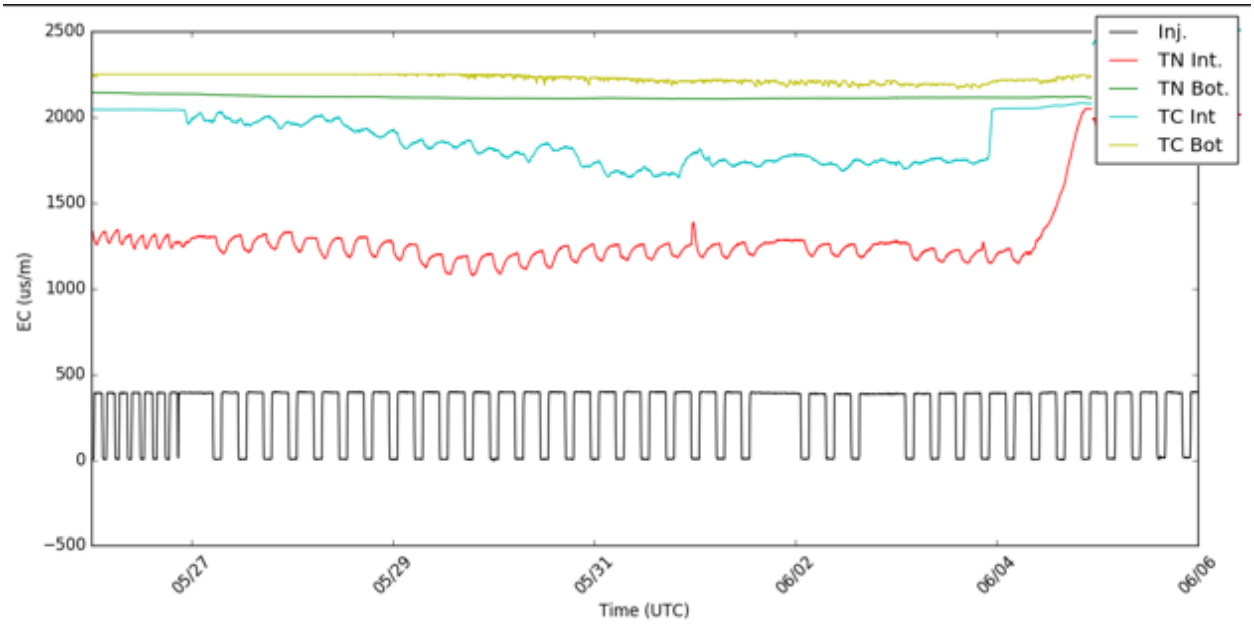

Figure 9.3. Time series of automated EC tracer data for select time window.

The EC of the injected water as well as the fluid produced at each of the production zones were recorded. The character of the dispersed and time delayed pulses varies at each production location

but are clearly evident in the primary producers. By automating the EC pulse cycling, temporal changes in the observed time delays can be used to infer changes in the flow system throughout the experiment (Figure 9.4). Time delay changes also showed some evidence of correlation to other parameters such as production outflow (Figure 9.5).

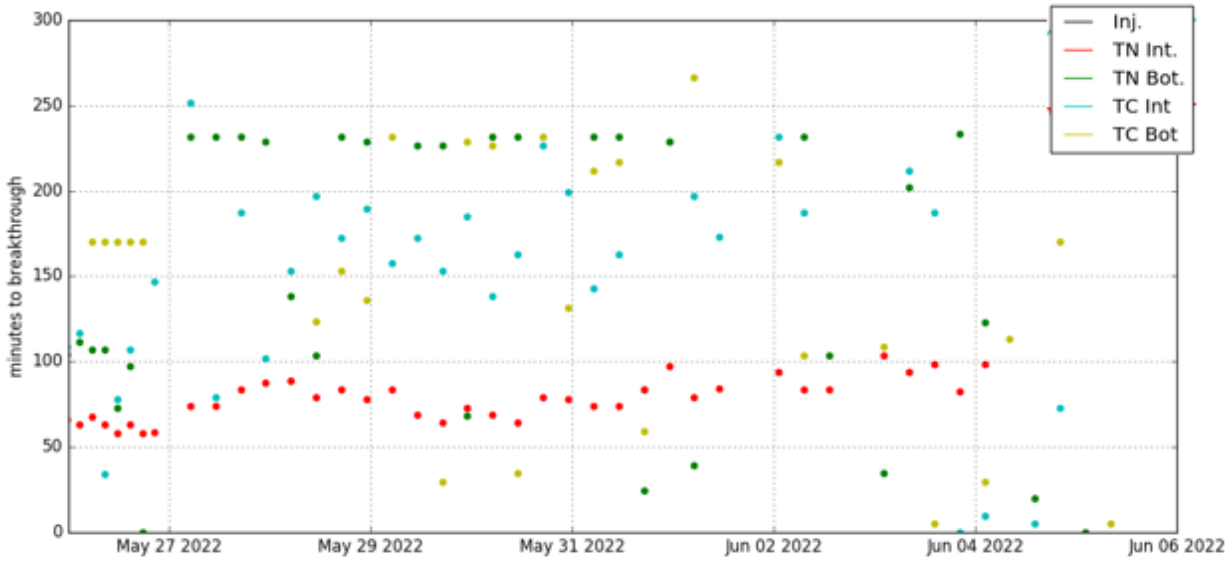

Figure 9.4. Approximate breakthrough times of the RO pulses over the selected time window in TN and TC interval and bottom zones.

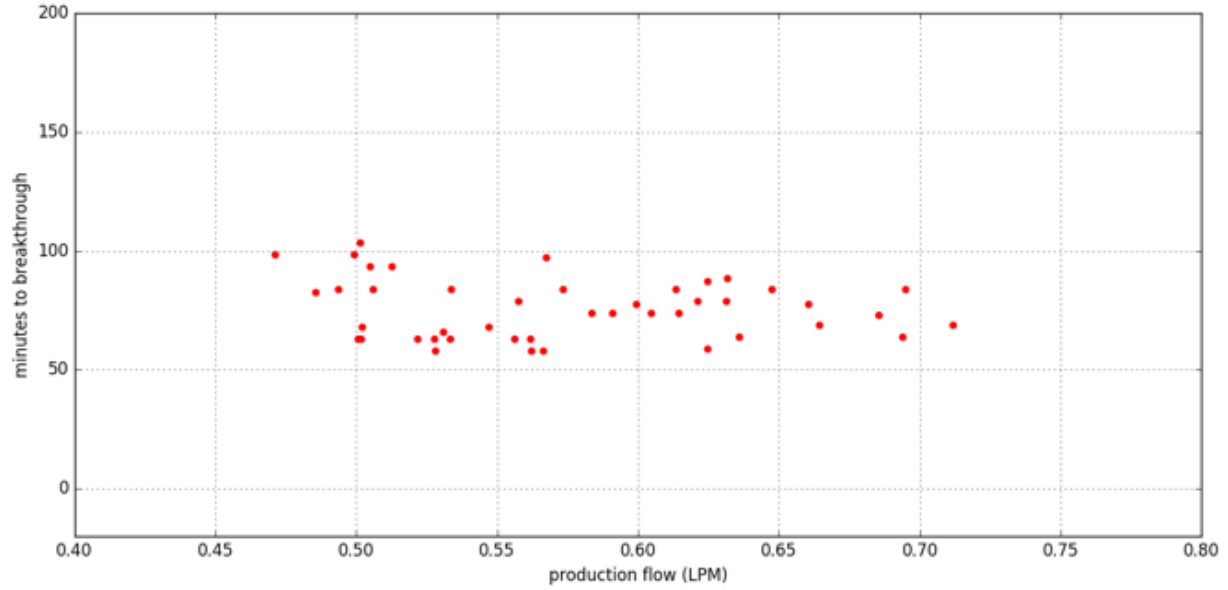

Figure 9.5. Breakthrough times in the TN interval are plotted against the production flow rate. Flow rates from TN bottom zone and the TC zones were very slow during the time window discussed.

9.2 Fluorescein tracer

Four fluorescein tracer tests were performed during the circulation test. All tests used the same injection point in TU located nominally at 177.9 ft. Tracer was detected at numerous points in the production wells, in two of the grouted monitoring wells, and at ceiling drips, wall weeps, and the floor of the drift (Figure 9.6). Complete tracer breakthrough curves were determined for a number of tracer detection points enabled by the available fraction collectors and accessibility to the 4100 level during these tests.

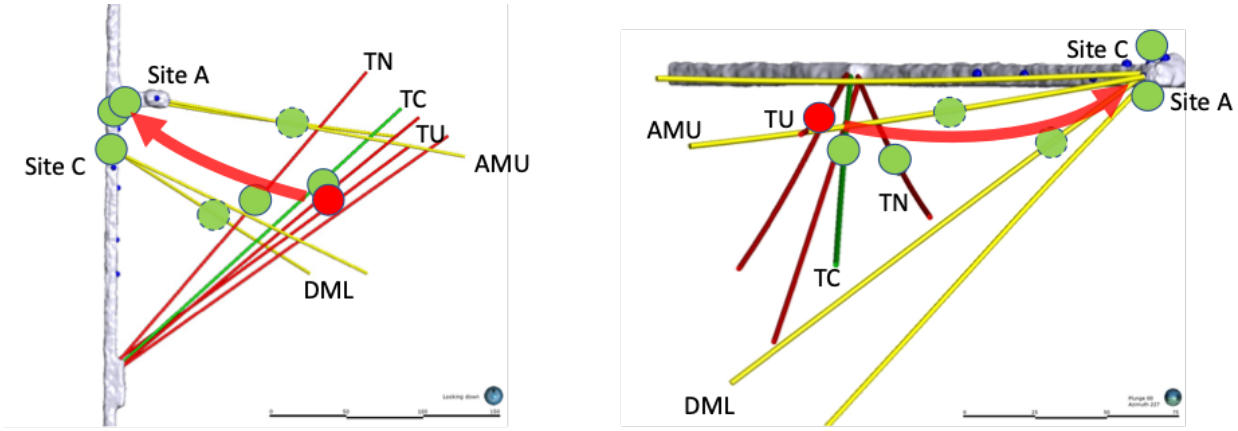

A. B.

Figure 9.6: Tracer detection locations from the 07/29/22 fluorescein injection. A. Plan view, B. vertical cross section looking to the southwest. Red dot is the approximate location of the TU injection site, green dots are known locations of detection, green dashed dots are approximate locations in wells, and the red arrow represents the general direction of the tracer-laden water. The scale bar lengths are 150 m.

9.2.1 Fluorescein Test Interpretations

Using water discharge measurements in the production wells and the drift ceiling/wall weeps, calculated water mass balance, and the first detection of tracer arrival during tracer tests, a conceptual model for water flow in the fractures was developed. This conceptual model was then used to interpret the role of production water discharge and its utility on predicting the water velocity in a fracture rock system.

During the 2.5-month flow test, water discharge varied from the production wells as a function of time suggesting a change in the flow dynamics within fractures at the 10-meter scale. In addition, these flow changes were also seen at the 50-meter scale (i.e., in the drift) as indicated by flow rate changes in ceiling and wall weeps. Variability in the discharge in both the production wells and the drift occurred despite attempts to maintain a constant injection rate.

The water mass balance calculations suggest the presence of major flowing fracture(s) from the TU injection location to the intersection at the alcove/drift intersection. This conceptual model is supported by the time of first detection of fluorescein tracer in the production wells and the drift. Figure 9.7A illustrates the spatial distribution of the time of first tracer detection for the July 26-

29 tracer tests. As seen in this figure, tracer is first detected in the two production wells (TC interval 0.3 hrs, TN interval 0.4 hrs) suggesting a fast flow pathway velocity of 34 and 40 m/hr (0.009 m/s and 0.011 m/s) for TC interval and TN interval respectively. The fastest tracer detection velocity, however, was located at the floor seep at the alcove/drift intersection (46 m/hr - 0.013 m/s) despite being about 3 times further from the TU injection point than the production wells. Other tracer detections in the drift (the Site C tarp and the Site A ceiling drip) took at least twice as long (i.e., ½ the velocity) compared to the alcove/drift detections even though the distance of all three tracer discharge points from TU interval are approximately the same.

The early detection of tracer at the alcove/drift floor is corroborated by the water mass balance analysis and suggests a major flow pathway has been developed from TU interval to the drift/Battery Alcove intersection location and is represented by the large red arrow in Figure 9.7A. This flow path appears to pass through/near the two production wells, the TC interval, and TN. The Site A and C detections suggest that there are secondary flow pathways that are either branching off from the main fracture near these detection locations, or the detections possibly represent long secondary flow pathways.

Although the water measurements and the tracer tests provide indications of the locations of travel pathways, the measurements do not provide quantitative information on the exact pathway the water and tracer travel through the fracture rock. Figure 9.7B includes a preliminary tomographic representation of the change in electrical conductivity of the July 26 sodium chloride tracer injection presented in Section 9.4 below (see Figure 9.9)

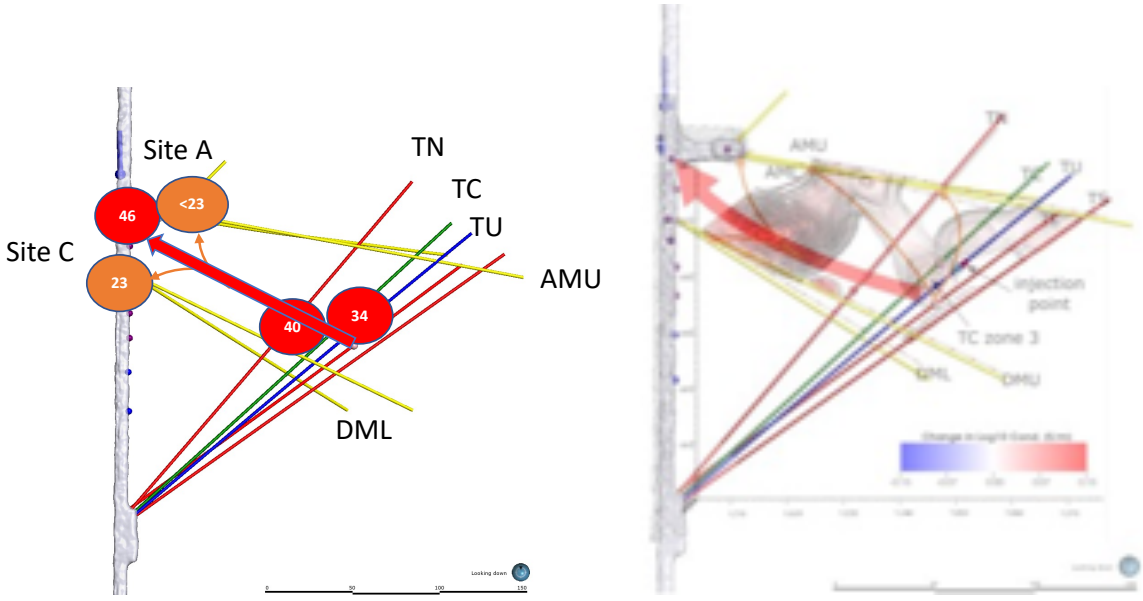

A. B.

Figure 9.7. A) Calculated tracer velocity of first detection of the July 26 – 29, 2023 fluorescein tracer test (in hours after injection) in the production wells and in the drift, B) conceptual model of tracer pathways from the injection well to discharge locations overlain with an electrical resistivity tomographic image from a salt water tracer injection on July 26.

9.3 Water discharge rate vs. flow velocity in fractures

The simplest conceptual model of water movement in a fracture from an injection well to a production well is a stream tube that connects the two points. In a model of the testbed, numerous stream tubes could exist from the injection location to the multiple discharge locations. In this case, the production well flow rate is considered to be the correct variable related to the tracer velocity in the stream tube. A second conceptual model of water flowing in a fracture could be described as a major flow pathway with points along the flow path where the water leaks into individual fracture pathways. Although a major fracture flow pathway could also be considered a stream tube, in this case the velocity in the main fracture is not controlled by individual discharge flows. Depending on the tracer residence time in the main fracture compared to the tracer residence time in the secondary fracture, the production well discharge rate may have a small influence on the calculated velocity of the tracer between the injection and production locations.

Figure 9.8 illustrates the calculated fluorescein fracture velocity from tracer tests conducted on June 1, 2022 and July 26, 2022 for the TN interval, TC interval and the Site C tarp plotted against the well discharge rate. Results from these limited data set support the first conceptual model (simple flow through a stream tube) because the production well flow rates appear to be linearly related to the average tracer velocity to each discharge point. According to the water mass balance analyses, the majority of fracture flow is being discharged to the base of the drift near the alcove/main drift intersection. Despite the fact that both the drift and the TN interval and TC interval production wells intervals are approximately atmospheric pressure and the production well packed off intervals are located approximately 1/3rd of the distance from the injection well compared to the discharge locations in the drift, these wells only captured about 25% of the injected water. (Schwering et al., 2023) examined the pressure response of the production wells during shut-in tests conducted at the end of the flow experiment. The producing zones of these wells quickly reached a near-steady-state shut-in pressure, which indicates the near-wellbore fracture aperture was maintained while the injection at TU continued. After the TU injection was terminated, the producing zones slowly lost pressure which suggests closure of these near-wellbore fractures and no significant shear residual permeability (e.g., from shearing). This production well skin effect could explain the low production well recovery of the injected water.

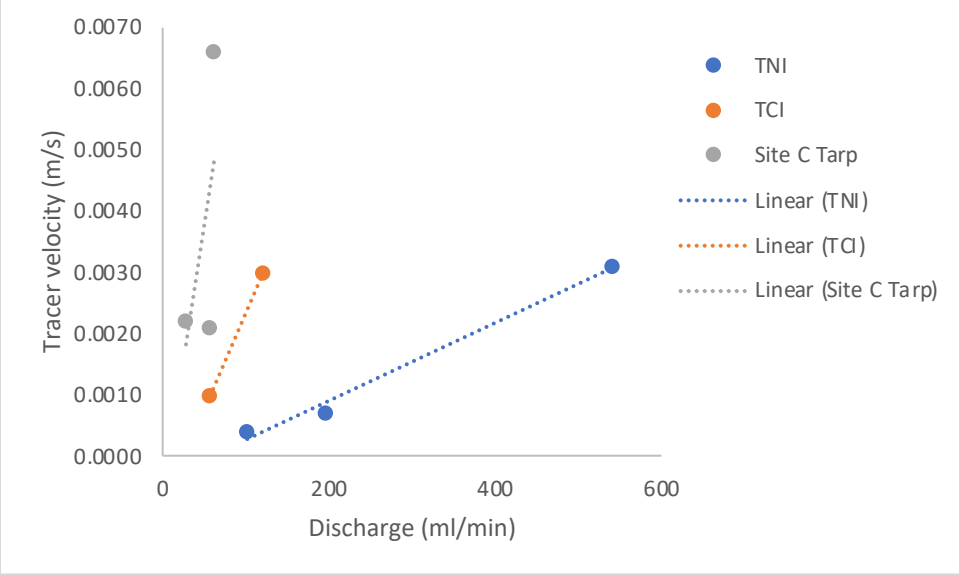

Figure 9.8. Relationship of tracer velocity in the fracture and production wells TNI and TCI water discharge rates (Note: 0.003 m/s = 10.8 m/hr).

9.4 Sodium chloride with ERT Observation

Throughout the flow test, the electrical conductivity of the injected water was changed in a step function as the reverse osmosis system was systematically turned on and off (Figure 8.1, Panel G). Changes in electrical conductivity of varying magnitude are observed in several of the production wells. It was hypothesized that the ERT system might also detect these changes, but the impact was not strongly observed. Injecting a sodium chloride solution, however, could strongly affect the conductivity of the injected water. On July 26th, a saline tracer was injected into the TU 177.4 - 179.6 ft interval for approximately 8 hrs. Fluid conductivity of the tracer was approximately 75 times greater than the water being produced to provide a high conductivity target for time-lapse ERT imaging. This was followed by a mine water purge of the tracer injection pump and tubing. Figure 9.9 shows the change in bulk electrical conductivity caused by the tracer after the bulk conductivity had reached a steady state on July 27th. In the ERT difference image, the tracer appears to originate from TC at the location where a connection between TU and TC was created on April 5th and 6th (Figure 9.9), suggesting a strong flow connection from TU to TC there. Tracer injected at TU 177.4 - 179.6 may not be visible in the ERT image due to poor data sensitivity in that location. However, from the injection point the tracer appears to travel in a well-defined path northwest toward well AMU, where the tracer then migrates southwest to the shallow regions of DML and DMU. The largest increase in bulk conductivity occurs near DML and DMU. The flow patterns indicated by the ERT imaging are consistent with observed outflows along the drift as shown in Figure 8.8. A smaller anomaly occurs in the north-eastern part of the image. This appears to emanate from tracer flowing into TS, and moves eastward and downward in the formation.

Note that changes in bulk conductivity observed during flow testing on May 18th through June 25th were caused primarily by changes in fracture apertures resulting from changes in fracture pressure. Positive increases in bulk conductivity occur where fractures are expanding, thereby increasing the conductive current flow pathways, and negative changes occur in the adjacent rock where corresponding compressive stresses cause compliant fracture apertures to compress (Johnson et al., 2022). The sodium chloride injection occurred after weeks of mine water injection at a constant pressure, meaning that the system was in a relatively steady state over the 8-hour sodium chloride injection period. Thus, the increase in electrical conductivity observed during the sodium chloride injection was caused by an increase in fluid conductivity along the fluid flow paths, and not by aperture expansion. In short, changes in electrical conductivity observed May 18th - 25th show where fracture apertures were expanding and contracting, and changes observed on July 26th show *the dominant* tracer flow pathway.

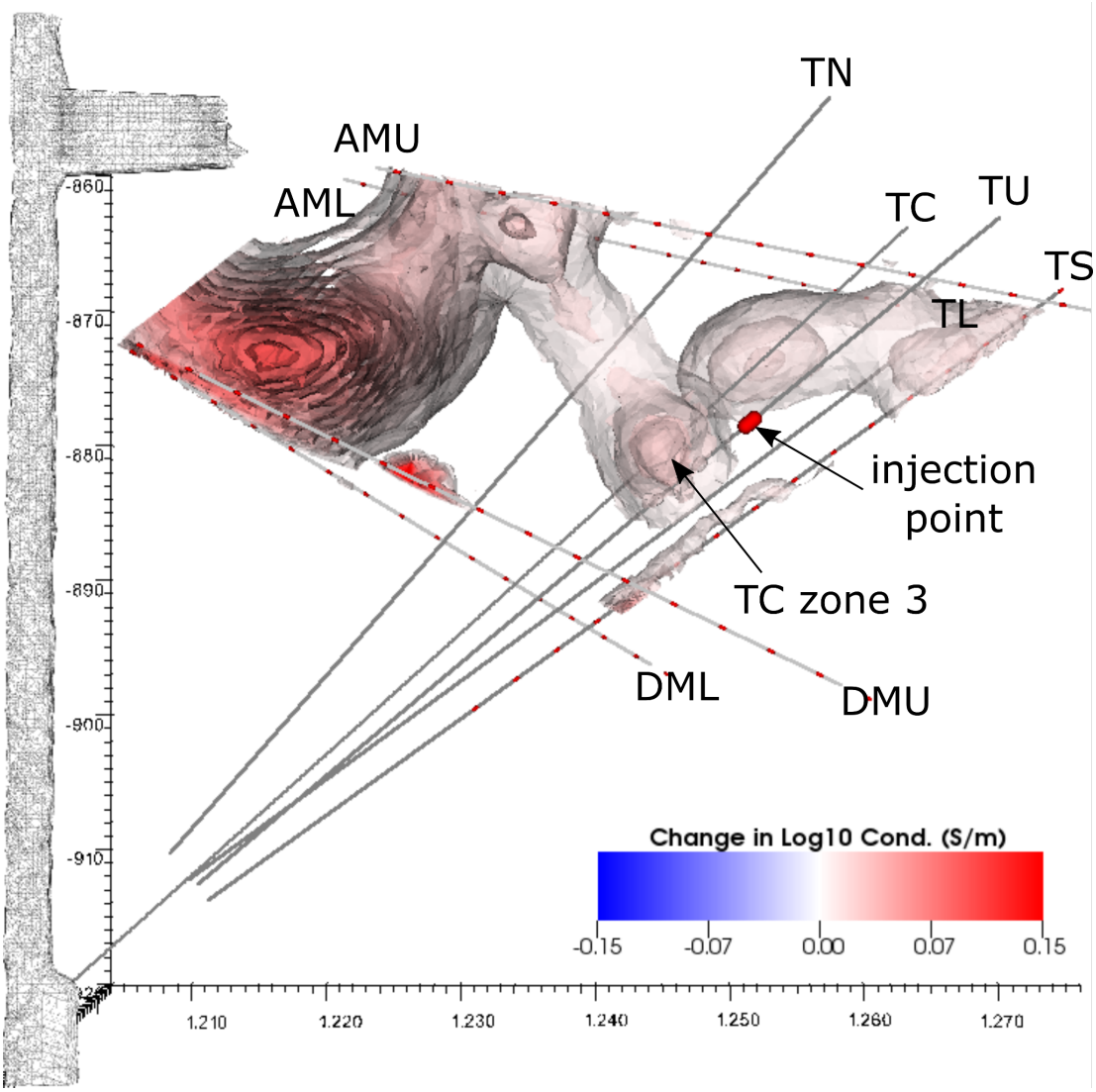

Figure 9.9. ERT Image of saline tracer distribution after injection at TU 177.4 - 179.6 ft for approximately 8 hours.

10 TEMPERATURE TESTS

The previous sections of this report have described the characterization of Testbed 2, the simulation and circulation experiments, and geophysical monitoring of changes to the testbed during stimulation and circulation. The results have produced a significant body of data. Of these data, perhaps the most significant for tying the experiment results to EGS are the temperature data, which allow inferences of the properties of the heat-exchange system, especially the fracture surface area for heat exchange. This section describes the initial temperatures in the testbed based on long-term cooling of the mine ventilation, the predictions of thermal performance of the chilled-water circulation and the performance of the chilled-water circulation test.

10.1 Thermal Breakthrough Predictions

To establish a baseline for the thermal modeling, the initial temperature distributions were modeled using STOMP-GT (Figure 10.1). The result of this effort was a temperature gradient between the mine drift and the host rock that was strongest within about 60 m from the drift. This distance overlays the location of the drilled wells. The estimate matches the DTS measurements of the thermal gradient well.

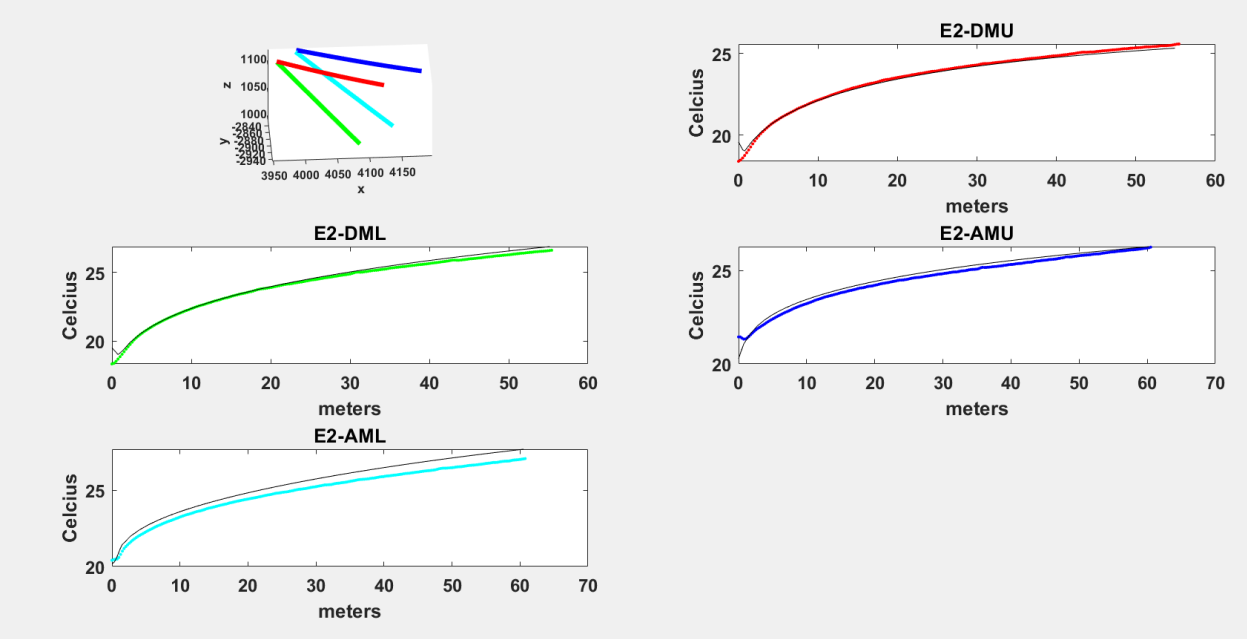

Figure 10.1. Measured and simulated temperature distributions for the four grouted monitoring wells showing very good agreement.

Thermal breakthrough predictions were completed to estimate the required injection rate that should induce at least a 10% decline in produced water temperature during the circulation test. At the time of planning, this meant that a breakthrough time of no longer than 6 months was our goal.

However, we anticipated that faster breakthroughs would be beneficial for model validation, if safely attainable. Thermal breakthrough modeling was completed using: 1) Gringarten theory (Gringarten et al., 1975) for heat extraction from rock (Figure 10.2), 2) STOMP-GT (Fig. 10.3), and 3) GeoDT (Figure 10.4). The Gringarten solution is an analytical solution for thermal decline as a function of fracture area, average flow velocity, and the properties of the rock and fluid. STOMP-GT is a high-fidelity numerical code using coupled physics and element-based solvers with embedded fracture capability. GeoDT is a simplified physics discrete fracture flow and heat transport solver that uses a pseudo-steady state heat flow approximation. All three analyses predicted similar required injection rates ranging from 3 to 20 L/min were needed to induce a 10% (or greater) reduction in the produced fluid temperature in the estimated timeframe. It is key to recognize the *production* (not injection) flowrate dependence on breakthrough time. Low production flowrates yield much longer breakthrough times than higher production flowrates. With the exception of GeoDT (Frash, 2022), these simulations did not consider geomechanical or seismic implications of the calculated flowrates, which were considered separately. The ideal flow rate depended on the distribution of flow within the site where it is possible that fast flow to a single production well could achieve thermal breakthrough more rapidly at a constant injection rate, than flow through a more diffuse fracture network. Key sources of uncertainty that were identified by this modeling effort included unknown fracture heterogeneity, unknown flowing fracture network geometry, and uncertainty regarding the thermal conductivity of the matrix rock. Of these, the unknown fracture geometry, and hence unknown heat transfer area, was the most significant and least constrained parameter with respect to predicting thermal drawdown behavior.

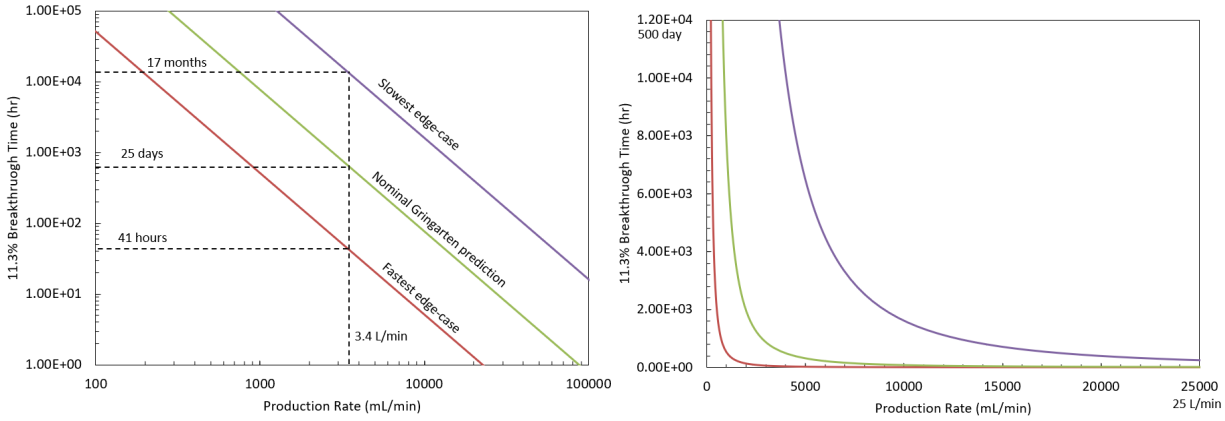

Figure 10.2. Thermal breakthrough predictions using Gringarten et al. (1975) analytical solution with uncertainty in the fracture area and rock's thermal properties.

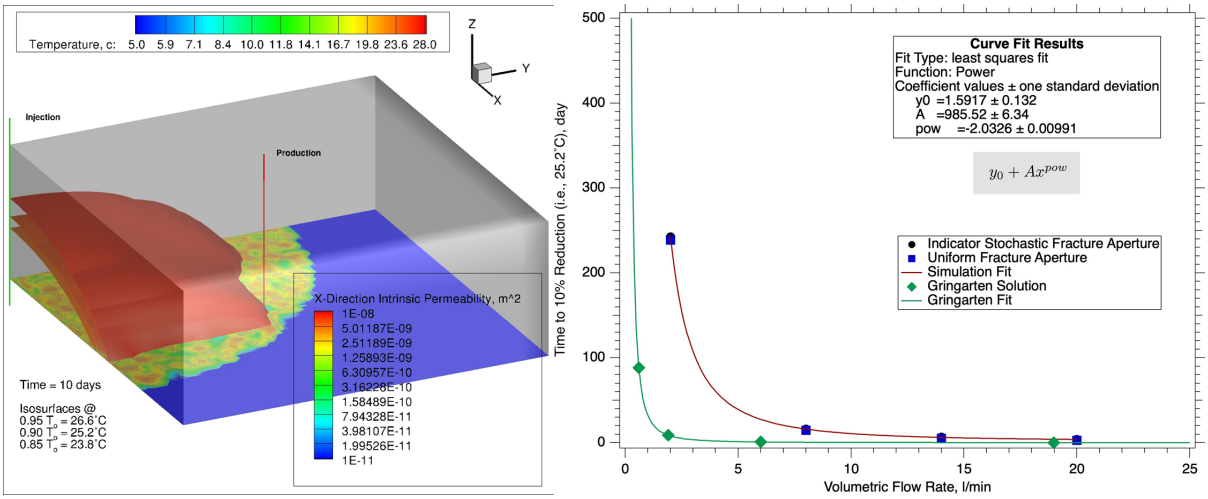

Figure 10.3. Thermal decline predictive analysis with fracture permeability heterogeneity completed using STOMP-GT. Nominal flow rates to achieve thermal breakthrough within 6 months were predicted to require a minimum 3 L/min injection rate.

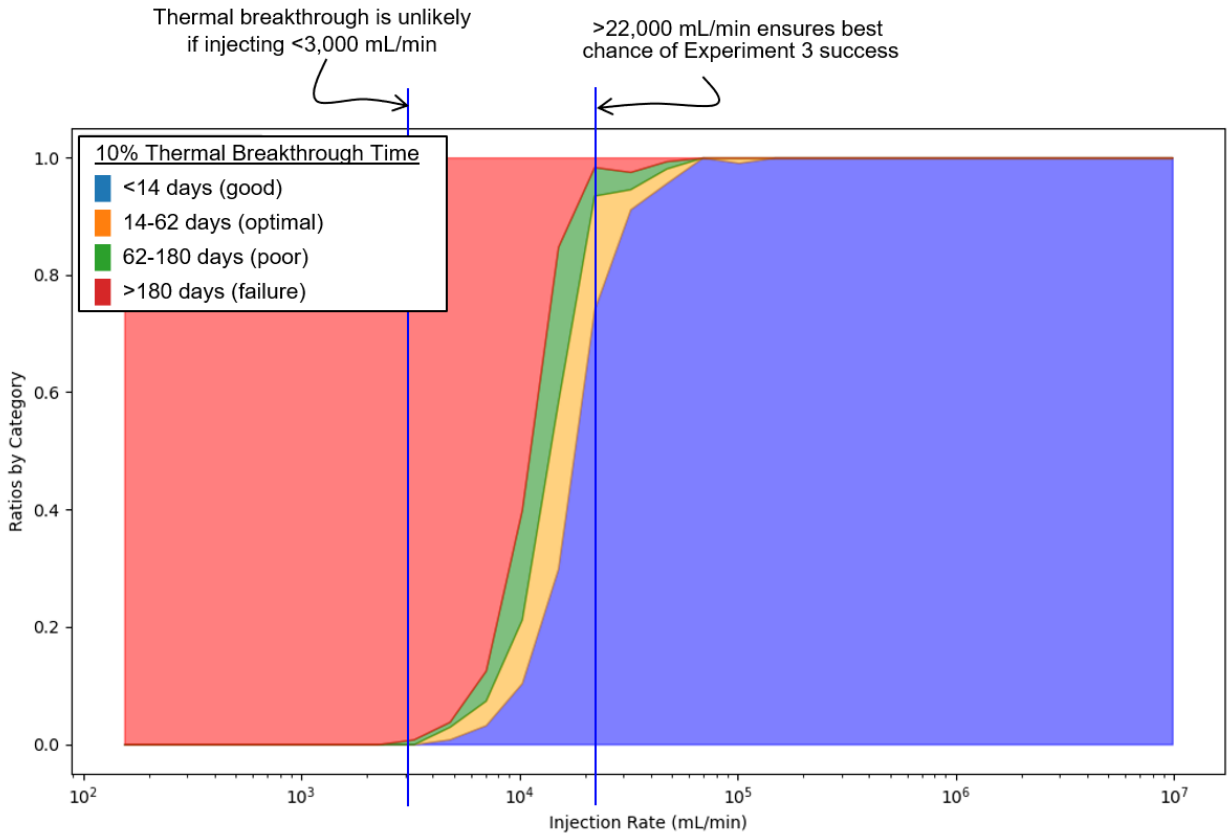

Figure 10.4. Predicted injection rate for thermal breakthrough as a function of injection rate into TC. This plot is a stacked categorical histogram constructed from more than 1,000 realizations from GeoDT. Due to uncertainty in the fracture geometry, flow paths, and thermal conductivity a precise predicted value for a suitable injection rate is impossible to determine. However, our predictions

clearly show that faster flow rates are preferable to ensure that breakthrough is observed within the duration of the experiment, being less than 6 months. Ratios by category can be interpreted as a predicted probability with 1.0 being 100% of the realizations (Frash et al., 2022).

10.2 Chilled-water Injection Test

In an operating EGS system, water that is cooler than the reservoir will be injected, flow through the hotter reservoir, and be extracted. As an analog to this process, we injected chilled water to observe the effects and look for thermal breakthrough in the system. Panel B in Figure 8.1 shows that all injection was at temperatures below the ambient temperature at the injection point (orange and blue lines indicate downhole temperatures at the upper (U) and lower (L) regions of the injection interval) because the mine water was slightly cooler than the host rock. This injection water is considered "ambient" temperature however as it is obtained from the water line in the drift. In spite of injection cooler water, water temperatures in the production wells were higher than the initial temperatures at those locations.

Chilled injection flow was initiated on June 2 resulting in an injection temperature of about 12.5°C. On June 4, a difficult-to-find fitting connecting the pump to the packer broke resulting in a 12-day period of non-injection where the downhole temperatures trended towards their normal ambient temperatures. On June 16 flow was restarted and the temperature of the injected fluid at the injection point was maintained at about 12.5°C for 55 days. Temperatures in wells TN and TC are plotted in Panels D and F of Figure 8.1. In Panel D, temperatures at the upper (U) and lower (L) measurement points in the TN packer interval (Int) and region beneath the interval (Bot) are presented. In Panel F, temperatures at similar locations in the TC packer are presented.

When flowing ambient temperature water (cooler than the initial temperature at the injection location), the temperatures at most of the monitored locations increased. This increase could be the result of 1. the produced water flowing through warmer rock prior to reaching the production location and 2. the Joule-Thomson effect which results in a temperature increase for water upon isenthalpic expansion or a combination of these effects. Over the period of time when the pump was shut-in (no injection while waiting for the new part), the temperatures in the injection interval of TU (Panel B Figure 8.1) increased towards their initial local temperature, while temperatures in the intervals of TN and TC cooled back towards their initial local temperatures. When flow was restarted on June 16, temperatures in TC and TN again increased, but to lower values than before. Flows into these regions (Panels C and E of Figure 8.1) were also lower after the flow was restarted, lending some support to the Joule-Thomson hypothesis. On June 21 nearly all measured parameters shown in Figure 8.1 were affected by three approximately 10-to-30 minute shut-in and 400 mL/min injection tests into the intervals of TC and TN. These were performed as part of Experiment 3 in an attempt to improve permeability between TU and the intervals in TN and TC. While continuing to inject into TU, the shut-in pressures in TCI and TNI were 2,740 psi and 3000 psi respectively. Using a Joule-Thomson coefficient of -0.00285 F/psi (Linstrom and Mallard, 2023) depressurizing from these pressure differences to atmospheric pressure could result in temperature changes of about 4.5°C for TN, and 4.1°C for TC although the temperature change would be expected to be less than this because of mixing with interval water and heat exchange with the rock. The actual temperature changes were almost 4°C in the TN interval and about 1°C in the TC interval - which are consistent with the Joule-Thomson effect. Recovered flows from each of these monitored regions changed over the duration of the test. Because the temperature change in the interval also depends on flow into the interval, changes in flow would impact the

temperature of the produced water. Lower flow will result in a lower Joule-Thomson effect, but also less impact of the chilled water. Measurements are consistent with the Joule-Thomson effect, however sorting out the magnitude of each effect has not been done.

Temperatures measured using the DTS system in the grouted monitoring boreholes indicate that chilled water may have reached DMU and AMU, even if its arrival at the production boreholes was not detected (Figure 8.3). Starting on July 7, 2022, cooling began to develop within a 7-m wide zone of centered at 36.2 m depth in DMU. This was followed on July 24, 2022 by a 10-m wide zone at 23.7 m depth in DMU and a 5-m wide zone at 45.9 m depth in AMU. These zones started narrow and broadened over time. All three zones of cooling persisted through the end of the experiment and did not return towards ambient temperature before the DTS system was shut down on September 14, 2022. These observations are difficult to reconcile with a lack of thermal breakthrough at the production boreholes, suggesting that larger flowrates of chilled water flowed upwards from the TU injection point while lower flowrates of chilled water or other fluid (formation water?) flowed into the production boreholes and intersecting the lower grouted boreholes, as indicated by Joule-Thomson heating signals. The majority of detected seismic events were located above the testbed, suggesting that pressure perturbations were greatest above the injection interval, but any causative relationship between these two observations is unclear. Regardless, the source of cooling is most likely the injected chilled water from TU given the depth and extent of the cooled zones. The zones are too limited in extent and too far from the drift for it to have had an effect, especially since the shallower sections of DMU and AMU are unaffected.

10.3 Chilled-water Injection Simulations Using GEOS

To simulate the chilled water injection, the flow rates recorded at injection well TU and at production wells, TC and TN, are approximated by stepwise constant functions of time and applied as flux boundary conditions in the fracture cells intersected by each well (See ***Appendix K-Simulation of Chilled-water Injection at EGS Collab Testbed 2 Using the GEOS Simulation Framework)***. Additionally, the injection temperature for well TU is also considered to be a stepwise constant function of time and prescribed as a Dirichlet boundary condition for fracture cells intersected by well TU. The time evolution of the fluid temperature at the injection temperature and of the volumetric flow rates is presented in Figure 10.5. Finally, since the fracture working fracture pressure was estimated to be 13.3 MPa, a sink term with a constant pressure $p_{fd} = 13\ MPa$ is considered for all fracture elements intersecting the drift. All fracture cells are also initialized at the working fracture pressure right before the beginning of injection.

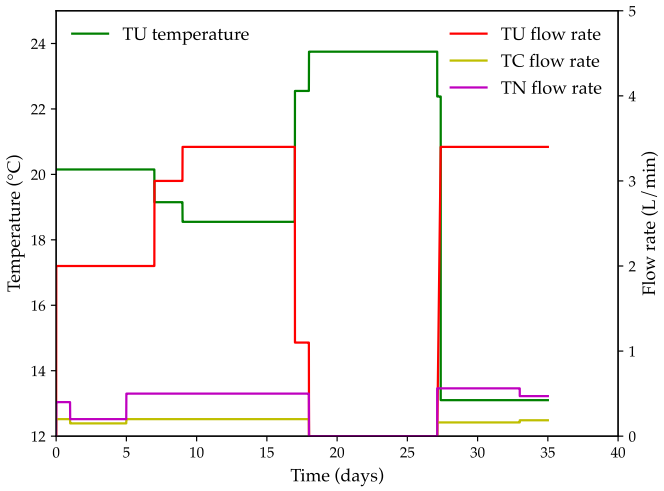

Figure 10.5: Fluid temperature at TU and volumetric flow rates at TU, TC, and TN as a function of time from onset of injection.

After having computed the initial condition as described in the previous paragraph, the chilled-water injection stage is simulated for 35 days. Figure 6 shows the temperature profile 35 days after the start of injection. Note that the GEOS model predicts a faster advancement of the cold temperature front compared to reference STOMP-GT model, and therefore an earlier thermal breakthrough. Additionally, differently from the results obtained with the STOMP-GT model, the cold waterfront reaches the drift.

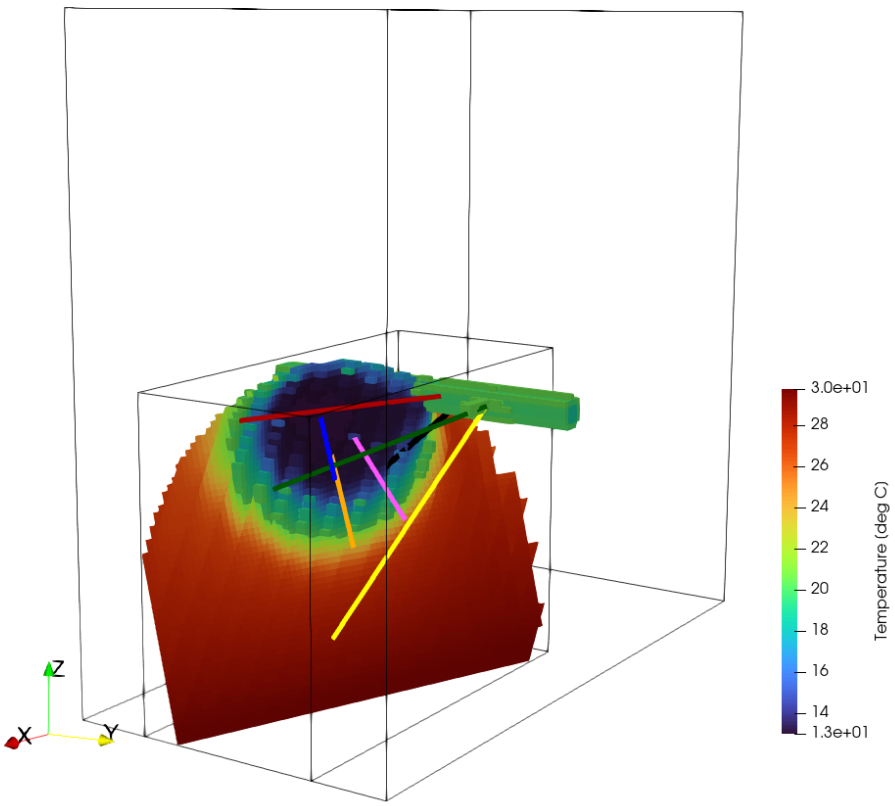

Figure 10.6: Temperature distribution in the fracture at simulation time 35 days after the start of the chilled water injection.

Figure 6: Temperature distribution in the fracture at simulation time 35 days after the start of the chilled water injection.

11 LESSONS LEARNED

The motivation of the EGS Collab project was to investigate stimulation to decrease risk in EGS development under a collaborative experiment and model comparison project, to allow data comparison to reservoir model predictions, and to provide data for validation of predictions using ~10 m-scale field experiment data. The collected data were to include in-depth fracture characterization and well-performed, well-monitored experiments collecting high-quality data using comprehensive instrumentation. A goal was to elucidate the basic relationship between permeability enhancement and stress, seismicity, and other parameters. Secondarily, the EGS Collab Project was tasked with facing and addressing problems that will occur in EGS, and to improve tools for EGS for the prediction of EGS development and performance. We sought to achieve the objectives of the EGS Collab Project by studying rock mass response to stimulation using accessible deep rock. We performed 10-m spatial scale experiments under stresses relevant to EGS (at 1.25 and 1.5 km depth) in crystalline rock, and our tests and analyses were performed to support the validation of thermal-hydrological-mechanical-chemical (THMC) modeling approaches. In addition, the EGS Collab project tested and improved novel and conventional field monitoring tools. By observation of system behavior during our experiments, we gained insight into permeability enhancement and evolution in crystalline rock. These observations and interpretations provide understanding of creating sustained and distributed permeability for heat extraction by generating new fractures that complement existing fractures.

Investigation within the EGS Collab project benefitted from characterization, stimulation, monitoring, and fluid circulation at using data densities, both spatial and temporal, and scales that could not be achieved anywhere other than a testbed from an underground structure. The experimentation assumes that the fundamentals of heat exchange from rock to stimulated fracture network are similar at low temperatures as high. Underground experiments allow characterization both pre- and post- stimulation using methods that surround the stimulated volume, and many types of tests, such as the SIMFIP measurement of fracture deformation, could not be conducted from the surface in an at-depth facility like FORGE.

Thus, experiments using underground test facilities like EGS Collab could gain insights to the several key EGS issues such as:

- Three-dimensional characterization of the stimulated volume by complementary geophysical methods
- Comprehensive tracer testing and detailed characterization of complex fluid movements
- Understand the geometry of the stimulated network and its implications for effective fracture surface area, rock block size, and heat exchange

Lessons learned from the project are presented in two groups. The first is a discussion of lessons learned that may be applicable to full-scale EGS. The second group is a collection of lessons learned grouped by topic including:

- Experiment Design
- Instrumentation
- Experimental Systems
- Characterization
- Stimulation

- Complexity
- Models
- Data Processing and Integration
- Flow Tests
- Collaboration Project
- Tracer Usage and Interpretation
- Field Experiments

Each lesson learned may indeed be obvious to some, but their mention is nonetheless important. In addition, addressing some of these lessons learned involve trade-offs and consideration. In many cases, it may not be possible to address some of these lessons even when considering them in advance. Some may not apply to particular situations. This discussion is somewhat comprehensive, but as in many projects, there are many other highly specific lessons learned not included here.

11.1 Lessons Learned at the Scale of our Experiments, Lessons Applicable to EGS at the Full Scale

The correlation between seismicity and permeability remains elusive. In Experiment 3, much of the detected seismicity occurred in the upper regions of the testbed, some even above the drift. Flow on the other hand apparently concentrated below the drift, as the bulk of the recovered water entered through the floor. The elevation of the drift floor is above the elevation of the top of the testbed. In E1, seismicity identified fracture opening along many planes that were confirmed to be hydraulically conductive. ERT data however showed that a large fraction of the flow occurred where little seismicity occurred. Seismicity occurs when energy is released in the rock, for example from fracture tips or unmatching asperity contacts from opposite sides of a fracture hitting each other during shear. The seismicity does not necessarily identify that the pathways are large or viable for conveying fluid, nor does it identify previously open pathways can take significant flow without inducing any new seismicity. Despite these constraints, microseismic monitoring proved to be a valuable tool for understanding the in-situ fracture behavior in a way that is directly relevant to full scale EGS. In other words, microseismic data were shown to be highly valuable for confirming the stimulation of fractures, but recognizing that the absence of seismicity does not confirm the absence of flow paths. In the instance of the particular test bed employed in this project, the data may point to a scenario wherein new fractures tend to be more prone to the generation of MEQ's whereas the ERT responded to larger flows in the existing fractures. In practice, this suggests that larger-scale reservoir developments relying heavily on the existence of MEQ's to describe the reservoir may be missing important components of the flow system. One of the key challenges faced in developing EGS reservoirs is to create distributed permeability throughout the reservoir to facilitate efficient thermal transfer of heat to the circulating fluid (e.g., Doe et al. (2022); Grant (2016)), so it is critical to understand where flow is actually occurring.

We did not cause significant **shear stimulation** which would establish viable flow systems at pressures below the minimum principal stress in either test bed. This does not mean shear stimulation below the minimum is not possible, however. In Testbed 2 healed or filled fractures would not open below the minimum stress, nor would they accept water to provide the needed hydraulic communication between the well and fracture. The test bed lacked naturally conductive fractures that might have shear-stimulated. Naturally conductive fractures elsewhere at the 4100 level were avoided over concerns that they might produce excessive flow to the underground openings without becoming adequately pressurized for shear stimulation.

We did not conclusively establish **thermal breakthrough** in either of our flow tests. Thermal breakthrough could have occurred at higher-flow weep locations where temperature was not monitored. Additionally, we encountered Joule-Thomson effects which caused temperature increases as the water depressurized from the fractures to the wells. Had warm water been used in the flow tests, perhaps even greater initial misinterpretation might have occurred.

Flow in our systems was distributed. In both Experiment 1 and Experiment 3 we hydraulically fractured the rock and connected our injection and production wells. In addition, the stimulated flow system connected to many other locations beyond the intended testbed, resulting in reduced recovery rates for the injected fluid at the production wells, especially when the connection between the injection well(s) and production well was minor. It is not known how this would impact fracture caging in a full-scale EGS system having many differences from the EGS Collab test beds. In both Experiments 1 and 3, a majority of the injected water was collected indicating flow from the high-pressure injection locations to the low-pressure production wells and low-pressure drift. Whether connecting to an existing fracture network or creating new fractures, flow was observed and quantified at numerous locations away from where flow was expected. If this is the general case, this could possibly be good for EGS because distributed flow may increase heat transfer area between the fluid and rock. More diffuse flow may also pose a greater risk for injection-induced seismicity when closed-loop flow is not attained. These questions require further study. All of our tests were performed under nonlithostatic stress gradients.

Our flow systems were dynamic. Throughout all of our experiments, flow rates from the many collection locations were always changing in spite of constant injection rate. In Experiment1, resuming pumping after any stop typically resulted in a decrease to the injection pressure required for a constant rate of injection. In Experiment 3, this same action appeared to relate to an increase in the injection pressure. Tracer studies indicated changes in flow paths over time and in response to stopping or changing the flow rate in both experiments. Changes induced by operational modifications were found to provide a wealth of information about the system. Shut-in experiments at the conclusion of both EGS Collab experiments provided new insights about flow paths and near well-bore flow resistances, that were previously unknown. Full-scale EGS will also have complications due to stress gradients applied from injection, production, and temperature changes, the injection and later degradation of proppants, and dynamic flow networks will change over time and in response to varying injection and production rates and fouling processes. Without a good understanding of the dynamic flow, controlling this phenomenon will be difficult.

There are many possible explanations for a dynamic system, and these may operate together. These include geomechanical, geochemical, and biological processes. In our tests, the geomechanical argument is that our systems were operated at pressures exceeding the minimum principal stress. Flow entering a fracture could exert a significant force on the rock blocks on either side of the fracture altering the existing stress distribution. This force could open fractures to an extent. When flow reached another intersecting fracture, the force balance and directions would change, again altering system apertures and flow, and changing flow paths. It is not clear whether pressure exceeding the minimum principal stress is required for this since under proper conditions shear stimulation occurs below the minimum principal stress. Biological processes are unlikely but possible in geothermal systems (consider the injection of cooler water), and this also needs consideration. Microbes could grow in our system (Zhang et al., 2020) where conditions are right, and change flow paths through biofouling. During early test bed characterization, fouling of wells was attributed to biofouling as seen in the optical logs, requiring the boreholes to be scrubbed; this

process may have been accentuated by introducing oxygenated waters into a reducing environment. One would expect that as the microbes grow that the conditions would change as nutrients were consumed, that new communities would flourish elsewhere impacting flow there. These flow path alterations would impact the pressures on rock blocks perhaps accentuating geomechanical processes. Geochemical processes cause dissolution and precipitation of solid phases that will impact permeability. Dissolution could concentrate flow as apertures increase, and this process could be self-enhancing. It is important to realize that for both biological and geochemical processes, that there are immense numbers of kinds of microbes and mineral phases. Research considering single mineral constituent or single organism systems can be informative but is excessively limiting and possibly misleading. (Dobson et al., 2020) showed nearly collocated dissolution and precipitation of polymineralic rocks under EGS conditions. EGS temperatures will hinder biologic processes but rock cooling will occur near injection wells. Temperatures of EGS systems will increase geochemical reaction rates.

The **role of the uncertain and heterogeneous stress gradients** should be carefully considered, especially with respect to the imperfect prediction of propagation direction of hydraulically stimulated fractures. The EGS Collab project highlighted the current inability to accurately predict the behavior of a planned EGS stimulation due to irreducible uncertainties and heterogeneity in the rock. Although changes in the mechanical properties of the rock mass may be due to stresses induced by pumping, modeling shows that stress gradients from temperature gradients created by the presence of the access drifts in our tests greatly affected the trajectories of induced fractures. In the EGS Collab tests, the temperature changes associated with the water being introduced into the reservoir are probably too subtle to have major effects, but larger scale operations may be affected by these types of temperature gradients, particularly in conjunction with infill drilling and refracturing.

The management of our "simple" systems was complex. Management required exercising a number of models from conceptual to numerical that had to be adjusted frequently to adapt to new responses from known or unknown stimuli. The experience indicates that successful reservoir management at any scale must be an active process requiring attention to, and interpretation and integration of important data streams. When interpreting multiple data sources of various types, we found that it was valuable to employ a wide-range of data sources, data analytics (e.g., inversion models, mapping, data integration, and machine learning methods), visualization methods, and a broad-spectrum of subject-matter expertise. Using this process in an open forum enabled our team to obtain the most comprehensive understanding of what we were observing, the most likely causes of the observations, and potential solutions to remedy the problems that were encountered.

The limited permeability shown by many crystalline rock masses is well-represented by the rocks of the current test beds. Division of the rock mass into separate reservoirs, often by high-angle fracture systems can result in different fluid pressures between those reservoirs depending upon the frequency of fracturing. Therefore, **extrapolation of results** from one of the separate reservoirs to an entire geothermal field should be done with care unless good reasons can be made to assume a sufficient number of fractures or fracture systems exist to allow communication.

11.2 Topical Lessons Learned

11.2.1 Experiment Design

1. The experiment goals and philosophy need to be understood by *all* project participants. All need to provide input at early stages so the abilities and limitations of each's contribution are understood. All specialties including modelers, experimentalists, measurement experts, and implementation experts have to understand each other's roles and to maximize project success.
2. Experiment design modeling and sharing: To the extent possible, all tools needed for the project should be identified at the start of the project. These tools should be obtained or developed at the start of the project if needed. Initially the EGS Collab project used whiteboard/PowerPoint sketches for developing the borehole layout and sharing ideas. This was fine for preliminary designs but was limited in that answers to the next level questions required much more separate analysis. All initial proposals for software to fill this gap were proprietary and not extensible. In this vacuum, the FatCrayonToolkit was developed and allowed us to easily share 3D models via email/GoogleDrive/etc. Written in Python, the FatCrayonToolkit allowed project participants to add features and perform analyses (total drilling depth, projected point of closes approach of a hydraulic fracture to a borehole, likelihood of the injection borehole intersecting shearable features, etc.). Such a tool/platform for shared model design and associated calculations should be established as part of the initial planning for similar projects.
3. Allow time throughout the project to think through every step of an experiment. This will maximize learning, reduce error, aid in understanding when something goes wrong or results are not as expected. Allow time for analysis of experimental observations. The density of experimental data generated within the volumes of rock for both EGS Collab experiments is truly impressive, and it can be tempting to dismiss observations that don't seem to gel with conceptualizations of the coupled thermal, hydrologic, geomechanical, and geochemical processes of EGS reservoirs. It's through closer consideration of experimental observations that we gain understandings of our experiments. One example of this is the observations of temperature increases in the DTS signatures at points along grouted monitoring boreholes. After applying numerical simulations and conducting a few simple laboratory experiments, this Joule-Thomson coupling of positive temperature change with negative pressure change for liquid water in the experimental pressure range, became not a misunderstanding, but a common practice of identifying fracture intersections with boreholes. There are several temperature observations in EGS Collab Experiment 2 that remain to be understood.
4. Plan for test repetitions if possible, to show repeatability and calibrate measurements.

11.2.2 Instrumentation

1. Multiphysics monitoring instrumentation enabled investigation of results from multiple lines of evidence, and was very important for converging on behavior understanding. Co-deployment of multiple geophysical tools in a borehole or testbed requires coordination and understanding of the techniques by all to minimize the impact of interferences caused by any tool actuation or technique need such as plumbing/wiring/connection to the rock. Synchronization in space and time is required to allow cross calibration and evaluation of the same events. This also supports confidence building/calibration of new tools.
2. Seismic (and other) instrumentation should be selected extremely carefully. The instrument response function should be known and the sensors should be sensitive enough to detect seismicity of the magnitudes expected for a given operation. The expected magnitudes, and

by extension the anticipated amplitude spectra of seismicity, should be modeled beforehand and sensors selected accordingly.

3. Durability vs. signal quality: Downhole instrumentation can be hardened against fracture intersection, fluid leakage, and other damage by using Tubing Encapsulated Cable (TEC) to transmit electrical signals along a grouted borehole. The tradeoff is that this TEC seemed to be a source of noise. The noise was likely a combination of electrical cross talk between the systems connected to it and the TEC acting as an extension of the CASSM sources. Every time a CASSM source fired, the elastic energy was partially transferred to the TEC, which acted like a line source along the borehole.
4. Novel instruments (SIMFIP and DORSA) were used to measure in-situ strain, stress and 3-dimensional displacement in boreholes to the micrometer scale in real time allowing unprecedented understanding of fracturing mechanisms. Further tool development can yield a tool able to withstand higher pressures and temperatures for use in even more adverse settings. The use of such tools may be highly beneficial for developers of EGS sites and even for long-term monitoring when in operation.

11.2.3Experimental system

1. Automated, real-time results raised the value of a given type of data significantly, regardless of data type. Automating processing of flows and delivering results quickly is as important, if not more important, than improving data fidelity or focusing on new modes of sensing.
2. System capability and robustness – Once test conditions have been established, the test system should be built with greater capacity and higher measurement fidelity if possible. Undoubtedly in testing like performed in EGS Collab a system will be asked to do more than originally planned, and produce finer resolution data, so it pays to overbuild the system to allow for increased flexibility in testing at later times.
3. Spare parts inventory - in remote locations having and maintaining an accurate inventory of spare parts as a matter of policy is of critical importance. The lack of available spare parts risked forward project motion and caused expensive delays while parts were rush shipped.

11.2.4 Characterization

1. Characterization and modeling before experiment planning - The EGS Collab project acquired multiple types of characterization data and monitoring data during testing. Modeling for some of the parameters was performed before experiment planning. The need and usefulness for some data streams was unclear, however. Having a better idea of what to expect and more established need for specific data streams would have helped us design better systems for near real-time or fast data analysis that could have provided additional information and helped guide the tests.
2. ‘Imaging Stress’ has been specified as an important research challenge for EGS. Electrical conductivity is very sensitive to stress in crystalline rock and stress regimes common to EGS. Stress changes were observed or inferred using several tools in the EGS Collab project including electrical and electromagnetic methods, DAS, and borehole tools such as SIMFIP and DORSA.
3. Characteristics of fractures – orientations, sets, extents, open or healed, flowing/non-flowing, etc. – of natural fractures are important during designing of testbeds/reservoirs. Gathering existing data (e.g. outcrop/drift, cores, image logs, and geophysical results) can

provide characteristics of the natural fractures. In the EGS Collab project, direct observation of complete cores, interpretation of image logs, fracture/shear zone mapping in the drift, and data collected with several geophysical and hydraulic measurements including tracer tests were employed to characterize the natural as well as created hydraulic fractures and flow paths in the testbed. Drift mapping, core observations, optical and acoustic televiewers images, production/leakage points, and geophysical data (DTS , ERT, and MEQ) provided data to develop conceptual flow pathways and fracture systems in the testbed. Quickly evaluated data sets were more valuable in guiding the project.

11.2.5 Stimulation

1. Tools to estimate induced seismic risk are lacking. Without such tools, there is no defensible means to quantitatively predict effects of the injection rates used and whether they would lead to seismicity and the related safety hazards. Experiments increased flow rate based on observations of lower flow rates. Defensible methods to forecast and revise induced seismic risk are needed in order to make EGS successful!
2. Shear stimulation may not be generally implementable, at least in the vicinity of the borehole, and should not be counted on in general for EGS stimulation. Shear stimulation requires natural features with a specific range of initial permeability (not too high or too low), mechanical strength, and in-situ stress conditions. While we detected indications of shear movement with our testbeds, none of our experiments resulted in shear-induced permeability despite careful characterization and design optimization around the state of stress and nature fractures. Shear stimulation may require an impractically narrow convergence of conditions in crystalline rock, and it remains to be seen whether induced permeability can be maintained without also maintaining injection pressure ("hydro-propping"). Other tools such as high strength, chemically resistant proppant or other methods of creating/maintaining permeability should be pursued (electrofracing, chemical treatments, other).

11.2.6 Complexity

1. Stress controlled fracturing and natural fracture complexity: Both Experiment 1 and Experiments 2-3 created hydraulic fractures normal to the minimum stress directions. Both experiments, however, also intersected complex fracture networks. The patterns of flow to boreholes and the drifts indicate that stress controlled hydraulic fractures but flow in intersecting fractures created complexity in flow.
2. Interrelationships of rock stress, rock property heterogeneity, and stimulation patterns: The interrelationship of rock stress to stimulation is well-known but difficult to define in rock that is highly heterogeneous. The EGS Collab project has an outstanding base of geophysical monitoring data from using multiple complementary signals for defining the heterogeneity of the rock masses, especially Test Bed 2. Furthermore, the SIMFIP and DORSA measurements add valuable constraints on fracture movements from the borehole deformations around fractures. A fundamental question of what happens during propagation, opening, and deflation after shut-in might be teased out Collab data sets. The community has been exploring a very significant data base for testing models of pressure transients during leakoff that have profound importance not only to EGS but to all applications of underground stimulation including unconventional oil and gas resource development and carbon sequestration.

3. Subsurface uncertainty is a key consideration for EGS design. Better understanding how local variations in stress will impact the creation and opening of fractures will be critical in EGS development, as well as determining what is responsible for the stress changes (presence of faults and fractures, variability in lithology, etc.). Tools that rapidly help to address subsurface uncertainty may be useful in design helping answer questions like injection flow rate and well placement. Instead of simplifying design analysis when lacking data, a design approach that assumes all reasonable possibilities in the initial design and then refines the design by eliminating the impossibilities as new information is obtained may be a more effective approach. Use of such an approach requires a change in thinking.
4. Thermal gradients matter: Thermal gradients between the rock and circulating fluids in hot-dry-rock geothermal reservoirs control the heat production rates. This aspect of EGS is well understood, and the nature of the large surface areas created by fracturing the rock is specifically directed at overcoming the poor thermal conductivity of rock. EGS Collab, however, taught us that thermal gradients additionally yield stress gradients, which have strong influence over the extension behavior of fractures. In both experiments, hydraulically stimulated fractures tended toward the mine drifts, which had experienced decades of cooling via active ventilation systems. It was very reassuring to see how the field observations correlated with the modeling predictions.

11.2.7 Models

1. Models proved quite useful in understanding the results of the experiments. Models were most effective when they were flexible enough to test hypotheses to explain new data. The paradigm of making measurements, performing post-experiment analysis, and providing the data to a modeler for even later furhter understanding is not conducive to effectively managing or understanding field experiments. The use of simpler more flexible modeling approaches allowing rapid updating is needed in addition to the traditional more refined paradigm. Engineering tools are needed to adapt to conditions that evolve, stimulation methods, methods for active or passive conformance control, and for addressing seismicity.
2. Models, with a few exceptions, have been of minimal value in *a priori* predictions, despite the level of characterization on the Collab project that no full-scale site will ever see.
3. To the extent possible, modeling the locations and number of sensors should performed as part of the experiment design to allow optimization of instrument placement.

11.2.8 Data, Processing, and Integration

1. Management, documenting, and curating of field test data is a major challenge in long-term dynamic projects. Our project was dynamic in that our testing plans were adapted to new challenges as they were identified. We swapped out instruments and tools, did stimulations and tests that were not initially planned. These all resulted in the data types, formats, and volumes changing suddenly during the project. All of these changes were needed for the project to be maximally successful and it would be unreasonable to either expect such developments to be anticipated at the start of a project or to maintain a rigid approach that does not allow for such changes. The approach to these changes that worked best was when there was a dedicated person offsite that was following and documenting these operational and data-related changes as the field work occurred. The approach that worked less well was to rely on the field crew to both conduct field operations while also documenting the work during or after the day's work was complete. When this was expected of the field crew, the quality of the documentation was much lower and required

a significant amount of work after the testing to parse through the data and reconstruct documentation of the changes. Realistically, it is simply too much to expect the field team to maintain focus on operations. get adequate rest between shifts, and prepare detailed notes. Pairing the field crew with a remote office worker monitoring and actively documenting the field operations is needed.

2. Broadcasting the data via a Zoom meeting allowed for this remote participation (pre-COVID!) in the field work.
3. Rapid interpretation of data is critical and enabling that should be part of the original planning. The Collab experiments involved collection of multiple data streams (ERT, microseismic, DAS, DTS, etc.) and the lead for each data stream performed post-experiment data reduction and analysis. It is important to spend enough time thinking about the output of each monitoring technology before experiments are conducted, and to work together to have data processing and integration tools ready to start analyzing data from day one. A single data stream cannot not tell the whole story, e.g. MEQ's are not always an indication of flow, fracture propagation and opening is not always accompanied by flow (DAS and DORSA signals observed way before DTS anomalies), etc. Having a robust way of integrating these datasets quickly during the experiment could inform ongoing experiment strategies. and better decision making.
4. Data integrator. There is a need for someone to be tasked to combine/manage all those data streams and develop the big picture. In Collab the method of interpretation used was simply using scripts summarizing data on a single page or screen and presenting this for group analysis allowing direct observation of stimulus and response. Such scripts can be somewhat automatic, but must change when tests, parameters, or sensors change. For complex experiments such as Collab or perhaps FORGE, a data scientist is needed that has enough foundational backing to support the needs of the experiment in real time and for archival purposes. Someone with experience in both data science and the science of the experiment would be ideal. Future projects should budget for such combined data products and a more formal multimodal analysis of the data.
5. Realtime seismic processing: There are few available software packages for realtime processing of seismic data in the 100s of kHz sampling range. The package used for Collab Exp 2 (called DUGseis) needed to be heavily modified to accommodate our recording system. A data recording setup similar to that used by ETH at the Bedretto Underground Laboratory for Geosciences and Geoenergies (for which DUGseis is tailored) might have been more effective. Other than that, a computer scientist collaborator could help code a plugin to write our recorders data to the hdf5 data format needed by DUGseis. This is not a problem for field scale experiments recording at lower frequencies currently, but will become more of an issue as sensor networks go deeper and sampling rates increase.
6. A 3D visualization capability that can incorporate different types of experiment and modeling data would be very valuable, especially if there is a person devoted to interacting with the originators of various experimental and modeling data sets to capture the key information from distinct data and figure out how to display it. The two major 3-D packages used - Fracman and Leapfrog - are a good starting point, but more could be done. Just as uploading data to the GDR is required for archiving, all data originators should work with the visualization person to determine the most effective way to display the data in an integrated 3D visualization platform. This interaction should begin early in the experiment, and with experience could become more automated and have a shorter turnaround time.

Point quantities like pressure, temperature, tracer concentrations at various locations should be straightforward, but fields could be displayed as slices or isosurfaces.

7. The volume of data that an operation will produce should be well-estimated in advance. Changes in the experiment, particularly the duration, had a large impact on the ability to transfer and process data in realtime and led to untimely, permanent data gaps during critical phases of the experiment. With reasonable allowances for the unpredictable nature of field experiments, these issues could have been mitigated with better planning.

11.2.9 Flow

1. Characterization of circulation pathways and implications for EGS: The pathways from the injection zones in both experiments were defined through combinations of geophysical monitoring and tracer testing. Tracer testing indicated that injection water velocities were rapid with breakthroughs in the order of hours to days. A major significant finding was the lack of a clear chilled-water breakthrough. There are two significant factors in the lack of observed breakthrough. The experiments identified a Joule-Thompson heating rather than a cooling effect at the production intervals. It is still an open question whether this effect masked the chilled water breakthrough or the chilled-water breakthrough never occurred. The second was the low portion of injection water that arrived at the production intervals, especially in Experiment 3. The circulation flowrates were designed to create thermal breakthrough, but actual flow rates to production intervals were lower than expected, and given the second power relationship of thermal breakthrough to rate, these low production rates may have been a major factor in the lack of chilled water breakthrough. Unravelling the story on thermal breakthrough will require a lot of thinking and modeling, and the story will likely be one to come out of a future data analysis.
2. Additional work is needed to assess under what conditions production wells will cage the growth of an EGS flow system where the injection pressure is greater than the minimum principal stress and the fractures are hydro-propped. The production wells at the Experiment 3 site only captured 25 to 30% of the injected water, the remainder of the water discharged in the drift. A review of previous EGS data indicates that water loss was a major concern at these sites. Although EGS is attempting to avoid faults, natural fractures will also be discharge structures that can alter the flow pathways to undesirable locations. Shut-in test results suggest that there exists a near well low permeability zone near the production wells. The use of proppants at the production well could increase the production well discharge rate by reducing well skin effects.
3. In our experiments, we found that the temperature of injection has an effect on the pressure of the injection zone - i.e., increasing injection temperature correlated with increasing injection pressure. This may have implications for circulation at the full/commercial scale in crystalline rock.

11.2.10 Collaboration Project

1. Increased understanding comes from a well-managed team that is inclusive of as many viewpoints as possible. The EGS Collab project converged to a streamlined collaboration method where science advancements were presented in an effective and timely manner through a seminar format (i.e., the modeling and simulation working group) while real-time field decisions were managed in a regular structured update and plan of the week format (i.e., the field call). Additionally, during experiments, continuous open Zoom meetings were held so participants could always see experiment data and communicate

openly. Having adequate crossover between the modeling and simulation working group meeting attendees and field meeting attendees proved key. Meetings with targeted topics were also held. All meetings other than the continuous experiment meetings required an agenda and time management. Having updates in both of the meeting formats, along with online accessible meeting recordings, provided ample means for all project participants to stay up to speed.

2. The culture of a collaboration is crucial to its success and sustainability. The culture of EGS Collab was established at the outset - that participants would have equitable chances to speak up and contribute; that all work would be conducted safely and with concurrence; and that curiosity and hypotheses were to be encouraged for testing with respect to the critical path. These pillars were necessarily maintained throughout the project.
3. Teaming for best results - in order to design and fabricate the stim and flow system to the best of our ability required input from a number of people, however, it still needs to come down to one person to approve it. Once that is done, design essentially needs to be led by one person, this can be revised. It is easy to fall into a situation of death by revision, if one does not eventually say, we are at a point of diminishing returns.

11.2.11 Tracer Usage

1. Quantifying flow-carrying fracture area is intrinsically difficult. Conservative tracer tests provide some indication of the fracture volume, but not fracture area. Sorbing tracer tests can provide useful information of fracture surface area swept (Hawkins et al., 2018). However, the excessive or insufficient (or heterogeneous) sorption of a sorbing tracer will inevitably cause inaccuracy in the estimate of the fracture area. Geophysical methods, such as MEQ imaging, electrical resistivity tomography (ERT), and active seismic methods such as CASSM, could have the necessary resolution for resolving the overall dimension of a fracture if the accuracy and spatial coverage of the sensors are optimal. However, the "geophysically differentiable fracture area", that is, the area that produces certain geophysical signals or signatures, is only loosely related to the flow-carrying aspect of a fracture.
2. Tracer Dispersion: Calculation of potential dispersion in a tracer injection/extraction system should be evaluated prior to conducting field tests. The Collab tracer tests exhibited significant tracer dispersion in the 300-foot injection and extraction hoses. Preliminary analyses suggest that fracturing at depths of 10,000 feet in EGS systems will also have significant Taylor dispersion in their injection and extraction systems as well.

11.2.12 Field Experiments

1. Conducting these tests from inside of a deep underground facility allowed for an unprecedented level of monitoring and instrumentation, which would not have been possible from the surface without several orders of magnitude increase in cost. The benefits of this were realized in terms of observing the fracture behavior in deep highly stressed rock to a degree not possible in any other EGS-relevant project. Along with this success, several unanticipated tradeoffs to this approach were observed. The primary tradeoff is that the mined drifts interacted with the fracture networks in both test beds in an unanticipated way. Initial thinking on this was that as long as we were ~3 drift diameters away the drift would have little interference with the tests. We learned that fluid drainage, cooling due to long-term ventilation, and highly permeable fracture zones all expanded the zone of influence of the mined drifts significantly. Because of this, our fluid recovery rates were

biased because of the proximity to the mined drifts. The drainage of the mine also resulted in a very large uncertainty in the initial pore fluid pressure within the testbed, which likely has significant impacts on the initial stress state and fluid losses. Future underground facility-based projects should anticipate and account for these effects, most likely by using much longer boreholes.

2. It is important to give yourself time to think through every step of an experiment and to carry out many repetitions if possible, in case something goes wrong and also to show repeatability and calibrate measurements.
3. Experimental observations matter: The density of experimental data generated within the volumes of rock for both EGS Collab experiments is truly impressive, and it can be tempting to dismiss observations that don't seem to gel with conceptualizations of the coupled thermal, hydrologic, geomechanical, and geochemical processes of EGS reservoirs. It's through closer consideration of experimental observations that we gain understandings of our experiments. One example of this is the observations of temperature increases in the DTS signatures at points along grouted monitoring boreholes. After applying numerical simulations and conducting a few simple laboratory experiments, this Joule-Thomson coupling of positive temperature change with negative pressure change for liquid water in the experimental pressure range, became not a misunderstanding, but a common practice of identifying fracture intersections with boreholes. There are several temperature observations in EGS Collab Experiment 2 that remain to be understood.
4. It's difficult to create an effective borehole seal when instrumentation is deployed in the borehole. In both testbeds, fractures intersected grouted monitoring wells affecting monitoring. In Testbed 2, we went to great lengths to redesign our monitoring systems configuration and grout properties to address wellbore seal issues we struggled with Testbed 1. Although the Testbed 2 seals held up better than the Testbed 1 seals, every seal still leaked.
5. Arrangements for 24/7 access to the site would have resulted in more complete data sets. Although we implemented an impressive remote monitoring/recording/control system, certain tasks cannot be completed in a four day 7 to 5 schedule.

11.2.13 Contractors

1. Carefully vet and manage contractors to assure you receive the expected product.

12 CONCLUDING REMARKS

The EGS Collab Project researchers performed an enormous amount of very careful and detailed work aimed at reducing risk in EGS. This work is reflected in numerous conference presentations, conference publications, and data sets, all of which are available for others to understand and use. The work was performed openly and collaboratively, allowing experts in many disciplines and subdisciplines to communicate their thoughts and ideas and understanding of experiment observations. It is not possible to have such a diverse group to interpret observed behavior on many projects. It is hoped that lessons learned, both summarized here and in the project publications, will benefit approaches to EGS, and EGS-related research.

The project had many successes notably the safely carrying out of three major field experiments at depths of 1.25 and 1.5 km in crystalline rock. All work was collaboratively planned and interpreted, and often carried out by teams of researchers composed from multiple institutions. Work carried out at the Sanford Underground Research Facility was supported by and coordinated with the South Dakota Science and Technology Authority, again part of the collaborative project. As with any project, not all work was successful. Many tools and thought processes had to be modified for application in deep crystalline rock from a mined tunnel and some did not work as anticipated, however some provided unexpected perspectives on the physical phenomena that occurred. Unsuccessful aspects were carefully analyzed in an effort to avoid or minimize the root causes of failures. Major findings include:

- Shear stimulation was not achieved, and testbeds were created with hydraulic fractures that were hydraulically propped. Hydraulic fractures propagated towards the drifts as expected.
- Thermal breakthrough was not definitively achieved in any experiment.
- MEQs didn't necessarily identify flow paths
- Hydraulic systems are dynamic
- Simple testbeds (field sites) provide significant complexity
- Tracer dispersion in tubing exceeded dispersion in rock limiting interpretation
- Engineering tools bounding expected seismicity are needed.

Ultimately, this experiment series represents a direct confrontation with the THMC challenges associated with EGS that provides critical insights at the fundamental science level. Predictions, and often assumptions of behavior going into these experiments were often defied during execution and had to be addressed through a continuous cycle of hypothesis, modeling, field trial, data analysis, interpretation of processes, and re-evaluation of understanding. This practice was constantly performed in a remote and challenging environment and is relevant for commercially viable EGS power production. Full-scale EGS applications will similarly have to confront the realities of stress/geologic heterogeneity, stimulated fracture propagation mechanics, the influence of natural fractures and geologic structure, evolving permeability pathways due to physical and chemical effects over time, and optimization of thermal circulation/conductivity. These challenges were commonplace for the five-year duration of EGS Collab activities at SURF and it is reasonable to expect similar of EGS work at the full scale. This project provided new insights, crucial observations, valuable updates to models, and a suite of both novel and commonplace stimulation, circulation, characterization, and monitoring tools/techniques to reduce uncertainties and increase

the probability of success for EGS applications. Researchers and practitioners should be encouraged to build upon both the successes and the unsolved complexities that the EGS Collab Team illuminated within the underground mine workings at SURF.

13 ACKNOWLEDGEMENTS

This material was based upon work supported by the U.S. Department of Energy, Office of Energy Efficiency and Renewable Energy (EERE), Office of Technology Development, Geothermal Technologies Office, under Award Number DE-AC02-05CH11231 with LBNL and other awards to other national laboratories. The United States Government retains, and the publisher, by accepting the article for publication, acknowledges that the United States Government retains a non-exclusive, paid-up, irrevocable, world-wide license to publish or reproduce the published form of this manuscript, or allow others to do so, for United States Government purposes. Sandia National Laboratories is a multimission laboratory managed and operated by National Technology & Engineering Solutions of Sandia, LLC, a wholly owned subsidiary of Honeywell International Inc., for the U.S. Department of Energy's National Nuclear Security Administration under contract DE-NA0003525. Portions of this work was performed under the auspices of the U.S. Department of Energy by Lawrence Livermore National Laboratory under Contract DE-AC52-07NA27344. This paper describes objective technical results and analysis. Any subjective views or opinions that might be expressed in the paper do not necessarily represent the views of the U.S. Department of Energy or the United States Government. The research supporting this work took place in whole or in part at the Sanford Underground Research Facility in Lead, South Dakota. The assistance of the Sanford Underground Research Facility and its personnel in providing physical access and general logistical and technical support is gratefully acknowledged. We also thank the crew from RESPEC, who logged the core upon recovery from drilling, and also supported the wireline logging operations. The earth model output for this paper was generated using Leapfrog Software, copyright Seequent Limited. Leapfrog and all other Seequent Limited product or service names are registered trademarks or trademarks of Seequent Limited.

15 REFERENCES

Augustine, C., 2016. Update to Enhanced Geothermal System Resource Potential Estimate. GRC Transactions, 40: 6.

Burghardt, J., Doe, T., Ingraham, M., Schwering, P., Ulrich, C., Roggenthen, W.M., Reimers, C. and EGS Collab Team, 2020. Integration of Shut-In Pressure Decline, Flow back, Hydraulic and Sleeve Re-Opening Tests to Infer In-Situ Stress, 54th U.S. Rock Mechanics/Geomechanics Symposium.

Burghardt, J., Knox, H.A., Doe, T., Blankenship, D., Schwering, P.C., Ingraham, M., Kneafsey, T.J., Dobson, P.F., Ulrich, C., Guglielmi, Y. and Roggenthen, W., 2022. EGS Stimulation Design with Uncertainty Quantification at the EGS Collab Site, 56th U.S. Rock Mechanics/Geomechanics Symposium, pp. ARMA-2022-2224.

Caddey, S.W., Bachman, R.L., Campbell, T.J., Reid, R.R. and Otto, R.P., 1991. The Homestake gold mine, an early Proterozoic iron-formation-hosted gold deposit, Lawrence County, South Dakota. 1857J.

Dobson, P., Kneafsey, T., Morris, J., Singh, A., Zoback, M., Roggenthen, W., Doe, T., Neupane, G., Podgorney, R., Wang, H., Knox, H., Schwering, P., Blankenship, D., Ulrich, C., Johnson, T., White, M. and EGS Collab Team, 2018. The EGS Collab Hydroshear Experiment at the Sanford Underground Research Facility – Siting Criteria and Evaluation of Candidate Sites, Geothermal Resources Council 2018 Annual Meeting. Geothermal Resources Council Transactions, Reno, NV, pp. 16.

Dobson, P., Kneafsey, T., Nakagawa, S., Sonnenthal, E., Voltolini, M., Smith, J.T. and Borglin, S., 2020. Fracture Sustainability in Enhanced Geothermal Systems: Experimental and Modeling Constraints. Journal of Energy Resources Technology: 1-37.

Doe, T., Riahi, A., Fu, P., Damjanac, B., Sonnenthal, E., Finnila, A., Kennedy, M.B. and Blankenship, D., 2022. Performance evaluation of engineered geothermal systems using discrete fracture network simulations, 47th Workshop on Geothermal Reservoir Engineering, Stanford University, Stanford, California.

Frash, L.P., 2022. Optimized Enhanced Geothermal Development Strategies with GeoDT and Fracture Caging, 47th Workshop on Geothermal Reservoir Engineering, Stanford University, Stanford, California.

Frash, L.P., Arora, K., Gan, Y., Lu, M., Gutierrez, M., Fu, P., Morris, J., Hampton, J. and EGS Collab Team, 2018a. Laboratory Validation of Fracture Caging for Hydraulic Fracture Control, 52nd U.S. Rock Mechanics/Geomechanics Symposium. American Rock Mechanics Association, Seattle, Washington, pp. 8.

Frash, L.P., Fu, P., Morris, J. and EGS Collab Team, 2018b. Fracture Caging: Can We Control the Extent of a Hydraulic Fracture Stimulated Zone?, 43rd Workshop on Geothermal Reservoir Engineering, Stanford University, SGP-TR-213.

Frash, L.P., Fu, P., Morris, J., Gutierrez, M., Neupane, G., Hampton, J., Welch, N.J., Carey, J.W. and Kneafsey, T., 2021. Fracture Caging to Limit Induced Seismicity. Geophysical Research Letters, 48(1): e2020GL090648.

Frash, L.P., Hampton, J.C., Gutierrez, M.S. and EGS Collab Team, 2020. Fracture Caging to Control Induced Seismicity with Inspiration from the EGS Collab Project, 45th Workshop on Geothermal Reservoir Engineering, Stanford University, Stanford, California, pp. 10.

Frash, L.P., Li, W., Meng, M., Carey, J.W. and Sweeney, M., 2022. Enhanced Geothermal System Design Using GeoDT and Fracture Caging — EGS Collab Stimulation Prediction Study, 56th U.S. Rock Mechanics/Geomechanics Symposium, pp. ARMA-2022-0278.

Fu, P., Schoenball, M., Ajo-Franklin, J.B., Chai, C., Maceira, M., Morris, J.P., Wu, H., Knox, H., Schwering, P.C., White, M.D., Burghardt, J.A., Strickland, C.E., Johnson, T.C., Vermeul, V.R., Sprinkle, P., Roberts, B., Ulrich, C., Guglielmi, Y., Cook, P.J., Dobson, P.F., Wood, T., Frash, L.P., Huang, L., Ingraham, M.D., Pope, J.S., Smith, M.M., Neupane, G., Doe, T.W., Roggenthen, W.M., Horne, R., Singh, A., Zoback, M.D., Wang, H., Condon, K., Ghassemi, A., Chen, H., McClure, M.W., Vandine, G., Blankenship, D., Kneafsey, T.J. and EGS Collab Team, 2021a. Close Observation of Hydraulic Fracturing at EGS Collab Experiment 1: Fracture Trajectory, Microseismic Interpretations, and the Role of Natural Fractures. Journal of Geophysical Research: Solid Earth, 126(7): e2020JB020840.

Fu, P., Weers, J., White, M., Knox, H., Schwering, P., Morris, J., Blankenship, D., Kneafsey, T. and EGS Collab Team, 2021b. Efforts and Innovations to Promote Data Sharing and Data Accessibility in the EGS Collab Experiments, 2021 Geothermal Rising Conference, GRC Transactions, Vol. 45, 2021.

Grant, M.A., 2016. Physical performance indicators for HDR/EGS projects. Geothermics, 63(2-4).

Gringarten, A.C., Witherspoon, P.A. and Ohnishi, Y., 1975. Theory of heat extraction from fractured hot dry rock. Journal of Geophysical Research (1896-1977), 80(8): 1120-1124.

Guglielmi, Y., Cappa, F., Avouac, J.-P., Henry, P. and Elsworth, D., 2015. Seismicity triggered by fluid injection–induced aseismic slip. Science, 348(6240): 1224.

Guglielmi, Y., Cook, P., Soom, F., Dobson, P., Kneafsey, T., Valley, B., Kakurina, M., Niemi, A., Tsang, C.F., Tatomir, A., Juhlin, C. and Basirat, F., 2021. Estimating Stress from Three-Dimensional Borehole Displacements Induced by Fluid Injection in Different Types of Fractured or Faulted Rocks, 55th US Rock Mechanics/Geomechanics Symposium, Houston, Texas, USA.

Guglielmi, Y.G., Cappa, F., Rutqvist, J., Tsang, C.F., Wang, J., Lançon, H., Durand, J. and Janowczyk, J.B., 2014. Step-Rate Injection Method for Fracture In-Situ Properties (SIMFIP): Monitoring Fractures Stimulation Efficiency, 48th U.S. Rock Mechanics/Geomechanics Symposium. American Rock Mechanics Association, Minneapolis, Minnesota.

Heise, J., 2015. The Sanford Underground Research Facility at Homestake. Journal of Physics: Conference Series, 606(1): 26.

Ingraham, M.D., Schwering, P.C., Burghardt, J., Ulrich, C., Doe, T., Roggenthen, W.M. and Reimers, C., 2020. Analysis of Hydraulic Fracturing on the 4100 Level at the Sanford Underground Research Facility, 54th U.S. Rock Mechanics/Geomechanics Symposium. American Rock Mechanics Association, pp. 6.

Johnson, T., Strickland, C., Burghardt, J., Knox, H., Hopp, C., Rodriguez-Tribaldos, V., Kneafsey, T., Schwering, P., Pope, J., Blankenship, D., Ajo Franklin, J.B. and Pyatina, T., 2022. 3D Electrical Resistivity Characterization and Monitoring at the EGS-Collab Testbed #1: Results and Lessons Learned Applied to Testbed #2, 56th U.S. Rock Mechanics/Geomechanics Symposium, Santa Fe, New Mexico, USA.

Johnson, T.C., Burghardt, J., Strickland, C., Knox, H., Vermeul, V., White, M., Schwering, P., Blankenship, D. and EGS Collab Team, 2021. 4D Proxy Imaging of Fracture Dilation and Stress Shadowing Using Electrical Resistivity Tomography During High Pressure

Injections Into a Dense Rock Formation. Journal of Geophysical Research: Solid Earth, 126(11): e2021JB022298.

Kneafsey, T., Blankenship, D., Dobson, P., Burghardt, J., White, M., Morris, J.P., Johnson, T., Ingraham, M., Ulrich, C., Roggenthen, W., Doe, T., Smith, M., Ajo-Franklin, J.B., Huang, L., Neupane, G., Pyatina, T., Schwering, P.C., Hopp, C., Tribaldos, V.R., Guglielmi, Y., Strickland, C., Vermuel, V., Fu, P., Knox, H.A. and EGS Collab Team, 2022. The EGS Collab – Initial Results from Experiment 2: Shear Stimulation at 1.25 km depth, 47th Workshop on Geothermal Reservoir Engineering, Stanford University, Stanford, California.

Kneafsey, T., Blankenship, D., Dobson, P., White, M., Morris, J., Fu, P. and Team, E.C., 2021a. Fracture Stimulation and Chilled-water Circulation Though Deep Crystalline Rock: Characterization, Modeling, Monitoring, and Heat-transfer Assessment, 46th Workshop on Geothermal Reservoir Engineering, Stanford University, Stanford, California, Stanford University, Stanford, California.

Kneafsey, T., Blankenship, D., Dobson, P., White, M., Morris, J.P., Fu, P., Schwering, P.C., Ajo-Franklin, J.B., Huang, L., Knox, H.A., Strickland, C., Burghardt, J., Johnson, T., Neupane, G., Weers, J., Horne, R., Roggenthen, W., Doe, T., Mattson, E. and EGS Collab Team, 2021b. The EGS Collab Project: Status and Accomplishments, 2021 Geothermal Rising Conference, GRC Transactions, Vol. 45, 2021.

Kneafsey, T.J., Dobson, P.F., Blankenship, D., Schwering, P.C., Morris, J.P., Fu, P., Wu, H., White, M.D., Knox, H.A., Ajo-Franklin, J.B., Huang, L., Neupane, G.H., Horne, R., Roggenthen, W., Weers, J., Doe, T.W., Mattson, E. and Team, T.E.C., 2021c. Field Experiments and Model Validation: The EGS Collab Project, 55th US Rock Mechanics/Geomechanics Symposium, Houston, Texas, USA.

Linstrom, P.J. and Mallard, W.G., 2023. NIST Chemistry WebBook, NIST Standard Reference Database Number 69.

Mattson, E., Neupane, G., Hawkins, A., Burghardt, J., Ingraham, M., Plummer, M. and EGS Collab Team, 2019a. Fracture Tracer Injection Response to Pressure Perturbations at an Injection Well, GRC Transactions.

Mattson, E., Plummer, M., Neupane, H., Vermeul, V., Sirota, D., Ingraham, M., Kneafsey, T. and Team, E.C., 2023. Fluorescein Tracer Testing on the 4100L – A Preliminary Examination of Initial Arrival in Wells and the Drift at the Second EGS Collab Testbed, 48th Workshop on Geothermal Reservoir Engineering, Stanford University, Stanford, California.

Mattson, E., Zhang, Y., Hawkins, A., Johnson, T., Ajo-Franklin, J., Neupane, G. and EGS Collab Team, 2019b. Preliminary Collab Fracture Characterization Results from Flow and Tracer Testing Efforts 44th Workshop on Geothermal Reservoir Engineering, Stanford University, Stanford, California.

Meng, M., Frash, L.P., Carey, J.W., Welch, N.J., Li, W. and Peterson, S.K., 2021a. Triaxial Direct-shear Reveals the True Magnitude of Shear Fracture Roughness Effects on Flow, SPE/AAPG/SEG Unconventional Resources Technology Conference.

Meng, M., Frash, L.P., Li, W., Welch, N.J. and Carey, J.W., 2021b. Measurement of Geomechanical and Hydrological Properties of EGS-Collab Geothermal Rocks, 55th US Rock Mechanics/Geomechanics Symposium, Houston, Texas, USA.

Meng, M., Frash, L.P., Li, W., Welch, N.J., Carey, J.W., Morris, J., Neupane, G., Ulrich, C. and Kneafsey, T., 2022. Hydro-Mechanical Measurements of Sheared Crystalline Rock

Fractures With Applications for EGS Collab Experiments 1 and 2. Journal of Geophysical Research: Solid Earth, 127(2): e2021JB023000.

Morris, J.P., Dobson, P., Knox, H., Ajo-Franklin, J., White, M.D., Fu, P., Burghardt, J., Kneafsey, T.J., Blankenship, D. and EGS Collab Team, 2018. Experimental Design for Hydrofracturing and Fluid Flow at the DOE Collab Testbed, 43rd Workshop on Geothermal Reservoir Engineering, Stanford University, Stanford, California.

Neupane, G., Mattson, E.D., Plummer, M.A. and EGS Collab Team, 2020. Results of Multiple Tracer Injections into Fractures in the EGS Collab Testbed-1, 45th Workshop on Geothermal Reservoir Engineering, Stanford University, Stanford, California, pp. 12.

Schwering, P., Ingraham, M., Vermeul, V., Burghardt, J., Johnson, T., Strickland, C., White, M., Hopp, C., Tribaldos, V.R., Kneafsey, T., Artz, T., Mattson, E., Doe, T. and Team*, E.C., 2023. Shut-In Testing on the 4100L - Implications on the State of Stress, Fractures, and Wellbores in the Second EGS Collab Testbed, 48th Workshop on Geothermal Reservoir Engineering, Stanford University, Stanford, California.

Singh, A., Zoback, M., Dobson, P.F., Kneafsey, T.J., Schoenball, M., Guglielmi, Y., Ulrich, C., Roggenthen, W., Uzunlar, N., Morris, J., Fu, P., Schwering, P.C., Knox, H.A., Frash, L., Doe, T.W., Wang, H., Condon, K., Johnston, B. and EGS Collab Team, 2019. Slip tendency analysis of fracture networks to determine suitability of candidate testbeds for the EGS Collab hydroshear experiment, Geothermal Resources Council Transactions, pp. 405–424.

Sollohub, L., Johnson, T., Sugama, T. and Pyatina, T., 2022. High Resistivity Well Cement for Underground Wells Suitable for Sealing Monitoring Equipment, 47th Workshop on Geothermal Reservoir Engineering, Stanford University, Stanford, California.

Stetler, L.D., 2015. Water geochemistry and pressure buildup in drill holes on the 4950-ft level at the Sanford Underground Research Facility, Proceedings of the South Dakota Academy of Sciences, pp. 317-327.

Ulrich, C., Dobson, P.F., Kneafsey, T.J., Roggenthen, W.M., Uzunlar, N., Doe, T.W., Neupane, G., Artz, T., Dobler, K., Schwering, P., Smith, M. and Burghardt, J.A., 2022. Characterizing Rock Fractures and Physical Properties for Experiment 2 of the EGS Collab Project, Sanford Underground Research Facility, 56th U.S. Rock Mechanics/Geomechanics Symposium, pp. ARMA-2022-0341.

Ulrich, C., Dobson, P.F., Kneafsey, T.J., Roggenthen, W.M., Uzunlar, N., Doe, T.W., Neupane, G., Podgorney, R., Schwering, P., Frash, L., Singh, A. and EGS Collab Team, 2018. The Distribution, Orientation, and Characteristics of Natural Fractures for Experiment 1 of the EGS Collab Project, Sanford Underground Research Facility, 52nd U.S. Rock Mechanics/Geomechanics Symposium. American Rock Mechanics Association, Seattle, Washington, pp. 8.

Weers, J., Frone, Z., Huggins, J. and Vimont, A., 2020. The Data Foundry: Secure Collaboration for the Geothermal Industry, 45th Workshop on Geothermal Reservoir Engineering, Stanford University, Stanford, California.

Weers, J., Porse, S., Huggins, J., Rossol, M. and Taverna, N., 2021. Improving the Accessibility and Usability of Geothermal Information with Data Lakes and Data Pipelines on the Geothermal Data Repository, GRC Transactions, Vol. 45, 2021.

Weers, J.D., Johnston, H. and Huggins, J.V., 2018. The EGS Data Collaboration Platform: Enabling Scientific Discovery, 43rd Workshop on Geothermal Reservoir Engineering.

National Renewable Energy Lab.(NREL), Golden, CO (United States), Stanford University, Stanford, California, .

White, M., Johnson, T., Kneafsey, T., Blankenship, D., Fu, P., Wu, H., Ghassemi, A., Lu, J., Huang, H., Neupane, G., Oldenburg, C., Doughty, C., Johnston, B., Winterfeld, P., Pollyea, R., Jayne, R., Hawkins, A., Zhang, Y. and EGS Collab Team, 2019. The Necessity for Iteration in the Application of Numerical Simulation to EGS: Examples from the EGS Collab Test Bed 1, 44th Workshop on Geothermal Reservoir Engineering, Stanford University, Stanford, California.

Williams, C.F., Reed, M.J., Mariner, R.H., DeAngelo, J. and Galanis Jr., S.P., 2008. Assessment of moderate- and high-temperature geothermal resources of the United States, pp. 4.

Wu, H., Fu, P., Morris, J.P., Settgast, R.R., Ryerson, F.J. and EGS Collab Team, 2019a. A Numerical Scheme to Reduce Numerical Diffusion for Advection-Dispersion Modeling: Validation and Application, 44th Workshop on Geothermal Reservoir Engineering, Stanford University, Stanford, California.

Wu, H., Fu, P., Morris, J.P., Settgast, R.R., Ryerson, F.J., Mattson, E.D., Hawkins, A.J. and Zhang, Y., 2019b. Stochastic modeling of a conservative tracer test for the characterization of fracture flow patterns in EGS Collab Experiment 1, 53rd US Rock Mechanics/Geomechanics Symposium. American Rock Mechanics Association, New York, NY, USA, pp. 6.

Zhang, Y., Dekas, A.E., Hawkins, A.J., Parada, A.E., Gorbatenko, O., Li, K. and Horne, R.N., 2020. Microbial Community Composition in Deep-Subsurface Reservoir Fluids Reveals Natural Interwell Connectivity. Water Resources Research, 56(2): e2019WR025916.

EGS COLLAB PROJECT BIBLIOGRAPHY

1. Ajo-Franklin, J. B., M. Schoenball, T. Wood, M. Robertson, P. Petrov, L. Huang, EGS Collab Team (2018), Imaging Hydraulic Fracture Propagation Using Semi-Permanent Continuous Active Seismic Source Monitoring: Results from the DOE EGS Collab Experiment, paper presented at American Geophysical Union Fall Meeting 2018, American Geophysical Union, Washington DC, December 12, 2018.
2. Blankenship, D., T. Kneafsey, and EGS Collab Team (2017), The EGS Collab Project: Stimulation Investigations for Geothermal Modeling Analysis and Validation, paper presented at AGU Fall Meeting Abstracts.
3. Burghardt, J., T. Doe, M. Ingraham, P. Schwering, C. Ulrich, W. M. Roggenthen, . EGS Collab Team (2020), Integration of Shut-In Pressure Decline, Flow back, Hydraulic and Sleeve Re-Opening Tests to Infer In-Situ Stress, paper presented at 54th U.S. Rock Mechanics/Geomechanics Symposium.
4. Burghardt, J., H. A. Knox, T. Doe, D. Blankenship, P. C. Schwering, I. M., . . . W. Roggenthen (2022), EGS Stimulation Design with Uncertainty Quantification at the EGS Collab Site, paper presented at 56th US Rock Mechanics/Geomechanics Symposium, Santa Fe, New Mexico, USA, June 26-29, 2022.
5. Chai, C., M. Maceira, H. J. Santos-Villalobos, and EGS Collab Team (2019), Subsurface Seismic Structure Around the Sanford Underground Research Facility, paper presented at 44th Workshop on Geothermal Reservoir Engineering, Stanford University, Stanford, California, February 11-13, 2019.
6. Chai, C., M. Maceira, H. J. Santos-Villalobos, S. V. Venkatakrishnan, M. Schoenball, and EGS Collab Team (2020a), Automatic Seismic Phase Picking Using Deep Learning for the EGS Collab project, paper presented at 45th Workshop on Geothermal Reservoir Engineering, Stanford University, Stanford, California, February 10-12, 2020.
7. Chai, C., M. Maceira, H. J. Santos-Villalobos, S. V. Venkatakrishnan, M. Schoenball, W. Zhu, . . . E. G. S. C. Team (2020b), Using a Deep Neural Network and Transfer Learning to Bridge Scales for Seismic Phase Picking, *Geophysical Research Letters*, *47*(16), e2020GL088651, doi:10.1029/2020GL088651.
8. Chai, C., M. Maceira, and E. C. Team (2022), Machine Learning Enhanced Seismic Monitoring at 100 km and 10 m Scales, paper presented at 47th Workshop on Geothermal Reservoir Engineering, Stanford University, Stanford, CA, February 7-9, 2022.
9. Chakravarty, A., C. Hopp, V. Rodríguez Tribaldos, S. Misra, and T. Kneafsey (2021), Self-supervised Machine Learning from Hydraulic Fracturing Induced Seismicity Signatures: Case Study of the EGS Collab Experiment 1, paper presented at AGU Fall Meeting 2021, New Orleans, LA, 13-17 December 2021.
10. Chakravarty, A., and S. Misra (2022), Unsupervised learning from three-component accelerometer data to monitor the spatiotemporal evolution of meso-scale hydraulic fractures, *International Journal of Rock Mechanics and Mining Sciences*, *151*, 105046, doi:https://doi.org/10.1016/j.ijrmms.2022.105046.

11. Chen, Y., L. Huang, J. Ajo-Franklin, T. J. Kneafsey, and EGS Collab Team (2018a), Toward Real-Time Microearthquake Event Detection and Location in Anisotropic Media Using a Multiscale Approach for EGS Collab Experiments, paper presented at Geothermal Resources Council 2018 Annual Meeting, Geothermal Resources Council Transactions, Reno, NV.
12. Chen, Y., L. Huang, and EGS Collab Team (2018b), Microearthquake Hypocenter-Location and Focal-Mechanism Inversions for the EGS Collab Project: A Synthetic Study, paper presented at 43rd Workshop on Geothermal Reservoir Engineering, Stanford University, Stanford, CA, February 12-14, 2018.
13. Chen, Y., L. Huang, and EGS Collab Team (2019a), Optimal design of 3D borehole seismic arrays for microearthquake monitoring in anisotropic media during stimulations in the EGS collab project, *Geothermics*, *79*, 61-66, doi:https://doi.org/10.1016/j.geothermics.2019.01.009.
14. Chen, Y., L. Huang, M. Schoenball, J. Ajo-Franklin, T. Kneafsey, and EGS Collab Team (2019b), Real-Time Microearthquake Event Detection and Location in Anisotropic Media Using a Multiscale Scanning Approach for EGS Collab Experiments, paper presented at 44th Workshop on Geothermal Reservoir Engineering, Stanford University, Stanford, California, February 11-13, 2019.
15. Chi, B., L. Huang, K. Gao, J. Ajo-Franklin, T. J. Kneafsey, J. Hampton, and EGS Collab Team (2020), Anisotropic Imaging of Created Fractures in EGS Collab Experiments Using CASSM Data, paper presented at 45th Workshop on Geothermal Reservoir Engineering, Stanford University, Stanford, California, February 10-12, 2020.
16. Condon, K., H. Sone, and H. F. Wang (2018), Influence of Foliation Orientation on Rock Strength and Elastic Properties of Poorman Schist from the EGS Collab Experiment 1 Site, H11Q-1693 paper presented at 2018 AGU Fall Meeting, Washington, D.C., December 10-14 2018.
17. Condon, K. J., H. Sone, H. F. Wang, J. Ajo-Franklin, T. Baumgartner, K. Beckers, . . . EGS Collab Team (2020), Low Static Shear Modulus Along Foliation and Its Influence on the Elastic and Strength Anisotropy of Poorman Schist Rocks, Homestake Mine, South Dakota, *Rock Mechanics and Rock Engineering*, doi:10.1007/s00603-020-02182-4.
18. Condon, K. J., H. Sone, H. F. Wang, and EGS Collab Team (2019), Anisotropic Strength and Elastic Properties of Poorman Schist at the EGS Collab Experiment 1 Site, paper presented at 53rd US Rock Mechanics/Geomechanics Symposium, American Rock Mechanics Association, New York, NY, USA, 23–26 June 2019.
19. Cook, P. J., Y. Guglielmi, and F. Soom (2019), Direct Downhole Measurement of a Stimulated Fracture Displacement First Results from the SIMFIP Tool Tests performed during the EGS Collab Project, paper presented at AGU Fall Meeting 2019, AGU.
20. Cook, P. J., Y. Guglielmi, F. Soom, P. F. Dobson, T. J. Kneafsey, A. Singh, . . . A. Tatomir (2020), Probing 3D fracture displacements under injection in deep vertical boreholes–Comparison of fracture hydromechanical response at two hard rock sites with differing stress regimes, paper presented at AGU Fall Meeting 2020, AGU.
21. Crowe, D., Schoenball, M., & Hao, Z. (2019). Support Vector Machine for Near Real-time Identification of Microseismic Events. Lawrence Berkeley National Laboratory EGS Collab Report.

22. Dobson, Patrick, Kneafsey, Timothy J., Blankenship, Doug, White, Mark D., Morris, Joseph P., FU, Pengcheng, Schwering, Paul, Ajo-Franklin, Jonathan, Huang, Lianjie, Knox, Hunter A., Strickland, Christopher, Burghardt, Jeffrey, Johnson, Timothy, Neupane, Ghanashyam, Weers, Jon, Horne, Roland, Singh, Ankush, Roggenthen, William, Ulrich, Craig, Hopp, Chet, Doe, Thomas, Ingraham, Mathew and Mattson, Earl D. (2021) The Power of Collaboration – Team Science To Address Key Questions For Enhanced Geothermal Systems: The EGS Collab Project. Geological Society of America Annual Meeting, Portland, Oregon, Abstracts with Programs, paper 114-5.
23. Dobson, P., T. Kneafsey, J. Morris, A. Singh, M. Zoback, W. Roggenthen, . . . EGS Collab Team (2018), The EGS Collab Hydroshear Experiment at the Sanford Underground Research Facility – Siting Criteria and Evaluation of Candidate Sites, paper presented at Geothermal Resources Council 2018 Annual Meeting, Geothermal Resources Council Transactions, Reno, NV.
24. Dobson, P., T. J. Kneafsey, D. Blankenship, J. Morris, P. Fu, H. Knox, . . . EGS Collab Team (2021), The EGS Collab Project – Fracture Stimulation and Flow Experiments for Coupled Process Model Validation at the Sanford Underground Research Facility (SURF), South Dakota, USA, paper presented at World Geothermal Congress 2020+1 Reykjavik, Iceland, April - October 2021.
25. Dobson, P., T. J. Kneafsey, D. Blankenship, C. Valladao, J. Morris, H. Knox, . . . EGS Collab Team (2017), An Introduction to the EGS Collab Project, paper presented at GRC Transactions, Vol. 41, 2017.
26. Feng, Z., Huang, L., Chi, B., Gao, K., Li, J., Ajo-Franklin, J., Fu, P., Blankenship, D. A., Kneafsey, T. J., & Team, T. E. C. (2023 submitted). Monitoring Spatiotemporal Evolution of Fractures during Hydraulic Stimulations at the First EGS Collab Testbed Using Anisotropic Elastic-Waveform Inversion. Geothermics.
27. Feng, Z., B. Chi, L. Huang, K. Gao, J. Li, J. Ajo-Franklin, . . . T. E. C. Team5 (2021), Temporal-Spatial Evolution of Anisotropic Rock Properties during Hydraulic Fracture Stimulations at the First EGS Collab Testbed, paper presented at 46th Workshop on Geothermal Reservoir Engineering, Stanford University, Stanford, California, February 15-17, 2021.
28. Frash, L. P. (2020), Fracture Caging to Control Earthquake Magnitude from Induced Seismicity: Preventing a Repeat of Pohang, paper presented at 54th U.S. Rock Mechanics/Geomechanics Symposium, American Rock Mechanics Association, 2020/9/18.
29. Frash, L. P. (2022), Optimized Enhanced Geothermal Development Strategies with GeoDT and Fracture Caging, paper presented at 47th Workshop on Geothermal Reservoir Engineering, Stanford University, Stanford, California, February 7-9, 2022.
30. Frash, L. P., K. Arora, Y. Gan, M. Lu, M. Gutierrez, P. Fu, . . . EGS Collab Team (2018a), Laboratory Validation of Fracture Caging for Hydraulic Fracture Control, paper presented at 52nd U.S. Rock Mechanics/Geomechanics Symposium, American Rock Mechanics Association, Seattle, Washington, 2018/8/21.
31. Frash, L. P., J. W. Carey, N. J. Welch, and EGS Collab Team (2019a), EGS Collab Experiment 1: Geomechanical and Hydrological Properties by Triaxial Direct Shear, paper presented at 44th Workshop on Geothermal Reservoir Engineering, Stanford University, Stanford, California, February 11-13, 2019.

32. Frash, L. P., P. Fu, J. Morris, and EGS Collab Team (2018b), Fracture Caging: Can We Control the Extent of a Hydraulic Fracture Stimulated Zone?, paper presented at 43rd Workshop on Geothermal Reservoir Engineering, Stanford University, SGP-TR-213.
33. Frash, L. P., P. Fu, J. Morris, M. Gutierrez, G. Neupane, J. Hampton, . . . T. Kneafsey (2021a), Fracture Caging to Limit Induced Seismicity, *Geophysical Research Letters*, *48*(1), e2020GL090648, doi:https://doi.org/10.1029/2020GL090648.
34. Frash, L. P., J. C. Hampton, M. S. Gutierrez, and EGS Collab Team (2020a), Fracture Caging to Control Induced Seismicity with Inspiration from the EGS Collab Project, paper presented at 45th Workshop on Geothermal Reservoir Engineering, Stanford University, Stanford, California, February 10-12, 2020.
35. Frash, L. P., J. P. Morris, and EGS Collab Team (2019b), Stochastic prediction of multi-well fracture connectivity and application to EGS Collab experiment 2, paper presented at 53rd US Rock Mechanics/Geomechanics Symposium, American Rock Mechanics Association, New York, NY, USA, 23–26 June 2019.
36. Frash, L. P., N. Welch, and J. W. Carey (2020b), Progress Towards a Scaling Relationship Between Shear Fracture Length, Aperture, and Permeability, paper presented at 54th U.S. Rock Mechanics/Geomechanics Symposium.
37. Frash, L. P., N. J. Welch, J. W. Carey, and EGS Collab Team (2019c), Geomechanical evaluation of natural shear fractures in the EGS Collab Experiment 1 testbed, paper presented at 53rd US Rock Mechanics/Geomechanics Symposium, American Rock Mechanics Association, New York, NY, USA.
38. Frash, L. P., N. J. Welch, M. Meng, W. Li, and J. W. Carey (2021b), A Scaling Relationship for Fracture Permeability After Slip, paper presented at 55th U.S. Rock Mechanics/Geomechanics Symposium. Frash, L. P. (2022). GeoDesignTool/GeoDT. https://github.com/GeoDesignTool/GeoDT.
39. Fu, P., M. Schoenball, J. B. Ajo-Franklin, C. Chai, M. Maceira, J. P. Morris, . . . EGS Collab Team (2021a), Close Observation of Hydraulic Fracturing at EGS Collab Experiment 1: Fracture Trajectory, Microseismic Interpretations, and the Role of Natural Fractures, *Journal of Geophysical Research: Solid Earth*, *126*(7), e2020JB020840, doi:https://doi.org/10.1029/2020JB020840.
40. Fu, P., M. Schoenball, J. Morris, J. Ajo-Franklin, H. Knox, T. Kneafsey, . . . EGS Collab Team (2019a), Microseismic Signatures of Hydraulic Fracturing: A Preliminary Interpretation of Intermediate-Scale Data from the EGS Collab Experiment, paper presented at 44th Workshop on Geothermal Reservoir Engineering, Stanford University, Stanford, California, February 11-13, 2019.
41. Fu, P., J. Weers, M. White, H. Knox, P. Schwering, J. Morris, . . . EGS Collab Team (2021b), Efforts and Innovations to Promote Data Sharing and Data Accessibility in the EGS Collab Experiments, paper presented at 2021 Geothermal Rising Conference, GRC Transactions, Vol. 45, 2021.
42. Fu, P., M. White, J. Morris, T. Kneafsey, and EGS Collab Team (2018b), Predicting Hydraulic Fracture Trajectory Under the Influence of a Mine Drift in EGS Collab Experiment I, paper presented at 43rd Workshop on Geothermal Reservoir Engineering, Stanford University, Stanford, California, February 12-14, 2018.
43. Fu, P., H. Wu, X. Ju, and J. Morris (2020), Analyzing Fracture Flow Channel Area in EGS Collab Experiment 1 Testbed, paper presented at 45th Workshop on Geothermal

Reservoir Engineering, Stanford University, Stanford, California, February 10-12, 2020.
44. Fu, P., H. Wu, and J. Morris (2019b), Analysis of hydraulic and thermal characteristics in a fracture network at the EGS Collab experiment through tracer and thermal modeling, paper presented at AGU Fall Meeting.
45. Fu, P., H. Wu, J. P. Morris, P. C. Schwering, C. Ulrich, J. A. Burghardt, . . . EGS Collab Team (2021c), Simulating Hydraulic Fracture Stimulations at the EGS Collab: Model Validation from Experiments 1 and Design-Phase Simulation for Experiment 2, paper presented at 46th Workshop on Geothermal Reservoir Engineering, Stanford University, Stranford, CA, February 15-17, 2021.
46. Gao, K., L. Huang, B. Chi, J. Ajo-Franklin, J. Hampton, and EGS Collab Team (2018), Imaging the Fracture Zone Using Continuous Active Source Seismic Monitoring for the EGS Collab Project: A Synthetic Study, paper presented at 43rd Workshop on Geothermal Reservoir Engineering, Stanford University, Stanford, California, February 12-14, 2018.
47. Gao, K., L. Huang, H. A. Knox, P. C. Schwering, C. R. Hoots, J. Ajo-Franklin, . . . EGS Collab Team (2020), Anisotropic Elastic Properties of the First EGS Collab Testbed Revealed from the Campaign Cross-Borehole Seismic Data, paper presented at 45th Workshop on Geothermal Reservoir Engineering, Stanford University, Stanford, California, February 10-12, 2020.
48. Guglielmi, Y., Cook, P., Soom, F., Dobson, P., Kneafsey, T., Valley, B., Kakurina, M., Niemi, A., Tsang, C.F., Tatomir, A., Juhlin, C., and Basirat, F. (2021) Estimating stress from three-dimensional borehole displacements induced by fluid injection in different types of fractured or faulted rocks. Proceedings, 55th US Rock Mechanics/Geomechanics Symposium, ARMA 21–1999, 9 p.
49. Guglielmi, Y., P. Cook, F. Soom, M. Schoenball, P. Dobson, and T. Kneafsey (2021b), In Situ Continuous Monitoring of Borehole Displacements Induced by Stimulated Hydrofracture Growth, *Geophysical Research Letters*, *48*, e2020GL090782, doi:https://doi.org/10.1029/2020GL090782.
50. Guglielmi, Y., M. McClure, J. Burghardt, J. P. Morris, T. Doe, P. Fu, . . . EGS Collab Team (2022), Estimating Stress from Fracture Injection Tests: Comparing Pressure Transient Interpretations with In-Situ Strain Measurements, paper presented at 47th Workshop on Geothermal Reservoir Engineering, Stanford University, Stanford, California, February 7-9, 2022.
51. Hopp, C., V. Rodríguez Tribaldos, M. Schoenball, Y. Guglielmi, J. B. Ajo-Franklin, A. Chakravarty, and E. Team (2020), The birth of a hydraulic fracture: Evolution of strain, displacement, seismicity, and temperature as measured by a borehole monitoring network during fracture propagation, paper presented at AGU Fall Meeting Abstracts.
52. Huang, H., G. H. Neupane, R. Podgorney, E. Mattson, and EGS Collab Team (2019), Mechanistically Modeling of Hydraulic Fracture Propagation and Interaction with Natural Fractures at EGS-Collab Site, paper presented at 44th Workshop on Geothermal Reservoir Engineering, Stanford University, Stanford, California, February 11-13, 2019.
53. Huang, H., J. Zhou, E. Mattson, and R. Podgorney (2018b), Mechanistically Modeling of Hydraulic Fracture Opening, Closure and Residual Fracture Permeability During

Cyclic Flow Injection Tests, paper presented at Geothermal Resources Council 2018 Annual Meeting Geothermal Resources Council Transactions, Reno, NV.
54. Huang, L., Y. Chen, K. Gao, P. Fu, J. Morris, J. Ajo-Franklin, . . . EGS Collab Team (2017), Numerical Modeling of Seismic and Displacement-Based Monitoring for the EGS Collab Project, paper presented at GRC Transactions, Vol. 41, 2017.
55. Ingraham, M., C. Strickland, V. Vermeul, B. Roberts, J. Burghardt, P. Schwering, . . E. C. Team (2021a), Design and Fabrication of a Remote-Control Hydraulic Fracturing System, paper presented at 2021 Geothermal Rising Conference, GRC Transactions, Vol. 45, 2021.
56. Ingraham, M. D., D. K. King, H. A. Knox, C. E. Strickland, V. R. Vermeul, Y. Guglielmi, EGS Collab Team (2018), Design of a long term hydraulic fracture and flow system, paper presented at 52nd US Rock Mechanics / Geomechanics Symposium, Seattle, Washington, USA, 17–20 June 2018.
57. Ingraham, M. D., H. A. Knox, C. E. Strickland, V. R. Vermeul, J. A. Burghardt, and EGS Collab Team (2019c), Analysis of pressure/flow response data from the EGS Collab Project, paper presented at 53rd US Rock Mechanics/Geomechanics Symposium, American Rock Mechanics Association, New York, NY, USA.
58. Ingraham, M. D., P. C. Schwering, J. Burghardt, C. Ulrich, T. Doe, W. M. Roggenthen, and C. Reimers (2020), Analysis of Hydraulic Fracturing on the 4100 Level at the Sanford Underground Research Facility, paper presented at 54th U.S. Rock Mechanics/Geomechanics Symposium, American Rock Mechanics Association, 2020/9/18.
59. Jafarov, E. E., N. Makedonska, S. Karra, R. Pawar, J. Beisman, G. Neupane, . . . EGS Collab Team (2020), Simulations of the 3D Geothermal Heat Flow in Fractured Media, paper presented at 45th Workshop on Geothermal Reservoir Engineering, Stanford University, Stanford, California, February 10-12, 2020.
60. Jahnke, B., Ruplinger, C., Bate, C.E., Trzeciak, M., Sone, H. and Wang, H.F., 2022. Fracture toughness of schist, amphibolite, and rhyolite from the Sanford Underground Research Facility (SURF), Lead, South Dakota. Scientific Reports, 12(1): 15941.
61. Johnson, T., C. Strickland, H. Knox, J. Thomle, V. Vermeul, C. Ulrich, . . . EGS Collab Team (2019a), EGS Collab Project Electrical Resistivity Tomography Characterization and Monitoring Status, paper presented at 44th Workshop on Geothermal Reservoir Engineering, Stanford University, Stanford, California, February 11-13, 2019.
62. Johnson, T. C., J. Burghardt, C. Strickland, H. Knox, V. Vermeul, M. White, . . . EGS Collab Team (2021), 4D Proxy Imaging of Fracture Dilation and Stress Shadowing Using Electrical Resistivity Tomography During High Pressure Injections Into a Dense Rock Formation, *Journal of Geophysical Research: Solid Earth*, *126*(11), e2021JB022298, doi:https://doi.org/10.1029/2021JB022298.
63. Johnson, T. C., C. E. Strickland, H. A. Knox, J. A. Burghardt, V. R. Vermeul, P. Schwering, . . . T. J. Kneafsey (2019b), Geomechanically-Induced Electrical Resistance Responses During High-Pressure Flow Tests in a Stimulated Fracture Zone, paper presented at AGU Fall Meeting 2019, AGU.
64. Kamali, A., and A. Ghassemi (2018), 3D Analysis of the Proposed "EGS Collab" Circulation Experiments in Sanford Underground Research Facility, SD, paper presented at 52nd US Rock Mechanics/Geomechanics Symposium, American Rock Mechanics Association.

65. Kneafsey, T., D. Blankenship, J. Burghardt, T. Johnson, P. Dobson, P. C. Schwering, . T. E. C. Team (2022a), The EGS Collab –Experiment 2 Stimulations at 1.25 km Depth, paper presented at Geothermal Rising Conference, Geothermal Rising, Reno, NV, August 28-31, 2022.
66. Kneafsey, T., D. Blankenship, P. Dobson, J. Burghardt, M. White, J. P. Morris, . . . EGS Collab Team (2022b), The EGS Collab – Initial Results from Experiment 2: Shear Stimulation at 1.25 km depth, paper presented at 47th Workshop on Geothermal Reservoir Engineering, Stanford University, Stanford, California, February 7-9, 2022.
67. Kneafsey, T., D. Blankenship, P. Dobson, J. Morris, M. White, P. Fu, . . . T. E. C. Team (2021a), The EGS Collab Preparing for Experiment 2, paper presented at AGU Fall Meeting 2021, New Orleans, LA, 13-17 December 2021.
68. Kneafsey, T., D. Blankenship, P. Dobson, M. White, J. Morris, P. Fu, and E. C. Team (2021b), Fracture Stimulation and Chilled-water Circulation Though Deep Crystalline Rock: Characterization, Modeling, Monitoring, and Heat-transfer Assessment, paper presented at 46th Workshop on Geothermal Reservoir Engineering, Stanford University, Stanford, California, Stanford University, Stanford, California, February 15-17, 2021.
69. Kneafsey, T., D. Blankenship, P. Dobson, M. White, J. P. Morris, P. Fu, . . . EGS Collab Team (2021c), The EGS Collab Project: Status and Accomplishments, paper presented at 2021 Geothermal Rising Conference, GRC Transactions, Vol. 45, 2021.
70. Kneafsey, T., D. Blankenship, P. F. Dobson, J. Morris, P. Fu, M. White, . . . M. Schoenball (2019a), The EGS collab project: Stimulating and simulating experiments in crystalline rock in an underground research site, paper presented at GSA Annual Meeting in Phoenix, Arizona, USA - 2019, Phoenix, Arizona, USA, September 22-25, 2019.
71. Kneafsey, T. J. (2021), Addressing enhanced geothermal system challenges, paper presented at Symposium on the Application of Geophysics to Engineering and Environmental Problems 2021, Society of Exploration Geophysicists and Environment and Engineering.
72. Kneafsey, T. J., and D. Blankenship (2017), The EGS Collab Project: Stimulation Investigations for Geothermal Modeling Analysis and Validation, paper presented at 2017 AGU Fall Meeting, AGU.
73. Kneafsey, T. J., D. Blankenship, P. Dobson, J. Morris, P. Fu, H. Knox, . . . EGS Collab Team (2018a), An Overview of the EGS Collab Project – Fracture Stimulation and Flow Experiments for Coupled Process Model Validation at the Sanford Underground Research Facility, paper presented at DESCRAMBLE Drilling in dEep, Super-CRitical AMBient of continentaL Europe Final Conference, Pisa, Italy, 28 March 2018.
74. Kneafsey, T. J., D. Blankenship, P. F. Dobson, H. A. Knox, T. C. Johnson, J. B. Ajo-Franklin, . . . EGS Collab Team (2018c), EGS Collab Project Experiment 1 Overview and Progress, paper presented at Geothermal Resources Council 2018 Annual Meeting, Geothermal Resources Council Transactions, Reno, NV.
75. Kneafsey, T. J., D. Blankenship, P. F. Dobson, H. A. Knox, T. C. Johnson, P. C. Schwering, . . . P. Fu (2018d), Investigations in Stimulating Crystalline Rock: Hypotheses and Uncertainties, paper presented at AGU Fall Meeting 2018.

76. Kneafsey, T. J., D. Blankenship, P. F. Dobson, J. Morris, M. D. White, P. Fu, . . . J. B. Ajo-Franklin (2020a), The EGS Collab Project: Stimulation and Flow at the 10-meter scale, paper presented at AGU Fall Meeting 2020, AGU.
77. Kneafsey, T. J., D. Blankenship, P. F. Dobson, J. Morris, M. D. White, P. Fu, . . . J. B. Ajo-Franklin (2019b), Stimulation and Flow Tests in Deep Crystalline Rock–The EGS Collab Project, paper presented at AGU Fall Meeting 2019, AGU.
78. Kneafsey, T. J., D. Blankenship, P. F. Dobson, J. Morris, M. D. White, H. Knox, . . . L. Huang (2018e), Overview of the EGS Collab Project: Stimulation and Validation, paper presented at AGU Fall Meeting 2018.
79. Kneafsey, T. J., D. Blankenship, P. F. Dobson, J. P. Morris, M. D. White, P. Fu, . . . EGS Collab Team (2020b), The EGS Collab Project: Learnings from Experiment 1, paper presented at 45th Workshop on Geothermal Reservoir Engineering, Stanford University, Stanford, California, February 10-12, 2020.
80. Kneafsey, T. J., D. Blankenship, P. F. Dobson, J. P. Morris, M. D. White, P. Fu, . . . E. C. Team (2020c), The EGS Collab Project: Mesoscale Rock Stimulations ISRM Specialized Conference CouFrac2020, November 11-13, 2020, Seoul, Korea, paper presented at ISRM Specialized Conference CouFrac2020, Seoul, Korea, November 11-13, 2020.
81. Kneafsey, T. J., D. Blankenship, H. A. Knox, T. C. Johnson, J. B. Ajo-Franklin, P. C. Schwering, . . . EGS Collab Team (2019c), EGS Collab Project: Status and Progress, paper presented at 44th Workshop on Geothermal Reservoir Engineering, Stanford University, Stanford, California, February 11-13, 2019.
82. Kneafsey, T. J., D. A. Blankenship, P. F. Dobson, J. Morris, M. D. White, H. A. Knox, E. C. Team (2019d), EGS Collab Project: Accomplishments and Plan, paper presented at GRC Transactions, Geothermal Resources Council.
83. Kneafsey, T. J., P. Dobson, D. Blankenship, J. Morris, H. Knox, P. Schwering, . . . EGS Collab Team (2018f), An Overview of the EGS Collab Project: Field Validation of Coupled Process Modeling of Fracturing and Fluid Flow at the Sanford Underground Research Facility, Lead, SD, paper presented at 43rd Workshop on Geothermal Reservoir Engineering, Stanford University, Stanford, California, February 12-14, 2018.
84. Kneafsey, T. J., P. F. Dobson, J. B. Ajo-Franklin, C. Valladao, D. A. Blankenship, H. A. Knox, . . . EGS Collab Team (2018g), The EGS Collab Project: Stimulation and Simulation, paper presented at 52nd US Rock Mechanics / Geomechanics Symposium, Seattle, Washington, USA, 17–20 June 2018.
85. Kneafsey, T. J., P. F. Dobson, D. Blankenship, P. C. Schwering, J. P. Morris, P. Fu, . . . EGS Collab Team (2021e), Field Experiments and Model Validation: the EGS Collab Project, paper presented at 55th U.S. Rock Mechanics/Geomechanics Symposium.
86. Kneafsey, T. J., P. F. Dobson, C. Ulrich, C. Hopp, V. Rodríguez Tribaldos, Y. Guglielmi, . EGS Collab Team (2022c), The EGS Collab Project – Stimulations at Two Depths, paper presented at 56th US Rock Mechanics/Geomechanics Symposium, Santa Fe, New Mexico, USA, 26-29 June 2022.
87. Kneafsey, T. J., D. P.F., J. B. Ajo-Franklin, Y. Guglielmi, C. A. Valladao, D. A. Blankenship, . . . EGS Collab Team (2019e), EGS Collab Project: Status, Tests, and Data, paper presented at 53rd US Rock Mechanics/Geomechanics Symposium, New York, NY, USA, 23–26 June 2019.

88. Kneafsey, T., Blankenship, D., Burghardt, J., Johnson, T., Dobson, P., Schwering, P. C., Hopp, C., White, M., Morris, J. P., Strickland, C., Vermeul, V., Fu, P., Ingraham, M., Roggenthen, W., Doe, T., Ajo-Franklin, J. B., Huang, L., Tribaldos, V. R., Guglielmi, Y., Knox, H., Cook, P., Soom, F., Ulrich, C., Frash, L., Neupane, G., Pyatina, T., Weers, J., Mattson, E., Robertson, M., & Team, T. E. C. (2023). *The EGS Collab – Discoveries and Lessons from an Underground Experiment Series*. Paper presented at the 48th Workshop on Geothermal Reservoir Engineering, Stanford University, Stanford, California.
89. Knox, H., P. Fu, J. Morris, Y. Guglielmi, V. Vermeul, J. Ajo-Franklin, . . . EGS Collab Team (2017), Fracture and Flow Designs for the Collab/Sigma-V Project, paper presented at GRC Transactions, Vol. 41, 2017.
90. Kutun, K. (2018), Hydraulic Fracture Modeling of an Enhanced Geothermal System (EGS) Experiment, Colorado School of Mines.
91. Kutun, K., J. L. Miskimins, and K. F. Beckers (2018), Hydraulic Fracture Modeling in Support of EGS Collab Treatment Designs, paper presented at 52nd U.S. Rock Mechanics/Geomechanics Symposium, American Rock Mechanics Association, Seattle, Washington, 2018/8/21.
92. Li, D., Huang, L., Zheng, Y., Li, Y., Schoenball, M., Rodríguez-Tribaldos, V., Ajo-Franklin, J., Hopp, C., Schwering, P., Johnson, T., Knox, H., Blankenship, D., Dobson, P., Kneafsey, T., Robertson, M., & Team, T. E. C. (2023 Submitted). Detecting Fractures and Monitoring Hydraulic Fracturing Processes at the first EGS Collab Testbed Using Borehole DAS Ambient Noise. Geothermics.
93. Li, D., L. Huang, B. Chi, J. Ajo-Franklin, V. R. Tribaldos, M. Schoenball, . . . EGS Collab Team (2020), Distributed Acoustic Sensing Monitoring at the First EGS Collab Testbeds, paper presented at 45th Workshop on Geothermal Reservoir Engineering, Stanford University, Stanford, California, February 10-12, 2020.
94. Li, J., L. Huang, Y. Chen, J. Morris, J. Ajo-Franklin, T. Kneafsey, and T. E. C. Team (2021a), Numerical Modeling of Microseismic Monitoring at the Second EGS Collab Testbed, paper presented at 46th Workshop on Geothermal Reservoir Engineering, Stanford University, Stanford, California, February 15-17, 2021.
95. Li, J., Qin, Y., Huang, L., Fu, P., Schoenball, M., Ajo-Franklin, J., Blankenship, D., Kneafsey, T. J., & Team, E. C. (2023 Submitted). Focal Mechanism Inversion of High-Frequency Microseismic Events Recorded in Multiple Boreholes at the First EGS Collab Testbed. Geothermics.
96. Li, Z., D. Elsworth, C. Wang, L. Boyd, Z. Frone, E. Metcalfe, . . . E. G. S. Collab (2021b), Constraining maximum event magnitude during injection-triggered seismicity, *Nature Communications*, *12*(1), 1528, doi:10.1038/s41467-020-20700-4.
97. Linneman, D. (2019), The EGS Collab Hydrofracture Experiment: Seismic Velocity and Elastic Moduli Characterization, Scripps Senior Theses. 1240. https://scholarship.claremont.edu ….
98. Linneman, D., H. Knox, P. Schwering, and C. R. Hoots (2018), The EGS Collab Hydrofracture Experiment at the Sanford Underground Research Facility – Campaign Cross-Borehole Seismic Characterization, H11Q-1689, paper presented at AGU Fall Meeting, Washington, D.C.
99. Linneman, D., P. Sprinkle, H. A. Knox, C. E. Strickland, T. C. Johnson, M. D. Ingraham, M. C. Grubelich (2019), Baseline Characterization for Change Detection

with Joint Inversion of ERT and Campaign Seismic Data, paper presented at AGU Fall Meeting 2019, AGU.

100. Lu, J., and A. Ghassemi (2019), Coupled THMS Modeling of Fractured Reservoir Stimulation with Application to EGS Collab, paper presented at 44rd Workshop on Geothermal Reservoir Engineering, Stanford University, Stanford, California, February 11-13, 2019.
101. Lu, J., and A. Ghassemi (2021), Coupled Thermo–Hydro–Mechanical–Seismic Modeling of EGS Collab Experiment 1, *Energies*, *14*(2), doi:10.3390/en14020446.
102. Makedonska, N., E. Jafarov, T. Doe, P. Schwering, G. Neupane, and EGS Collab Team (2020), Simulation of Injected Flow Pathways in Geothermal Fractured Reservoir Using Discrete Fracture Network Model, paper presented at 45th Workshop on Geothermal Reservoir Engineering, Stanford University, Stanford, California, February 10-12, 2020.
103. Mattson, E., D. Blankenship, H. Johnston, L. Frash, J. Morris, T. Kneafsey, and J. Miskimins (2018a), Potential Experimental Topics for EGS Collab Experiment 3, paper presented at 43rd Workshop on Geothermal Reservoir Engineering, Stanford University, Stanford, California, Feb 12-14, 2018.
104. Mattson, E., G. Neupane, A. Hawkins, J. Burghardt, M. Ingraham, M. Plummer, and EGS Collab Team (2019a), Fracture Tracer Injection Response to Pressure Perturbations at an Injection Well, paper presented at GRC Transactions.
105. Mattson, E., M. White, Y. Zhang, B. Johnston, A. Hawkins, and EGS Collab Team (2018b), Collab Fracture Characterization: Preliminary Results from the Modeling and Flow Testing of Experiment 1, paper presented at Geothermal Resources Council 2018 Annual Meeting, Geothermal Resources Council Transactions, Reno, NV.
106. Mattson, E., Y. Zhang, A. Hawkins, T. Johnson, J. Ajo-Franklin, G. Neupane, and EGS Collab Team (2019b), Preliminary Collab Fracture Characterization Results from Flow and Tracer Testing Efforts paper presented at 44th Workshop on Geothermal Reservoir Engineering, Stanford University, Stanford, California, February 11-13, 2019.
107. Mattson, E. D., G. Neupane, M. D. White, M. D. Ingraham, and T. E.-C. Team (2021), EGS-Collab Experiment 1 Flow and Tracer Tests at the Sanford Underground Research Facility, paper presented at 55th US Rock Mechanics/Geomechanics Symposium, Houston, Texas, USA, 20-23 June 2021.
108. Mattson, E., Plummer, M., Neupane, H., Vermeul, V., Sirota, D., Ingraham, M., Kneafsey, T., & Team, E. C. (2023). *Fluorescein Tracer Testing on the 4100L – A Preliminary Examination of Initial Arrival in Wells and the Drift at the Second EGS Collab Testbed*. Paper presented at the 48th Workshop on Geothermal Reservoir Engineering, Stanford University, Stanford, California.
109. McClure, M. W. (2022), Commentary on Four New DFIT Papers: (a) In-Situ Measurements from EGS Collab; (b) Comparison of Techniques at the Bedretto Project; (c) Statistical Review of 62 DFITs; and (d) An Article Advocating the Tangent Method, edited, arXiv, doi:10.48550/ARXIV.2202.03536.
110. Meng, M., L. P. Frash, J. W. Carey, N. J. Welch, W. Li, and S. K. Peterson (2021a), Triaxial Direct-shear Reveals the True Magnitude of Shear Fracture Roughness Effects on Flow, paper presented at SPE/AAPG/SEG Unconventional Resources Technology Conference.

111. Meng, M., L. P. Frash, W. Li, N. J. Welch, and J. W. Carey (2021b), Measurement of Geomechanical and Hydrological Properties of EGS-Collab Geothermal Rocks, paper presented at 55th US Rock Mechanics/Geomechanics Symposium, Houston, Texas, USA, 20-23 June 2021.
112. Meng, M., L. P. Frash, W. Li, N. J. Welch, J. W. Carey, J. Morris, . . . T. Kneafsey (2022), Hydro-Mechanical Measurements of Sheared Crystalline Rock Fractures With Applications for EGS Collab Experiments 1 and 2, *Journal of Geophysical Research: Solid Earth*, *127*(2), e2021JB023000, doi:https://doi.org/10.1029/2021JB023000.
113. Morris, J. P. (2021), Fat Crayon Toolkit, https://github.com/joepmorris/FatCrayonToolkit.
114. Morris, J. P., P. Dobson, H. Knox, J. Ajo-Franklin, M. D. White, P. Fu, . . . EGS Collab Team (2018a), Experimental Design for Hydrofracturing and Fluid Flow at the DOE Collab Testbed, paper presented at 43rd Workshop on Geothermal Reservoir Engineering, Stanford University, Stanford, California, February 12-14, 2018.
115. Morris, J. P., P. Fu, P. Dobson, J. Ajo-Franklin, T. J. Kneafsey, H. Knox, . . . EGS Collab Team (2018b), Experimental Design for Hydrofracturing and Fluid Flow at the DOE EGS Collab Testbed, paper presented at 52nd US Rock Mechanics / Geomechanics Symposium, Seattle, Washington, USA, 17–20 June 2018.
116. Munguia, E., M. Shapovalov, H. Knox, P. Sprinkle, D. Linneman, J. Ajo-Franklin, . . . D. Blankenship (2021), High Frequency Seismic Interferometric Measurements and Characterization of Stimulation Induced Velocity Changes in the EGS Collab Experiment 1: Evaluation of the Stretching Method, paper presented at AGU Fall Meeting 2021, New Orleans, LA, 13-17 December 2021.
117. Neupane, G., E. D. Mattson, M. A. Plummer, and EGS Collab Team (2020), Results of Multiple Tracer Injections into Fractures in the EGS Collab Testbed-1, paper presented at 45th Workshop on Geothermal Reservoir Engineering, Stanford University, Stanford, California, February 10-12, 2020.
118. Neupane, G., R. K. Podgorney, H. Huang, E. D. Mattson, T. J. Kneafsey, P. F. Dobson, . . . EGS Collab Team (2019c), EGS Collab Earth Modeling: Integrated 3D Model of the Testbed, paper presented at GRC Transactions, Geothermal Resources Council, Palm Springs, CA.
119. Pan, W., L. Huang, K. Gao, J. Ajo-Franklin, T. J. Kneafsey, and EGS Collab Team (2019), Anisotropic Full-Waveform Inversion and Least-Squares Reverse-Time Migration of CASSM Data for Experiment I of the EGS Collab Project paper presented at 44th Workshop on Geothermal Reservoir Engineering, Stanford University, Stanford, California, February 11-13, 2019.
120. Qin, Y., J. Li, L. Huang, Z. Feng, K. Gao, D. Li, . . . D. Blankenship (2021), Moment Tensor Inversion of Microearthquakes in Anisotropic Rocks of the EGS Collab Experiment 1 Testbed, paper presented at AGU Fall Meeting 2021, New Orleans, LA, 13-17 December 2021.
121. Roggenthen, W. M., and T. W. Doe (2018), Natural Fractures and Their Relationship to the EGS Collab Project in the Underground of the Sanford Underground Research Facility (SURF), paper presented at 52nd U.S. Rock Mechanics/Geomechanics Symposium, American Rock Mechanics Association, Seattle, Washington, 2018/8/21.
122. Roggenthen, W. M., Johnson, T. C., Crandall, D. M., Paronish, T. J., & Ulrich, C. (2022). *Composition and Structure of the EGS Collab Test Bed 1 Based Upon*

Electrical Resistivity Tomography, Core Compositions, and Wireline Logging. Paper presented at the 56th U.S. Rock Mechanics/Geomechanics Symposium. https://doi.org/10.56952/ARMA-2022-0421

123. Ruplinger, C., R. O'Connell, H. Sone, M. Trzeciak, and H. Wang (2020), Anisotropic Fracture Toughness of Poorman Schist Rocks from EGS Collab Experiment 1 Site, paper presented at 54th U.S. Rock Mechanics/Geomechanics Symposium, American Rock Mechanics Association, 2020/9/18.
124. Schoenball, M., J. Ajo-Franklin, D. Blankenship, P. Cook, P. Dobson, Y. Guglielmi, . . . EGS Collab Team (2019a), Microseismic monitoring of meso-scale stimulations for the DOE EGS Collab project at the Sanford Underground Research Facility, paper presented at 44th Workshop on Geothermal Reservoir Engineering, Stanford University, Stanford, California, February 11-13, 2019.
125. Schoenball, M., J. B. Ajo-Franklin, D. Blankenship, C. Chai, A. Chakravarty, P. Dobson, . . . EGS Collab Team (2020a), Creation of a Mixed-Mode Fracture Network at Mesoscale Through Hydraulic Fracturing and Shear Stimulation, *Journal of Geophysical Research: Solid Earth*, *125*(12), e2020JB019807, doi:https://doi.org/10.1029/2020JB019807.
126. Schoenball, M., J. B. Ajo-Franklin, T. Wood, M. Robertson, P. Cook, V. Rodríguez Tribaldos, . . . EGS Collab Team (2020b), Lessons learned from passive seismic monitoring of EGS Collab Experiment 1, paper presented at 45th Workshop on Geothermal Reservoir Engineering, Stanford University, Stanford, California, February 10-12, 2020.
127. Schoenball, M., Y. Guglielmi, J. B. Ajo-Franklin, P. J. Cook, P. Dobson, C. Hopp, . . . C. Ulrich (2021), In-situ observation of pre-, co-and post-seismic shear slip at 1.5 km depth, *Earth and Space Science Open Archive* doi:10.1002/essoar.10506700.1.
128. Schoenball, M., Y. Guglielmi, J. B. Ajo-Franklin, P. J. Cook, P. F. Dobson, T. J. Kneafsey, . . . C. Ulrich (2019c), Direct Observation of Co-seismic Deformation at 1.5 km Depth: The EGS Collab Fracture Stimulation Test, paper presented at AGU Fall Meeting 2019, AGU.
129. Schwering, P. C., D. Blankenship, R. K. Podgorney, G. H. Neupane, T. Doe, C. Ulrich, . . . M. M. Smith (2018b), The First EGS Collab Testbed at the Sanford Underground Research Facility-Discrete Fracture Network Characterization, paper presented at AGU Fall Meeting 2018.
130. Schwering, P. C., T. W. Doe, W. M. Roggenthen, G. H. Neupane, H. Johnston, P. F. Dobson, . . . C. Reimers (2020), Deterministic Discrete Fracture Network (DFN) Model for the EGS Collab Project on the 4850 Level of the Sanford Underground Research Facility (SURF), paper presented at 54th U.S. Rock Mechanics/Geomechanics Symposium, American Rock Mechanics Association, 2020/9/18.
131. Schwering, P. C., H. A. Knox, C. R. Hoots, D. Linneman, J. Ajo-Franklin, and EGS Collab Team (2018c), The EGS Collab Hydrofracture Experiment at the Sanford Underground Research Facility – Campaign Cross-Borehole Seismic Characterization, paper presented at Geothermal Resources Council 2018 Annual Meeting Geothermal Resources Council Transactions, Reno, NV, October 14-17, 2018.
132. Schwering, P., Ingraham, M., Vermeul, V., Burghardt, J., Johnson, T., Strickland, C., White, M., Hopp, C., Tribaldos, V. R., Kneafsey, T., Artz, T., Mattson, E., Doe, T., & Team*, E. C. (2023). *Shut-In Testing on the 4100L - Implications on the State of Stress,*

Fractures, and Wellbores in the Second EGS Collab Testbed. Paper presented at the 48th Workshop on Geothermal Reservoir Engineering, Stanford University, Stanford, California.

133. Shapovalov, M., E. Munguia, P. Sprinkle, H. Knox, D. Linneman, J. Ajo-Franklin, . . . T. Kneafsey (2021a), High-Frequency Seismic Interferometry and Monitoring of Stimulation Induced Velocity Changes in the EGS Collab Experiment 1, paper presented at AGU Fall Meeting Abstracts.
134. Singh, A., M. Zoback, P. F. Dobson, T. J. Kneafsey, M. Schoenball, Y. Guglielmi, . . . EGS Collab Team (2019), Slip tendency analysis of fracture networks to determine suitability of candidate testbeds for the EGS Collab hydroshear experiment, paper presented at Geothermal Resources Council Transactions.
135. Singh, A. (2021). *Stress Layering, Fault Slip and Hydraulic Fracture Propagation: Integrating Field Studies, Laboratory Experiments and Numerical Simulations.* (Ph.D. Dissertation). Stanford University. Retrieved from http://purl.stanford.edu/kh437qm0234
136. Smith, M., S. Carroll, and EGS Collab Team (2018), High-Temperature Laboratory Experiments to Support EGS Stimulations: Permeability Response in Fractured Phyllite Samples, paper presented at 43rd Workshop on Geothermal Reservoir Engineering, Stanford University, Stanford, California, February 12-14, 2018.
137. Sollohub, L., T. Johnson, T. Sugama, and T. Pyatina (2022), High Resistivity Well Cement for Underground Wells Suitable for Sealing Monitoring Equipment, paper presented at 47th Workshop on Geothermal Reservoir Engineering, Stanford University, Stanford, California, February 7-9, 2022.
138. Sonnenthal, E. L., P. F. Dobson, T. J. Kneafsey, G. H. Neupane, and T. C. Johnson (2019), Reactive-Transport Modeling of Redox-Driven Reactions and Fracture Sealing During Hydraulic Stimulation Experiments at the Homestake Mine, South Dakota COLLAB Site, paper presented at AGU Fall Meeting Abstracts.
139. Strickland, C., J. Burghardt, H. Knox, P. Fu, P. Schwering, T. Johnson, and T. Kneafsey (2021), Integrated Research & Development for Advancing EGS Commercialization – Tipping the Scales, paper presented at 2021 Geothermal Rising Conference, GRC Transactions, Vol. 45, 2021.
140. Templeton, D., J. Morris, M. Schoenball, T. Wood, M. Robertson, P. Cook, . . . EGS Collab Team (2019), Microseismic Correlation and Cluster Analysis of DOE EGS Collab Data, paper presented at 44th Workshop on Geothermal Reservoir Engineering, Stanford University, Stanford, California, February 11-13, 2019.
141. Templeton, D. C., J. Morris, M. Schoenball, T. Wood, M. Robertson, P. J. Cook, . . . T. J. Kneafsey (2018), What Can Microseismicity at the First EGS Collab Site Tell Us About the Subsurface Fracture Network?, paper presented at AGU Fall Meeting 2018.
142. Ulrich, C., P. F. Dobson, T. J. Kneafsey, W. M. Roggenthen, N. Uzunlar, T. W. Doe, . . EGS Collab Team (2018), The Distribution, Orientation, and Characteristics of Natural Fractures for Experiment 1 of the EGS Collab Project, Sanford Underground Research Facility, paper presented at 52nd U.S. Rock Mechanics/Geomechanics Symposium, American Rock Mechanics Association, Seattle, Washington, 2018/8/21.
143. Ulrich, C., Dobson, P. F., Kneafsey, T. J., Roggenthen, W. M., Uzunlar, N., Doe, T. W., Neupane, G., Artz, T., Dobler, K., Schwering, P., Smith, M., & Burghardt, J. A. (2022). Characterizing Rock Fractures and Physical Properties for Experiment 2 of the

EGS Collab Project, Sanford Underground Research Facility. Paper presented at the 56th U.S. Rock Mechanics/Geomechanics Symposium. https://doi.org/10.56952/ARMA-2022-0341

144. Wang, C., P. Winterfeld, B. Johnston, and Y.-S. Wu (2018), An Embedded 3D Fracture Modeling Approach for Simulating Fracture-Dominated Fluid Flow and Heat Transfer in Geothermal Reservoirs, paper presented at 43rd Workshop on Geothermal Reservoir Engineering, Stanford University, Stanford, California, February 12-14, 2018.
145. Weers, J., Porse, S., Huggins, J., Rossol, M., and Taverna, N (2021). Improving the Accessibility and Usability of Geothermal Information with Data Lakes and Data Pipelines on the Geothermal Data Repository. GRC Transactions, Vol. 45, 2021.
146. Weers, J., Z. Frone, J. Huggins, and A. Vimont (2020), The Data Foundry: Secure Collaboration for the Geothermal Industry, paper presented at 45th Workshop on Geothermal Reservoir Engineering, Stanford University, Stanford, California, February 10-12, 2020.
147. Weers, J., and J. Huggins (2019), Getting Data Out of the Ground: Modern Challenges Facing EGS Collab, the DOE Geothermal Data Repository, and the Geothermal Industry, paper presented at 44th Workshop on Geothermal Reservoir Engineering, Stanford University, Stanford, CA, February 11-13, 2019.
148. Weers, J. D., H. Johnston, and J. V. Huggins (2018), The EGS Data Collaboration Platform: Enabling Scientific Discovery, paper presented at 43rd Workshop on Geothermal Reservoir Engineering, National Renewable Energy Lab.(NREL), Golden, CO (United States), Stanford University, Stanford, California, , February 12-14, 2018.
149. White, M., P. Fu, H. Huang, A. Ghassemi, and EGS Collab Team (2017), The Role of Numerical Simulation in the Design of Stimulation and Circulation Experiments for the EGS Collab Project paper presented at GRC Transactions, Vol. 41, 2017
150. White, M., T. Johnson, T. Kneafsey, D. Blankenship, P. Fu, H. Wu, . . . EGS Collab Team (2019), The Necessity for Iteration in the Application of Numerical Simulation to EGS: Examples from the EGS Collab Test Bed 1, paper presented at 44th Workshop on Geothermal Reservoir Engineering, Stanford University, Stanford, California, February 11-13, 2019.
151. White, M. D., J. A. Burghardt, and EGS Collab Team (2021), Modeling the Dynamic Flow Resistance Across the Fracture Network of EGS Collab Experiment 1, paper presented at 46th Workshop on Geothermal Reservoir Engineering, Stanford University, Stanford, California, February 15-17, 2021.
152. White, M. D., P. Fu, and EGS Collab Team (2020), Application of an Embedded Fracture and Borehole Modeling Approach to the Understanding of EGS Collab Experiment 1, paper presented at 45th Workshop on Geothermal Reservoir Engineering, Stanford University, Stanford, California, February 10-12, 2020.
153. White, M. D., P. Fu, A. Ghassemi, H. Huang, J. Rutqvist, B. Johnston, and EGS Collab Team (2018), Numerical Simulation Applications in the Design of EGS Collab Experiment 1, paper presented at 43rd Workshop on Geothermal Reservoir Engineering, Stanford University, Stanford, California, February 12-14, 2018.
154. Winterfeld, P., B. Johnston, K. Beckers, Y.-S. Wu, and EGS Collab Team (2019), Code Modifications for Modeling Chemical Tracers and Embedded Natural Fractures at EGS Collab, paper presented at 44th Workshop on Geothermal Reservoir Engineering, Stanford University, Stanford, California, February 11-13, 2019.

155. Winterfeld, P. H., and Y.-S. Wu (2020), An Overview of our Coupled Thermal-Hydrological-Mechanical Simulator for Porous and Fractured Media, paper presented at 54th U.S. Rock Mechanics/Geomechanics Symposium.
156. Wu, H., P. Fu, Z. Frone, M. D. White, J. B. Ajo-Franklin, J. P. Morris, . . . D. A. Blankenship (2021a), Modeling heat transport processes in enhanced geothermal systems: A validation study from EGS Collab Experiment 1, *Geothermics*, *97*, 102254, doi:https://doi.org/10.1016/j.geothermics.2021.102254.
157. Wu, H., P. Fu, and J. Morris (2019a), Analysis of hydraulic and thermal characteristics in a fracture network at the EGS Collab experiment through tracer and thermal modeling, paper presented at AGU Fall Meeting 2019, AGU.
158. Wu, H., P. Fu, and J. P. Morris (2020a), Predicting thermal responses at the EGS Collab testbed based on tracer test-inferred flow fields, paper presented at 45th Workshop on Geothermal Reservoir Engineering, Stanford University, Stanford, California, February 10-12, 2020.
159. Wu, H., P. Fu, J. P. Morris, E. D. Mattson, A. J. Hawkins, Y. Zhang, . . . EGS Collab Team (2019b), Characterizing Fracture Flow in EGS Collab Experiment Based on Stochastic Modeling of Tracer Recovery, paper presented at 44th Workshop on Geothermal Reservoir Engineering, Stanford University, Stanford, California, February 11-13, 2019.
160. Wu, H., P. Fu, J. P. Morris, E. D. Mattson, G. Neupane, M. M. Smith, . . . T. Kneafsey (2021b), Characterization of flow and transport in a fracture network at the EGS Collab field experiment through stochastic modeling of tracer recovery, *Journal of Hydrology*, *593*, 125888, doi:https://doi.org/10.1016/j.jhydrol.2020.125888.
161. Wu, H., P. Fu, J. P. Morris, R. R. Settgast, F. J. Ryerson, and EGS Collab Team (2019c), A Numerical Scheme to Reduce Numerical Diffusion for Advection-Dispersion Modeling: Validation and Application, paper presented at 44th Workshop on Geothermal Reservoir Engineering, Stanford University, Stanford, California, February 11-13, 2019.
162. Wu, H., P. Fu, J. P. Morris, R. R. Settgast, F. J. Ryerson, E. D. Mattson, . . . Y. Zhang (2019d), Stochastic modeling of a conservative tracer test for the characterization of fracture flow patterns in EGS Collab Experiment 1, paper presented at 53rd US Rock Mechanics/Geomechanics Symposium, American Rock Mechanics Association, New York, NY, USA, 23–26 June 2019.
163. Wu, H., P. Fu, X. Yang, J. P. Morris, and EGS Collab Team (2018), Imaging hydraulic fracture extents and aperture using electrical resistivity tomography, paper presented at 43rd Workshop on Geothermal Reservoir Engineering, Stanford University, Stanford, California, February 12-14, 2018.
164. Wu, H., P. Fu, X. Yang, J. P. Morris, T. C. Johnson, R. R. Settgast, and F. J. Ryerson (2019e), Accurate imaging of hydraulic fractures using templated electrical resistivity tomography, *Geothermics*, *81*, 74-87, doi:https://doi.org/10.1016/j.geothermics.2019.04.004.
165. Wu, H., P. Fu, J. Zhang, and J. P. Morris (2020b), Interpretation of Tracer Data Using a Markov Chain Monte Carlo Approach for the Characterization of the EGS Collab Testbed, paper presented at 54th U.S. Rock Mechanics/Geomechanics Symposium, American Rock Mechanics Association, 2020/9/18.

166. Wu, H., J. Zhang, P. Fu, J. P. Morris, and E. C. Team (2021c), Inferring fracture aperture distribution at the EGS Collab Experiment 1 testbed through a deep learning accelerated Bayesian approach, paper presented at 46th Workshop on Geothermal Reservoir Engineering, Stanford University, Stanford, California, February 15-17, 2021.
167. Wu, Y.-S., X. Yu, S. Wang, C. Wang, P. Winterfeld, and EGS Collab Team (2020c), Modeling Thermal-Hydrologic-Mechanical Processes for EGS Collab Thermal Circulation Tests using Embedded Discrete Fracture Model, paper presented at 45th Workshop on Geothermal Reservoir Engineering, Stanford University, Stanford, California, February 10-12, 2020.
168. Wu, Y. S., X. Yu, S. Wang, and P. H. Winterfeld (2019f), Modeling Thermal-Hydraulic-Mechanical Processes in Enhanced or Engineered Geothermal Systems, paper presented at ARMA-CUPB Geothermal International Conference.
169. Ye, Z., A. Ghassemi, and T. Kneafsey (2020a), Deformation, Failure and Permeability Evolution of Sealed Fractures in EGS Collab Poorman Schist, paper presented at 45th Workshop on Geothermal Reservoir Engineering, Stanford University, Stanford, California, February 10-12, 2020.
170. Ye, Z., A. Ghassemi, and T. Kneafsey (2020b), Deformation, Failure and Permeability Evolution of Sealed Fractures/Foliations in EGS Collab Poorman Schist, paper presented at 54th U.S. Rock Mechanics/Geomechanics Symposium, American Rock Mechanics Association, 2020/9/18.
171. Ye, Z., A. Vachaparampil, X. Zhou, A. Ghassemi, and T. Kneafsey (2019), Failure Behavior of the Poorman Schist and Its Fractures from EGS Collab Stimulation Site, paper presented at 44th Workshop on Geothermal Reservoir Engineering, Stanford University, Stanford, California, February 11-13, 2019.
172. Yildirim, E. C., K. Im, D. Elsworth, and EGS Collab Team (2018), Co-Evolution of Fracture Permeability and Friction in Rocks From the EGS Collab Experiment 1 Site, paper presented at 52nd U.S. Rock Mechanics/Geomechanics Symposium, American Rock Mechanics Association, Seattle, Washington, 2018/8/21.
173. Zhang, Y., A. E. Dekas, A. J. Hawkins, A. E. Parada, O. Gorbatenko, K. Li, and R. N. Horne (2020), Microbial Community Composition in Deep-Subsurface Reservoir Fluids Reveals Natural Interwell Connectivity, *Water Resources Research*, *56*(2), e2019WR025916, doi:https://doi.org/10.1029/2019WR025916.
174. Zhang, Y., C. Doughty, L. Pan, T. Kneafsey, and EGS Collab Team (2018a), What Could We See at the Production Well Before the Thermal Breakthrough?, paper presented at 43rd Workshop on Geothermal Reservoir Engineering, Stanford University, Stanford, California, February 12-14, 2018.
175. Zhang, Y., Q. Zhou, S. Finsterle, T. Kneafsey, R. Jayne, and EGS Collab Team (2018c), Thermal breakthrough predictions based on multiple flow paths characterized by tracer tests, paper presented at TOUGH Symposium, Lawrence Berkeley National Laboratory. Berkeley, California, October 2018.
176. Zhou, J., H. Huang, E. Mattson, R. Podgorney, and EGS Collab Team (2018a), Three-Dimensional Quasi-Static Discrete Element Modeling of Hydraulic Fracture Propagation in Crystalline Rock Under Thermal-Mechanical Stress Gradients, paper presented at 2nd International Discrete Fracture Network Engineering Conference, American Rock Mechanics Association, Seattle, Washington, USA, 2018/11/5/.

177. Zhou, Q., C. M. Oldenburg, T. J. Kneafsey, and EGS Collab Team (2018b), Modeling Transport of Multiple Tracers in Hydraulic Fractures at the EGS Collab Test Site, paper presented at 43rd Workshop on Geothermal Reservoir Engineering, Stanford University, Stanford, California, February 12-14, 2018.
178. Zhou, Q., C. M. Oldenburg, J. Rutqvist, T. J. Kneafsey, and EGS Collab Team (2018c), Analytical and Numerical Modeling of Heat Transport in Fractured Reservoirs, paper presented at 43rd Workshop on Geothermal Reservoir Engineering, Stanford University, Stanford, California, February 12-14, 2018.

EGS COLLAB GDR DATA SUBMISSIONS
https://gdr.openei.org/egs_collab#browseData

Experiment #1:

EGS Collab Experiment 1: Time-series geochemistry data of the long-term circulation test
This submission presents the weekly geochemistry data of the long-term flow test performed within EGS Collab Experiment 1 from early 2019 to early 2020. The fluids from each producing borehole/interval (PI, PB, PDT and PST) along with the injectate were sampled roughly weekly from April 2019 to January 2020 for geochemistry analysis.

Stanford University. (2022). EGS Collab Experiment 1: Time-series geochemistry data of the long-term circulation test [data set].
Retrieved from https://dx.doi.org/10.15121/1897034

EGS Collab Experiment 1: Continuous Active-Source Seismic Monitoring (CASSM) Data
The U.S. Department of Energy's Enhanced Geothermal System (EGS) Collab project aims to improve our understanding of hydraulic stimulations in crystalline rock for enhanced geothermal energy production through execution of intensely monitored meso-scale experiments. The first experiment was performed at the 4850 ft level of the Sanford Underground Research Facility (SURF), approximately 1.5 km below the surface at Lead, South Dakota.

The data reported here were collected by the continuous active-source seismic monitoring (CASSM) system (Ajo-Franklin et al., 2011). This system was permanently installed in the testbed and consisted of 17 piezoelectric sources that were recorded by 2-12 channel hydrophone arrays, 18 3-C accelerometers, and 4 3-C geophones at a Nyquist frequency of 24kHz. The source array was activated in a repeated sequence of shots (each source fired 16 times and stacked into resultant waveforms) for the duration of the experiment (April 25, 2018 - March 7, 2019) with few exceptions. Please see the attached documents describing the source / receiver geometry.

Lawrence Berkeley National Laboratory. (2018). EGS Collab Experiment 1: Continuous Active-Source Seismic Monitoring (CASSM) Data [data set]. Retrieved from https://dx.doi.org/10.15121/1890464.

EGS Collab Circulation Testing Processed data
This submission includes processed and reduced data for circulation testing that was conducted at the 164' fracture on the 4850 ft level of the Sanford Underground Research Facility. The circulation tests were done to test the flow through the 164' fracture in the EGS Collab Experiment 1 testbed on the 4850 ft level of the Sanford Underground Research Facility in order to validate computer models concerned with flow processes and heat exchange processes in EGS. This data

was processed from raw data that is available in the GDR submission linked below: "EGS Collab Circulation Testing Raw Data and Documentation." Python scripts used to process and reduce the data are included. The scripts also serve as "documentation" as well as examples for data processing.

Lawrence Livermore National Laboratory. (2021). EGS Collab Circulation Testing Processed data [data set]. Retrieved from https://dx.doi.org/10.15121/1780911.

EGS-Collab Experiment 1: Time-lapse ERT Data and E4D Inversion Files for 10-24-2018 through 11-07-2018 Flow Test

This data submission includes the raw time-lapse ERT (electrical resistivity tomography) monitoring data, flow system data, operator logs, E4D (https://e4d.pnnl.gov) inversion files, and metadata necessary to reproduce the 4D ERT inversion for the Oct. 24 through Nov. 7 2018 post-stimulation flow test in testbed 1. The tests were done at the Sanford Underground Research Facility at Homestake Mine in South Dakota.

Pacific Northwest National Laboratory. (2021). EGS-Collab Experiment 1: Time-lapse ERT Data and E4D Inversion Files for 10-24-2018 through 11-07-2018 Flow Test [data set]. Retrieved from https://dx.doi.org/10.15121/1811498.

EGS Collab Experiment 1: Core Logs

Core logs from the EGS Collab project Experiment 1 for the stimulation (Injection) well (E1-I), the Production well (E1-P), and monitoring wells (E1-OT, E1-OB, E1-PST, E1-PSB, E1-PDT, and E1-PDB) on the 4850 Level of SURF (the Sanford Underground Research Facility), single PDF file, 5-ft run intervals. In the monitoring well IDs, "O" indicates that the well is orthogonal to the anticipated fracture plane, "P" indicates that the well is parallel to the anticipated fracture plane, "S" indicates a shallow well, "D" indicates a deep well, "T" refers to top, and "B" refers to bottom.

Logs include: experiment number; borehole ID; depth interval; run number; final packed core box number; scribe line (yes/no; red-on-right convention); logging dates; logger initials; as well as sketches of core foliation, folding, and fracturing with additional details and notes on other features of interest.

Lawrence Berkeley National Laboratory. (2019). EGS Collab Experiment 1: Core Logs [data set]. Retrieved from https://dx.doi.org/10.15121/1504480.

EGS Collab Experiment 1: DNA tracer data on transport through porous media

This submission contains DNA tracer data that supports the analysis and conclusions of the publication, "DNA tracer transport through porous media -The effect of DNA length and adsorption." https://doi.org/10.1029/2020WR028382. This experiment used DNA as an artificial

reservoir tracer. Groundwater tracing is an effective way to identify fluid flow pathways and estimate hydrogeologic properties, which are important premises for building reliable hydrological models for transport predictions or contamination mitigations. The objective of this study was to understand the effect of DNA length (i.e., number of base pairs for dsDNA) and adsorption on DNA transport.

Stanford University. (2020). EGS Collab Experiment 1: DNA tracer data on transport through porous media [data set]. Retrieved from https://dx.doi.org/10.15121/1806573.

EGS Collab Experiment 1: In-situ observation of pre-, co- and post-seismic shear slip preceding hydraulic fracturing

Understanding the initiation and arrest of earthquakes is one of the long-standing challenges of seismology. Here we report on direct observations of borehole displacement by a meter-sized shear rupture induced by pressurization of metamorphic rock at 1.5 km depth. We observed the acceleration of sliding, followed by fast co-seismic slip and a transient afterslip phase. Total displacements were about 7, 5.5 and 9.5 micrometers, respectively for the observed pre-slip, co-seismic slip and afterslip. The observed pre-slip lasted about 0.4 seconds. Co-seismic slip was recorded by the 1 kHz displacement recording and a 12-component array of 3-C accelerometers sampled at 100 kHz. The observed afterslip is consistent with analytical models of arrest in a velocity-strengthening region and subsequent stress relaxation. The observed slip vector agrees with the activation of a bedding plane within the phyllite, which is corroborated by relocated seismic events that were observed during the later stages of the injection experiment. This submission includes the pressure and deformation data recorded by the SIMFIP probe during the first injection at the 164 ft (50 m) notch of borehole E1-I. The injection was performed on on 05/22/2018 as part of Experiment 1 of the EGS Collab project.

Lawrence Berkeley National Laboratory. (2018). EGS Collab Experiment 1: In-situ observation of pre-, co- and post-seismic shear slip preceding hydraulic fracturing [data set]. Retrieved from https://dx.doi.org/10.15121/1768008.

EGS Collab Circulation Testing

These data and test descriptions comprise a chilled circulation test conducted at the 164' fracture in the EGS Collab Experiment 1 testbed on the 4850 ft level of the Sanford Underground Research Facility. Descriptions of the meta data, design drawings for the flow testing system, and evaluation of the thermistor data are provided here. The test ran from April 2019 through early March of 2020, when testing was concluded at the experiment 1 site. These data are complementary to the stimulation data provided in another submission which is linked below (i.e. stimulation at the 164' notch).

Lawrence Berkeley National Laboratory. (2019). EGS Collab Circulation Testing [data set]. Retrieved from https://dx.doi.org/10.15121/1814005.

EGS Collab - 4850L Downhole Camera Surveys During Injection

This package includes data and footage from two rounds of downhole camera surveys performed at the Sanford Underground Research Facility (SURF) on the 4850 level. The exercise was performed once on 25 May 2018 and once on 21 December 2018. On May 25th, the first round was done during fluid injection at the 164-ft stimulation zone in the injection well (E1-I). On December 21st, the second round was carried out during fluid injection at the 142-ft stimulation zone. Prior to the injections, downhole instrumentation was removed from the production well (E1-P) to allow room for the downhole camera system. The water within E1-P was then lifted out by the application of air pressure and the downhole camera system was conveyed into the production well. Finally, the water was injected into E1-I and the camera was used to scan for jetting points, or fluid entry, in E1-P. There is a survey description in this package that further describes the procedure of the survey and the overall results. Additionally, there is a detailed analysis of the surveys in the form of a PowerPoint, which includes animations/visualizations from the camera footage, presents interpretations in detail, and provides some general conclusions. Three animations, along with the two video segments that show the jetting into E1-P, are also provided. The video footage was collected using a GeoVISION Dual-Scan Micro Video Camera, the specs of which are also included in this package as a resource.

Sandia National Laboratories. (2018). EGS Collab - 4850L Downhole Camera Surveys During Injection [data set]. Retrieved from https://dx.doi.org/10.15121/1651099.

EGS Collab Testbed 1- Common Discrete Fracture Network

This package includes data and models that support hydraulic fracture stimulation and fluid circulation experiments in the Sanford Underground Research Facility (SURF). A paper by Schwering et al. (2020) describes the deterministic basis for developing a "common" discrete fracture network (CDFN) model of significant natural fractures in EGS Collab Testbed 1 on the 4850-Level of SURF. The ReadMe for this model shows drift, wells, scanlines, fracture data, interpreted fractures, and geophysical visualizations. There is also a summary of the data that was used in this experiment and includes results from reviewing core, televiewer (TV) logs, core-TV depth/feature registration, and from mapping weeps in the 4850-Level drift. The CDFN is intended to be a baseline model of the pre-stimulated testbed (though some observations from stimulation helped inform the model).

Sandia National Laboratories. (2019). EGS Collab Testbed 1- Common Discrete Fracture Network [data set]. Retrieved from https://dx.doi.org/10.15121/1632116.

EGS Collab Experiment 1: 3D Seismic Velocity Model and Updated Microseismic Catalog Using Transfer-Learning Aided Double-Difference Tomography

This package contains a 3D Seismic velocity model and an updated microseismic catalog associated with a proceedings paper (Chai et al., 2020) published in the 45th Workshop on Geothermal Reservoir Engineering. The 3D_seismic_velocity_model text file contains x (m),

y(m), z(m), P-wave velocity (km/s), P-wave velocity quality indicator (1 for well-constrained; 0 for poorly constrained), S-wave velocity (km/s), and S-wave velocity quality indicator (1 for well-constrained; 0 for poorly constrained). The Updated_MEQ_catalog text file contains event origin time, x(m), y(m), z(m), error in x (m), error in y (m), error in z (m), and RMS misfit (millisecond). The 3D_seismic_P-wave_velocity_model animation file shows slices of the 3D P-wave velocity model. The 3D_seismic_S-wave_velocity_model animation file shows slices of the 3D S-wave velocity model. The Interactive_MEQ_locations API file is an interactive visualization of the updated microseismic event locations. The visualization allows users to view the event locations by dragging, rotating, and zooming in.

Oak Ridge National Laboratory. (2020). EGS Collab Experiment 1: 3D Seismic Velocity Model and Updated Microseismic Catalog Using Transfer-Learning Aided Double-Difference Tomography [data set]. Retrieved from https://dx.doi.org/10.15121/1632061.

EGS Collab Modeling and Simulation Working Group Teleconference Series (1-98)

This submission contains the presentation slides and recordings from the first 98 EGS Collab Modeling and Simulation Working Group teleconferences. These teleconferences served three objectives for the project: 1) share simulation results, 2) communicate field activities and results to the simulation teams, and 3) hold open scientific discussions on EGS topics.

Pacific Northwest National Laboratory. (2020). EGS Collab Modeling and Simulation Working Group Teleconference Series (1-98) [data set].
Retrieved from https://dx.doi.org/10.15121/1642465.

EGS Collab Testbed 1 Earth Model Input Files

The EGS Collab is conducting experiments in hydraulic fracturing at a depth of 1.5 km in the Sanford Underground Research Facility (SURF) on the 4850 Level. A total of eight ~60m-long subhorizontal boreholes were drilled at that depth on the western rib of the West Access Drift. Six of these holes are used for geophysical monitoring, one is used for hydraulic fracturing and the remaining hole was designed as a production borehole. In addition to these eight boreholes, 4 5-m Jack leg boreholes were drilled for housing geophones. This submission package includes various data type that were assembled to create Earth Models of the testbed. Note: The coordinate system used is local Homestake Mine Coordinate (HMC) system from an old gold mine that was in operation for over 100 years.

Idaho National Laboratory. (2019). EGS Collab Testbed 1 Earth Model Input Files [data set].
Retrieved from https://dx.doi.org/10.15121/1593286.

EGS Collab Testbed 1: Second Set Tracer Test Results

The EGS Collab project is developing ~10-20 m-scale field sites where fracture stimulation and flow models can be validated against controlled, small-scale, in-situ experiments. The first multi-well experimental site was established at the 4850 level in the Homestake Mine in Lead, South

Dakota, where hydraulic fractures were created at an injection well drilled sub-horizontal from the drift. This file contains the second set of tracer data (also include the data uploaded previously, https://gdr.openei.org/submissions/1128) for the EGS Collab testbed. The tracer tests were conducted during October 2018 - November 2019. Injected tracers include DNA, C-dots (fluorescein nano particles), fluorescein, rhodamine-b, sodium chloride, lithium bromide and cesium iodine. The tracers have been detected in three flowing wells located about 7.5 to 9 meters away from the injection interval. The tracer breakthrough curves from these locations have been adjusted to account for the residence time in the injection and production tubing. The details about the tracer test can be found in Background and Methods of Tracer Tests (Mattson et al. (2019,a,b)) (also included in this package).

Idaho National Laboratory. (2019). EGS Collab Testbed 1: Second Set Tracer Test Results [data set]. Retrieved from https://dx.doi.org/10.15121/1593283.

EGS Collab/SIGMA-V Testbed-1 well locations and orientations.

The EGS Collab is conducting experiments in hydraulic fracturing at a depth of 1.5 km in the Sanford Underground Research Facility (SURF) on the 4850 Level. A total of eight ~60m-long subhorizontal boreholes were drilled at that depth on the western rib of the West Access Drift. Six of these holes are used for geophysical monitoring, one is used for hydraulic fracturing and the remaining hole was designed as a production borehole. In addition to these eight boreholes, 4 5-m Jack leg boreholes were drilled for housing geophones. This submission package includes well head locations, total lengths of boreholes, their orientations (gyro data). The reported boreholes orientation data were primarily obtained with REFLEX GYRO (TM) survey right after the completion of each hole. Gyro based orientations were later verified and refined with the results of magnetic orientation survey. Well head locations were ascertained by Laser/Lider survey of the drift around the Testbed.

Idaho National Laboratory. (2018). EGS Collab/SIGMA-V Testbed-1 well locations and orientations. [data set]. Retrieved from https://dx.doi.org/10.15121/1576950.

EGS Collab Experiment 1: Microseismic Monitoring

The U.S. Department of Energy's Enhanced Geothermal System (EGS) Collab project aims to improve our understanding of hydraulic stimulations in crystalline rock for enhanced geothermal energy production through execution of intensely monitored meso-scale experiments. The first experiment is being performed at the 4850 ft level of the Sanford Underground Research Facility (SURF), approximately 1.5 km below the surface at Lead, South Dakota.

Here we report on microseismic monitoring of repeated stimulation experiments and subsequent flow tests between two boreholes in the Poorman Formation. Stimulations were performed at several locations in the designated injection borehole at flow rates from 0.1 to 5 L/min over temporal durations from minutes to hours. Microseismic monitoring was performed using a dense

3D sensor array including two cemented hydrophone strings with 12 sensors at 1.75 m spacing accompanied by 18 3-C accelerometers, deployed in 6 monitoring boreholes, completely surrounding the stimulation region. Continuous records were obtained over a two-month period using a novel dual recording system consisting of a conventional 96 channel exploration seismograph and a high-performance 64 channel digitizer sampling sensors at 4 and 100 kHz respectively.

Using a standard STA/LTA triggering algorithm, we detected thousands of microseismic events with recorded energy in a frequency range generally above 3 kHz and up to 40 kHz. The locations of these events are consistent with creation of a hydraulic fracture and additional reactivation of pre-existing structures. Using manual pick refinement and double-difference relocation we are able to track the fracture growth to high precision. We estimate the times and locations of the fracture intersecting a monitoring and the production borehole using microseismic events. They are in excellent agreement with independent measurements using distributed temperature sensing, in-situ strain observations and measurements of conductivity changes.

This submission includes a microearthquake catalog, raw event files, a subset of the continuous microseismic monitoring data collected during stimulations and flow test activity on 05/22/2018, 05/23/2018, 05/24/2018, 05/25/2018, 06/25/2018, 07/19/2018, 07/20/2018, 12/7/2018, 12/20/2018, and 12/21/2018 (in binary format), and a binary file interpreter to read the continuous microseismic monitoring data. A Stanford Geothermal Workshop paper is also included to describe microseismic monitoring activities at SURF during these periods.

Lawrence Berkeley National Laboratory. (2019). EGS Collab Experiment 1: Microseismic Monitoring [data set]. Retrieved from https://dx.doi.org/10.15121/1557417.

EGS Collab Experiment 1: TOUGH2-CSM Simulation of Embedded Natural Fractures and Chemical Tracer Transport and Sorption

The EGS Collab SIGMA-V project is a multi-lab and university collaborative research project that is being undertaken at the Sanford Underground Research Facility (SURF) in South Dakota. The project consists of studying stimulation, fluid-flow, and heat transfer processes at a scale of 10-20 m, which is readily amenable to detailed characterization and monitoring. One objective of the project is to establish circulation from injector to producer by hydraulically fracturing the injector.

Data generated during these experiments is to be compared with predictions from coupled thermal, hydrological, mechanical, and chemical simulators. One such simulator, TOUGH2-CSM, has been enhanced in order to simulate EGS Collab SIGMA-V project experiments. These modifications include adding tracers, the capability to model tracer sorption, and an embedded fracture formulation.

A set of example problems validate our conservative tracer transport and sorption formulations. We then simulated tracer transport and thermal breakthrough for the first EGS Collab SIGMA-V experiment.

This dataset includes the TOUGH2-CSM input and output files associated with the thermal and tracer simulations.

National Renewable Energy Laboratory. (2019). EGS Collab Experiment 1: TOUGH2-CSM Simulation of Embedded Natural Fractures and Chemical Tracer Transport and Sorption [data set]. Retrieved from https://dx.doi.org/10.15121/1525476.

EGS Collab Testbed 1: Tracer data tests

This file contains the first set of tracer data for the EGS Collab testbed. The first set of tracer tests were conducted during October-November, 2018. We have included tracer data for C-dots, chloride, fluorescein, and rhodamine-B. The details about the tracer test can be found in Background and Methods of Tracer Tests (Mattson et al. (2019)) (also included in this package).

Idaho National Laboratory. (2019). EGS Collab Testbed 1: Tracer data tests [data set]. Retrieved from https://dx.doi.org/10.15121/1512084.

EGS Collab Testbed 1: Temperature profile

This submission includes an input file, plot file, Fortran conversion file, and 3D data file from the simulation of the temperature profile within the Test Bed #1 of the EGS Collab project. The simulation was executed with PNNL's STOMP-GT simulator, which reads the input file, and produces the STOMP-GT Simulated 2D Temperature Distribution Data (plot.001302 file). The Fortran conversion file, converts the STOMP-GT Simulated 2D Temperature Distribution Data (plot.001302) 2D results in local coordinates to 3D results in Homestake coordinates.

Pacific Northwest National Laboratory. (2019). EGS Collab Testbed 1: Temperature profile [data set]. Retrieved from https://dx.doi.org/10.15121/1512083.

EGS Collab Testbed 1: Baseline Cross-well Seismic

As part of the geophysical characterization suite for the first EGS Collab testbed, here are the baseline cross-well seismic data and resultant models. The campaign seismic data have been organized, concatenated with geometry and compressional (P-) & and shear (S-) wave picks, and submitted as SGY files. P-wave data were collected and analyzed in both 2D and 3D, while S-wave data were collected and analyzed in 2D only. Inversion models are provided as point volumes; the volumes have been culled to include only the points within source/receiver array coverage. The full models space volumes are also included, if relevant. An AGU 2018 poster by Linneman et al. is included that provides visualizations/descriptions of the cross-well seismic characterization method, elastic moduli calculations, and images of model inversion results.

Sandia National Laboratories. (2018). EGS Collab Testbed 1: Baseline Cross-well Seismic [data set]. Retrieved from https://dx.doi.org/10.15121/1497682.

EGS Collab: 3D Geophysical Model Around the Sanford Underground Research Facility

This package contains data associated with a proceedings paper (linked below) submitted to the 44th Workshop on Geothermal Reservoir Engineering. The Geophysical Model text file contains density, P- and S-wave seismic speeds on a 3D grid. The file has six columns and provides latitude (degree), longitude (degree), depth (km), P-wave speed (km/s), S-wave speed (km/s), and density (g/cm^3) at each grid point. The Interactive Geophysical Model API file is an interactive visualization of the 3D geophysical model. The visualization allows users to view depth slices and vertical profiles of the model side by side. The depth of the slices and the location of the profile can be changed.

Lawrence Berkeley National Laboratory. (2019). EGS Collab: 3D Geophysical Model Around the Sanford Underground Research Facility [data set]. Retrieved from https://dx.doi.org/10.15121/1494316.

EGS Collab Experiment 1: SIMFIP Notch-164 GRL Paper

Characterizing the stimulation mode of a fracture is critical to assess the hydraulic efficiency and the seismic risk related to deep fluid manipulations. We have monitored the three-dimensional displacements of a fluid-driven fracture during water injections in a borehole at ~1.5 km depth in the crystalline rock of the Sanford Underground Research Facility (USA). The fracture initiates at 61% of the minimum horizontal stress by micro-shearing of the borehole on a foliation plane. As the fluid pressure increases further, borehole axial and radial displacements increase with injection time highlighting the opening and sliding of a new hydrofracture growing ~10 m away from the borehole, in accordance with the ambient normal stress regime and in alignment with the microseismicity. Our study reveals how fluid-driven fracture stimulation can be facilitated by a mixed-mode process controlled by the complex hydromechanical evolution of the growing fracture.

The data presented in this submission refer to the SIMFIP measurements and analyses of the stimulation tests conducted on the 164 ft (50 m) notch of the Sanford Underground Research Facility (SURF), during the EGS-Collab test 1. In addition to the datafiles, there is the draft of a manuscript submitted to Geophysical Research Letters (GRL).

Lawrence Berkeley National Laboratory. (2020). EGS Collab Experiment 1: SIMFIP Notch-164 GRL Paper [data set]. Retrieved from https://dx.doi.org/10.15121/1737366.

EGS Collab Experiment 1: Accelerometer orientations

Document describing the methodology used to determine the accelerometers' three-component orientations at the first EGS Collab testbed using Continuous Active-Source Seismic Monitoring (CASSM) data and hodogram analysis.

Lawrence Berkeley National Laboratory. (2020). EGS Collab Experiment 1: Accelerometer orientations [data set]. Retrieved from https://gdr.openei.org/submissions/1230.

EGS Collab Experiment 1 Stimulation Data

Stimulation data from Experiment 1 of EGS Collab, which occurred on the 4850 ft level of the Sanford Underground Research Facility (SURF). A detailed description of the stimulation data is provided in the StimulationDataNotes.docx and is also available on the EGS Collab Wiki. A Meta Data Cheat Sheet, which describes all of the channels in the Raw CSV files, is available as well. Note that this cheat sheet is a comprehensive meta data descriptor and channels were added as the experiment evolved. This means that some columns may not be populated in early data. Additionally, we have included the chat logs from these experiments. The experiments were broadcast over teleconferencing software and real-time data displays were available to remote observers. The logs contain important observations from those personnel performing the experiment and the remote contributors. Finally, we have included summary and individual plots of all of the data for the user to compare to.

Pacific Northwest National Laboratory. (2020). EGS Collab Experiment 1 Stimulation Data [data set]. Retrieved from https://dx.doi.org/10.15121/1651116.

EGS Collab Experiment 1: 3D Seismic Velocity Model and Updated Microseismic Catalog from Double-Difference Seismic Tomography

This package contains a 3D Seismic velocity model and an updated microseismic catalog obtained for a double-difference seismic tomography study.

The 3D_seismic_velocity_model text file contains x (m), y(m), z(m), P-wave velocity (km/s), P-wave velocity quality indicator (1 for well-constrained; 0 for poorly constrained), S-wave velocity (km/s), and S-wave velocity quality indicator (1 for well-constrained; 0 for poorly constrained).

The Updated_MEQ_catalog text file contains event origin time, x(m), y(m), z(m), error in x (m), error in y (m), error in z (m), and RMS misfit (millisecond).

The 3D_seismic_P-wave_velocity_model animation file shows slices of the 3D P-wave velocity model. The 3D_seismic_S-wave_velocity_model animation file shows slices of the 3D S-wave velocity model.

The Interactive_MEQ_location_comparison API file is an interactive visualization of the updated microseismic event locations and the original seismic catalog. The visualization allows users to view and compare the event locations by dragging, rotating, and zooming in.

An updated version of 3D_seismic_velocity_model and associated animations were included,

which were calculated with a more strict assumption for quality indicators.

Oak Ridge National Laboratory. (2020). EGS Collab Experiment 1: 3D Seismic Velocity Model and Updated Microseismic Catalog from Double-Difference Seismic Tomography [data set]. Retrieved from https://dx.doi.org/10.15121/1642468.

Experiment #2:

EGS Collab Experiment #2

The EGS Collab experiment 2 was focused on testing shear stimulation techniques. Shear stimulation, in this case, means using hydraulic pressure to cause shear slip on pre-existing fracture or fault planes such that the hydraulic conductivity of the fracture or fault increases. The concept is to create a percolating network of permeable fractures by enhancing the permeability of a primarily pre-existing network of fractures.

To test this concept the hydraulic pressures for experiment 2 were kept below the estimated magnitude of the least compressive principal stress based on a set of stress measurements in nearby well TV4100. All tests for experiment 2 were performed by applying hydraulic pressure to well E2-TC. Subsequent stimulations in both E2-TC and E2-TU where the injection pressure was increased above the least compressive principal stress are considered part of experiment 3, which is documented separately.

Lawrence Berkeley National Laboratory. (2023). EGS Collab Experiment #2 [data set]. Retrieved from https://gdr.openei.org/submissions/1476.

EGS Collab - Hydraulic Fracturing Test Measurements on the 4100L of SURF

This package includes data from two days of testing at the Sanford Underground Research Facility (SURF) on the 4100 level. The tests were performed in borehole TV4100 in the battery charging alcove south of the Yates shaft. TV4100 is a vertical borehole ~50 meters deep. A series of hydraulic fracture (mini-frac) and reopening tests were conducted at various depths to investigate the magnitude and direction of the minimum principal stress in that area of the mine. Apparent features of the pressure time/pressure injected volume curves are the onset of fracture, peak pressure, and the initial shut in pressure (ISIP).

The raw data files include a Readme with the day, time, and location of each file. The files are organized into 9 columns: time (sec), flow meter (V), Pressure of Return (V), Pressure of Packer (V), Pressure of Injection (V), flow (gpm), Pressure of Return (psi), Pressure of Packer (psi), Pressure of Injection (psi). The shift reports are a short log of how the tests were run in the two-day period. An American Geophysical Union (AGU) 2019 presentation by Ingraham et al. is shown to provide visualization/interpretation of the data. The columns which report voltage (V) show the unscaled voltage value from the transducer, which was recorded in case pressure values

needed to be rescaled due to incorrect calibration factors. This was not necessary.

Sandia National Laboratories. (2019). EGS Collab - Hydraulic Fracturing Test Measurements on the 4100L of SURF [data set]. Retrieved from https://dx.doi.org/10.15121/1632298.

EGS Collab 4100 Thermal Circulation Testing

These data and test descriptions are from a chilled water circulation test conducted by injecting in well E2-TU on the 4100 level of the Sandford Underground Research Facility (SURF). Circulation ran semi-continuously from May 19 through August 26, 2022, though chilled water injection began on June 3. Data for the several stimulations in the 4100 testbed, including the one used for this thermal circulation test, are found in a separate submission. More information about the test, rationale, and processing of data is available on the EGS Collab Experiment 3 wiki page, which is linked below.

Pacific Northwest National Laboratory. (2022). EGS Collab 4100 Thermal Circulation Testing [data set]. Retrieved from https://gdr.openei.org/submissions/1414

EGS Collab Experiment #2: Distributed Fiber Optic Temperature Data (DTS)

Distributed fiber optic sensing was an important part of the monitoring system for EGS Collab Experiment #2. A single loop of custom fiber package was grouted into the four monitoring boreholes that bracketed the experiment volume. This fiber package contained two multi-mode fibers and four single-mode fibers. These fibers were connected to an array of fiber optic interrogator units, each targeting a different measurement.

The distributed temperature system (DTS) consisted of a Silixa XT-DTS unit, connected to both ends of one of the two multi-mode fibers. This system measured absolute temperature along the entire length of fiber for the duration of the experiment at a sampling rate of approximately 10 minutes. This dataset includes both raw data in XML format from the XT-DTS, as well as a processed dataset with the sections of data pertaining only to the boreholes are extracted.

Lawrence Berkeley National Laboratory. (2023). EGS Collab Experiment #2 [data set]. Retrieved from https://gdr.openei.org/submissions/1476.

EGS Collab Experiment #2: Continuous Broadband Seismic Waveform Data

Two broadband seismometers were installed on the 4100 level and recorded for the duration of EGS Collab Experiment #2. Inspired by published data from similar instruments installed in the Aspo Hard Rock Lab, these long-period instruments aimed to measure the tilting of the drift in response to the injection of fluid into the testbed.

One instrument was installed underneath the wellheads in Site A (aka the "battery" alcove) and the other was installed along the east wall of the drift, south of Site B. Due to the feet of gravel (ballast) laid along the floor of the drift, we were unable to anchor the sensors directly to the rock.

As a result, the coupling of the sensors to the experiment rock volume is likely poor. In addition, there are a number of noise sources that complicate the interpretation of the data. For example, sensor BBB is installed adjacent (within 3 ft) to the rail line that runs towards the Ross shaft. Trains (motors) run along this line almost daily and produce a large signal in these data. Careful extraction of periods of interest, as well as filtering for specific signals, is necessary.

The sensors are Nanometrics Trillium Compact Posthole seismometers, sensitive down to 120 seconds period. They were installed as close to the drift wall and as deep as we could manually excavate (only about 1 ft or so). The holes were leveled with sand and the sensors were placed on a paver before backfilling with sand. The hole was then covered by a bucket filled with insulation to improve the sensor's isolation from daily temperature variations, which are minor but present due to drift ventilation from the surface.

Lawrence Berkeley National Laboratory. (2022). EGS Collab Experiment #2: Continuous Broadband Seismic Waveform Data [data set].
Retrieved from https://dx.doi.org/10.15121/1907655.

EGS Collab Testbed 2: Laser Scanned 4100 L Drift Map

The EGS Collab project is evaluating a site for Experiment 2 (hydraulic fracturing/shearing) at a depth of 1.25 km in the Sanford Underground Research Facility (SURF) on the 4100 Level. Two early test holes were drilled in an alcove (formerly known as Battery Charging Station) near Yates Shaft. Recently, we conducted a laser survey around the Testbed 2 to capture the details of the drift. This submission package includes the laser scanned drift map around the Testbed 2. The drift map data are presented in AutoCAD (*dxf), Leapfrog mesh (*.msh), and point cloud (*.csv) file formats.

Idaho National Laboratory. (2019). EGS Collab Testbed 2: Laser Scanned 4100 L Drift Map [data set]. Retrieved from https://dx.doi.org/10.15121/1593285.

EGS Collab Testbed 2 Preliminary Test Wells Locations and Orientations

The EGS Collab project is evaluating a site for Experiment 2 (hydraulic fracturing/shearing) at a depth of 1.25 km in the Sanford Underground Research Facility (SURF) on the 4100 Level. Two early test holes were drilled in an alcove (formerly known as Battery Charging Station) near Yates Shaft. One of the test hole is about 50 m whereas the other hole is about 10 m. This submission package includes well head locations, total lengths of boreholes, their orientations (gyro data). The reported boreholes orientation data were primarily obtained with REFLEX GYRO (TM) survey right after the completion of each hole. Well head locations were ascertained by Laser/LiDAR survey of the drift around the Testbed 2. Note: The coordinate system used is the local Homestake Mine Coordinate (HMC) system from an old gold mine that was in operation for over 100 years.

Idaho National Laboratory. (2019). EGS Collab Testbed 2 Preliminary Test Wells Locations

and Orientations [data set]. Retrieved from https://dx.doi.org/10.15121/1593284.

EGS Collab Experiment 2 ERT Data and Imaging Results

The repository contains the complete sequence of time-lapse ERT data collected during EGS Collab Experiment 2, including:
- meta data files
- raw data files
- files used for inversion with the E4D code (https://e4d.pnnl.gov)
- time-lapse imaging inversion results in E4D format

Pacific Northwest National Laboratory. (2023). EGS Collab Experiment 2 ERT Data and Imaging Results [data set]. Retrieved from https://gdr.openei.org/submissions/1480.

EGS Collab Experiment 2: 4100 Foot Level Elastic Property Data

Static and dynamic elastic properties (Young's modulus, Shear Modulus, P-wave Modulus, and Poisson's Ratio) of amphibolites and rhyolites from the TV4100 and TH4100 boreholes at the Sanford Underground Research Laboratory (SURF). Elastic properties include Young's modulus, Poisson's ratio, shear modulus, and p-wave modulus. Raw data from the experiments and slides describing the experimental procedure and a summary of results are included, along with a readme file with additional definitions and information.

Lawrence Berkeley National Laboratory. (2020). EGS Collab Experiment 2: 4100 Foot Level Elastic Property Data [data set]. Retrieved from https://dx.doi.org/10.15121/1798190.

EGS Collab Experiment 2: Core Logs

Core logs and photos from the EGS Collab project Experiment 2 for the Top Vertical well (TV4100) and the Top Horizontal well (TV 4100) on the 4100 Level of SURF (the Sanford Underground Research Facility). The core logs are stored in a single PDF file with 5-ft run intervals. In the monitoring well IDs, "O" indicates that the well is orthogonal to the anticipated fracture plane, "T" refers to top, and "H" refers to horizontal. A core log CT scan for TV4100 and a layout image of the 4100 wells are included as well.

Logs include: experiment number; borehole ID; depth interval; run number; final packed core box number; scribe line (yes/no; red-on-right convention); logging dates; logger initials; as well as sketches of core foliation, folding, and fracturing with additional details and notes on other features of interest.

Shift reports include: date, location, personnel, summary of site activity, and field notes.

Lawrence Berkeley National Laboratory. (2019). EGS Collab Experiment 2: Core Logs [data set]. Retrieved from https://dx.doi.org/10.15121/1772931.

Experiment #3:

EGS Collab Modeling and Simulation Working Group Teleconference Series (99-128)

This submission contains the presentation slides and recordings from EGS Collab Modeling and Simulation Working Group (MSWG) teleconferences number 99 through 128. These teleconferences served three objectives for the project: 1) share simulation results, 2) communicate field activities and results to the simulation teams, and 3) hold open scientific discussions on EGS topics.

Pacific Northwest National Laboratory. (2022). EGS Collab Modeling and Simulation Working Group Teleconference Series (99-128) [data set].
Retrieved from https://dx.doi.org/10.15121/1871551.

Appendix C - EGS Collab Testbed 2 Fractures and Visualizations

Ghanashyam Neupane, Nuri Uzunlar, William Roggenthen, Craig Ulrich, Tom Doe, and Megan Smith

1. Introduction

The EGS Collab Project performed a series of tests to increase the understanding of crystalline rock mass responses to stimulations and fluid circulation. The EGS Collab team created two underground testbeds (Figure 1) at the Sanford Underground Research Facility (SURF) in Lead SD at a depth of approximately 1.5 km (4850 level) and 1.25 km (4100 level) to examine hydraulic fracturing and hydraulic shearing, respectively. Experiment 2 was designed to examine hydraulic shearing and fluid flow in Testbed 2 in amphibolite under a controlled set of stress and fracture conditions. This document summarizes the general geology, natural fractures, and conceptual model(s) of stimulated fracture networks in the Testbed 2.

2. Geology

EGS Collab Testbed 2 was constructed entirely within the Yates Unit of the Poorman Formation. Yates unit consists of amphibolite that shows strong textural (grain-size) as well as compositional layering (hornblende and plagioclase). Amphibolite is cross-cut by calcite veins (Caddey et al. 1991). Along with these calcite veins, local oxidized sulfide layers define the zones of weakness in the rock. At the testbed site, the host rock consists of amphibole, plagioclase, and chlorite with minor amounts of sulfides.

Structurally, the testbed is located on the eastern limb of a southerly plunging Lead Anticline (Figure 1). Over the geologic history, the host rock was subject to multi-deformation phases and igneous intrusions. Some of the noted deformation occurred during the Precambrian (Paleoproterozoic) time that created fractures which were subsequently healed with vein minerals consisting primarily of calcite and quartz. During the Tertiary (Paleogene) time, rhyolitic intrusions occurred that resulted in a series of fractures and shear zones. Tertiary rhyolite dikes, mostly striking along NW-SE direction, intersect several geologic units in the area including Yates. Most of the rhyolite dikes in the vicinity of testbed are located to the western side; however, one of the exploratory holes (e.g., Borehole TV4100) encountered a thick rhyolite dike, and it is expected that this rhyolite body is extended to the area underneath the stimulated volume of rock in the Testbed 2 (Figure 1).

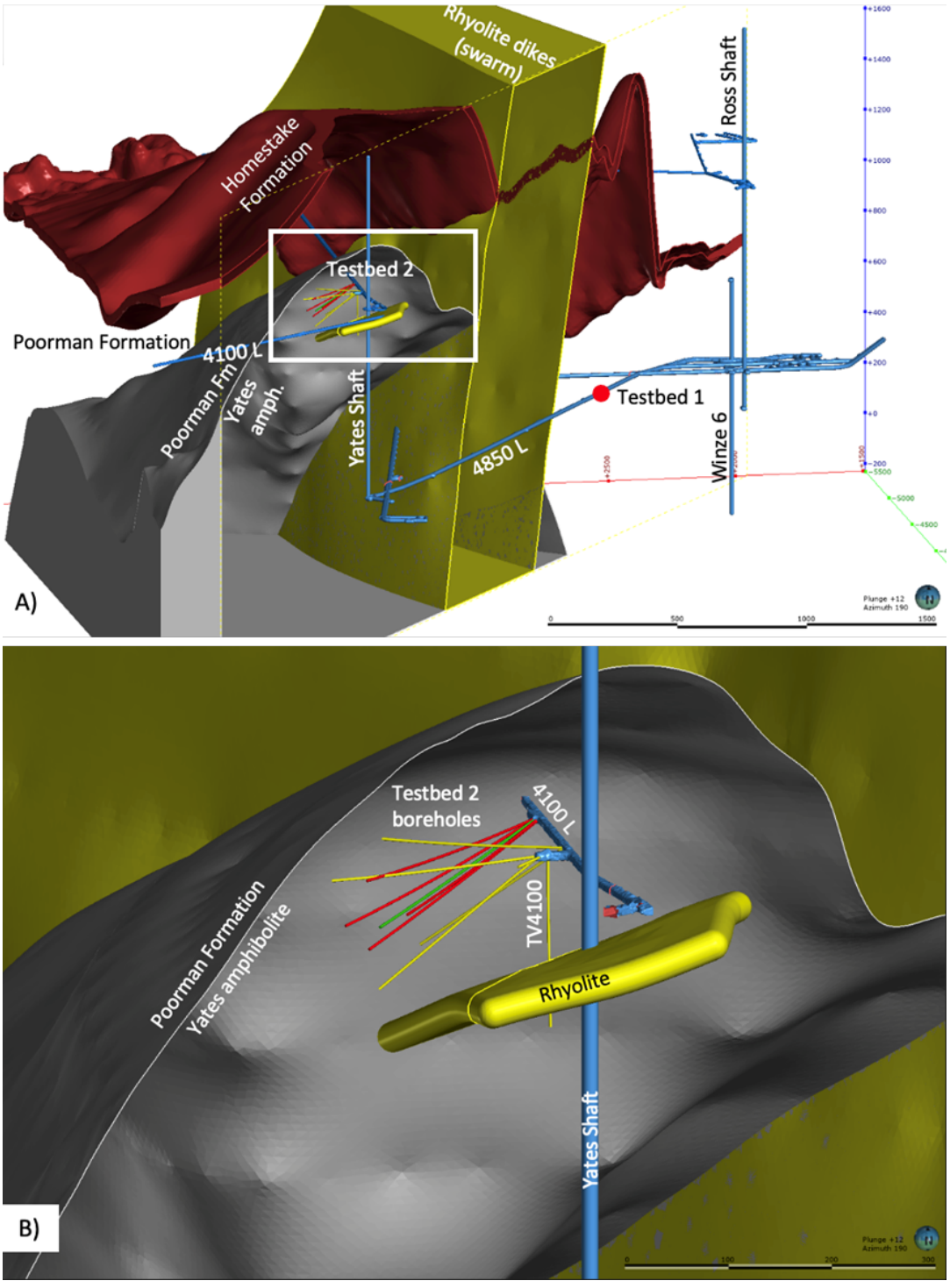

Figure 1. Location of EGS Collab testbeds. (A) Testbed 1 is located entirely within metasediments of the Poorman Formation on the western limb of Lead Anticline, and Testbed 2 is located in the metabasalt (amphibolite) of Yates unit of the Poorman Formation on the eastern limb of the anticline. Scale bar length 1,500 m. (B) Enlarged region showing Testbed 2, the host rock, and location of the rhyolite encountered in an exploratory hole (TV4100). The grouted-monitoring wells are yellow and open test wells are red and green. Scale bar length 300 m.

3. Fractures along the Drift (N. Uzulnar and W. Roggenthen, SDSMT)

Prior to the construction of Testbed 2, a detailed fracture mapping (Figure 2) was conducted along the 4100-level drift south from the Yates Shaft and Battery Alcove. The exposure of fractures varied from excellent within the battery alcove to adequate in the drift. The fresh face at the end of the battery alcove allowed the full extent of fracturing to be seen and showed many healed and, sometimes, unhealed fractures. The fine-scale fracturing identified in the alcove was not as evident in the drifts due to lack of fresh surfaces, although the larger features were still evident in the drifts.

Mapping in the drifts extended from about 100 ft in the direction of the Yates Shaft from the battery alcove and then southward to the contact between the Yates and Ross Members of the Poorman Fm. Locations of fractures, identification of type of fractures, and orientations were recorded as part of this exercise. The results of the mapping are included as Figure 2.

3.1 Types of Fractures

Three main types of fractures near the battery alcove were identified. They include: 1) large fractures that may have experienced shearing, 2) foliation-parallel features and 3) small width, healed fractures that may be conjugate shear sets. Although many small joints (<0.1 mm aperture) filled with calcite and quartz without consistent orientations occur, they are only identifiable on fresh surfaces and probably do not have lateral continuity. The presence of the smaller fractures was noted but attitudes were not measured.

3.1.1 Large Fractures

The large shear(?) fractures are characterized by fracture traces between one and two cm wide and have cement fillings consisting of calcite, probably quartz, and gypsum. In some instances, they have unfilled space with well-developed calcite and/or selenite spar. Figure 3 shows such a fracture that is exposed in the east face of the battery alcove. This fracture probably is also exposed in the drift showing 10+ meters lateral continuity, and its projection is considered further in Section 3.3 below. These types of fractures are characterized with high dips with strikes in a generally NW-SE direction. The unfilled nature of many of the fractures and the mineralogy of the filling indicate that they are probably related to the Tertiary uplift and intrusions. This type of Large Tertiary-age Shear (LTS) can be seen in a few locations along the drift, but the fracture frequency is low.

3.1.2 Foliation Parallel Features

The amphibolite in the vicinity of the Yates Shaft has a shallow dipping foliation that is defined by quartz stringers and sulfidic layers that are now oxidizing to a bright yellow color. Figures 3 and 4 show the foliation well and were taken in the east face of the battery alcove.

Within the drift, the sulfidic layers (Figure 5) appear to have had small amounts of seeping water associated with them although amounts appear to be minor. These layers are generally parallel or semi-parallel to the overall foliation, and they may be mechanically weaker, which could focus localized shearing and water movement.

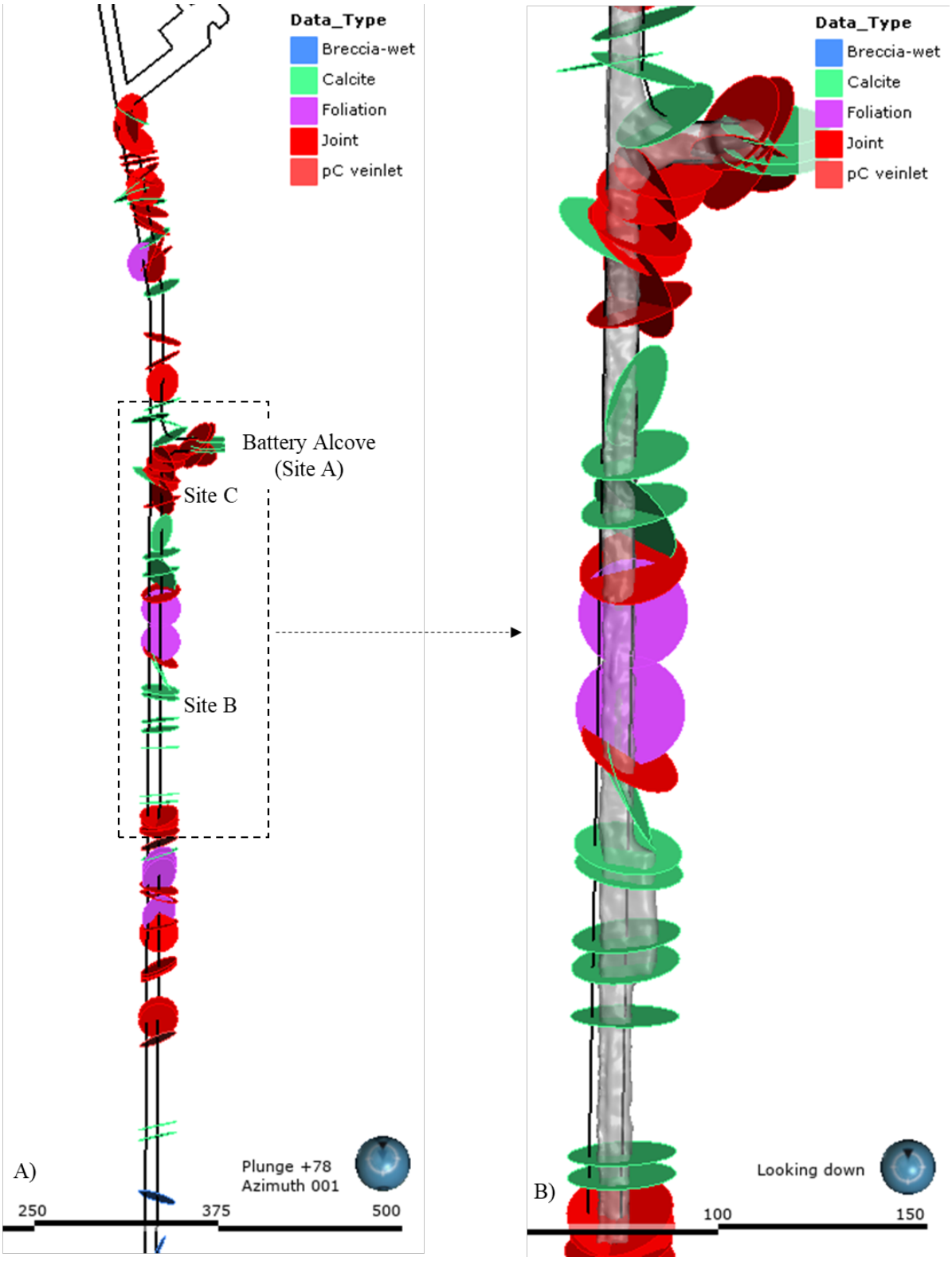

Figure 2. (A) Map showing various fractures identified along the 4100-level drift south from Yates Shaft. Scale bar length 500 m. (B) Enlarged portion of the map showing fractures at

Testbed 2 location. Scale bar length 150 m. Fracture mapping was conducted on 9/18/2018 and 3/27/2019.

A thin sheared chlorite zone also was identified within the amphibolite in one small area of the battery alcove (upper left of Figure 4). It has a shallowly dipping surface with an orientation different from the overall foliation. This sheared chlorite is likely to be Precambrian in age. Identification of additional sheared chloritic zones of this type in the drift are unlikely due to the relatively subtle nature of the zone.

Figure 3. Large fracture near the tape measure for scale (intervals on the tape are 1 ft). The fracture is filled in this photograph but other, similar fractures are exposed in the drift with open space.

3.1.3 Thin Conjugate Shear Sets

Thin fractures can be seen frequently in the fresh face of the battery alcove and may be represented in the drift mapping as well. Fracture widths were very thin (<0.5 mm) and the fractures appear to be healed. They may be a better developed side of a conjugate shear set, as one possibility. Small amounts of offset (~1-2 mm) sometimes can be seen.

Figure 4. Foliation within the Yates amphibolite dips to the right (south) in this photograph.

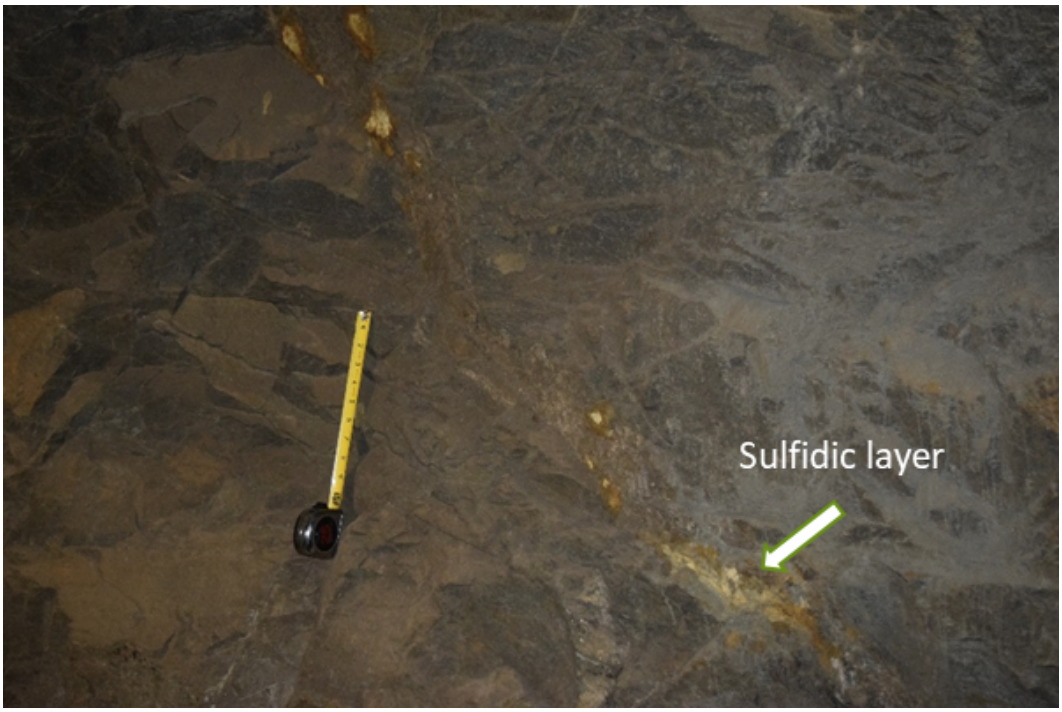

Figure 5. Sulfidic layer exposed in the drift about 60 ft south of the battery alcove.

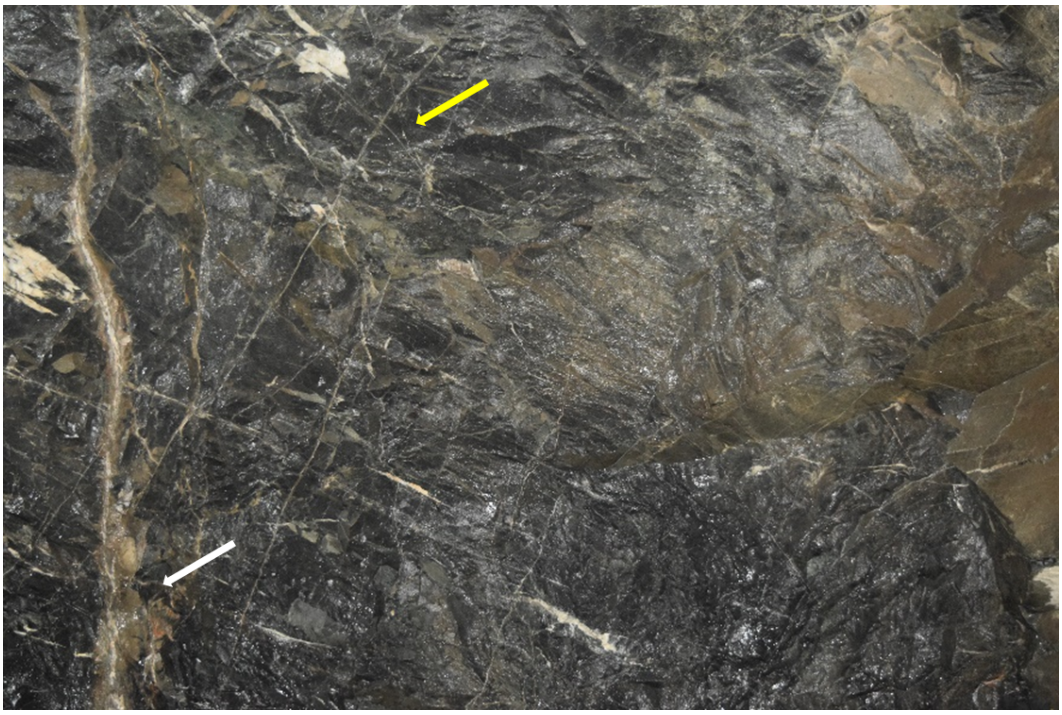

Figure 6. Photo from battery alcove showing the large fracture on the left (white arrow), a conjugate shear in the middle (yellow arrow), and the general orientation of the foliation in the amphibolite.

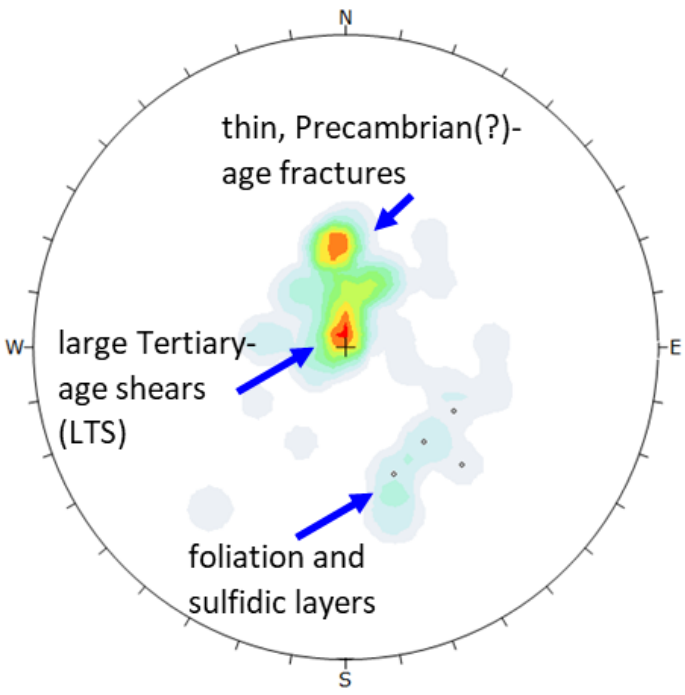

Color	Density Concentrations
	0.00 - 1.50
	1.50 - 3.00
	3.00 - 4.50
	4.50 - 6.00
	6.00 - 7.50
	7.50 - 9.00
	9.00 - 10.50
	10.50 - 12.00
	12.00 - 13.50
	13.50 - 15.00

Contour Data	Dip Vectors
Maximum Density	14.02%
Contour Distribution	Fisher
Counting Circle Size	1.0%

Plot Mode	Dip Vectors
Vector Count	54 (54 Entries)
Hemisphere	Lower
Projection	Equal Angle

Figure 7. Stereogram of dip vectors showing the foliation in the Yates amphibolite, the large TAS, and the many smaller, healed fractures that may be a better developed side of conjugate shears.

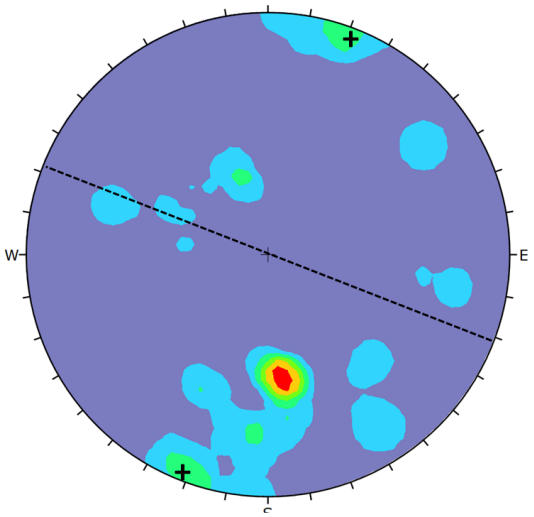

Figure 8. Stereogram of poles of all features and fractures. The crosses show the orientation of the large fracture sets and the dashed line shows the orientation of the nearly vertical fractures striking to the northwest.

3.2 Orientations

A total of 54 measurements of orientations of fractures were taken as part of this work. Figures 5 and 6 show stereograms of the dip vectors of all of the features (Fig. 7) and the pole vectors (Fig. 8). The dip vector plot shows two maxima, and the fractures with the highest dips shown with a (+) are representative of the well-defined shear(?) sets (LTS). The pole vector plot in Figure 8 indicates that these planes strike at ~290° and are nearly vertical.

The second maximum results from measurements of the many thin fractures. These are primarily in the alcove, but thin fractures with similar orientations were found in the drift as well. These features are thought to be healed Precambrian fractures due to their degree of filling and general tightness.

Some orientation bias may occur because fractures parallel to the drift would not intersect the drift and, therefore, would not be recognizable although this effect would be rare.

3.3 Projections from the Drift

Two prominent features were found to the north of the battery alcove. One was the well-defined Tertiary fracture shown in Figure 1, and the other was a sulfidic layer in the amphibolite that was semi-parallel to the foliation. A large fracture exposed in the drift (yellow in Figure 9a) is probably the same fracture in the battery alcove face. These are shown in the plan view in a) where they are projected into the area of the battery alcove and in cross-section view in b) in relation to a proposed vertical drill hole. Although the drill hole would not be expected to intersect the larger fracture (yellow), it would be expected to intersect the sulfidic zone (red in Figure 9a) at about 5-10 ft depth in the borehole.

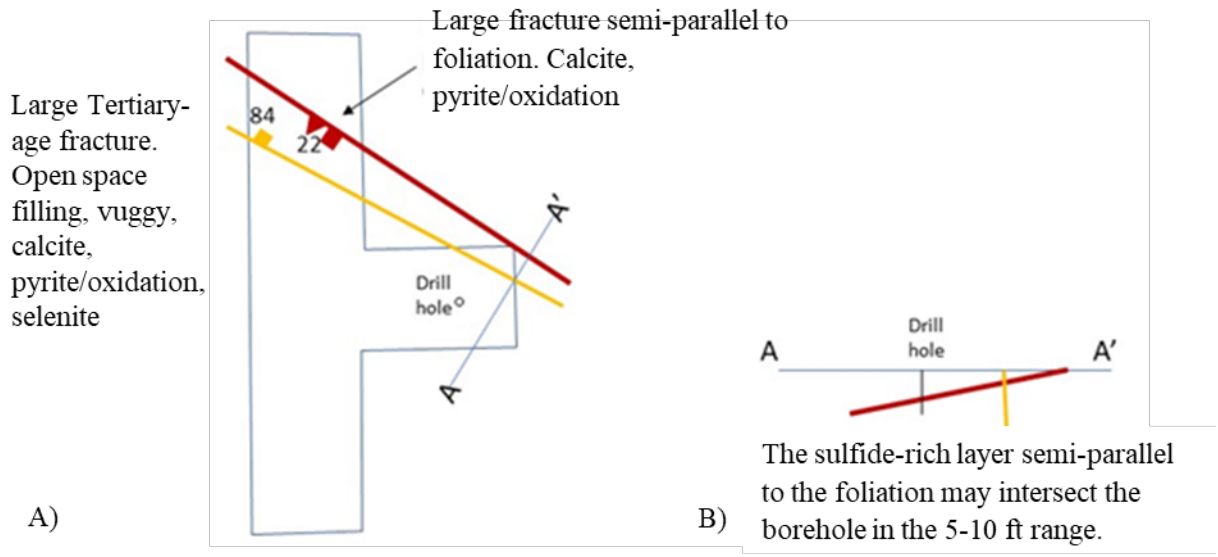

Figure 9. A) plan view showing relationship between the battery alcove, a large shear(?) fracture, and a sulfidic zone within the amphibolite. B) the sulfidic zone can be projected downwards towards a probable intersection with the proposed vertical drillhole. Because the large fracture exposed in the east face of the alcove is nearly vertical, it would not be expected to be found in the drillhole.

3.4 Takeaways

- Three types of fracture systems were identified.
- Many thin, healed fractures with consistent orientations were identified.
- The large, probably Tertiary-age, fractures are good targets but are relatively rare.
- The large fractures are nearly vertical and generally have a NW-SE strike and appear to have some lateral continuity.
- The sulfidic zones appear to be related to the foliation and may be a complicating factor.

4. Fractures in Testbed 2 boreholes

4.1 Testbed 2 boreholes

Testbed 2 consists of 9 boreholes drilled from three nearby locations (Sites A, B, and C) along the 4100-level drift south from the Yates Shaft (Figure 10). Initial characterization (identifying rock types, fracture and stress orientations) for testbed layout was investigated by core-drilling two HQ (nominally 96 mm) boreholes with one in the vertical direction (TV4100) and one in the horizontal direction (TH4100) shown in Figure 10B. Following the characterization, an additional nine boreholes (AML, AMU, DML, DMU, TC, TL, TN, TS and TU) were core-drilled to depths ranging from 55 to 80 m to perform controlled hydro shear experiments using TC or TU borehole at Site C.

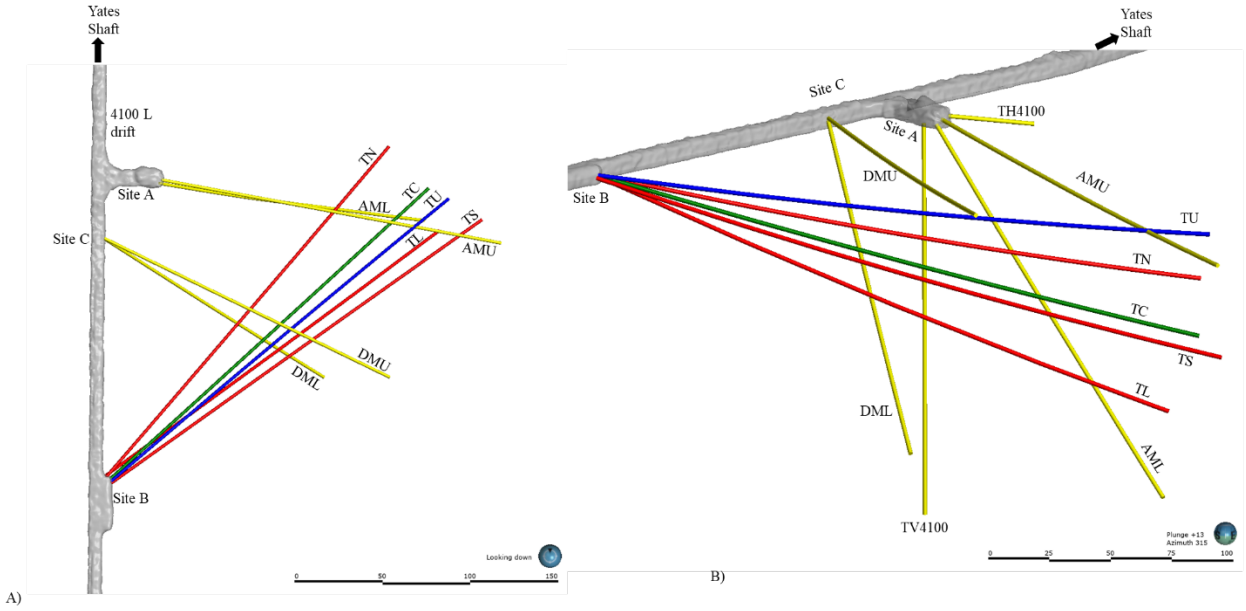

Figure 10. Plan view (A) and cross-sectional view. Scale bar length 150 m. (B) of Testbed 2 boreholes showing Sites A (Alcove), B, and C along the drift on the 4100 level for stimulation and flow experiments. Scale bar length 100 m.

4.2 Fractures in boreholes (OTV images interpreted by C. Ulrich)

Different methods were used to identify and characterize fractures along the Testbed 2 boreholes. During drilling, the recovered cores were observed, logged, and photographed. Besides general descriptions of the lithology, the logs also included presence of fractures and open/voids/vugs, and nature and types of filling minerals, etc. Subsequently, several researchers re-visited archived cores to study in detail to identify alterations, weak zones, fractures, etc. After the completion of drilling, each borehole was scrub-cleaned for acoustic and optical televiewer logs Several other rock properties logs were also prepared using a suite of wireline geophysical tools (Ulrich et al., 2022).

The optical televiewer images were interpreted to identify and pick discontinuity features in boreholes. Three types of discontinuities – foliations, healed fractures, and open fractures - were identified in boreholes. Figure 11 shows examples of open and healed fracture types on the optical televiewer images. All discontinuities picked in Testbed 2 boreholes are illustrated in Figure 12. A few of the features are picked as unidentified and labeled as 'No Data' category in Figure 12. The majority of the features identified in the boreholes are healed fractures. Figure 13 shows the plots of healed fractures as disks and poles. These healed fractures are distributed as two conjugate sets of fractures, one set of fractures dipping due SW and another group dipping due NW. Another set of healed fractures are nearly orthogonal to the previous two sets with shallower dip due SE.

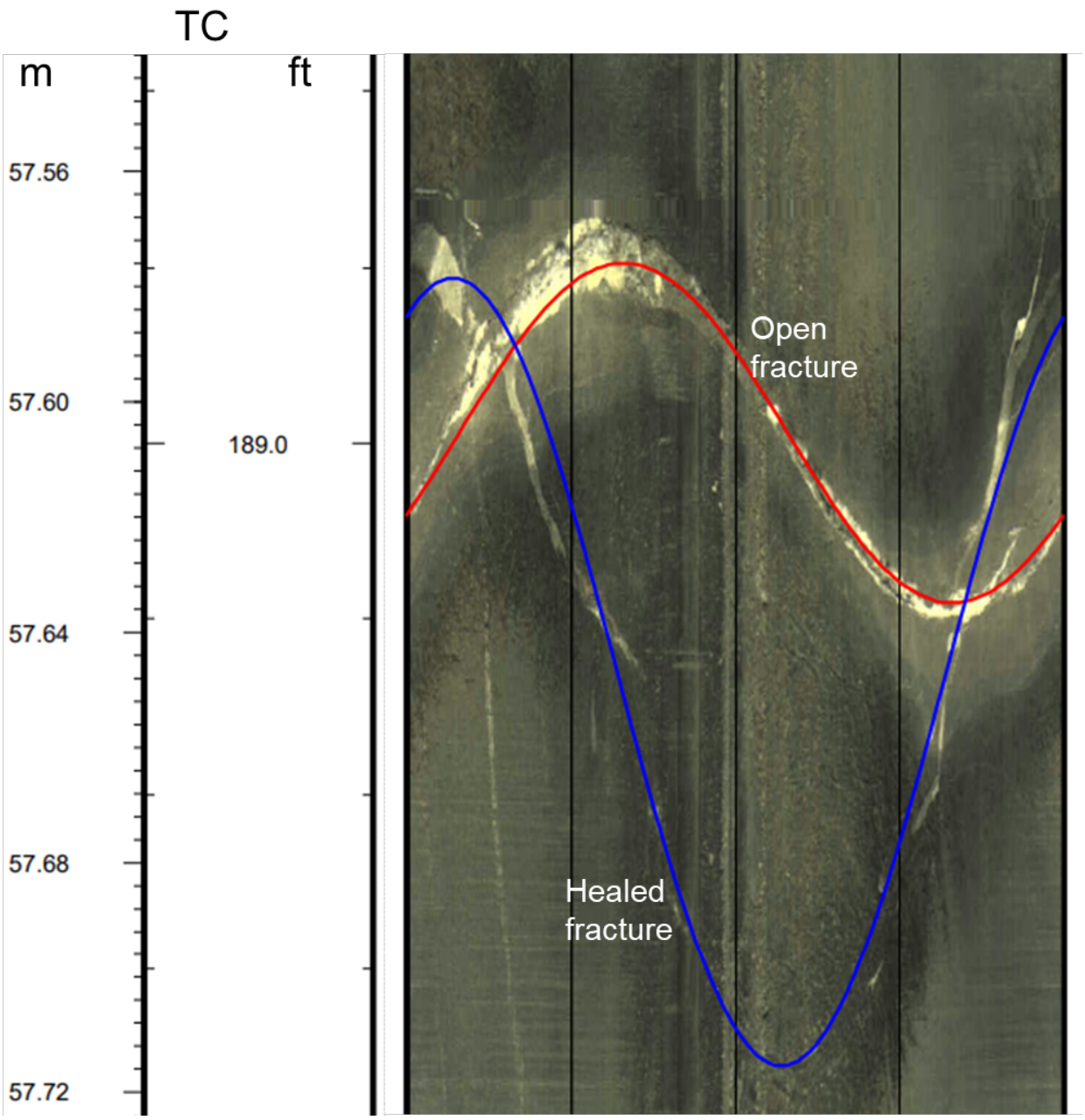

Figure 11. Example of open and healed fractures as observed on the optical televiewer image.

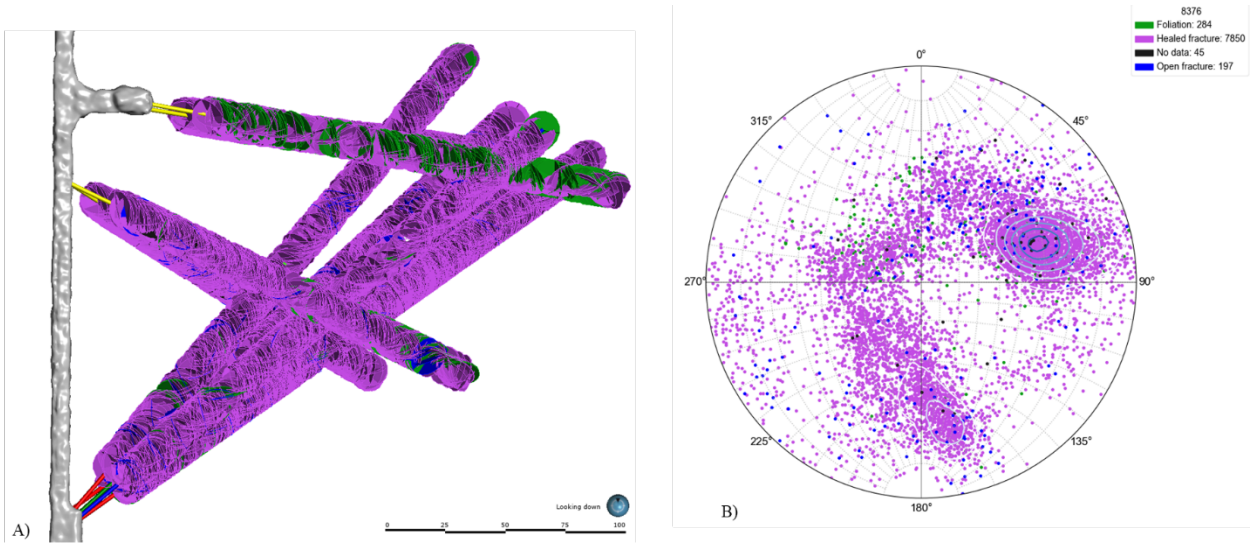

Figure 12. Discontinuity features identified after optical televiewer image interpretation for all Testbed 2 boreholes. (A) Discontinuity features plotted as circular disks along the boreholes. Scale bar length 100 m. (B) stereonet pole plots (equal angle, lower hemisphere) of the discontinuity features. Foliations are green disks and points, healed fractures are purple disks and points, open fractures are blue disks and points, and unidentified (no data) are black disks and points.

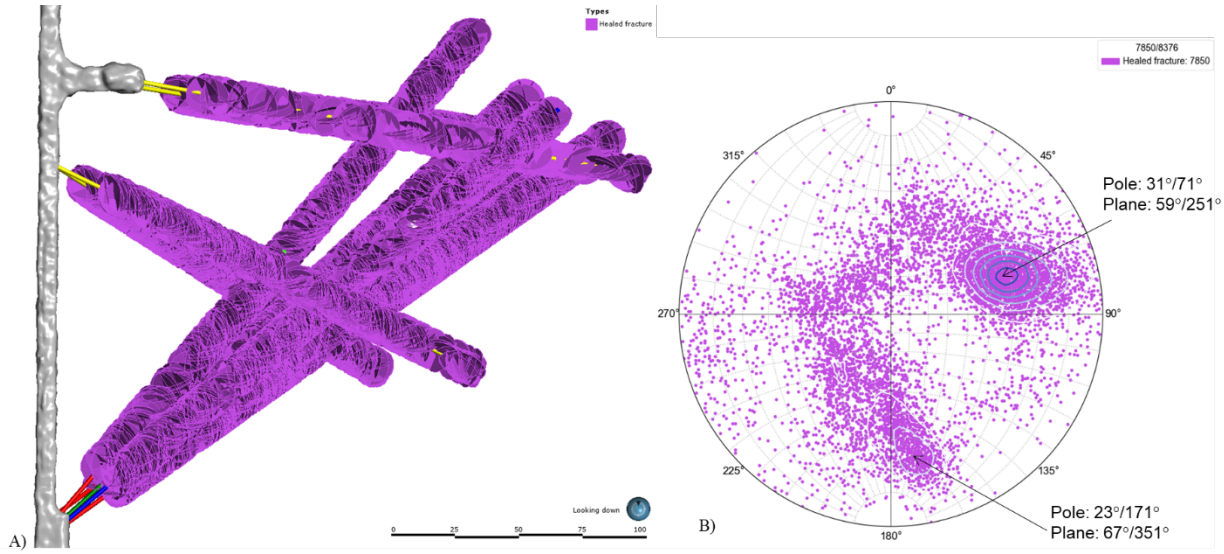

Figure 13. Healed fractures (A) disk. Scale bar length 100 m. (B) pole plots identified after optical televiewer image interpretation for all Testbed 2 boreholes.

Figure 14 shows disk and pole plots for the identified foliations along the Testbed 2 boreholes. The distributions of foliation poles (Figure 14B) indicate two major sets of foliations features, the first set being dipping due SW and the second set dipping due SE. Since the foliations in the host rocks are not exhibited prominently, features identified as foliation could be healed

fractures. The distributions of these foliations also match with the first and third sets of healed fractures as shown in Figure 13.

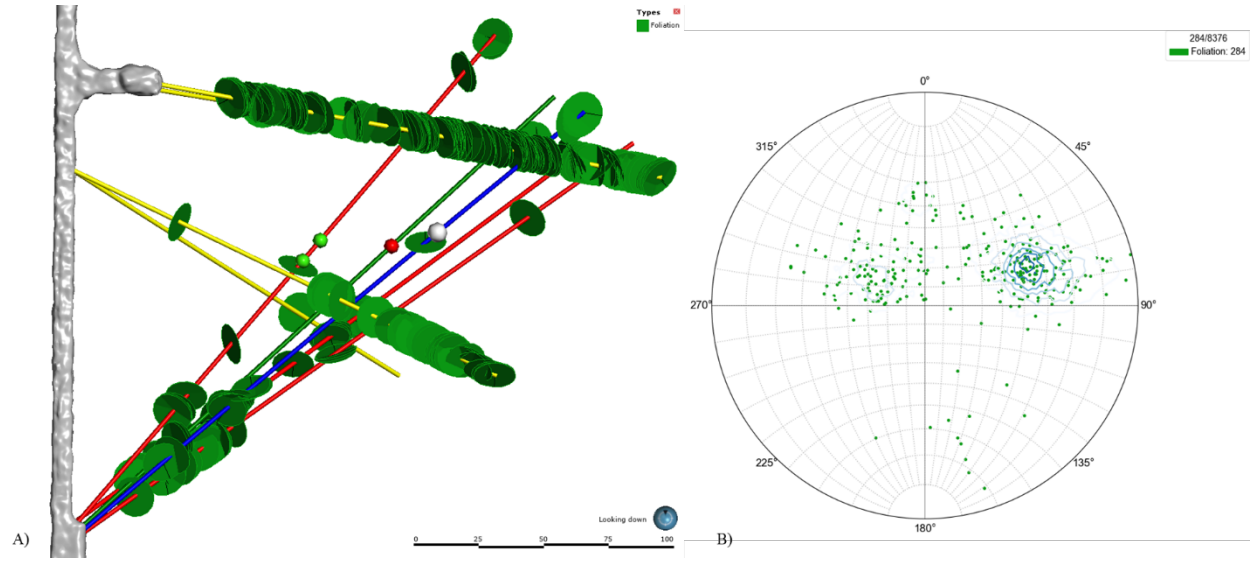

Figure 14. Foliations (A) disks. Scale bar length 100 m. (B) pole plots identified after optical televiewer image interpretation for all Testbed 2 boreholes.

The open fractures (Figure 15) are discontinuities with observable open space or vugs identified in the optical televiewer logs (images). The pole distribution plot for the open fractures (Figure 14B) shows three sets of open fractures, with two fracture sets correlating with healed fractures. The third set of open fractures are dipping due NE and have steeper dip angle, and mostly correlate with Tertiary fracture mapped in the drift (Figure 9A).

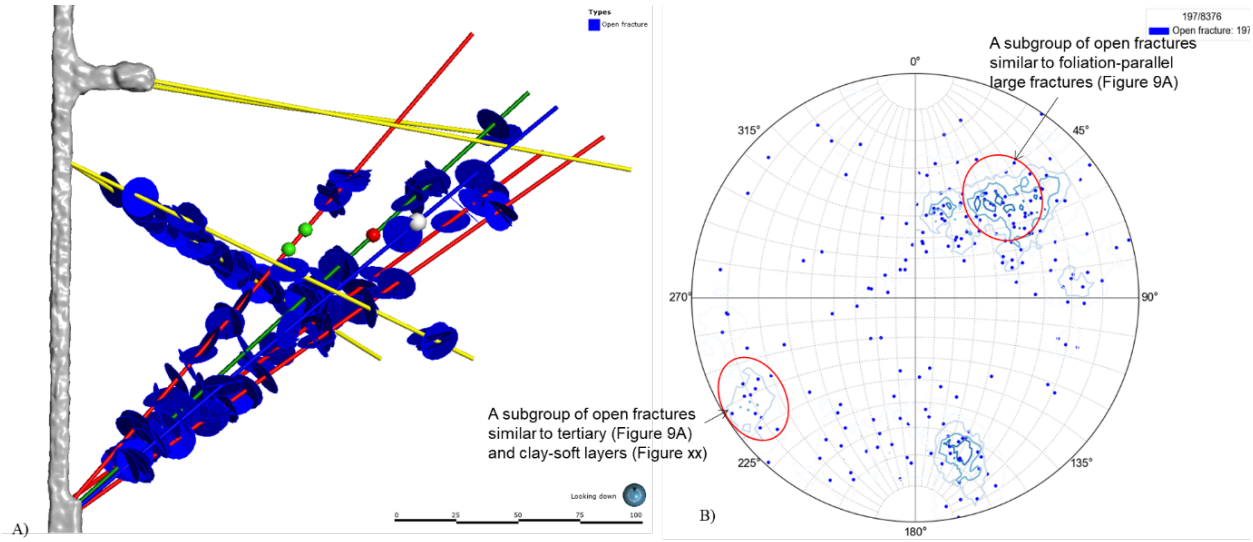

Figure 15. Open fractures (A) disks. Scale bar length 100 m. (B) pole plots identified after optical televiewer image interpretation for all Testbed 2 boreholes.

4.3. Features in the boreholes (examination of core photos, by W. Roggenthen)

Examinations of core photos revealed some interesting features such as alteration seams, calcite and quartz calcite veins (ranging from ~1-2 cm to as large as ~1 m), fractures lined with non-calcite/quartz minerals (e.g., anhydrite), and open spaces along the boreholes. Figure 16A shows three feature types represented by pink, altered, and space. The features represented by pink (e.g. several along TC and TN) are fractures lined with minerals other than calcite or quartz. These features are taken from the core description sheets rather than identifying in core photos. The features represented by altered (blue in Figure 16A) are seams that show chemical changes from amphibolite to minerals such as clay or in many instances, are just a color change to a "non-amphibolite" color. Finally, the features illustrated as space (green) show visually-detectable open spaces and microporosity.

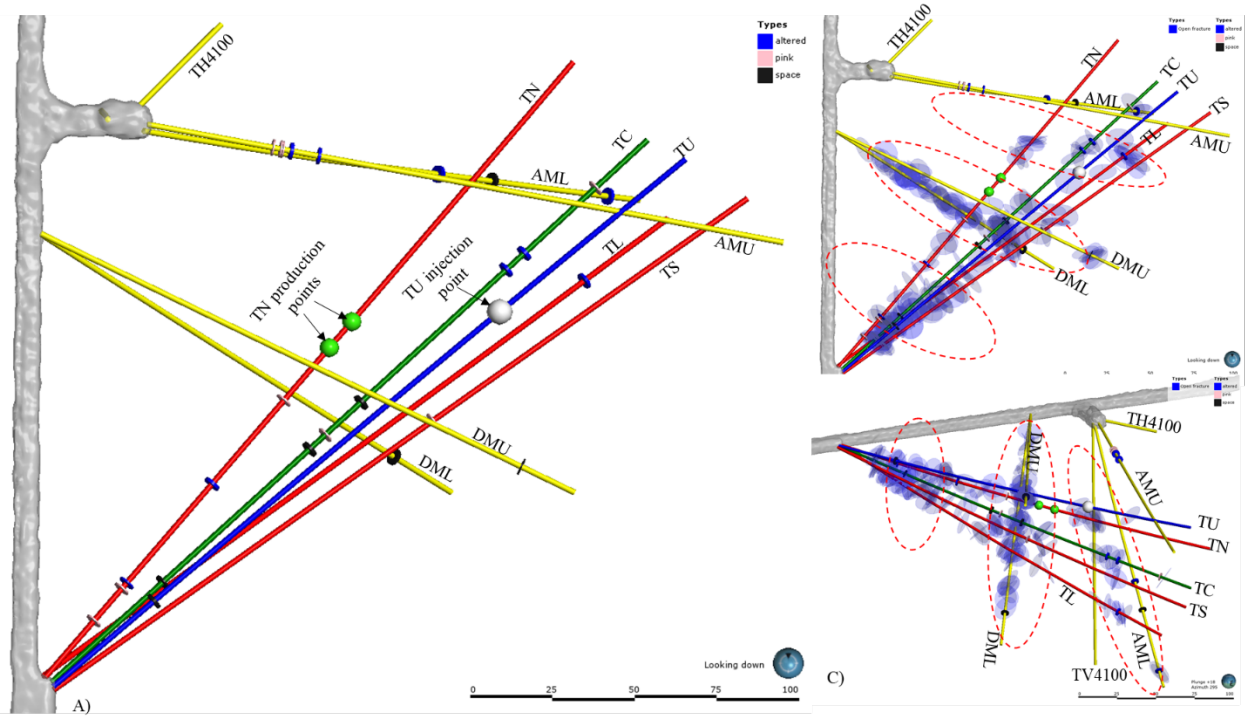

Figure 16. (A) Features identified during examinations of core photos. Pink features are fractures lined with minerals other than calcite or quartz, altered features are seams of clay or other non-amphibole minerals, and space features are large open spaces and microporosity. Scale bar length 100 m. (B & C) Core examination features plotted along with open fractures identified by interpretation of optical televiewer images. Scale bar length 100 m.

Figures 16B&C show core examination features along with open fractures identified by interpretation of optical televiewer images. The distributions of these features indicate that these features are concentrated along repeating NW-SE extending zones. The general orientations of these zonal patterns appear to be similar in orientations to that of the large Tertiary fracture in the drift (Figure 3), and likely to be related to deformations related to the Tertiary rhyolitic intrusions.

5. Stimulated fracture zones and flow paths

5.1 Tertiary fracture and clay/soft layers

Testbed 2 has very few discontinuity features that can be traced from one borehole to the others. Features that have some similarities in properties and locations are the clay/soft section identified in TC and TL (as shown in Figure 17A). However, during low-pressure hydraulic tests prior to stimulations, cross flow between these sections was not observed. Nevertheless, these features in TC and TL have similar orientations as that of the large Tertiary fracture mapped in the drift (Figure 3). These fractures also share the general strike directions of the hydraulic fractures created at the deeper sections in the TV4100, but they differ in dip directions. (Figure 16B).

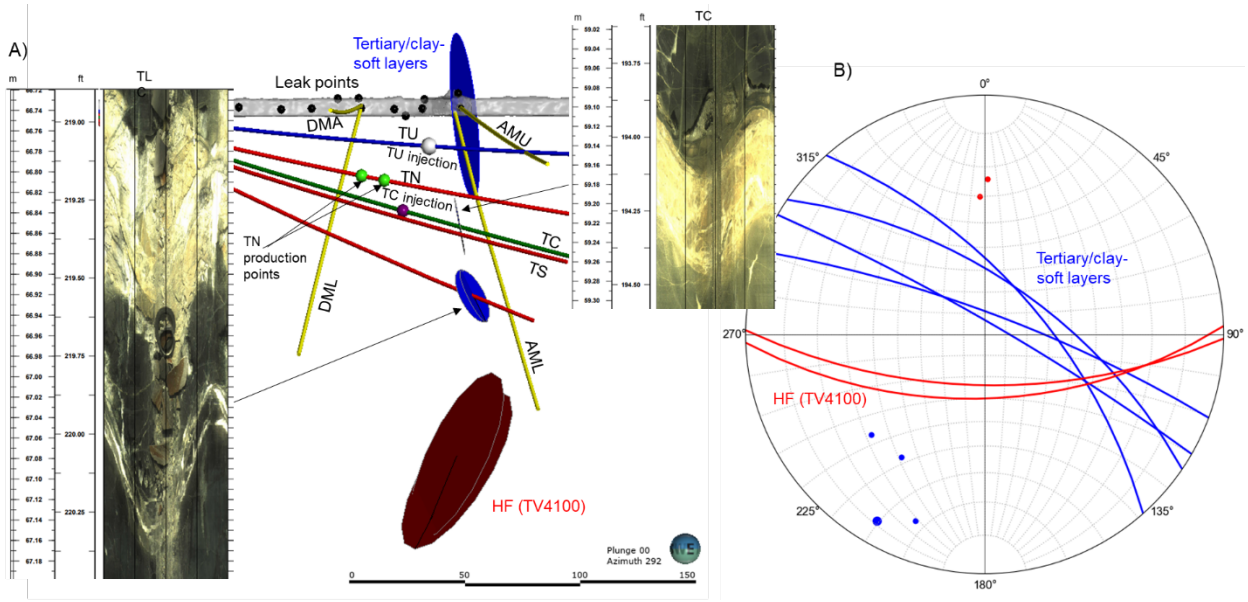

Figure 17. (A) Orientations of Tertiary fracture and clay/soft layers in TC and TL in the testbed. Scale bar length 150 m. (B) Stereonet plot showing Tertiary fracture and clay/soft layers and TV4100 hydraulic fractures.

5.2 DTS anomalies and open fractures

Several DTS anomalies (Figure 18A) were recorded mostly during the long-term flow tests with injection in TU. Only one DTS anomaly was detected at 111.55 ft in AMU on 4/12/2022 during TC stimulation at the interval between 192.4-200.3 ft. Several DTS anomalies were detected along DML and DMU during flow tests in TU with the interval centered at 178.7 ft (Figure 18A). Open fractures picked after interpretation of DML and DMU optical televiewer images are included in Figure 18B along with the DTS anomalies. Each DTS anomaly appears to be associated with an open fracture that is slightly offset for an anomaly at 141 ft in DMU. It is likely that the open fractures provided a pathway for high-pressure fluid to intersect the grouted DML and DMU from main activated fracture zones (discussed below) and caused positive temperature anomaly through Joule-Thomson heating due to pressure drops. Although open fractures were not picked along AML and AMU, a higher number of open fractures were identified in TC, TU, and TL nearby these anomalous points, indicating creation of potential flow paths to AML and AMU DTS anomaly points (Figure 18C).

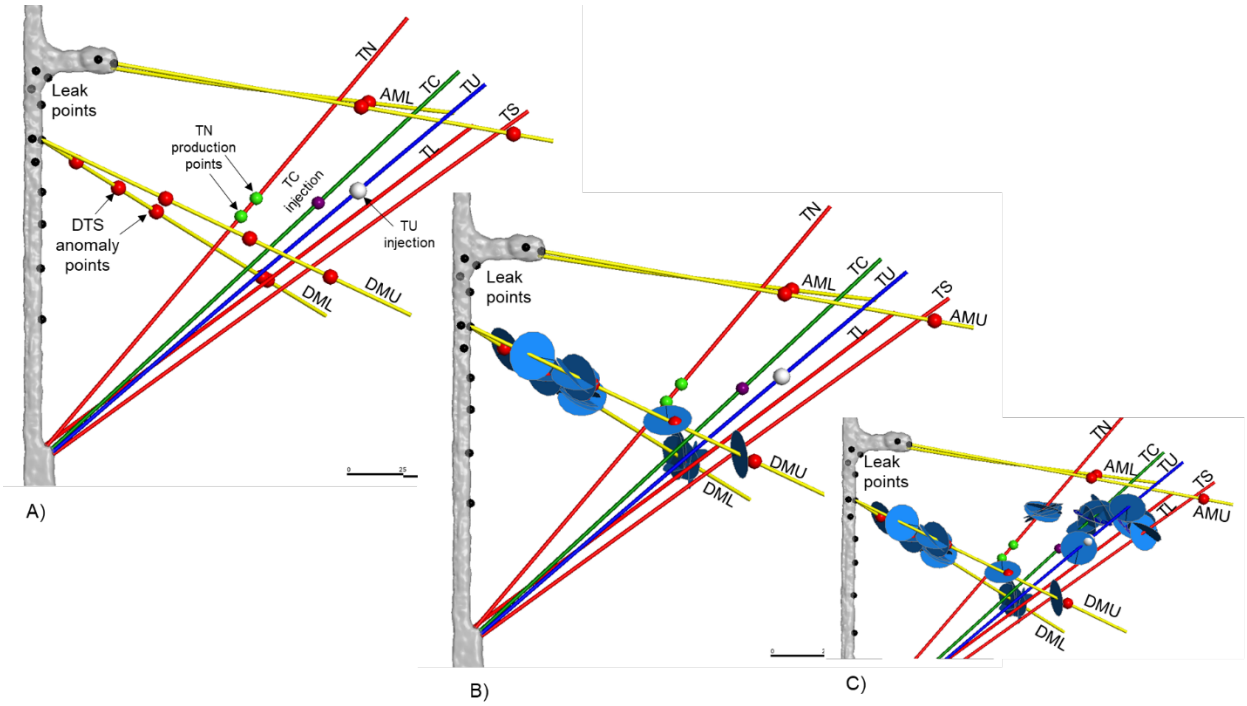

Figure 18. (A) DTS anomalies (red spheres) along AML, AMU, DML, and DMU. (B and C) Open fractures plotted along with DTS anomalies.

5.3 ERT anomalies and open fractures

Figure 19 shows the changes in electrical conductivity measured on July 27 after injection of sodium chloride electrolyte on July 26. Higher positive changes in electrical conductivity are observed in areas with higher density of open fractures in the testbed.

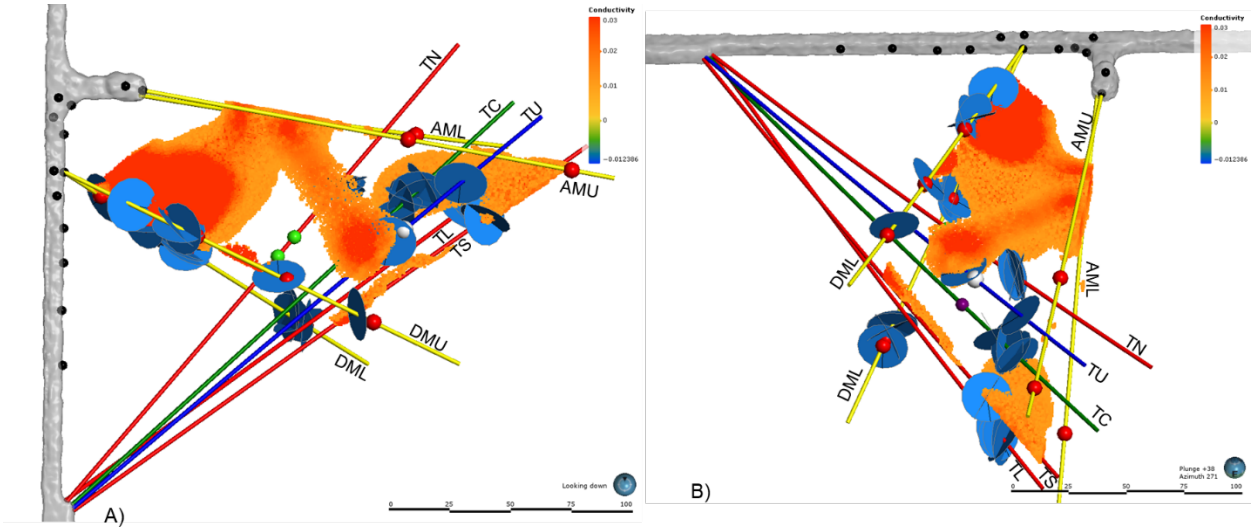

Figure 19. ERT results showing positive electrical changes in the testbed. (A) Plan. Scale bar length 100 m. (B) elevation views of the Testbed 2. The higher (>0.01) positive changes in

electrical conductivity (log S/m) after injection of saline water are illustrated with hotter-colored cells. The cells with lower positive changes in electrical conductivity are filtered out.

5.4 MEQ locations and fracture zones

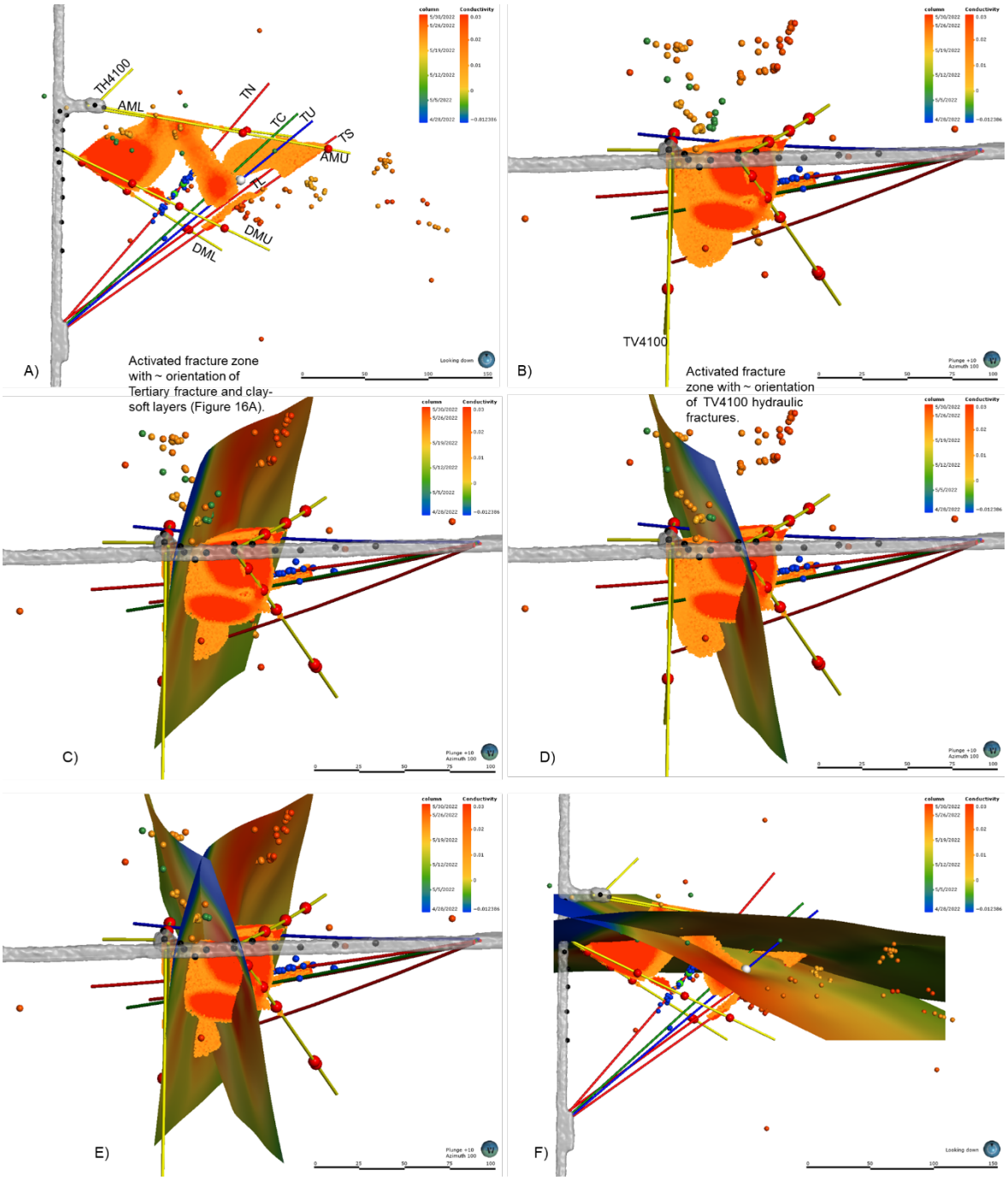

Figure 20. Scale bar length 100 m. Plan (A) and elevation (B) views of distribution MEQ locations along with ERT results. (C and D) visually fitted surfaces along two sets of MEQ locations, one surface has orientation similar to that of the large Tertiary fracture and soft/clay layers in TC and TL (Figure 17) whereas the surface has orientation similar to the hydraulic

fractures created in TV4100 (Figure 17). Elevation (E) and plan (F) views with both surfaces. These surfaces represent the activated fracture zones that provide fluid flow paths to different production points. Color in these fracture surfaces represented electrical conductivity values evaluated from ERT results.

Figure 20 shows distributions of MEQ locations detected during 4/28/2022 to 5/29/2022 along with ERT results. As illustrated in Figure 20B, the distributions of MEQ locations can be associated with two intersecting planner features, loosely defined as activated fracture zones. One of the fracture zones has orientation similar to that of the large Tertiary fracture and soft/clay layers in TC and TL whereas the other fracture zone has orientation similar to those of the hydraulic fractures created in TV4100 (Figure 17).

Finally, Figure 21 shows an integrated illustration for the two fracture zones along with other observational and monitoring data. The available observational evidence suggests that the Testbed 2 is likely to have two intersecting activated fracture zones. The intersection of these two fracture zones seems to be controlled by the existing open fractures. The majority (up to 70%, Mattson et al., 2023) of the injected water into TU appears to flow through these fracture zones to the drift between Site C and Site A corner. A fraction of injected (~30%) water was intercepted by production zones in TN.

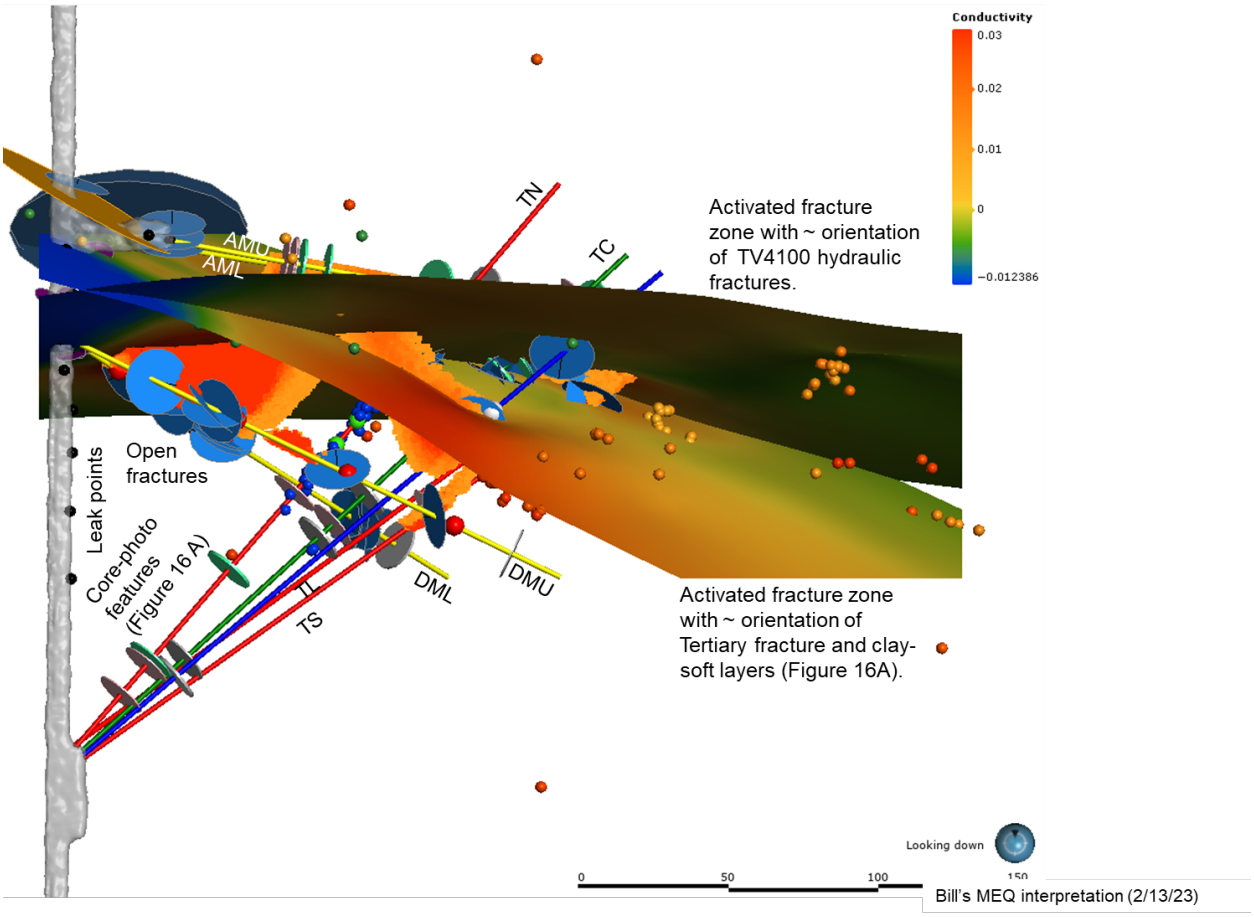

Figure 21. Stimulated fracture zones integrated with various observational and monitoring data.

References

Caddey, S.W., R.L. Bachman, T.J. Campbell, R.R. Reid, and R.P. Otto. 1991. The Homestake Gold Mine, An Early Proterozoic Iron-Formation-Hosted Gold Deposit, Lawrence County, South Dakota. U.S. Geological Survey Bulletin 1857-J, 67 p.

Mattson, E., Plummer, M., Neupane, G., Vermeul, V., Sirota, D., Ingraham, M., Kneafsey, T. and Team, T.E.C., 2023. Fluorescein Tracer Testing on the 4100L–A Preliminary Examination of Initial Arrival in Wells and the Drift at the Second EGS Collab Testbed. In 48th Workshop on Geothermal Reservoir Engineering, Stanford University, Stanford, California.

Ulrich, C., Dobson, P. F., Kneafsey, T. J., Roggenthen, W. M., Uzunlar, N., Doe, T. W., Neupane, G., Artz, T., Dobler, K., Schwering, P., Smith, M., & Burghardt, J. A. (2022). *Characterizing Rock Fractures and Physical Properties for Experiment 2 of the EGS Collab Project, Sanford Underground Research Facility*. Paper presented at the 56th U.S. Rock Mechanics/Geomechanics Symposium. https://doi.org/10.56952/ARMA-2022-0341

Appendix D - Mineralogic and Petrologic Characterization of the 4100 Test Bed

Bill Roggenthen

1.0 Mineralogic and Petrologic Characterization of the 4100 Test Bed

Figure 1 is a geologic map showing a portion of the 4100 Level where EGS Test Bed 2 was constructed. These data were derived from the Homestake/SDSTA geologic database that was developed over the long history of mining in the facility, and three units were mapped on this level. The Poorman Formation consists of the two informal units including the Yates Unit (purple) defined as the lower part of the Poorman Formation and the upper part of the Poorman which is a metasedimentary carbonate mica phyllite (Caddey and others, 1991). Other formations in this figure include the Homestake Formation (brown), and the Ellison Formation (blue).

Only two geologic units were encountered during the drilling and site characterization of Test Bed 2. These were the rocks of the Yates Unit, a metamorphosed tholeiitic basalt, and a rhyolite intrusive that was encountered in Borehole TV4100. The amphibolite in the test bed consists of an assemblage of amphibole, chlorite, and plagioclase that is generally massive although a weak foliation can be recognized where the rock is freshly exposed. The rock faces usually are not well well-exposed because dust and surface alteration have accumulated over the extended time since it was mined. Work in the test bed was confined to the amphibolite, and the test bed was designed to avoid the rhyolite.

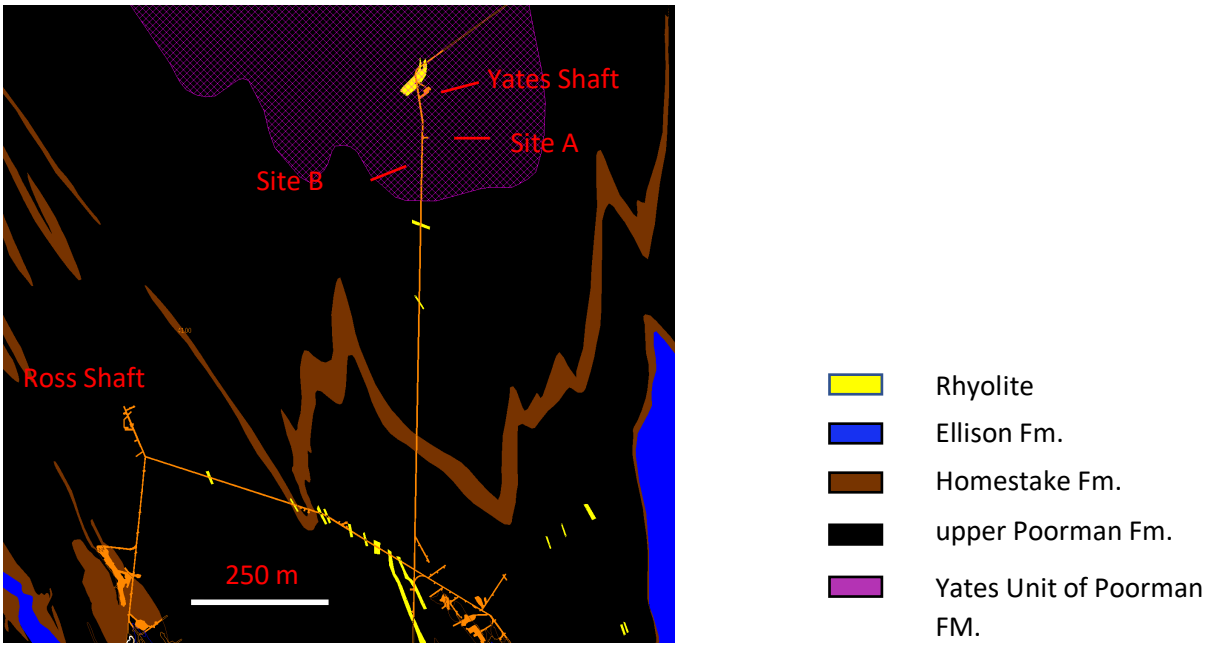

Figure 1. Geologic map of the 4100 Level. The map units are all Paleoproterozoic (Precambrian) in age with the exception of the rhyolite which was intruded during the Paleogene (early Tertiary). The rhyolite is only mapped where encountered in drifts and drill holes.

Amphibolite

Figure 2 is a photomicrograph of an amphibolite sample from a measured depth of 63 ft (19.2 m) in Borehole TV4100. All depths referred to in the discussion are measured depths along the length of the boreholes. The texture of the amphibolite is controlled by alignment of the elongated hornblende crystals producing a nematoblastic texture. Semi-quantitative analysis using X-ray diffraction (XRD analysis) of amphibolite from a measured depth of 106.5 ft (32.5 m) of TV4100 (Fig. 3) shows that hornblende makes up the bulk of the mineralogy with significant amounts of chlorite and feldspar. Caddey and others (1991) noted that chlorite probably was not a major original constituent of the amphibolite in most areas but can occur in moderate amounts locally.

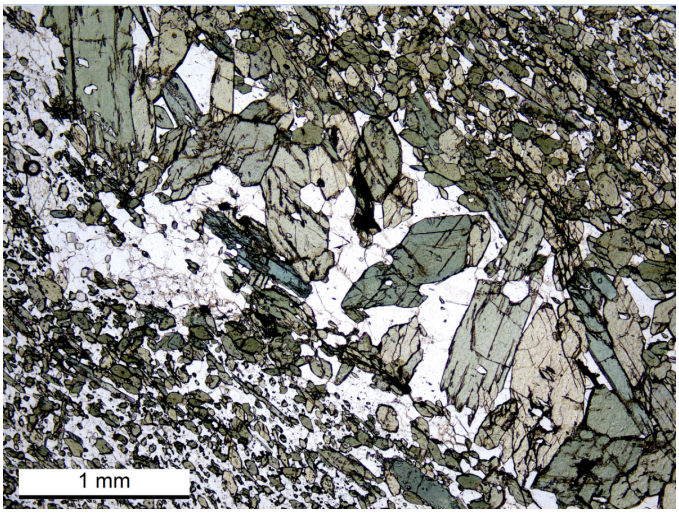

Figure 2. Photomicrograph from TV4100 amphibolite (63 ft) showing a nematoblastic fabric of the amphiboles (small green grains). The clear minerals in the photograph are plagioclase.

Hornblende - 59%

Chlorite – 25%

Feldspar – 15%

Quartz – 0.5%

Figure 3. Semiquantitative X-ray diffraction (XRD) analysis of a sample of amphibolite from 106.5 ft (32.4 m) measured depth in borehole TV 4100.

Rhyolite

Borehole TV4100 was the first hole to be drilled and was a test to begin determination of the mechanical and petrologic characteristics of the testbed. Rhyolite intrusives were encountered in the borehole, and these bodies apparently are exposed in the 4100 Level drift to the northeast near the Yates Shaft. The intersection in TV4100 represents the downward continuation of that intrusive body. Once the rhyolite was located, the Test Bed was designed to work in the volume above the rhyolite to reduce complications that might be due to the differences in lithology and geomechanical behavior.

Table 1: XRD Analysis of Rhyolite Samples

Sample	Description	Alkali Feldspars	Quartz	Calcite	Pyrite	Clay	Muscovite
HYS-1	Rhyolite near Yates Shaft	67.7%	29.4%	1.2%	1.0%		0.6%

TV4100	Rhyolite from 106.7 ft of TV4100	54%	28.9	1.6%		15.5%	

The appearance of the two rhyolite occurrences is markedly different in that the rhyolite from near the Yates Shaft is a fresh and unaltered igneous body whereas the rhyolite found in TV4100 has clearly been altered. Much of the alkali feldspars in the rhyolite of TV4100 have been converted to clay with the centers being particularly subject to alteration. The altered rhyolite is easily distinguishable from the fresher material in hand specimen. The type of clay shown in Table 1 was not determined as part of this XRD analysis but probably is kaolinite given it association the altered feldspars.

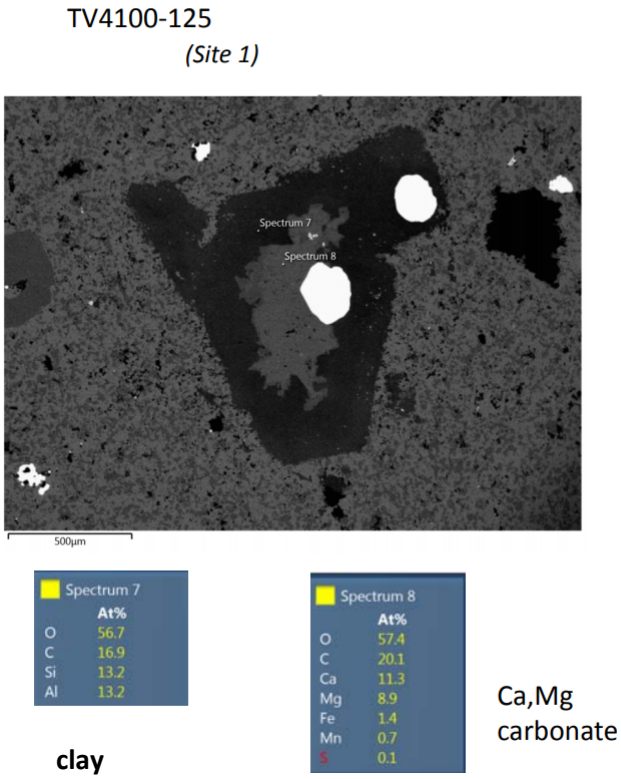

Figure 4. Scanning electron microscope (SEM) image derived from the TV4100 rhyolite at 125 ft (38.1 m) showing the effects of hydrothermal alteration of what was probably a potassium feldspar. Compositions shown are in atomic percent. The rim of the original potassium aluminum silicate was replaced by kaolinite (Spectrum 7), and Spectrum 8 shows that the interior was replaced by calcite. In many instances, the interior of these types of grains has large pore spaces.

Fractures and Fracture Fillings

Fractures encountered during drilling of the monitoring, production, and injection result from episodes of fracturing during Precambrian deformation and Tertiary-age uplift and intrusion.

Precambrian fractures –

These fractures are healed with no discernable permeability and are often folded and dominated by quartz filling. An example of these fractures, as well as Tertiary-age fractures is shown in Figure 5 where the Proterozoic fractures tend to be parallel to the weak foliation in the amphibolite. Other Precambrian features recognized during core examination includes frequent occurrences of what is termed non-mineralized shears. They are subtle features that show shear structures related to the presence of chlorite. These small-scale structures in the cores do not have calcite or quartz as fillings and their effect on potential fluid flow appears to be minimal.

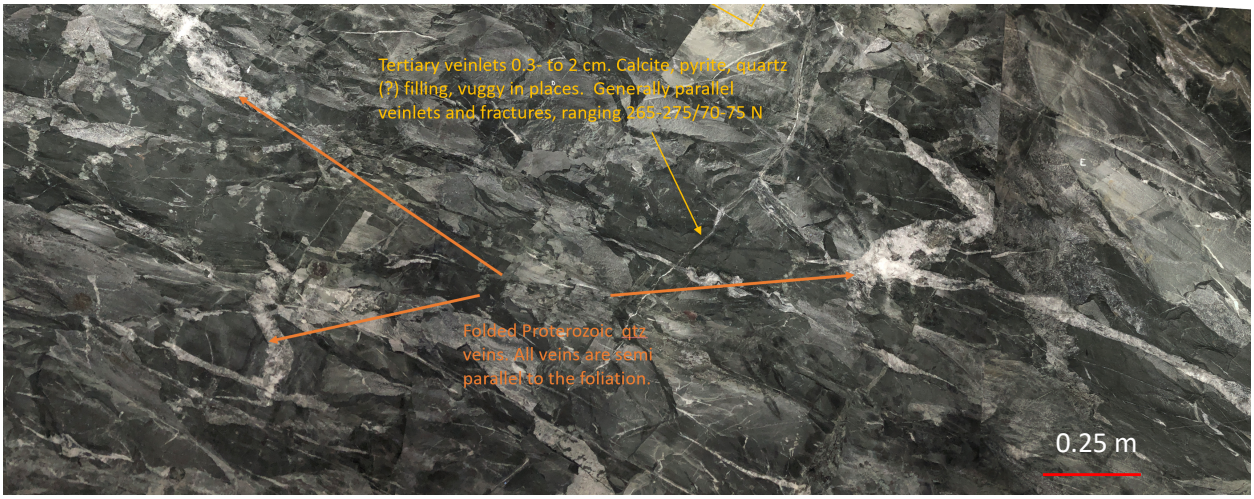

Figure 5. Portion of the freshly excavated face on the east side of Site B in the EGS Collab Test Bed 2. The fractures and fracture fillings shown as Precambrian age are folded and generally parallel to the foliation that can be seen in Site B. The cross-cutting fractures are interpreted as being related to Tertiary-age deformation.

Healed Tertiary-age fractures –

Figure 5 also shows one of these features that cross-cut the Precambrian fractures, and it has infrequent small open pore spaces distributed along its trace. The fracture filling is often an intimate intergrowth of calcite and quartz but can also consist of other minerals typically associated with the intrusion of such silicic bodies (Fig. 6). This figure from AMU 11.5 ft (3.5 m) shows an intersection exposing a euhedral fluorite crystal. An XRD analysis of a pink mineral identified in several boreholes proved to be anhydrite which is a common mineral associated with the first stage of mineralization associated with the silicic intrusions at Homestake (Uzunlar 1993). Many of the thin (1-2 mm) healed fractures that are probably Tertiary in age have halos of lighter color that have thicknesses of 1-3 mm and that are symmetrically parallel the fractures. All cores acquired during drilling of the test bed were HQ in size with a nominal diameter of 63.5 mm.

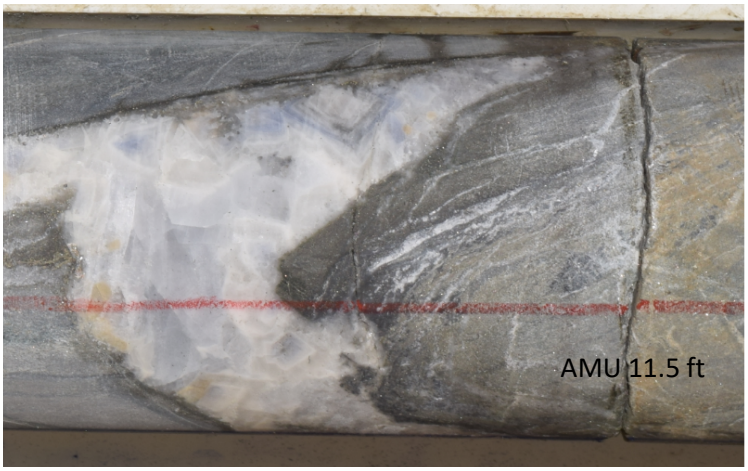

Figure 6. Photograph of core from AMU at 11.5 ft (3.5 m) that is a large, healed fracture containing euhedral purple fluorite. This is HQ core with a nominal diameter of 63.5 mm.

Tertiary-age fractures with small pore spaces --

Not all Tertiary fracturing resulted in porosity that was filled entirely. Infrequently, small, unconnected pores with apparently little or no connected permeability were preserved. Figures 7 and 8 show occurrences of this type of permeability. Figure 7 is a photo of a single vuggy pore from hole E2-TS at a depth of 207 ft (63.1m) that was developed in a brecciated zone which was not entirely healed. Permeability measurements using a handheld permeameter were not successful in identifying any measurable permeability.

Figure 7. Single vuggy pore, ~207' (63.1 m) depth, E2-TS. An attempted permeability measurement using a NER "Tinyperm" permeameter was unsuccessful because values were below the instrument's limit.

A zone of small pore spaces was encountered in hole E2-DMU and the color change as well as the prominent layered aspect of the core suggests that this was an area of shearing and deformation. Although rare, the changes from dark gray of the amphibolite to the brown and sometimes green coloration marks areas of chemical change due to hydrothermal alteration.

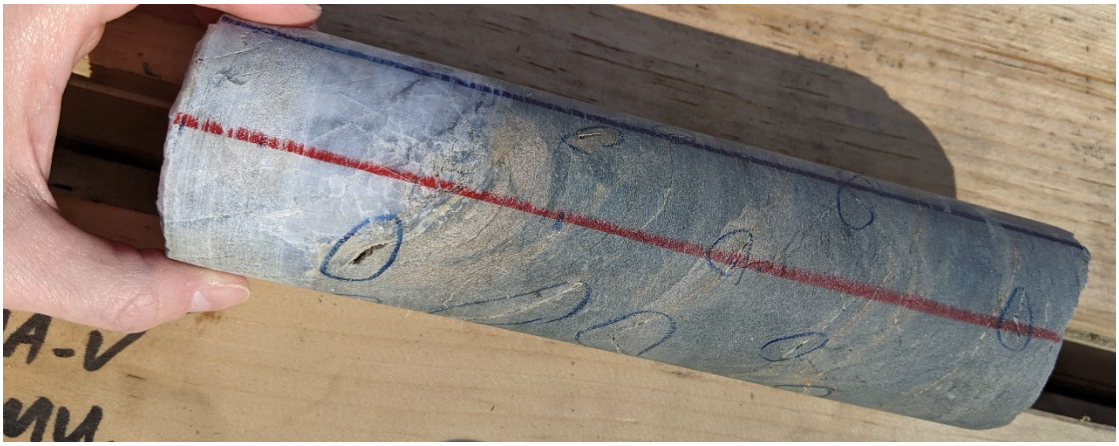

Figure 8. Pore spaces found at ~163' (49.7 m) depth, E2-DMU. Handheld permeability measurements were unable to identify any measurable permeability.

Tertiary-age open fractures –

Large open fractures were found in hole AML at a measured depth of 183 ft (55.8 m) (Fig. 9). The core was intact, and the open portion of the fractures did not extend across the total diameter of the core. Therefore, the aperture shown is the actual width *in situ*, but the lateral extent of the large openings is not known. The section is developed within a heavily fractured and altered zone and may simply be a larger analogue to the isolated microporosity found in other drillholes.

Figure 9. Photograph of the HQ core at 183 ft (55.8 m) in borehole AML. This altered section of amphibolite contains large open fractures with abundant, almost stockwork-like, fractures along with marked changes in color. Note for comparison the unaltered section of amphibolite at the top and bottom of the picture.

Further insights regarding the alteration products encountered were provided by analyses of a heavily altered section encountered at a depth of 218.5 ft (66.6 m) while drilling E2-TL (Fig. 10). The 0.3 m long

section of amphibolite has been altered to a gray-green color, and the central section marked by the arrow is a clay layer that is ductile and plastic. This layer probably represents the area of localized and intensive shearing that provided a pathway for fluids producing the changes in the chemistry of the amphibolite. Sections in other boreholes show similar color modifications although they do not have open porosity nor development of such a clay layer.

Clay composition of the section indicated by the arrow was determined using semi-quantitative XRD analyses as shown in Figure 10. The clay mineralogy was determined using the glycolation and heating procedures described in Poppe and others (2001). Comparisons with the analyses in the adjacent dark amphibolite and with the analysis listed in Figure 3, show that amphibole was removed, and carbonate was introduced along with conversion of hornblende to clay minerals. It also appears that potassium was introduced as well, which points to the intrusion of the nearby rhyolite as a source of the fluids. The small amount of amphibole found in the clay seam is probably due to incorporation of small grains of unaltered hornblende. The adjacent green altered section has a composition similar to the clay seam although it does not show the addition of potassium, but it does show the alteration of the hornblende to illite.

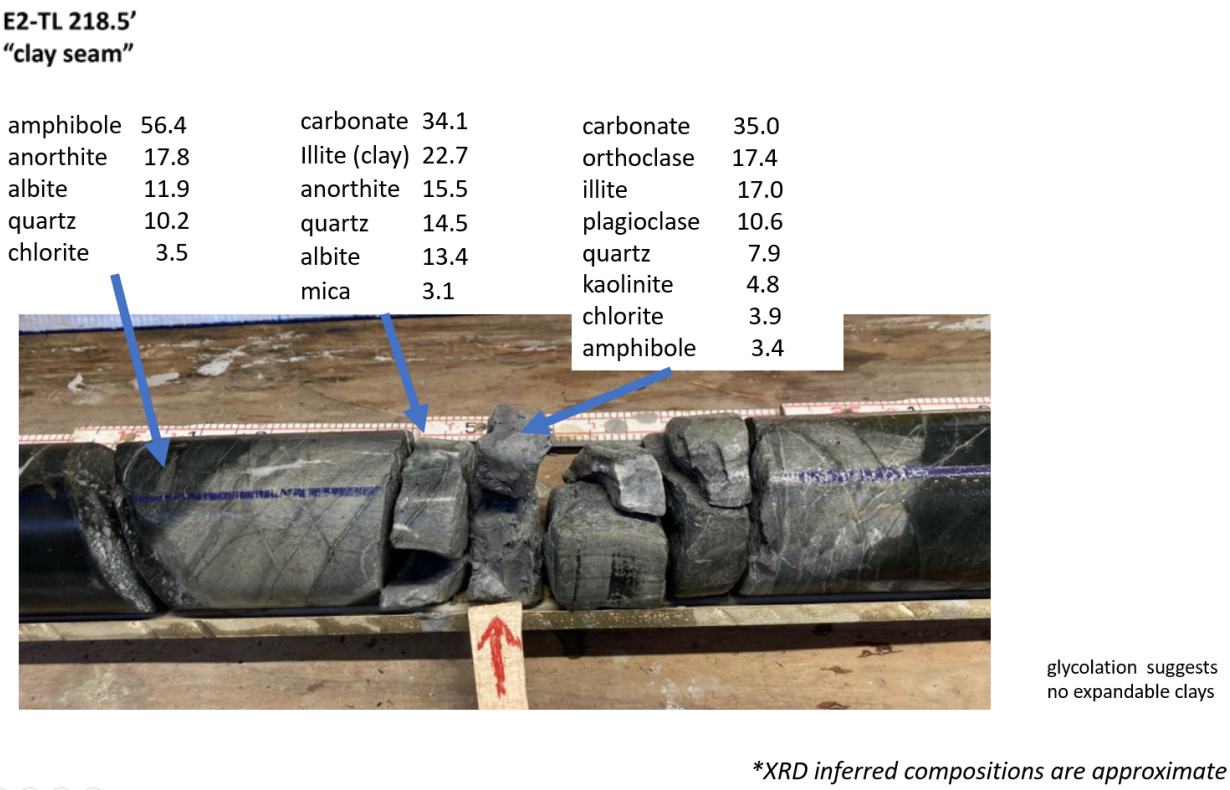

Figure 10. Heavily altered area of E2-TL at a depth of 218.5 ft (66.6 m). The altered section shows a sharp boundary between the unaltered amphibolite and the altered section, and the boundary appears to be bounded by a fracture surface. The center of the altered section was marked by a clay layer which was ductile and easily deformed. The approximate compositions of the various sections of the altered material were estimated from XRD analysis. In general, it appears that the primary changes in mineralogy due to the alteration are elimination of amphibole and production of carbonate and illite, the latter of which was determined by repeated XRD analysis of glycolation and heating as specified by Poppe and others (2001). The chlorite content remains the same across the altered area and the overall feldspar content is also constant. Although the relative proportions of alkali feldspars to calcic plagioclase changes, this may just be due to ambiguities in determining the types of feldspars using XRD analyses.

References Cited

Caddey, S. W., Bachman, R. L., Campbell, T. J., Reid, R. R., and R. P. Otto (1991). Chapter J: The Homestake Gold Mine, An Early Proterozoic Iron-Formation Hosted Gold Deposit, Lawrence County, South Dakota, U.S. Geol. Surv. Bull. 1857-J.

Poppe, L.J., Paskevich, V.F., Hathaway, J.C., and Blackwood, D.S., 2001, A Laboratory Manual for X-Ray Powder Diffraction, U. S. Geol. Surv. Open-File Report 01-041.

Uzunlar, N., 1993, *Genesis of Tertiary Epithermal-Mesothermal Gold-Silver Deposits in the Lead-Deadwood Dome, Northern Black Hills*, South Dakota, unpub. Ph.D. dissert., South Dakota School of Mines and Technology, Rapid City, SD, USA.

Appendix E – Hole Locations, Registration of Core to Geophysical Logs, and Seismic Calibration Locations

Bill Roggenthen

Hole Locations and Registration of Core to Geophysical Logs

The location of the boreholes used in Testbed 2 were determined by surveying and were tied to the original Homestake coordinates (a set of coordinates consistently used in the much of the Homestake mine and Sanford Underground Research Facility). The survey was complicated by a lack of established reference on the 4100 Level of SURF. Therefore, the reference coordinate system used on this level for EGS Test**b**ed 2 was acquired using the corners of the Yates Shaft on this level and then transferred to the pertinent boreholes and reference points of Testbed 2. The hole locations are shown in the following table (Table 1) that shows the center of the borehole and the position of a small dot on the top of each casing. The geophysical log depths are registered to the top of the casing which was grouted into place after drilling. The top of the casing is threaded and has a removable flange. However, the logging measurements are registered to the top of the casing and not the top of the flange as the top of the casing is not expected to change whereas it might be possible to change the flange type and thickness in the future.

Table 1. Location of Tops of Boreholes.

20-4530 Berkeley Lab 4100L survey data from 20 September 2021 effort					Units are Homestake Coordinate system assumed from improvements in US Survey Feet											
Submitted by Professional Mapping and Surveying 22 September 2021 by Rand Deibert																
Survey Point Number	northing	easting	elevation	code	Codes	Long Name										
800	-2830.032	3992.619	1126.963	CL E2-AMU	CL	Centerline	(suffix is boring name)									
804	-2830.037	3992.284	1126.881	E2-AMU AZ1	REF	Reference Mark punch on top of casing (0.05 meters back from end of casing) (prefix is boring name)										
805	-2829.235	3987.768	1127.538	E2-AMU AZ2	AZ 1	One of two locations for Azimuth, elevations represent tilt/dip (prefix is boring name)										
809	-2830.052	3992.792	1127.125	E2-AMU REF	AZ 2	One of two locations for Azimuth, elevations represent tilt/dip (prefix is boring name)										
802	-2832.035	3991.442	1124.870	CL E2-AML												
806	-2831.277	3986.267	1129.018	E2-AML AZ1												
807	-2832.012	3991.070	1125.004	E2-AML AZ2												
810	-2832.082	3991.694	1124.886	E2-AML REF												
811	-2863.206	3960.224	1127.642	CL E2-DMU												
815	-2863.302	3960.401	1127.841	E2-DMU REF												
816	-2860.969	3955.822	1127.696	E2-DMU AZ1												
817	-2863.020	3959.884	1127.549	E2-DMU AZ2												
812	-2863.458	3960.433	1126.579	CL E2-DML												
814	-2863.607	3960.665	1126.604	E2-DML REF												
818	-2860.630	3956.195	1129.883	E2-DML AZ1												
819	-2863.285	3960.090	1126.673	E2-DML AZ2												
827	-2997.687	3960.827	1125.624	CL E2-TL												
832	-2997.930	3960.523	1125.637	E2-TL AZ1												
833	-3000.612	3957.026	1127.242	E2-TL AZ2												
847	-2997.555	3961.015	1125.712	E2-TL REF												
828	-2997.981	3961.563	1126.348	CL E2-TN												
834	-2998.328	3961.300	1126.313	E2-TN AZ1												
835	-3001.019	3959.038	1126.973	E2-TN AZ1												
846	-2997.808	3961.715	1126.476	E2-TN REF												
829	-2999.400	3963.576	1126.454	CL E2-TC												
836	-2999.599	3963.320	1126.423	E2-TC AZ1												
837	-3001.635	3961.058	1127.313	E2-TC AZ2												
845	-2999.253	3963.775	1126.573	E2-TC REF												
830	-3000.737	3964.045	1127.013	CL E2-TU												
838	-3001.070	3963.668	1126.936	E2-TU AZ1												
839	-3003.113	3961.292	1127.300	E2-TU AZ2												
844	-3000.598	3964.223	1127.164	E2-TU REF												
831	-3001.770	3964.184	1126.113	CL E2-TS												
840	-3002.036	3963.805	1126.114	E2-TS AZ1												
841	-3003.896	3961.190	1127.043	E2-TS AZ2												
843	-3001.635	3964.384	1126.233	E2-TS REF												
853	-3012.009	3955.119	1123.450	GYRO MARK FLOOR MAG NAIL												
854	-3028.623	3960.146	1129.941	GYRO MARK RIB SCREW												

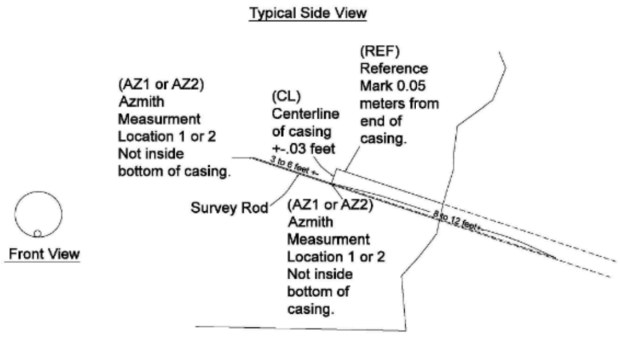

The core depths for each of the core runs were provided by the driller and generally were related to where the initial run began in relation to the rock face. As a result, the core depth does not correspond to the depths used for the geophysical logs. The following table (Table 2) provides a reference between the depth of individual features as determined from examination of core photos compared to the optical televiewer log for the wells drilled from Site B. In general, errors in those correlations are expected to be in the range of +- 0.1 m although may be greater in some instances due to uncertainties in location of depth of features noted in the core log or loss of core.

Table 2. Registration of Core to Optical Televiewer Log.

Hole Name	**Amount Core Depth less than OTV depth (ft)**	**(m)**
TC	0.91	0.28
TL	1.13	0.34
TN	0.78	0.24
TS	1.44	0.44
TU	0.98	0.30

Seismic Calibration Locations

Calibration points used for seismic calibration locations also were located by surveying. They are identified as yellow circles with a small black dot on the drift wall. These surveyed points have proven to be useful in identifying locations along the drift to map features, water inflow, or infrastructure. The locations for the points are shown in the following table (Table 3).

Table 3. Seismic calibration locations.

	SURF Coordinates (ft)					**SURF Coordinates (ft)**		
Description	**Northing**	**Easting**	**Elevation**		**Description**	**Northing**	**Easting**	**Elevation**

S-1	-2758.01	3999.726	1126.956		S-7	-2943.06	3970.155	1126.278
S-2	-2790.91	3994.419	1126.421		S-8	-2980.99	3963.764	1127.543
S-3	-2818.47	3991.186	1125.364		S-9	-3036.47	3954.997	1126.018
S-4	-2854.83	3984.619	1126.722		S-10	-3067.3	3950.652	1126.359
S-5	-2887.94	3978.965	1125.982		S-11	-3094.75	3945.863	1125.745
S-6	-2921.06	3973.136	1126.629					

Appendix F - **EGS Collab 4100' borehole core review**
Physical core review conducted Oct 5-6, 2021
Personnel: Richard Goetz (SURF), Taylor Myers (SNL, 10/5), Joseph Pope (SNL,10/5), Bill Roggenthen (SDSMT), Megan Smith (LLNL)

The discussion and photographs of the core are not detailed studies but, rather, are intended to provide examples of the textures and features encountered in the core material.

EGS Collab 4100’ borehole core review Physical core review conducted Oct 5-6, 2021

Personnel:
Richard Goetz (SURF)
Taylor Myers (SNL, 10/5)
Joseph Pope (SNL, 10/5)
Bill Roggenthen (SDSMT)
Megan Smith (LLNL)

The ‘holy grail’:

This feature is unique among the 4100’ boreholes.

This visible, open fracture (marking *huge* sustained conductivity increase to end of borehole) stands out as a bit of an anomaly

Approximate location:
AML-186-188’

Given that open fractures like the previous one (AML-186') are atypical of the 4100' core, we look instead to:

- smaller fractures, identified with small pore spaces and/or thin hairline apertures;
- isolated pockets of porosity (e.g., DMU-163');
- regions of high shear/deformation;
- "brecciation" or chaotic fracture/vein orientations;
- boundaries between contrasting textures (e.g., amphibolite 'groundmass' next to a thick alteration halo)

See examples from borehole TC in the slides to follow.

There does appear to be vein "sets" or families, that appear in similar orientations (noted in both TC and TU borehole). I count three of them (slight angle, slightly higher angle, and less frequent very high angle sets). There are cross-cutting relationships that might be of interest but for the moment, I'm not sure how this observation is helpful.

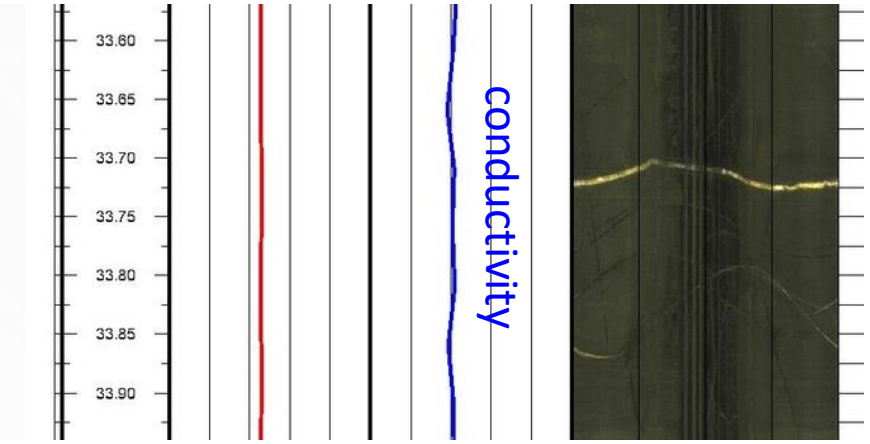

Nice little fracture.
Does not appear open in downhole camera log; did drilling “enhance” its attractiveness/aperture?

Near-transverse orientation may not be ideal?

Approximate location:
TC-109’

Slim odds of correlating across borehole until other features pinned down

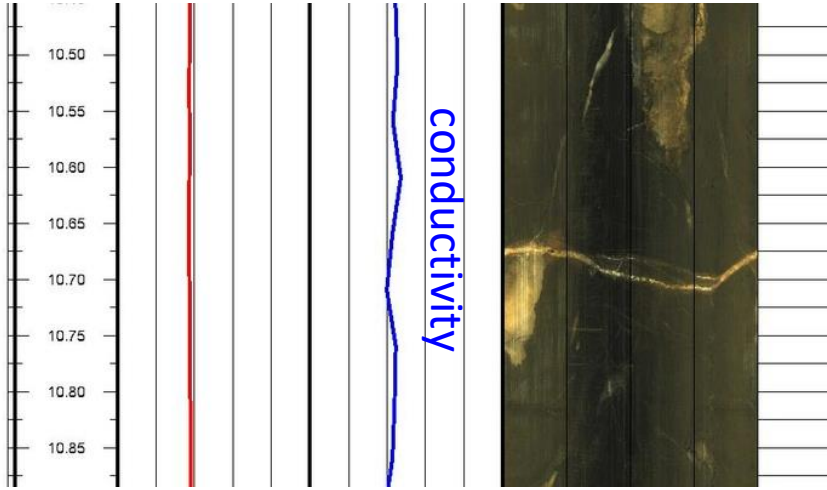

Approximate location:
TC-33.5’

This feature is too shallow to be of use, correct?

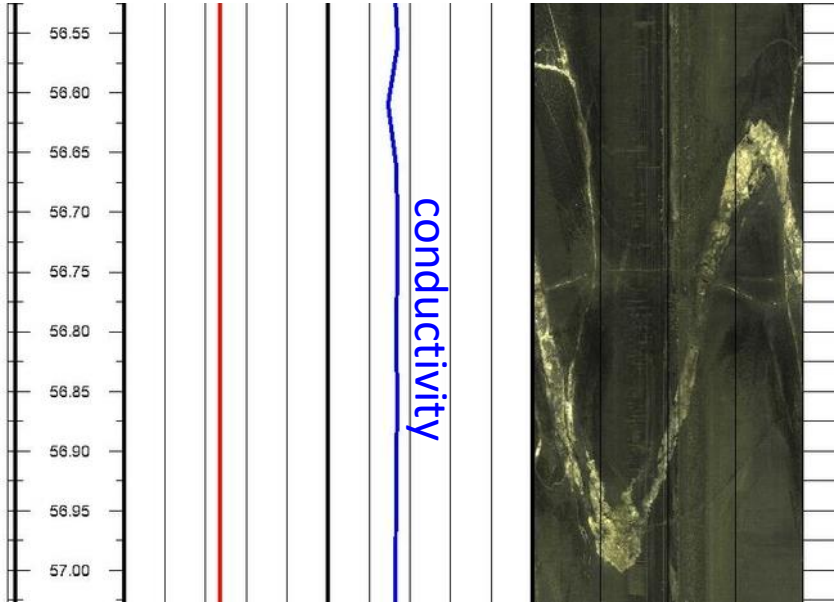

Absent obvious existing fractures, the next best bet may be associated with deviations in amphibolite ‘fabric’ or features other than the “3(ish) vein sets”

Approximate location:
TC-185.5’

Notable, “cottage cheese vein”
(B. Roggenthen)
possible correlation to TC-166’?

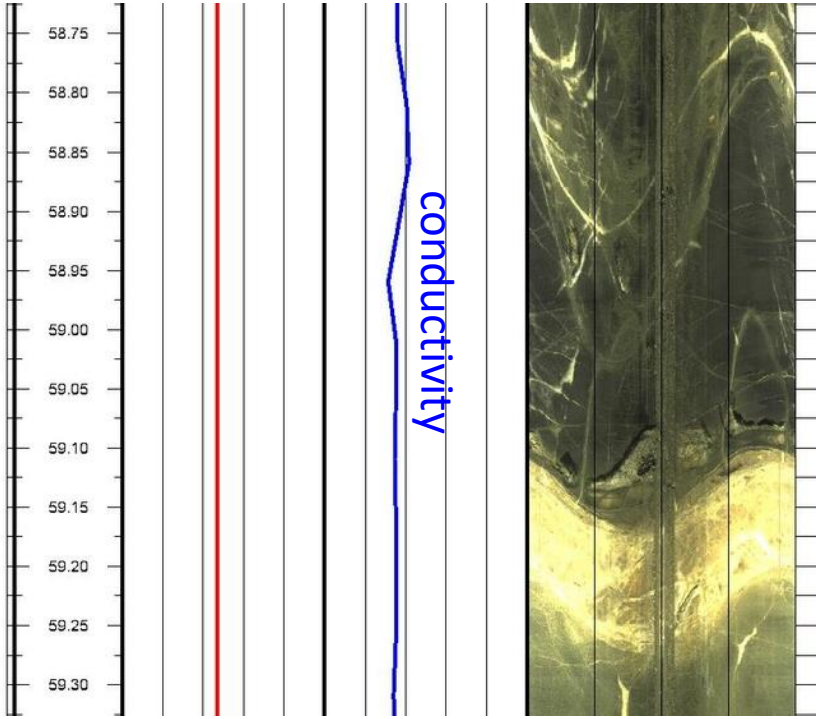

Thick feature (from 191.5’ on), intense, chaotic veining in wide alteration zone with abrupt contact with “matrix” amphibolite

Approximate location:
TC-193’

This feature (or TC-206?) may correlate with TU-226’

“brecciated” zone

Fairly extensive in length

Overall rock strength may differ from surrounding material?

Approximate location:
TC-58-60’

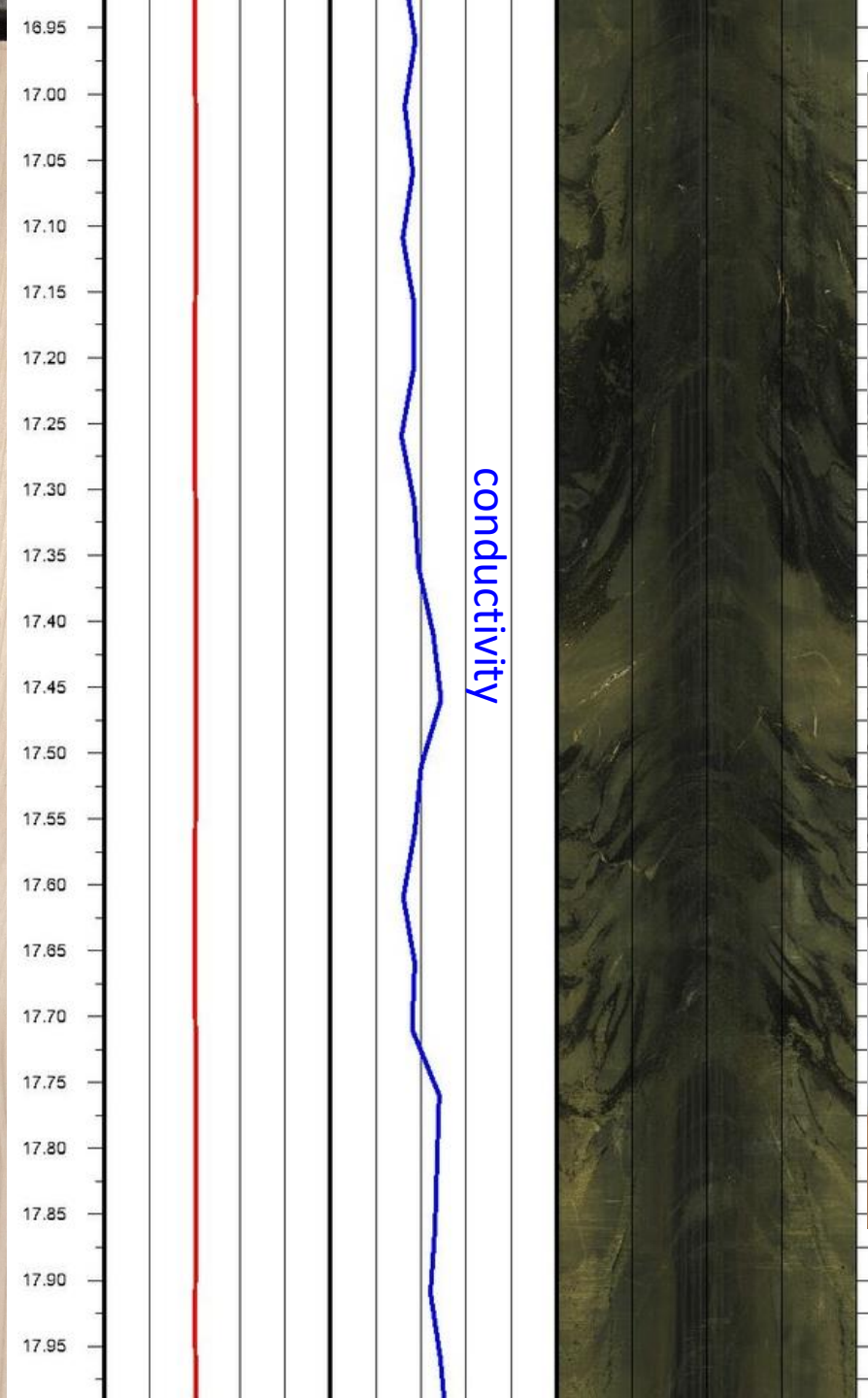

Thick poker-chipped quartz band

Useful primarily for cross-borehole correlation (TU-226’?)

Approximate location:
TC-206’

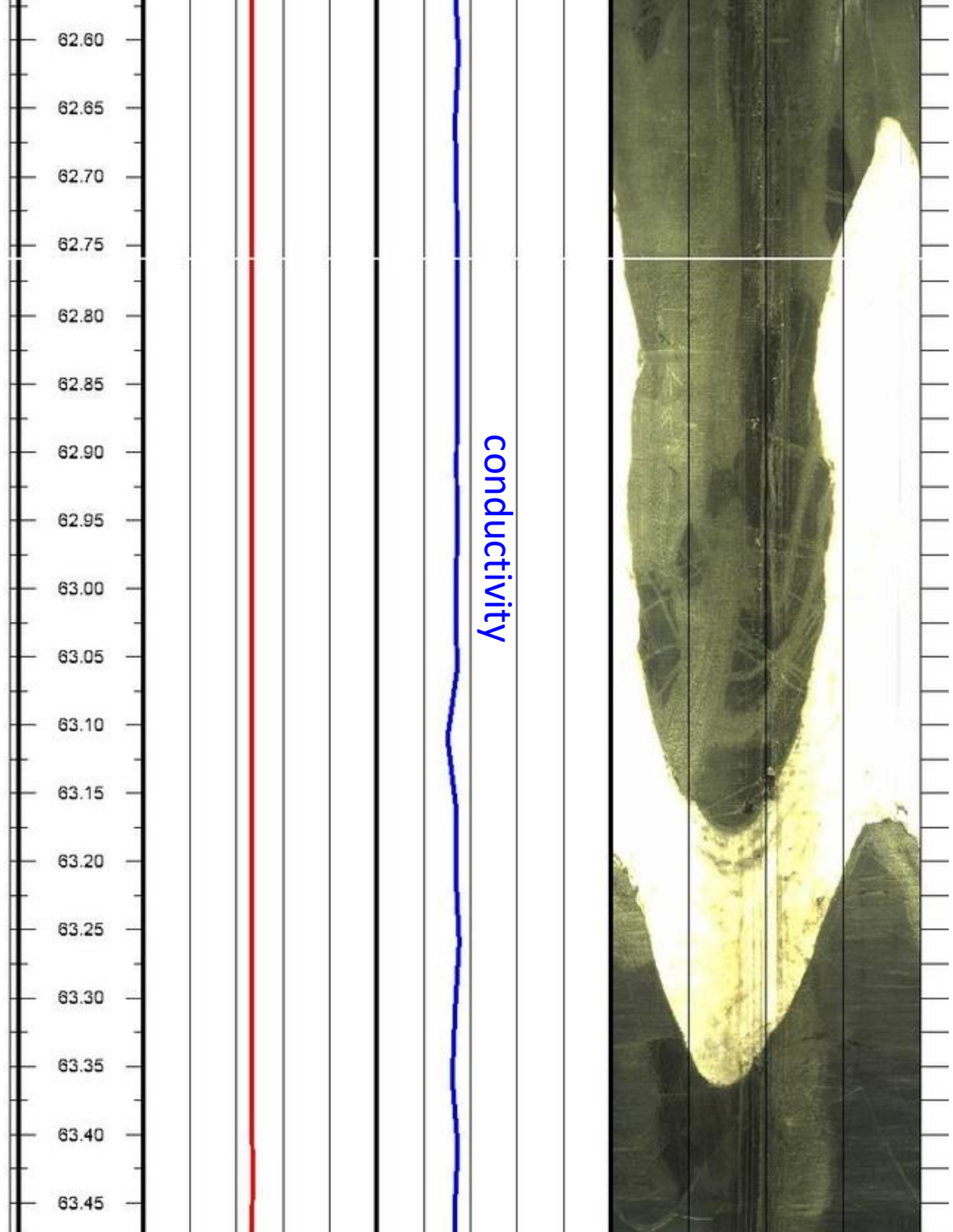

More dense veining, near-parallel to core axis.

No indication of actual fracture or porosity, simply an interesting orientation

Example section:

This is not really a serious suggestion – think of it as a straw, that I'm reaching towards…

Approximate location:
TC-237-242-EOH'

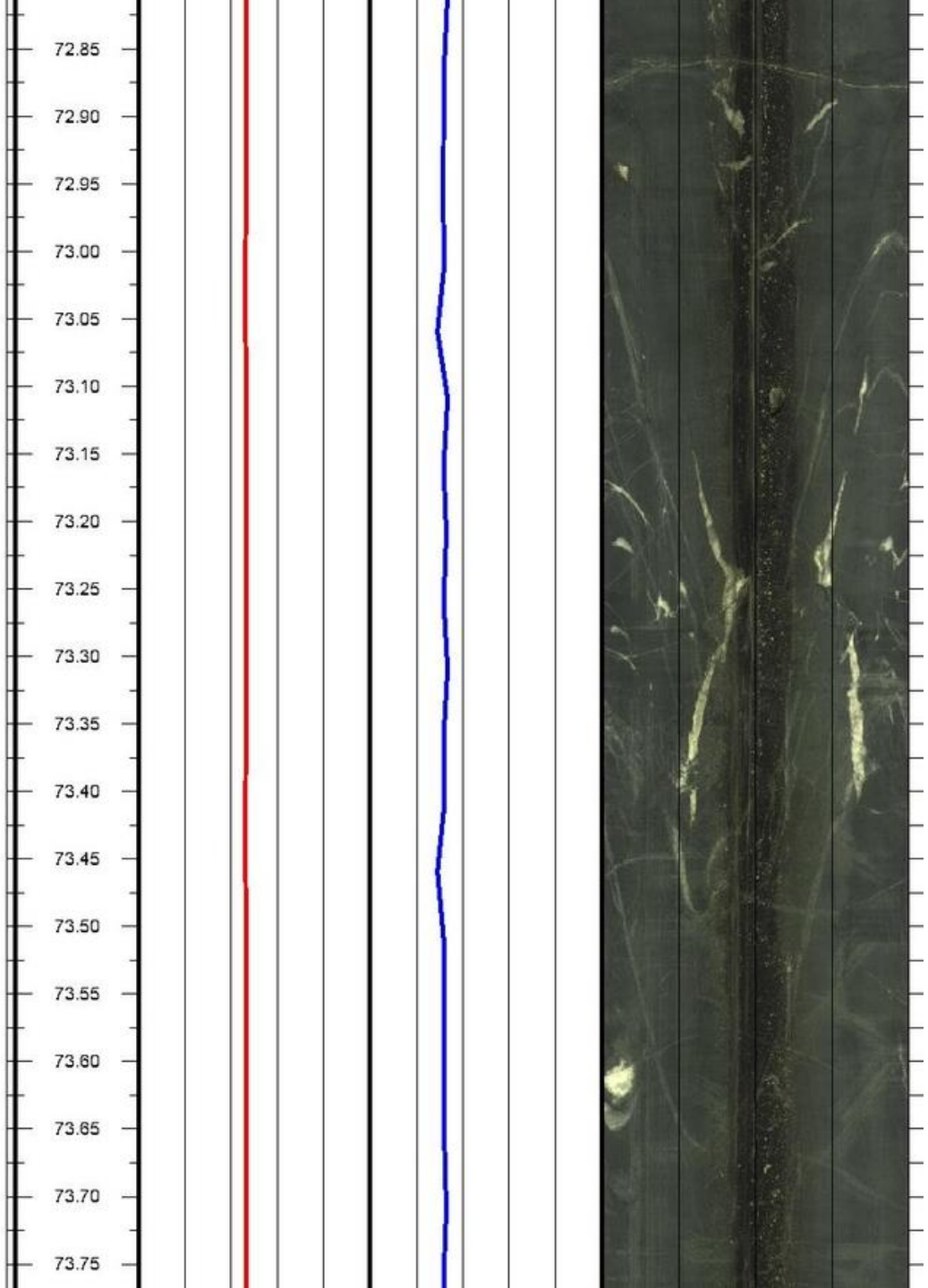

Qz/veins, TC (ft):	TC, OTV (m):
18-19	
34-36	(11-13)
47.5	(15.95-16.15)
51	
65	(20.2; 20.8)
73-74	(22.6-23.1)
85	(26.5)
89-91	(27.5-28.4)
96	(29.7)
170	(51.9-52.3)
185-186*curdy	(56.6-57)
193 (altered)	(59.2)
206	(63)

185.5 is 7.5' above
193 which is 13' above
206

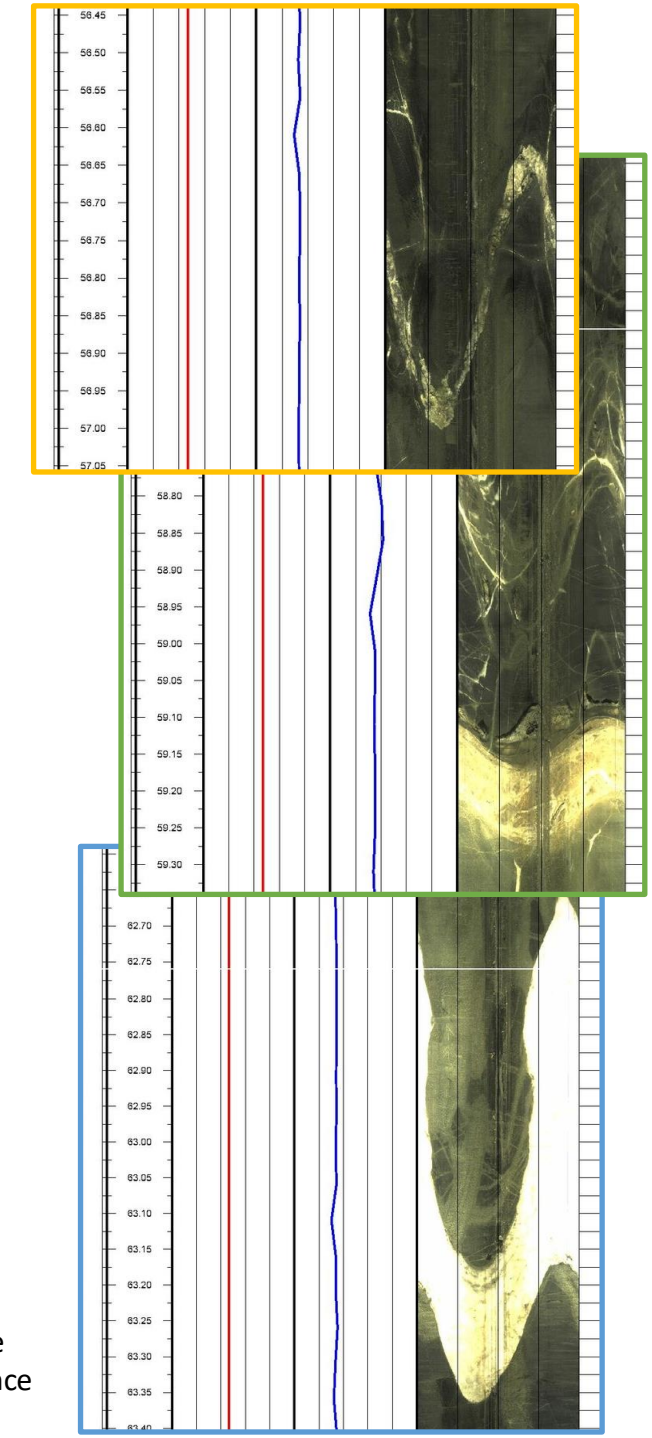

Dang that's more steeply dipping than I would have expected given the distance

TU (ft):	TU, OTV (m):
	(14.4-15.2)
	(23.3-24.1)
	(33.6)
	(47.8)
166.5-167*	(50.9)
199-200	(60.5)
225.5-226	(68.5)

Note that 199' doesn't display similar level of alteration as observed in TC

166.75 is ~33' above
199.5 which is 26.25' above
225'

these distances don't pass the laugh test… ☹

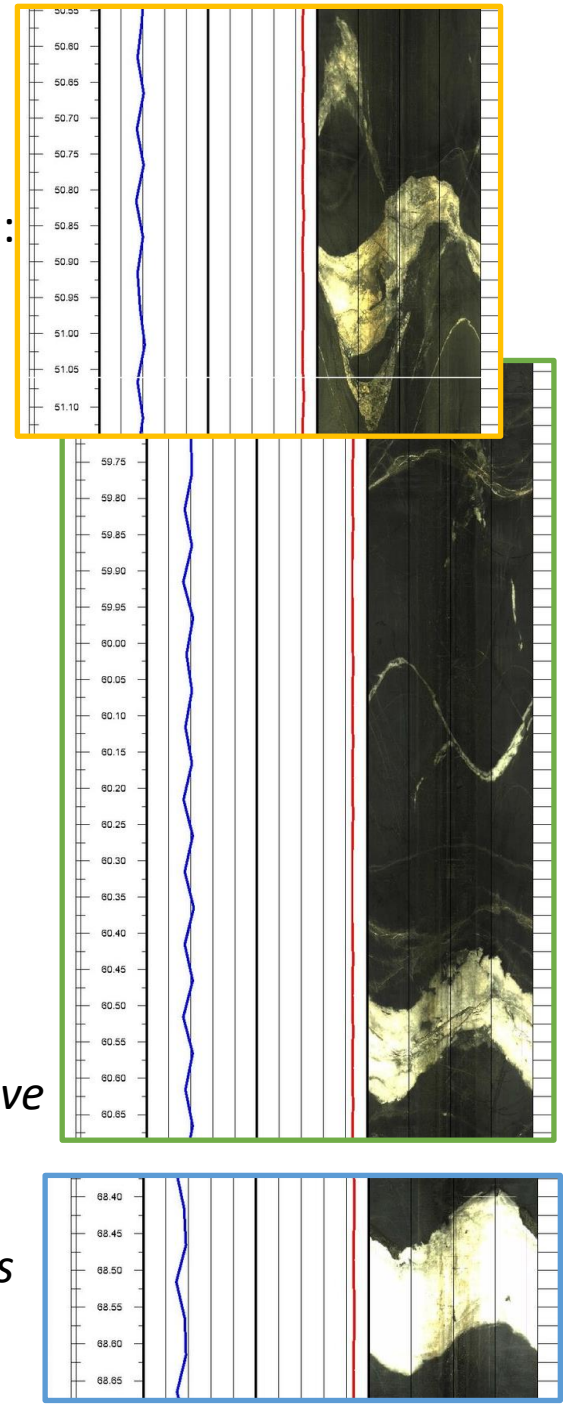

Anomaly Logs for AML, AMU, DML, DMU, TC, TL, TN, TS, TU

Bill Roggenthen

Anomaly log for E2-AML based on core logs (Feb 2021):

General Comments:

The bulk of the hole consists of amphibolite with frequent thin (0.5 mm – 3 mm) calcite-filled fractures. Occasional thicker (up to 1 cm) fractures occur and are usually filled with calcite and quartz. Zones of non-mineralized shearing characterized by planar, commutated, foliated amphibolite without calcite filling occur infrequently. These intervals are thin but often extend through the core at high angles to the core axis.

Anomalies:

8.1 – 8.2	thin non-mineralized shear zone
11.5	thin non-mineralized shear zone
19.5	thin non-mineralized shear zone
21.3	thin non-mineralized shear zone ~3mm thick
23.6 – 24.5	qtz vein 5 cm thick
36.1	two thin non-mineralized shear zones 8mm and 5 mm thick
36.6	two thin non-mineralized shear zones 7mm and 1 cm thick
63.6 – 65	5 mm wide qtz vein nearly parallel to core axis with 3 cm wide alteration halo associated with the vein
64.5	small group of pinhole porosity ((0.5 – 1mm); crystals can be seen inside of the pinhole porosity
64.9	thin fractures (0.5 mm thick) fade as they approach the alteration halo
70.9	thin non-mineralized shear zone; 6 mm thick
73.8	two thin non-mineralized shear zones
74.3	thin non-mineralized shear zone with complex internal structure
81.5	qtz layer; 1.5 cm thick but irregular
81.6 – 82	area of more intense micro-fracturing
82.6 – 83	qtz-filled fracture; very irregular and associated with micro-fracturing; alteration halo 1.5 cm thick surrounds the vein
83.2	thin non-mineralized shear zone; 6mm thick
84.7	thin non-mineralized shear zone; 4 mm thick
85.6	thin non-mineralized shear zone
88.2	two small filled fractures (1 mm) with alteration halos

117.5 – 118.5 core is one-half qtz and one-half olive green amphibolite; qtz consists of brecciated clear qtz in a matrix of cloudy qtz; amphibolite is fractured with a stockwork appearance. Possible fluorite and sanidine is associated with rare micro-vugs

134.6 2.5 cm wide shear

141.6 shear 5 mm wide

143.4 1 cm wide shear

146.2 5 mm wide qtz vein with small group of pinhole porosity

185.9 – 186.4 cloudy qtz with small (2-3 mm) wide pore space

186.4 – 186.6 open porosity lined with micro crystals. Varies from 1.5 cm wide down to 0 mm and is 7 cm long.

186.6 – 187 altered to a dark green olive color; heavily fractured

187 – 187.3 open porosity/fracture; width varies from 1.2 cm wide down to 0 mm and is 6 cm long. Fracture porosity does not continue through the core (core remained intact).

187.3 – 187.5 one 2.5 cm of the fracture appears to contain a silicified breccia

194.9 - 196 Calcite and qtz-filled fracture (3 – 5 cm wide);

Anomaly log for E2-AMU based on core logs (Feb 2021):

General Comments:

The bulk of the hole consists of amphibolite with frequent thin (0.5 mm – 3 mm) calcite-filled fractures. Occasional thicker (up to 1 cm) fractures occur and are usually filled with calcite and quartz. Zones of non-mineralized shearing characterized by planar, commutated, foliated amphibolite without calcite filling occur infrequently. These intervals are thin but often extend through the core at high angles to the core axis.

Anomalies:

0.5 – 1.25’	non-mineralized shear zone
2 – 3’	non-mineralized shear zone
3 – 4’	non-mineralized shear zone with a width of ~0.5 – 1 cm
8 – 8.4’	non-mineralized shear zone
9.1 – 3.7’	non-mineralized shear zone
10.8 – 11.5	non-mineralized shear zone
3.8 – 4.5’	fracture containing fluorite
13.6 – 14.2’	non-mineralized shear zone containing pyrite
17.6 - 18.5’	non-mineralized shear zone with pyrite
19.519.7’	non-mineralized shear zone with pyrite
21 – 21.8	non-mineralized shear zone
22.2 – 22.5	porous partially filled calcitic fracture ~1mm wide
26.2 – 27	calcite-filled shear zone ~3mm thick
33.5 – 34	quartz-calcite filled shear zone ~1 cm thick
36.8	isoclinally-folded quartz/calcite fill fracture 2-3 mm wide at 36.8’
38.8	pyrite filled shear zone + calcite
37.4	amphibolite with feldspar (pink) and quartz (lampohyre [*sic*]) with pyrite throughout
37.7 – 40.2	amphibolite with feldspar (pink) and quartz (lampohyre [*sic*]) with pyrite throughout

Note: examination of the core shows that the section described here has a cataclastic texture where qtz was comminuted to medium size rounded grains and the amphibolite similarly was micro-brecciated. This occurrence is interpreted as a fault gouge.

41.3 – 42	amph + feldspar + quartz (lamprophyre)
43 - 44	amph with qtz and plagioclase feldspar (lamprophyre)

45.3 – 45.9 porous partially-filled fracture 1mm wide

49.4 non-mineralized shear zone

53 non-mineralized shear zone

57 – 57.4 thick quartz zone with brecciated amphibolite

68 – 69 non-mineralized shear zone

75.5 – 75.8 non-mineralized shear zone qtz mineralization on outer edges (perhaps ~2 cm thick?)

81 - 81.3 non-mineralized shear zone ~1 cm thick

90 – 94 qtz vein at 60° from core axis. Mostly homogeneous with some amphib stringers

95.7 non-mineralized shear zone

97.8 non-mineralized shear zone; porous with pyrite

126.1 – 126.5 qtz filled fracture with calcite

127.7 - 128.3 calcite mineralized shear zone with qtz

144 porous fracture

145 non-mineralized shear zone with pyrite

168.9 porous partially-filled calcitic fracture

192 – 192.5 breccia qtz/amph

Anomalies with non-mineralized shear zones removed for clarity

3.8 – 4.5' fracture containing fluorite

22.2 – 22.5 porous partially filled calcitic fracture ~1mm wide

36.8 isoclinally-folded quartz/calcite fill fracture 2-3 mm wide at 36.8'

37.4 amphibolite with feldspar (pink) and quartz (lampohyre [*sic*]) with pyrite throughout

37.7 – 40.2 amphibolite with feldspar (pink) and quartz (lampohyre [*sic*]) with pyrite throughout

Note: examination of the core shows that the section described here has a cataclastic texture where qtz was comminuted to medium size rounded grains and the amphibolite similarly was micro-brecciated. This occurrence is interpreted as a fault gouge.

41.3 – 42 amph + feldspar + quartz (lamprophyre)

43 - 44 amph with qtz and plagioclase feldspar (lamprophyre)

45.3 – 45.9	porous partially-filled fracture 1mm wide
57 – 57.4	thick quartz zone with brecciated amphibolite
90 – 94	qtz vein at 60^{o} from core axis. Mostly homogeneous with some amphib stringers
126.1 – 126.5	qtz filled fracture with calcite
144	porous fracture
168.9	porous partially-filled calcitic fracture
192 – 192.5	breccia qtz/amph

Anomaly Log DML

24.5-25.1	2.5 cm wide qtz/feldspar-filled fracture with calcite; about 60^{o} from core axis
26 26.5	calcite-filled fractures with bleached halos (1-2 mm wide)
68	fracture with feldspar and kaolinite(?); amph is altered around fracture
71.5 – 72	shear zones with calcite ~1.5” wide
93.7	feldspar + calcite in fracture (thin)
96.5	calcite-filled fractures (1-4 mm width) some with feldspar and pyrite
102.5	shear zone with calcite 2 cm wide; 75^{o} from core axis
105.1	shear zone (2-3 cm width) with some calcite
106.5	calcite-filled fractures and one calcite/feldspar fracture
110.5	calcite/feldspar-filled fracture and shear zones
113.3	feldspar/calcite fractures (thin)
114.5	feldspar/calcite fractures (thin)
118.5	feldspar/calcite fracture (thin)
125.5	feldspar/calcite fracture (thin)
163.5	calcite-filled fractures (<= 1 mm width) with bleached halos
172.4 174	sanidine + calcite-filled fractures (~1 cm width)
173.7-177	shear zone with lots of feldspar + pyrite and amph
181	EOH

Anomaly Log E2-DMU

ft.	
3.45	halo
16.3	might be halo or could be thin nms
63.9	small filled, white fracture that is 9 mm thick
71.6	halo; three closely-spaced fractures with indistinct halos
78.4	thin massive qtz vein; 15 mm thick
79.2	diffuse halo; 3 cm thick surrounding fracture
81.95	fracture with sheared (?) filling; ~1 mm thick
99.3	thin massive qtz vein; 1.5 cm thick
101.9	halo
111.1	halo
116.2	halo
123.9	very thin qtz vein; 9 mm thick
125.4	very thin qtz vein with dark streaks; 9 mm thick
130.4 and 130.5	two fractures that appear to be filled with sulfides
131.9	halo (two fractures)
133.4 – 133.8	four halos
135.7 – 136.5	zone of shearing (?)
139.5	very well developed small fold
150.9	halo but thick (12 mm)
156.6	shows relative age; thin fracture cutting thicker; relation between two fracture sets
157.3 – 158.3	rock has a distinct layered fabric; may be rock fabric rather than fractures
159.5	more rock fabric
160.5	brown zone 15 mm thick; offset by irregular white fracture
162.05	* two instance of small pore spaces developed along healed fracture
162.25	*string of open pore space along filled fracture
162.3 – 162.6	massive qtz vein (extends into next core run)

165 – 165.4	continuation of massive qtz vein; total thickness appears to be 0.85 m; bottom boundary irregular
170 – 173	layered rather than closely-fractured
173.3	massive qtz vein; 4.5 cm thick
180 EOH	

Anomaly Log for E2-TC:

The amphibolite of E2-TC is similar to that found at Site A, although a more pronounced foliation/layering was observed in the shallow part of the hole. Thin, filled fractures occur frequently and fractures/ft of 15 or more are common.

The core descriptions below are taken from the core description sheets. Editorial notes are added inside square brackets [ ]

Anomalies of interest include:

6.4 ft	pronounced foliation
8.5	pronounced foliation
37.4 – 41	thick quartz vein
43.4 – 44	shear zone with minor elongate pitting
51.2 – 52	shear zone with crenulated folding
58.2 – 59	calcite-healed breccia zone 4 – 20 mm thick
88.7 – 90.8	thick quartz vein
109.2	break along fluorite [white, good cleavage, hardness 4, does not react to HCl] vein with minor pyrite. Possible open fracture
	[Note: the occurrence is on a break in the core and fitting the pieces together looks like it could have some porosity; the white marking zone is calcite and quartz (more quartz than calcite0. Do not see any development of euhedral crystals suggesting vugs, however. Picture shown as Figure 1]
131	fluorite vein with pyrite possible open fracture (1-2mm)
	[Note: the possible porosity is not convincing. The core is broken along a thin fracture (~2 mm thick), and the fit between the fractures appears to be tight. The mineral looks more like sanidine than fluorite in that it appears harder than fluorite.]
192.5 192.7	highly altered olive green, very soft
192.7 – 193	white vein, cemented breccia
204.8 – 206.5	quartz vein
	[Note: The core is partially quartz and amphibolite during this long extent.]

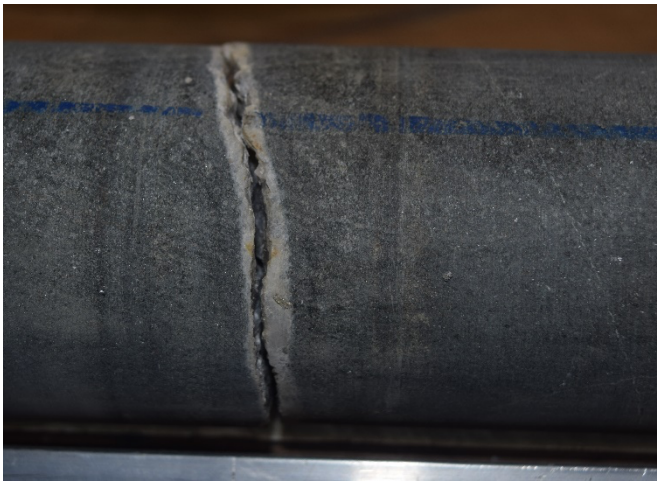

Figure 1. Possible fracture at 109.2 after fitting pieces along the drilling break, although the presence of the break may have caused some loss of material resulting in a greater aperture.

Anomaly Log E2-TL

ft.	
0 - 5	thin qtz vein parallel to core axis; 3 cm thick
2.5	massive qtz skims along one side of core; <20% of core
22.1 – 22.9	thin qtz vein that anastomoses into at least two smaller veins; 12 mm thick
32.2 – 33.9	very irregular qtz vein; occupies <20% of core
36.3 – 37	patchy qtz bodes; ~15% of core
37 – 37.8	patchy qtz continues
43.6	ribbony qtz vein; 3 cm thick
44.5	ribbony qtz vein; 4.5 cm thick
69.8	thin, qtz-rich vein nearly parallel to core; 6 mm thick
71.3	think qtz-rich vein ~parallel to core axis; 4.5 mm thick
71.8	irregular qtz vein with amphibole inclusions; 4.5 cm thick
75.7	massive qtz vein; ~9 mm thick
82.95	halo
85.8	qtz vein with irregular borders and internal structure; 4.5 cm thick
98.6	thin qtz vein with irregular borders; 3 cm thick
100.2	qtz vein with amphibole inclusions; 2 cm thick
112.6 – 113.1	three fractures with indistinct halos
120.1 – 120.5	halo fractures (two)
123.5	fracture with white filling and included dark material; has dark border (darker than country rock); 3 mm thick
124.9	fracture as above
136.4	qtz pod; irregular; 3 mm thick but stretches along the core to 137.9’
144.6	thin qtz vein; 12 mm thick
148	halo
148.4	halo
151.6	irregular qtz mass; max 3 mm thick
153,2	indistinct halo

155.3 – 155.9	irregular qtz mass; ~25% of core
157.6	thin qtz vein; 9 mm
174 – 174.3	irregular qtz mass; ~20% of core
178.6	halo
182.4 – 182.6	four fractures with halos
192	EOH

Anomaly Log E2-TN

General Comments:

E2-TN is located at Site B on the 4100 Level and is close to E2-TC, TS, and TU with generally similar characteristics. It is typically massive amphibolite with thin calcite-filled fractures. Occasional thicker veins of quartz occur.

Ft	Descriptions
8.4 – 9.6	massive quartz vein 8.5“ thick and 80^{o} to core axis
22.6 – 22.9	quartz/calcite mix occupying a portion of the core diameter
23 – 23.5	quartz/calcite/feldspar mix occupying a portion of the core diameter
36.2 – 37.4	altered zone/healed fractures; qtz/feldspar mix with amphibolite
38.6	altered grey amphibolite with qtz-filled fracture below
39.2 – 40.5	qtz, clear, semi-transparent light brown with calcite mixed in and some amphibolite
44.3 - 45	healed breccia zone with qtz/calcite
48 – 48.5	qtz-filled fracture ~6” wide
56 – 57.6	large healed shear zone with abundant pyrite and calcite
61.9 – 63.8	long section of massive quartz with many mechanical breaks – healed stress fractures parallel to the core axis
64.4	feldspar-filled fracture with altered and 1” wide bleached halo on both sides of the fracture 1”
84.5	possibly slightly porous on this thin fracture(?)
90 - 90.6	qtz-filled fracture ~0.7’ long at 30^{o} to core axis
113.6 – 115	feldspar/qtz mix filled fracture (healed)
119.7	healed shear zone, light gray amphibolite with abundant pyrite
172.7	light gray bleached altered amphibolite
183.2 – 183.7	qtz-filled healed fracture with minor calcite; amphib bleached around quartz and altered to light gray
246.5 – 247	possibly porous fractures/partially filled with calcite
251	END of E2-TN

Anomaly Log E2-TS

General Description: Generally massive amphibolite with frequent thin calcite and quartz healed fracture traces. In many locations, the hole seems to have been drilled parallel to rock fabric. Some breccia zones identified as well as the significant sections of massive amphibolite.

12 – 16.7	quartz with some amphibolite inliers, which only occupy a portion of the core diameter
24.1 – 25.5	heavily fractured section; discontinuous calcite fracturing. porosity parallel to v-shaped calcite fracture retains moisture
45 – 46.5	brecciated shear zone with pyrite, calcite, and quartz. deeper part has sanidine-filled fracture at 46.3 ft
55.2 – 56	shear zone with calcite, quartz, pyrite
57 – 58	shear zone
61 – 61.4	isolated sanidine nodules, thin calcite-filled fractures
62.8 – 63	sanidine-filled fractures
77.2 - 77.3	porous partially filled calcite fracture
80.4 – 81.3	massive quartz/quartz-filled fracture
130.8 – 131.7	quartz and quartz rubble
146.2 – 146.5	healed breccia zone/filled fracture, feldspars, qtz, calcite filled
183.9 – 184.2	quartz-filled breccia, healed
204.2 – 204.3	shear zone (thin) healed, qtz/calcite infill
207.1	small vug in calcite/qtz filled fracture
216.6	possible porous, not visible to naked eye but retains water
258.3 – 258.5	qtz breccia zone, healed with pyrite and a little calcite
266	end of hole

Anomaly Log E2-TU:

The amphibolite of E2-TU is similar to that found in Site E2-TC, although considerable problems with core recovery was encountered. This was due to the rock fabric being roughly parallel to the core axis in many instances. No large open fractures were encountered although two thin fractures with some porosity were reported.

The core descriptions below are taken from the core description sheets. Editorial notes, if any, are added inside square brackets [ ]

Anomalies of interest include:

18.4-18.7 ft	small pod of yellow-tan hard material with irregular fractures(?) in the interior and rounded irregular spheres at the top (~3 mm radius [probably ~3 mm diameter]
39.9 ft	sanidine-filled fracture ~6 mm wide
47.2-48	qtz-filled fracture 8" wide with somp amphh. And minor calcite; 45^{o} from core
48.4-49.6	qtz-filled fracture 9" wide with some amph. Nd minor calcite; 70^{o} from core axis
53.2-53.6	healed calcite filled breccia zone; 5mm wide calcite veins/nodules
76.2-78.8	qtz—massive, stress joints parallel to core axis
89.6	sanidine-filled fracture with pyrite and qtz
100.4	thin calcite-filled fractures with some porous fractures/partially-filled ~1 mm wide
116.6	sanidine-filled fracture 3 mm wide
156.3-157.4	qtz-filled fracture (~65o from core axis) 2.5" wide; qtz has parallel stress joints perpendicular to core axis)
	[Note: the diagram and extent of the indicated qtz seems to suggest that the qtz vein is wider than the noted 2.5"]
158.2-158.5	porous calcite partially filled fracture <1 mm wide
166.5-167.4	qtz/amph breccia zone/filled-fracture
198.6-199.1	qtz-filled fracture 3" wide, 30^{o} from core axis
22.5-22.6	qtz
230-230.2	healed shear zone/breccia; qtz, calcite, amp., feldspar present in core
250.5-251	qtz until the End of Core

EGS COLLAB PHYSICAL PROPERTIES

1. Jahnke, B., Ruplinger, C., Bate, C. E., Trzeciak, M., Sone, H., & Wang, H. F. (2022). Fracture toughness of schist, amphibolite, and rhyolite from the Sanford Underground Research Facility (SURF), Lead, South Dakota. Scientific Reports, 12(1), 15941. doi:10.1038/s41598-022-20031-y

Abstract.

The Cracked Chevron Notched Brazilian Disc (CCNBD) method was selected for Mode I fracture toughness tests on Poorman schist, Yates amphibolite, and rhyolite dikes from the EGS Collab site at the SURF in Lead, South Dakota. The effects of lithology, anisotropy, and loading rate were investigated. Fracture toughness was greatest in amphibolite, with schist and rhyolite having similar toughness values ($K_{amphibolite} > K_{rhyolite} \approx K_{schist}$). The effects of anisotropy on fracture toughness were investigated in the foliated schist samples. Schist samples were prepared in three geometries (divider, arrester, and short transverse) which controlled how the fracture would propagate relative to foliations. The divider geometry was strongest and short transverse geometry was the weakest ($K_{divider} > K_{arrester} > K_{shorttransverse}$). Fracture toughness was observed to decrease with decreasing loading rate. Optical and SEM microscopy revealed that for the short transverse geometry, fractures tended to propagate along grain boundaries, whereas in arrester and divider geometries fractures tended to propagate through grains. In foliated samples, the tortuosity of the fracture observed in thin section was greater in arrester and divider geometries than in short transverse geometries.

2. B. Jahnke, H. Sone, and H. Wang, EGS Collab Experiment 2: 4100 Foot Level Elastic Property Data

DOI10.15121/1798190 (https://gdr.openei.org/submissions/1270 accessed on 24 Feb. 2023)

3. C. Ruplinger, R. O'Connell, H. Sone, M. Trzeciak, and H. Wang (2020), Anisotropic fracture toughness of Poorman Schist rocks from EGS Collab Experiment 1 Site, 54th US Rock Mechanics/Geomechanics Symposium, AMRA Paper 20-2120, 6 pp.

ABSTRACT: We investigate the mode 1 fracture toughness and its anisotropy of Poorman Schist rocks recovered from the Enhanced Geothermal Systems Collaboration (EGS Collab) Experiment 1 site. The EGS Collab team is conducting a series of intermediate (10- 20m) scale stimulation and inter-well flow tests with comprehensive instrumentation and characterization at the Sanford Underground Research Facility to validate existing theories and description of hydraulic fractures propagation and associated fluid flow. An important parameter to constrain is how the fracture toughness varies depending on the orientation of the fracture and the direction of fracture propagation, which may have controls on hydraulic fracture propagation. Fracture toughness relative to foliation orientation was determined through the utilization of Cracked Chevron Notched Brazilian Disk (CCNBD) samples in three different orientations (Divider, Arrester, and Foliation Splitting/Short Transverse). Each sample group contains at least three 25.4 mm diameter and 12.7 mm thick CCNBD samples, one of each sample type. Arrester and Foliation Splitting samples were obtained from the

same sub-core while Divider samples were obtained from a separate sub-core obtained in close proximity. We found fracture toughness to be weakest in the Foliation Splitting orientation and strongest in the Divider orientation, similar to findings from anisotropic fracture toughness measured in shale rocks. Our findings on the influence of foliation orientation on fracture toughness are presented here.

4. K. Condon, H. Sone, H. F. Wang, and EGS Collab Team (2020), Low static shear modulus along foliation and its influence on the elastic and strength anisotropy of Poorman Schist rocks, Homestake Mine, South Dakota, Rock Mech. and Rock Eng., DOI: 10.1007/s00603-020-02182-4.

Abstract
We investigate the influence of foliation orientation and fine-scale folding on the static and dynamic elastic properties and unconfined strength of the Poorman schist. Measurements from triaxial and uniaxial laboratory experiments reveal a significant amount of variability in the static and dynamic Young's modulus depending on the sample orientation relative to the foliation plane. Dynamic P-wave modulus and S-wave modulus are stiffer in the direction parallel to the foliation plane as expected for transversely isotropic mediums with average Thomsen parameters values 0.133 and 0.119 for epsilon and gamma, respectively. Static Young's modulus varies significantly between 21 and 117 GPa, and a peculiar trend is observed where some foliated sample groups show an anomalous decrease in the static Young's modulus when the symmetry axis (x3-axis) is oriented obliquely to the direction of loading. Utilizing stress and strain relationships for transversely isotropic medium, we derive the analytical expression for Young's modulus as a function of the elastic moduli E_1, E_3, ν_{31}, and G_{13} and sample orientation to fit the static Young's modulus measurements. Regression of the equation to the Young's modulus data reveals that the decrease in static Young's modulus at oblique symmetry axis orientations is directly influenced by a low shear modulus, G_{13}, which we attribute to shear sliding along foliation planes during static deformation that occurs as soon as the foliation is subject to shear stress. We argue that such difference between dynamic and static anisotropy is a characteristic of near-zero porosity anisotropic rocks. The uniaxial compressive strength also shows significant variability ranging from 21.9 to 194.6 MPa across the five sample locations and is the lowest when the symmetry axis is oriented 45° or 60° from the direction of loading, also a result of shear sliding along foliation planes during static deformation.

5. EGS Collab Experiment 2 Parameter Table *Appendix G - EGS Collab Experiment 2 Parameter Table*
https://openei.org/wiki/EGS_Collab_Experiment_2_Parameter_Table (accessed on 24 Feb. 2023)

EGS Collab Experiment 2 Parameter Table

Amphibolite 4100L & 4850 L

Parameter	value	unit	source	Level
Unconfined Compressive Strengths	110 (TH4100) 295 (TV4100)	MPa	Ben Jahnke, Hiroki Sone, Herb Wang	4100L
Unconfined Compressive Strengths	182.71 81.7	MPa	Hlaydysz, 2009; Lachel Felice, 2009	4850L
Young's Modulus	89.8 - 98.0	GPa	Ben Jahnke, Hiroki Sone, Herb Wang	4100L
Young's Modulus	89 110	GPa	DUSEL, RESPEC 2010 SUSEL, RESPEC 2010	4850L
Poisson Ratio	0.17 - 0.18		Ben Jahnke, Hiroki Sone, Herb Wang	4100L
Poisson Ratio	0.23 0.28 0.3	GPa	DUSEL, RESPEC 2010 SUSEL, RESPEC 2010 Golder Associates, Jan. 2010	4850L
Shear Modulus	38.0 - 41.8	GPa	Ben Jahnke, Hiroki Sone, Herb Wang	4100L
Shear Modulus	30	GPa	DUSEL, RESPEC 2010	4850L
Bulk Density	3.04 3.02	g/cm^3	https://foundry.openei.org/5/modelparams	4100L
Bulk Density	2.925 3.01 2.7-3.1	g/cm^3 g/cm^3 g/cm^3	DUSEL, RESPEC 2010 SUSEL, RESPEC 2010 Golder Associates, 2009	4850L
Uniaxial Compressive Strength	115 200	MPa MPa	DUSEL, RESPEC 2010 SUSEL, RESPEC 2010	4850L
P-wave velocity	5660 - 5882	m/s	Ben Jahnke, Hiroki Sone, Herb Wang	4100L
P-wave velocity	~4000-7000	m/s	Roggenthen & Berry 2016	4850L
S-wave velocity	3529 - 3703	m/s	Ben Jahnke, Hiroki Sone, Herb Wang	4100L
S-wave velocity	3,532.00	m/s	Roggenthen & Koch 2013, avg value	4850L
Tensile Strength	14	MPa	DUSEL, RESPEC 2010	4850L
Differential Stress	97.7 - 105.5	GPa	Ben Jahnke, Hiroki Sone, Herb Wang	4100L
Thermal Conductivity	2.55 3.81	W/m--K	https://foundry.openei.org/5/modelparams	4100L
Heat Flow	0.08	W/m^2	https://foundry.openei.org/5/modelparams	4100L
Maximum Potential In-Situ Shear Stress	7.7	MPa	Frash, L.P., Welch, N.J., Carey, J.W. (2019). Geomechanical evaluation of natural shear fractures in the EGS Collab Experiment 1 test bed. Proceedings of the 53rd US Rock Mechanics / Geomechanics Symposium Frash, L.P., Carey, J.W., Welch, N.J., EGS Collab Team. (2019). EGS Collab Experiment geomechanical and hydrological properties by triaxial direct shear. Proceedings of the 44th Workshop on Geothermal Reservoir Engineering.	4100L
Vertical In-Situ Stress	36	MPa	Frash, L.P., Welch, N.J., Carey, J.W. (2019). Geomechanical evaluation of natural shear fractures in the EGS Collab Experiment 1 test bed. Proceedings of the 53rd US Rock Mechanics / Geomechanics Symposium Frash, L.P., Carey, J.W., Welch, N.J., EGS Collab Team. (2019). EGS Collab Experiment geomechanical and hydrological properties by triaxial direct shear. Proceedings of the 44th Workshop on Geothermal Reservoir Engineering.	4100L
Horizontal In-Situ Stress 1	37.3	MPa	Frash, L.P., Welch, N.J., Carey, J.W. (2019). Geomechanical evaluation of natural shear fractures in the EGS Collab Experiment 1 test bed. Proceedings of the 53rd US Rock Mechanics / Geomechanics Symposium Frash, L.P., Carey, J.W., Welch, N.J., EGS Collab Team. (2019). EGS Collab Experiment geomechanical and hydrological properties by triaxial direct shear. Proceedings of the 44th Workshop on Geothermal Reservoir Engineering.	4100L
Horizontal In-Situ Stress 2	18.3	MPa	Frash, L.P., Welch, N.J., Carey, J.W. (2019). Geomechanical evaluation of natural shear fractures in the EGS Collab Experiment 1 test bed. Proceedings of the 53rd US Rock Mechanics / Geomechanics Symposium Frash, L.P., Carey, J.W., Welch, N.J., EGS Collab Team. (2019). EGS Collab Experiment geomechanical and hydrological properties by triaxial direct shear. Proceedings of the 44th Workshop on Geothermal Reservoir Engineering.	4100L
Critical Pressure	9.5	MPa	Frash, L.P., Welch, N.J., Carey, J.W. (2019). Geomechanical evaluation of natural shear fractures in the EGS Collab Experiment 1 test bed. Proceedings of the 53rd US Rock Mechanics / Geomechanics Symposium Frash, L.P., Carey, J.W., Welch, N.J., EGS Collab Team. (2019). EGS Collab Experiment geomechanical and hydrological properties by triaxial direct shear. Proceedings of the 44th Workshop on Geothermal Reservoir Engineering.	4100L
Maximum Pressure	36	MPa	Frash, L.P., Welch, N.J., Carey, J.W. (2019). Geomechanical evaluation of natural shear fractures in the EGS Collab Experiment 1 test bed. Proceedings of the 53rd US Rock Mechanics / Geomechanics Symposium Frash, L.P., Carey, J.W., Welch, N.J., EGS Collab Team. (2019). EGS Collab Experiment geomechanical and hydrological properties by triaxial direct shear. Proceedings of the 44th Workshop on Geothermal Reservoir Engineering.	4100L
Cohesion	8.2	MPa	Frash, L.P., Welch, N.J., Carey, J.W. (2019). Geomechanical evaluation of natural shear fractures in the EGS Collab Experiment 1 test bed. Proceedings of the 53rd US Rock Mechanics / Geomechanics Symposium Frash, L.P., Carey, J.W., Welch, N.J., EGS Collab Team. (2019). EGS Collab Experiment geomechanical and hydrological properties by triaxial direct shear. Proceedings of the 44th Workshop on Geothermal Reservoir Engineering.	4100L

Rhyolite 4100L &4850L

Rhyolite

Parameter	Value	Unit	Source	Level
P-wave velocity	5172 - 5263	m/s	Ben Jahnke, Hiroki Sone, Herb Wang	4100L
P-wave velocity	5189	m/s	DUSEL, RESPEC 2010	4850L
S-wave velocity	3125 - 3158	m/s	Ben Jahnke, Hiroki Sone, Herb Wang	4100L
S-wave velocity	3094	m/s	DUSEL, RESPEC 2010	4850L
Young's Modulus	59.2 - 60.8	GPa	Ben Jahnke, Hiroki Sone, Herb Wang	4100L
Young's Modulus	70	GPa	DUSEL, RESPEC 2010	4850L
Poisson Ratio	0.21 - 0.22		Ben Jahnke, Hiroki Sone, Herb Wang	4100L
Poisson Ratio	0.21		DUSEL, RESPEC 2010	4850L
Shear Modulus	24.4 - 24.9	GPa	Ben Jahnke, Hiroki Sone, Herb Wang	4100L
Shear Modulus	31	GPa	DUSEL, RESPEC 2010	4850L
Differential Stress	66.9 - 69.2	GPa	Ben Jahnke, Hiroki Sone, Herb Wang	4100L
Unconfined Compressive Strengths	329 402	GPa	Ben Jahnke, Hiroki Sone, Herb Wang	4100L
Unconfined Compressive Strengths	165.47	MPa	Hlaydysz, 2009; Lachel Felice, 2009	4850L
Average bulk density	25-2.6	g/cm^3	Golder Associates 2009	4850L
Uniaxial Compressive Strength	111	MPa	DUSEL, RESPEC 2010	4850L
Tensile Strength	10	MPa	DUSEL, RESPEC 2010	4850L
Maximum Potential In Situ Shear Stress	7.7	MPa	Frash, L.P., Welch, N.J., Carey, J.W. (2019). Geomechanical evaluation of natural shear fractures in the EGS Collab Experiment 1 test bed. Proceedings of the 53rd US Rock Mechanics / Geomechanics Symposium Frash, L.P., Carey, J.W., Welch, N.J., EGS Collab Team. (2019). EGS Collab Experiment geomechanical and hydrological properties by triaxial direct shear. Proceedings of the 44th Workshop on Geothermal Reservoir Engineering.	4100L
Vertical In-Situ Stress	36	MPa	Frash, L.P., Welch, N.J., Carey, J.W. (2019). Geomechanical evaluation of natural shear fractures in the EGS Collab Experiment 1 test bed. Proceedings of the 53rd US Rock Mechanics / Geomechanics Symposium Frash, L.P., Carey, J.W., Welch, N.J., EGS Collab Team. (2019). EGS Collab Experiment geomechanical and hydrological properties by triaxial direct shear. Proceedings of the 44th Workshop on Geothermal Reservoir Engineering.	4100L
Horizontal In-Situ Stress 1	37.3	MPa	Frash, L.P., Welch, N.J., Carey, J.W. (2019). Geomechanical evaluation of natural shear fractures in the EGS Collab Experiment 1 test bed. Proceedings of the 53rd US Rock Mechanics / Geomechanics Symposium Frash, L.P., Carey, J.W., Welch, N.J., EGS Collab Team. (2019). EGS Collab Experiment geomechanical and hydrological properties by triaxial direct shear. Proceedings of the 44th Workshop on Geothermal Reservoir Engineering.	4100L
Horizontal In-Situ Stress 2	18.3	MPa	Frash, L.P., Welch, N.J., Carey, J.W. (2019). Geomechanical evaluation of natural shear fractures in the EGS Collab Experiment 1 test bed. Proceedings of the 53rd US Rock Mechanics / Geomechanics Symposium Frash, L.P., Carey, J.W., Welch, N.J., EGS Collab Team. (2019). EGS Collab Experiment geomechanical and hydrological properties by triaxial direct shear. Proceedings of the 44th Workshop on Geothermal Reservoir Engineering.	4100L
Critical Pressure	9.5	MPa	Frash, L.P., Welch, N.J., Carey, J.W. (2019). Geomechanical evaluation of natural shear fractures in the EGS Collab Experiment 1 test bed. Proceedings of the 53rd US Rock Mechanics / Geomechanics Symposium Frash, L.P., Carey, J.W., Welch, N.J., EGS Collab Team. (2019). EGS Collab Experiment geomechanical and hydrological properties by triaxial direct shear. Proceedings of the 44th Workshop on Geothermal Reservoir Engineering.	4100L
Maximum Pressure	36	MPa	Frash, L.P., Welch, N.J., Carey, J.W. (2019). Geomechanical evaluation of natural shear fractures in the EGS Collab Experiment 1 test bed. Proceedings of the 53rd US Rock Mechanics / Geomechanics Symposium Frash, L.P., Carey, J.W., Welch, N.J., EGS Collab Team. (2019). EGS Collab Experiment geomechanical and hydrological properties by triaxial direct shear. Proceedings of the 44th Workshop on Geothermal Reservoir Engineering.	4100L
Cohesion	11.3	MPa	Frash, L.P., Welch, N.J., Carey, J.W. (2019). Geomechanical evaluation of natural shear fractures in the EGS Collab Experiment 1 test bed. Proceedings of the 53rd US Rock Mechanics / Geomechanics Symposium Frash, L.P., Carey, J.W., Welch, N.J., EGS Collab Team. (2019). EGS Collab Experiment geomechanical and hydrological properties by triaxial direct shear. Proceedings of the 44th Workshop on Geothermal Reservoir Engineering.	4100L

Appendix H
Hydrogeology of the Experiment 2 Testbed
Tom Doe

1 Background

This section describes the efforts to identify natural conductive fractures and determine pore pressures in the Experiment 2 Test Bed on the 4100-level of the SURF facility. The igneous and metamorphic rocks of the COLLAB test beds have very low porosities and permeabilities, hence the groundwater flow in the experimental areas occurs through natural fractures.
Naturally conductive fractures are important to the experiment design for multiple reasons including

- Identifying targets for shear stimulation if favorably oriented to the in-situ stress field and
- Determining the initial pore pressure, which is important term controlling shear deformation on fracture and in the rock itself.

Characterization work for proposed physics experiments on the 4850-level performed in the late 2000's (DUSEL, Stetler, 2016) showed that fracture networks overall had low conductivity and they were poorly connected. Most of the DUSEL boreholes were non-flowing, and the three that were had highly variable pore pressures varying from 15% to 60% of the pressure based on a hydrostatic gradient to the surface. Within the context of variable connectivity, fracture networks with connection to water sources exhibit seepage, while isolated fracture networks exhibit no seepage at all or drain completely to the mine openings.

Observations in the Experiment 1Test Bed area showed that minor seepage occurs on widely spaced shear zones including the "weep zone" that intersected the production and injection boreholes near their collars. Where the shear zones are more transmissive, the seepage appears as minor drips and wetted areas on drift walls. Where zones are less transmissive, the air circulation of the mine's ventilation system removes the liquid water leaving crusts of evaporative salts. A key finding of the Experiment 1 Test Bed characterization was the presence of highly conductive, but isolated fractures, such has the OT-P connector, which had a significant impact on the stimulation and circulation of the experiments.

2 Drift Wall Mapping

Drift-wall mapping along the 4100-level drift in the vicinity Test Bed 2 identified numerous fractures, including an open, large aperture fracture at the north corner of the battery alcove. This fracture was not flowing water and appeared to be similar to the open but isolated fractures observed in the Experiment 1 Test Bed. The drift mapping revealed no evidence of seepage either as flowing water or evaporative crusts except approximately 100 meter south of the test bed in fractures along the Yates-Poorman contact where there is also an exposure of rhyolite.

3 Key Fractures Observed

TV-4100 Rhyolite Flowing Fracture: Only two flowing fractures were encountered during the drilling of the Experiment 2 boreholes. Flowing water appeared in TV-4100, the exploration borehole drilled in the Battery Alcove. This borehole produced <0.1 liter/min water flow from a fracture in the rhyolite dike. Pressure buildup tests recovered to approximately 100 psi (0.7 MPa or ~6% of hydrostatic).

DMU Flowing Fracture (Figure 1a): A second flowing fracture appeared near the end of the last test-bed borehole drilled, E2-DMU. This fracture was encountered at a measured length of 49.7-49.9 m (163.0-163.3 feet) with a fracture pole orientation of 336, 10. The flow rate from this fracture was ~500 ml/day (0.3 ml/min). Televiewer logs show the flowing porosity is not a single open fracture but small openings (vugs?) in brecciated rock adjacent to a prominent quartz vein. Extrapolations of the fracture from its E2-DMU intersection show that it would intersect the Site B boreholes near the drift and the fracture does not cross the test bed volume circumscribed by the monitoring and production boreholes.

AML Open Fracture (Figure 1a): Open fractures associated with a quartz vein (Figure 4.5 Main Report) were encountered in E2-AML at measured depths of 56.9 m (186.7 ft) and 57.4 (188.3 ft) with fracture pole orientations of 158,25 and 168,30 respectively. These fractures produced anomalies in conductivity logs as discussed in Figure 4.5; however, the fractures did not sustain an outflow indicating that they are largely hydraulically isolated. Like the fractures in E2-DMU, the conductive porosity appears to be vuggy openings in brecciated rock. Also, like the E2-DMU flowing zone, these fractures do not project into the core of the test bed borehole array.

TL Clay Fracture and TC Alteration Zone (Figure 1 b): Highly altered zones were encountered in E2-TL between 66.9 m (219.3 ft), pole orientation 221,26 and E2-TC at 58.5 (192.0 feet), pole orientation 200, 11. The E2-TL intersection was altered to a plastic clay, while the E2-TC intersection is a visibly altered but cohesive rock. While not perfectly aligned they could be intersection of a single altered zone. The intersections are not open or apparently hydraulically conductive, but the alteration suggests past hydraulic or hydrothermal activity as well as significant softening of the rock stiffness and potential for local effects on the rock stresses. These two features, or possible single feature, lies within the Experiment 2 Test Bed in a location with potential for affecting rock stress and fracture stimulation.

4. Hydraulic Characterization: Flow Monitoring

The hydraulic characterization work involved two activities,

- Monitoring of flow into or out of boreholes during drilling and for two months afterward
- Packer testing of over the open lengths of all Test Bed 2 boreholes and shorter zones in planned injection borehole E2-TC.

The project developed a protocol for careful measurement of water flows from boreholes during the drilling activity. Once it became clear that water was flowing into the boreholes (water levels declining) the protocol evolved to record the amount of water required to fill the borehole to the casing lip on a daily shift basis. The field crew added manometers to improve the accuracy and reproducibility of the measurements on most of the boreholes. The field crew also

performed tests of evaporation rate to confirm that the water level declines were due to water losses to the rock and not evaporation.

The activity applied only to completed boreholes and not the borehole in the process of drilling due to impaired access to the borehole collars. Also, the site C boreholes, E2-DML and E2-DMU, were not monitored during the site C drilling, but measurements were taken in September 2021 after the mid-August hydraulic tests.

The flow monitoring results appear in Figure 2 and Table 1. All of the borehole flows were losses to the rock except for a brief period of water production from E2-AMU and the production from the flowing fracture E2-DMU. The results also show that while the flows are uniformly very low they do vary among the boreholes. This was especially clear in the September 2021 results ("after drilling" in Table 4.1) where four of the boreholes had no recorded losses over a an eight-day period. Interestingly, the borehole with the largest losses was E2-AML, which had a clear open fracture described above. E2-TN, which produced the most flow during stimulation and circulation also had relatively higher water losses.

The water losses indicate flow to a sink at a lower elevation than the experiment, and a likely candidate for the that sink would be the nearby Yates Shaft. While the presence of flowing fractures in the vicinity of the test bed indicates highly heterogeneous fracture connectivity and pore pressure distributions, we expect the mine drainage is the main influence on pore pressures, and pore pressure value will be a relatively small, if not negligible fraction of the pressures required to open or stimulate fractures in the test bed.

Hydraulic Characterization: Packer Testing

A major target of Experiment 2 has been shear stimulation of a naturally conducting fracture. With only a few exceptions the fractures in the Experiment 2 test bed are healed and show little indication of being significantly transmissive. The water losses show the rock has some conductivity, and packer tests were performed to try to locate sections of preferential fracture transmissivity. The tests used a single, low-pressure packer to determine hydraulic conductivity using pressure-pulse tests, which look at pressure decay after charging a test zone to a pre-determined pressure value. The volume of flow into the test section can be determined from the pressure decay and the total compressibility of the test zone and the test equipment.

The tests were performed over the entire open length of each borehole from 9.1 m (30 feet) to total depth (Figure 4). Three additional tests were performed in E1-TC borehole with the packer set at 30.5, 45.7, and 61.0 m (30, 100, and 150 feet), as E2-TC was planned to be the stimulation-source borehole.

The test procedure had three steps (Figure 3). The first step was pressuring the test interval to mine-water pressure (~70 psi or 500 kPa) while monitoring the flow rate. For the second step, the test zone was then shut-in to allow the pressure to decay for 30 minutes. Given the low conductivity of the rock the pulses decayed by only about 10% over the 30-minute durations. The third step was a 2-3 minute 25 ml/min injection using an ISCO syringe pump. For this duration in tight rock, the linear pressure buildup reflects primarily the total compressibility of

the test zone and the equipment. Knowing the total compressibility allows calculating the water loss to the borehole during the pulse decay period. Dividing this loss by the time-duration of the pulse gives a flow rate for calculation of transmissivity and hydraulic conductivity assuming a steady state flow, which is reasonable approximation for the relatively small pulse drops. The flowing borehole, E2-DMU was too conductive for the pulse methods. Instead, the flow rate at constant mine-water pressure achieved a steady value of 180 ml/min, which was used for the hydraulic property calculations.

6 Discussion

The pressure-pulse results (Table 2, Figure 5) demonstrate the low permeability of rocks in Testbed 2 with the exception of the single conducting fracture in E2-DMU. That said, the permeability values are not uniform, with E2-AML and E2-TN having higher values than the other boreholes. The slightly higher permeability of E2-AML may reflect the open fracture that is prominent in that borehole, which nonetheless would appear to be discontinuously connected based on the borehole's overall low permeability.

We did not obtain a pressure build-up value for the flowing fracture in E2-DMU. The fact that all of the other borehole lose water rather than produce water strongly suggests that the pore pressures in Test Bed 2 are very low. The pressure buildup values in TV-4100 would indicate that an upper limit to pore pressure would be less than 2 MPa or approximately 10% of the minimum horizontal stress.

Table 1. Water loss rates to boreholes during drilling and after drilling (September 2021). Gains (outflow from hole) in red.

Borehole	During Drilling		Post Drilling (Sept. 2021)	
	Flow Rate			
	ml/day	m^3/s	ml/day	m^3/s
E2-AMU	90	1.0E-09	23	2.6E-10
E2-AML	107	1.2E-09	114	1.3E-09
E2-DMU	Not Measured		**521**	**6.0E-09**
E2-DML			44	5.1E-10
E2-TU	31	3.6E-10	-	-
E2-TS	21	2.4E-10	-	-
E2-TC	177	2.0E-09	-	-
E2-TN	52	6.0E-10	87.5	1.0E-09
E2-TL	28	3.2E-10	-	-

Table 2. Hydraulic test results.

Borehole	Packer Set Depth m	Zone Length m	Head m	Transmissivity m^2/s	Hydraulic Conductivity m/s	Permeability m^2	Test Type
E2-TC	9.1	68.0	47.1	1.9E-09	2.8E-11	2.9E-18	Pressure-Pulse
E2-TU	9.1	67.4	49.3	4.7E-10	6.9E-12	7.1E-19	Pressure-Pulse
E2-TL	9.1	67.4	47.3	2.0E-09	2.9E-11	3.0E-18	Pressure-Pulse
E2-TN	9.1	67.4	47.2	3.1E-09	4.6E-11	4.7E-18	Pressure-Pulse
E2-TS	9.1	71.9	48.0	1.5E-09	2.1E-11	2.2E-18	Pressure-Pulse
E2-DML	9.1	46.0	47.2	1.5E-09	3.3E-11	3.3E-18	Pressure-Pulse
E2-DMU	9.1	45.7	45.8	6.8E-08	1.5E-09	1.5E-16	Steady Outflow
E2-AML	9.1	51.2	47.2	4.0E-09	7.9E-11	8.0E-18	Pressure-Pulse
E2-AMU	9.1	51.2	47.0	1.3E-09	2.5E-11	2.6E-18	Pressure-Pulse
E2-TC	30.5	46.6	47.4	1.5E-09	3.3E-11	3.3E-18	Pressure-Pulse
E2-TC	45.7	31.4	47.3	2.0E-09	6.5E-11	6.6E-18	Pressure-Pulse
E2-TC	61.0	16.2	47.0	2.2E-09	1.3E-10	1.4E-17	Pressure-Pulse

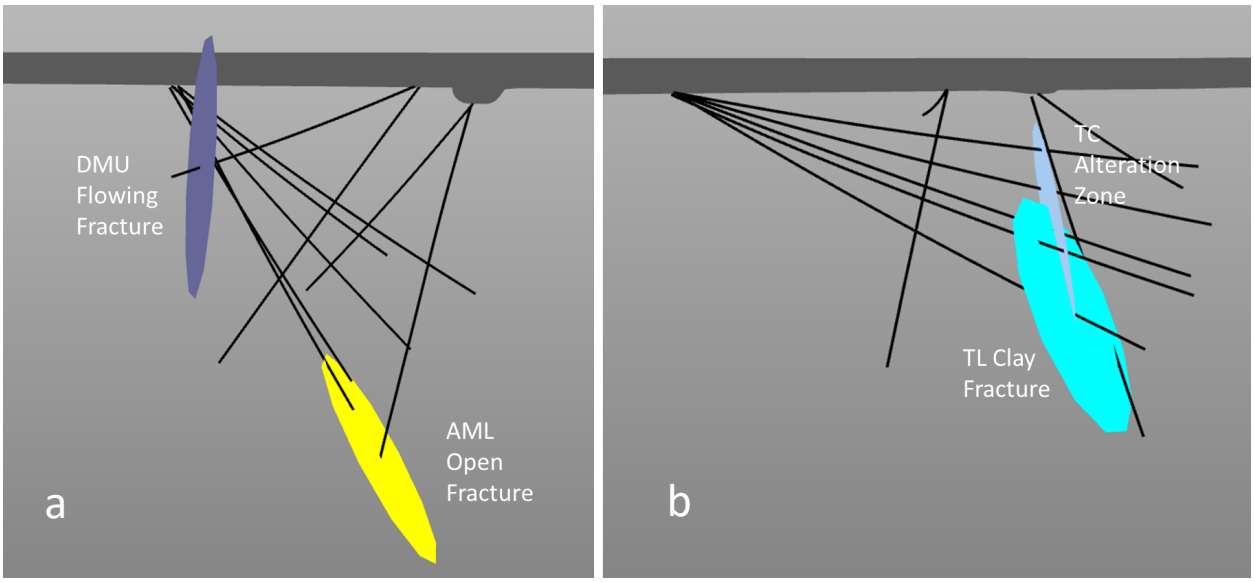

Figure 1. Locations and orientations of key fractures intersected in the Experiment 2 Test Bed boreholes. Left (a), DMU flowing fracture and AML open fractures, right (b) TL clay fracture and TC alteration zone.

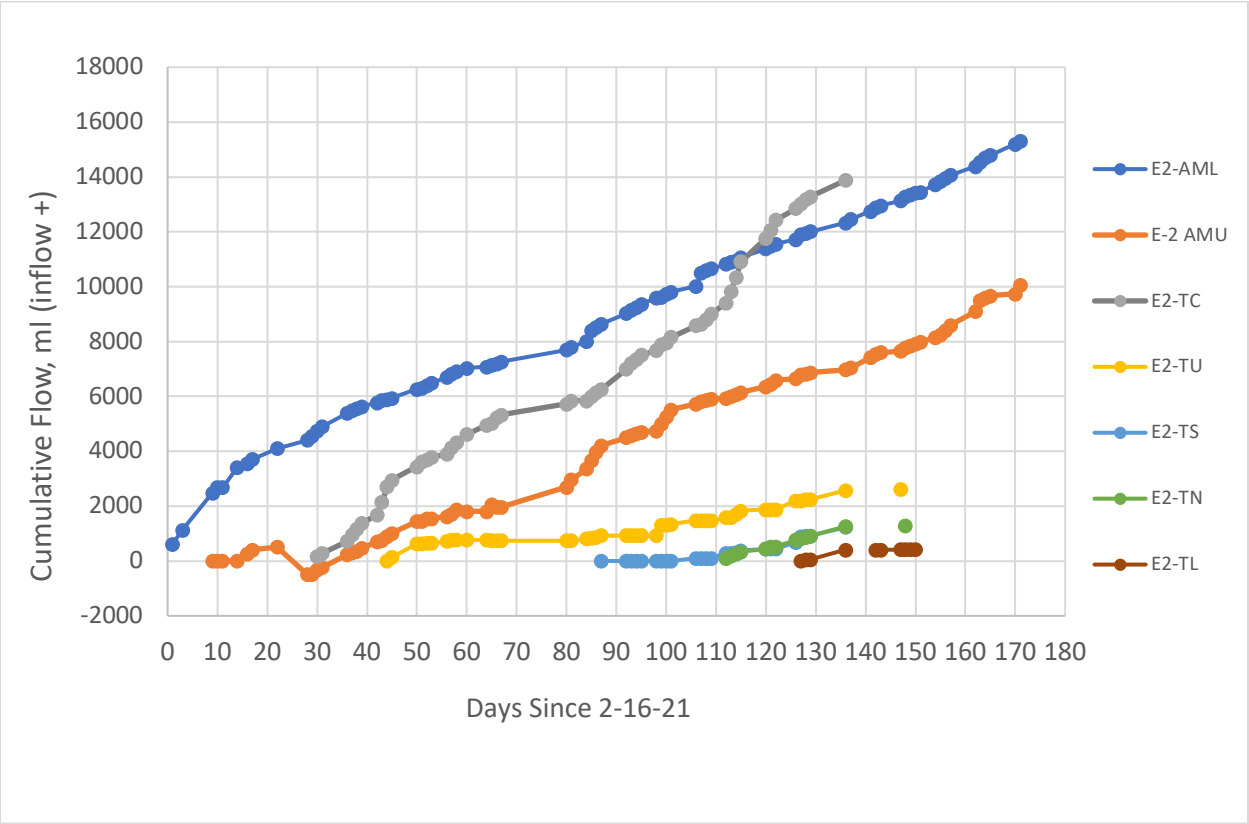

Figure 2 Cumulative water losses (gains) from Test Bed 2 boreholes during drilling. Flows into boreholes are positive, produced water from boreholes are negative.

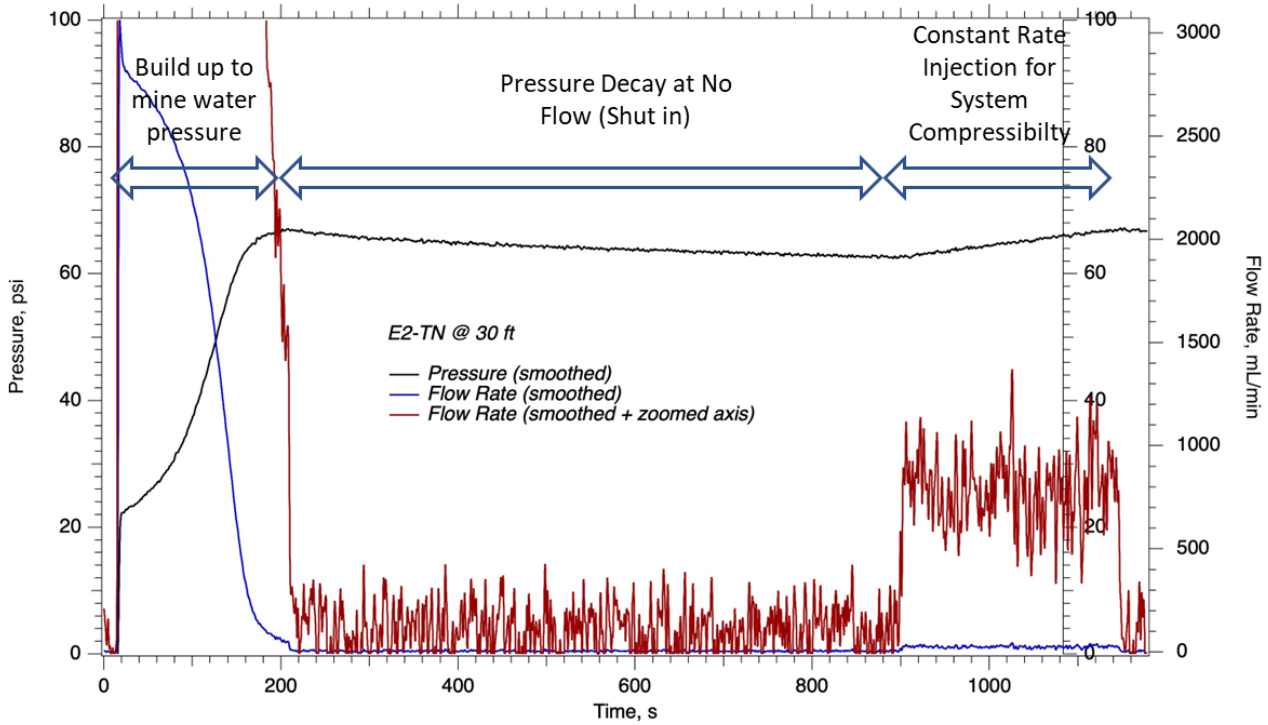

Figure 3 Pressure pulse test. The test starts by setting the packer and building up test zone to mine water pressure (~0.5 MPa, 70 psi). Then the zone is "shut in" and the pressure decays as water flows into the rock. After 30 minutes of pressure decay, the injection resumes at 25 ml/min. The pressure buildup indicates the compressibility of the test zone. From the compressibility and pressure decay one calculates the water loss volume and the rate of flow. Assuming approximate steady flow, the transmissivity can be determined from the flow rate and the pressure change (converted to hydraulic head).

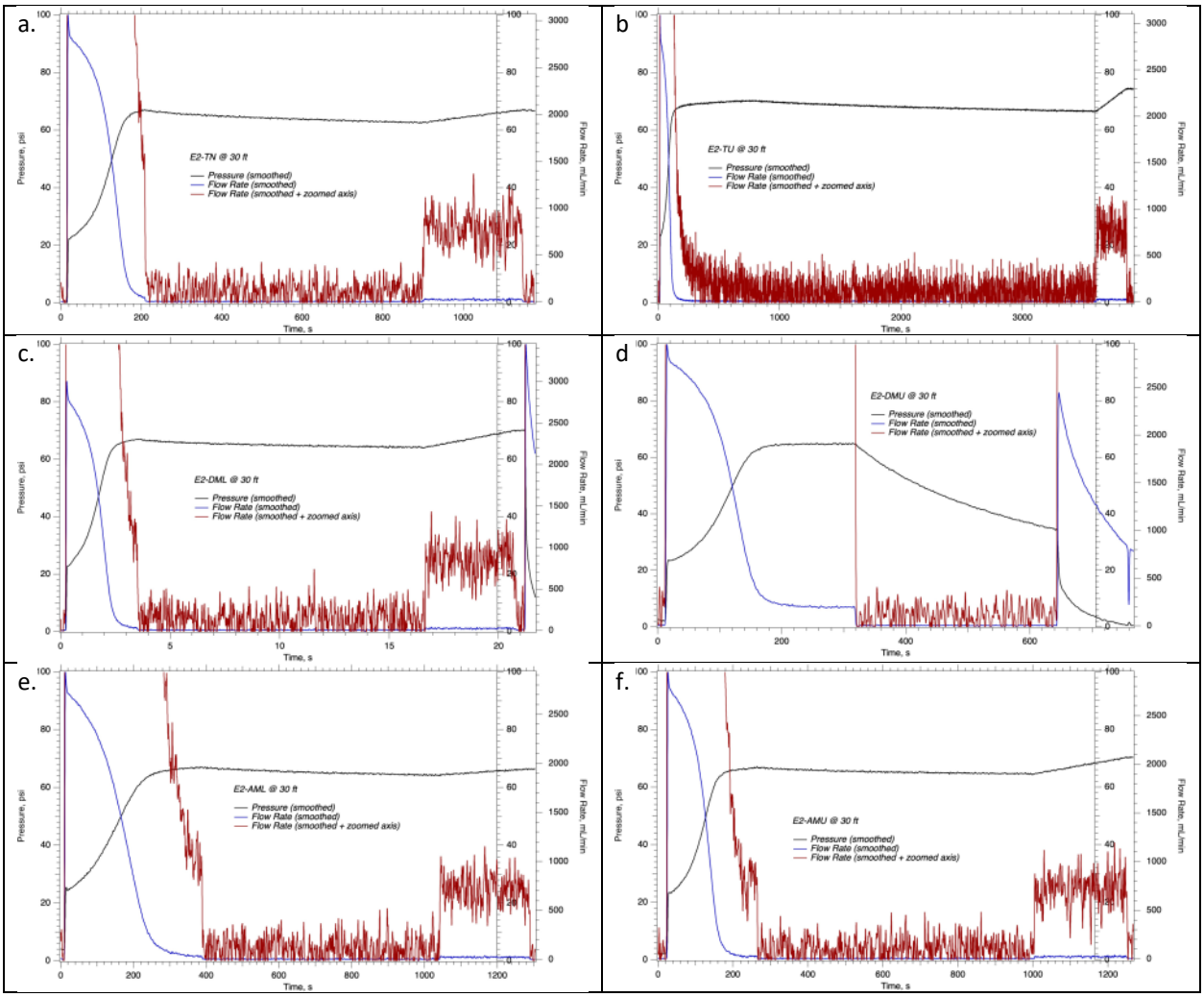

- The black line is the pressure and corresponds to the vertical axis on the left.
- The blue line is the flow rate and corresponds to the vertical axis that is on the far right.
- The red line is the flow rate again, but zoomed in on the low end and thus corresponds to the vertical axis that is second from the right (to see some of the more subtle responses)

Figure 4. Whole-borehole hydraulic characterization test results from six E2 boreholes: a. TN pulse-decay test and 25 mL/min constant rate test; b. TU pulse-decay test and 25 mL/min constant rate test; c. DML pulse-decay test and 25 mL/min constant rate test; d. DMU pulse-decay test; e. AML pulse-decay test; and, f. AMU pulse decay test. The black line is the pressure and corresponds to the vertical axis on the left. The blue line is the flow rate and corresponds to the vertical axis that is on the far right. The red line is the flow rate zoomed in on the low end and corresponds to the vertical axis that is second from the right.

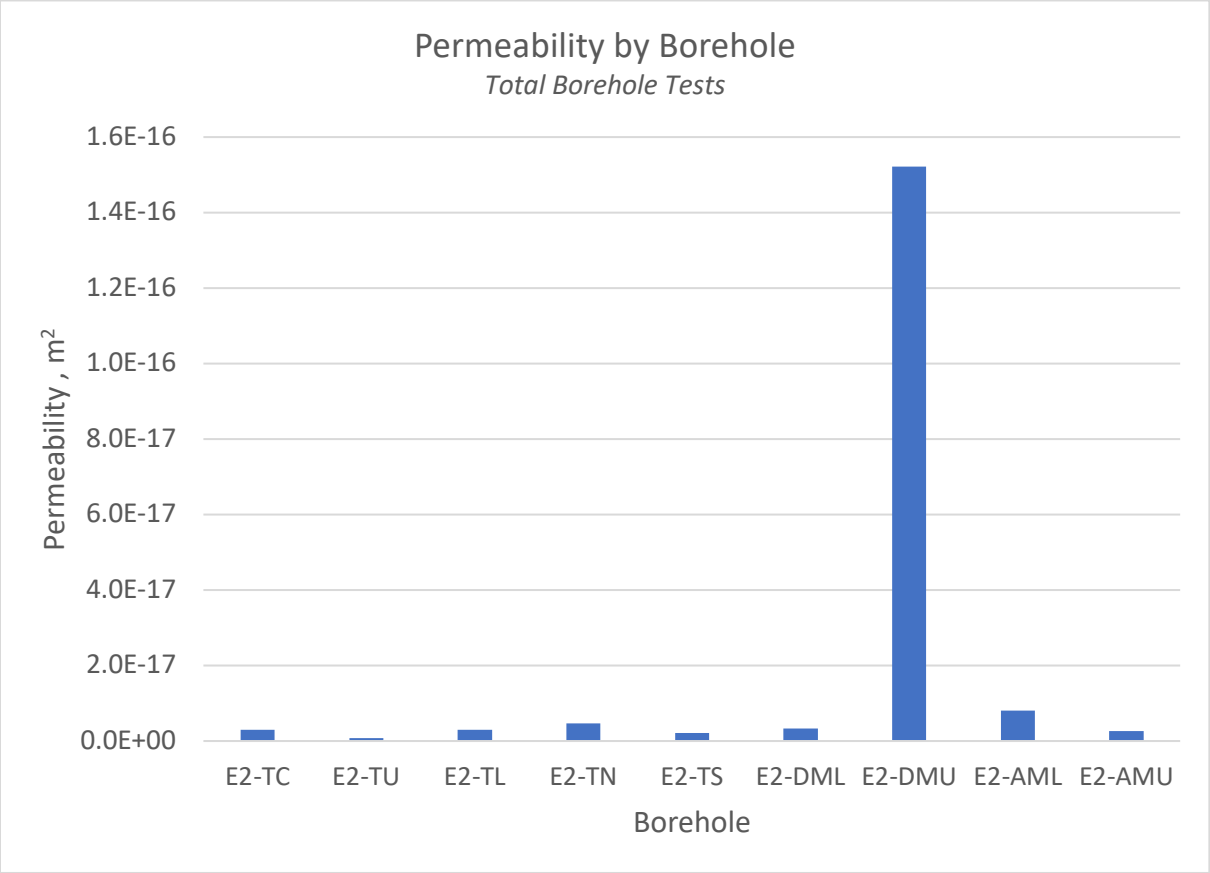

Figure 5 Permeability from hydraulic tests by borehole. Total hole test, packer set at 9.1 m depth.

BERKELEY LAB

EGS Collab Experiment 2

Passive seismic monitoring system

Report no: LBNL-2001514
LBNL EESA
March 2023

AUTHOR (Last, First):
Hopp, Chet
DATE:
3-24-2023
TITLE:
EGS Collab Experiment 2: Passive seismic monitoring system

Contents

1 Terminology

- **SURF**: Sanford Underground Research Facility. The old Homestake gold mine in Lead, SD, USA where the EGS Collab experiment has taken place.
- **OD**: Outer diameter
- **ERT**: Electrical Resistivity Tomography
- **CASSM**: Continuous Active Source Seismic Monitoring. A network of piezoelectric sources and seismic receivers for cross-well seismic tomography.
- **LBNL or LBL**: Lawrence Berkeley National Lab (Berkeley, CA)
- **SNL**: Sandia National Lab (Albuquerque, NM)
- **PNNL**: Pacific Northwest National Lab (Richland, WA)

2 Introduction

The EGS Collab Experiment #2 took place from approximately February–September 2022 at the Sanford Underground Research Facility in Lead, SD. The project was the continuation of a years-long experiment aiming to validate models of enhanced geothermal systems through a series of high-pressure injections into rock between 1200 and 1500 meters below the surface. These injection experiments were extensively monitored by a number of systems including seismic waveform recording, pressure and temperature probes, active source seismic tomography, electrical resistivity tomography, and a full suite of distributed fiber optic interrogators.

This report details the passive seismic monitoring system that monitored, in real time, the timing and location of small earthquakes in the testbed resulting from the injection of fluid and fracturing of the rock. This monitoring system consisted of accelerometers and hydrophones placed in various boreholes surrounding the injection zones and operated continuously throughout the experiment.

3 Installation

The passive seismic monitoring system for EGS Collab Experiment 2 consisted of two types of seismic sensors: piezoelectric accelerometers and hydrophones. These sensors were recorded by two different recording systems each targeting a different application. One recording system recorded 64-channels of data continuously for the purpose of monitoring for seismicity that was induced and/or triggered by the injection operations. These data were processed in real-time in an attempt to monitor seismicity to inform decision-making during the experiment. The other recording system recorded the same sensors only at a lower sampling rate and in triggered mode. This system was a part of an active-source monitoring system called CASSM (Continuous Active-Source Seismic Monitoring) that uses waves emitted from custom-built piezoelectric sources installed in the boreholes to estimate various properties of the rock volume with time. While the sensors are common across both systems, this report focuses on the continuous, high-frequency recording system.

3.1 Sensors

The piezoelectric accelerometers were manufactured by MMF of Germany. They are model KS943B100 triaxial sensors that conform to the IEPE (Integrated Electronics Piezo Electric) standard. They have a sensitivity of 100 mV/g (the sensors installed on the 4850 level for EGS Collab Experiment 1 had a sensitivity of 1 V/g) and a linear frequency response range of 0.5 Hz to 22 kHz within 3 dB. The full specsheet can be found here. Each of the 16 MMF accelerometers was packaged into a stainless steel housing at the Geosciences Measurement Facility (GMF) at LBNL (Figure 6A and B). Calibration certificates for three of these accelerometers were purchased and are included in the GDR submission for the continuous waveform data. For analyses requiring correction of the data to real units (i.e. sensor frequency response removal) the user is directed to these certificates that can be used to construct sensor response files. While some minor discrepancies exist between sensors, we feel it is reasonable to treat all sensors as having a response curve equivalent to the average of these three calibration curves.

A string of 24 hydrophones was installed in one of the open boreholes, TS (water-coupled; not grouted). This string consisted of HTI-96-MIN/V 5/8 sensors manufactured by High Tech, Inc. The hydrophones have a flat frequency response from 2 Hz to 2 kHz. Due to a misunderstanding in the ordering process, a 2 kHz hardware lowpass-filter was installed. This means that much of the anticipated frequency content of the seismicity for this experiment (into the 10s of kHz) was not recorded on these instruments. The array had an inter-sensor spacing of 2.5 m.

Finally, 20 active seismic sources were installed. These sources are cylindrical piezoelectric crystals manufactured at the Geosciences Measurement Facility at LBNL. Sources are fired by applying a voltage to the piezoelectric ceramic and the signal is recorded across the

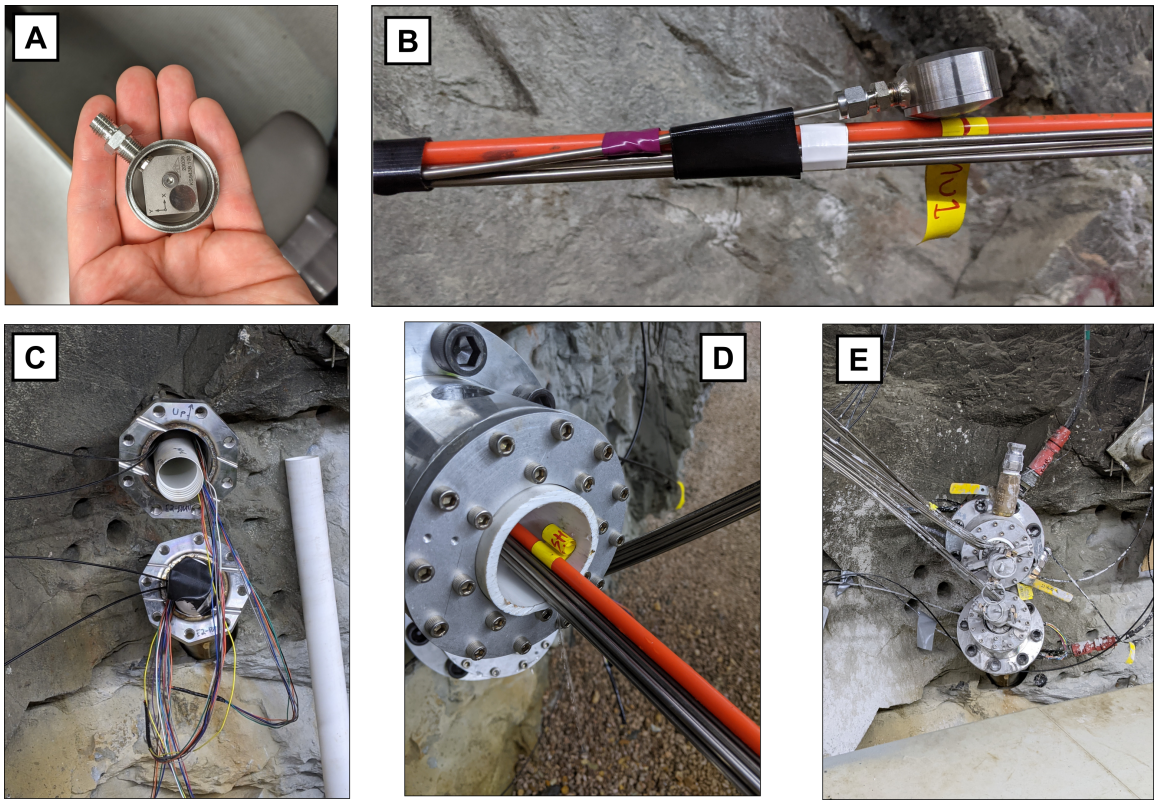

Figure 1: Pictures of the various stages of accelerometer fabrication and installation. A) A single triaxial accelerometer inside an open steel housing B) Completed housing attached to TEC and taped to a conveyance rod (orange fiberglass). C) Schedule 40 PVC shrouds protruding from the wellheads. These were necessary to isolate the ERT electrodes from all of the metal involved in the wiring and housings for the seismic sensors. D) The wellheads were sealed off using a custom machined cap from SNL that left the inside of the shroud open to lower the seismic sensor package E) Final state of the fully grouted boreholes DMU and DML with all sensor cables fed through the wellcaps.

array of sensors described above. This system is known as Continuous Active Source Seismic Monitoring or CASSM [2].

To protect the cables as they ran up the grouted boreholes, stainless steel tubing encapsulated cable (TEC) was used. This choice was made mostly to avoid fluid infiltrating the CASSM sources and accelerometers, which damaged a number of sensors in Experiment #1 on the 4850 level of the mine.

3.2 Borehole array design

Each of the monitoring array boreholes needed to fit many different sets of sensing equipment, each with unique requirements. This equipment included not only the seismic sensors and their cables, but also a steel encased fiber optics package and also a number of electrodes for the electrical resistivity tomography (ERT) system. One major consideration was that any metal in the borehole would severely interfere with the ERT system and would therefore need to be electrically isolated. This was done by placing all of the seismic instrumentation inside a 2.5-inch schedule 40 PVC "shroud". The ERT electrodes were strapped to the outside of the shroud along with the fiber optic package (which was steel encapsulated but coated in a non-conductive material). The one non-grouted monitoring borehole, TS, was designed in a similar way, with the exception being that it contained no steel cables for the CASSM sources or the hydrophone string (they were plastic coated instead). Cross sections for both grouted and non-grouted boreholes are shown in Appendix 6.4.

3.3 Array layout

Figure 2 shows the geometry of the seismic array with grouted boreholes shown in black, open boreholes shown in blue, and seismic sensors shown as red inverted triangles.

Each of the grouted boreholes contained four CASSM sources and four three-component accelerometers. The spacing and location of these instruments were chosen to maximize the ability of the accelerometers to constrain the location and mechanism of detected seismicity as well as to maximize the raypath coverage of the CASSM system. In borehole TS, four CASSM sources were installed alongside the 24-channel hydrophone array. The locations for each sensor are given in Table 3 within the Homestake Mine Coordinate system. This is a cartesian system used for most data coming out of the mine. Units are given in feet.

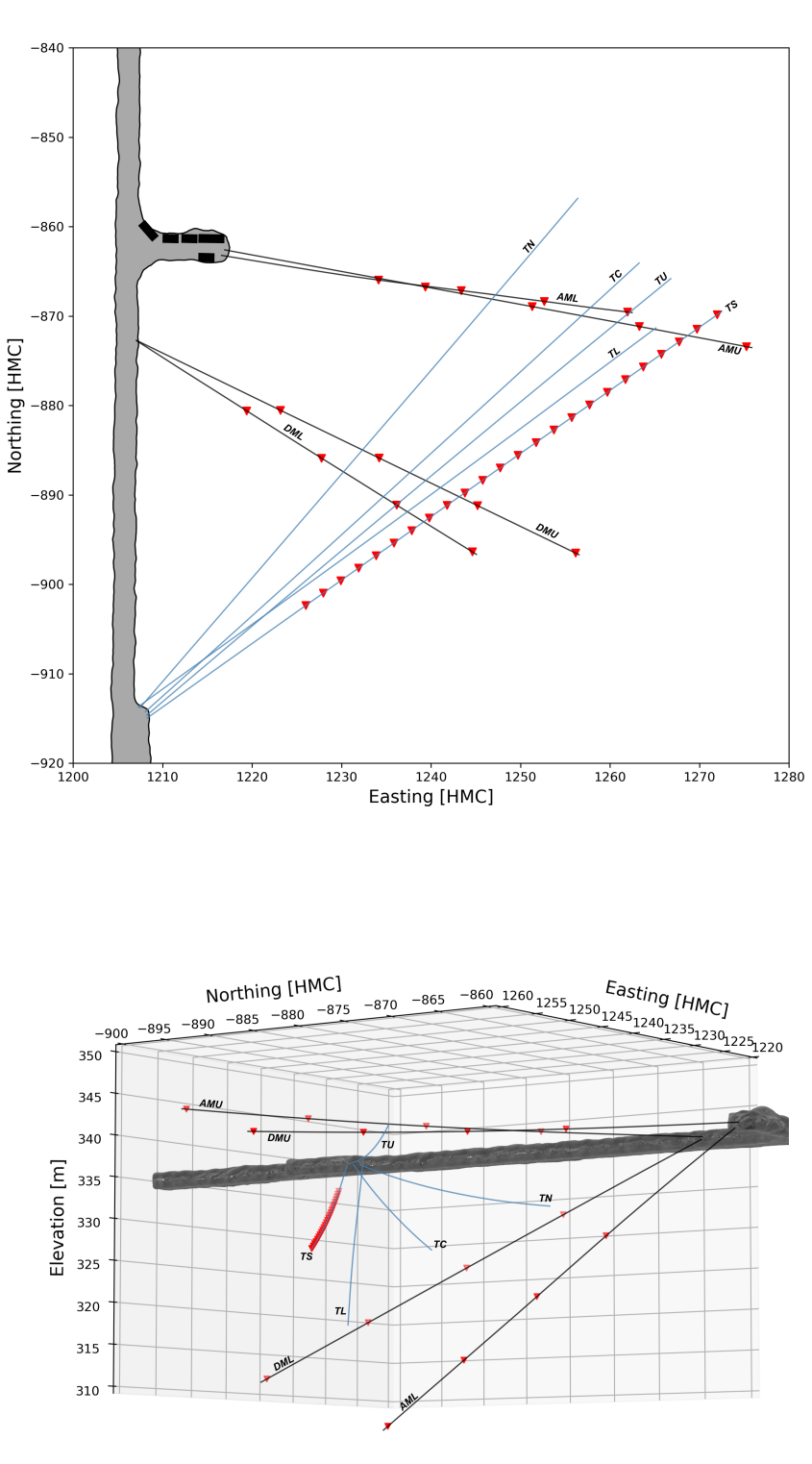

Figure 2: Overview of the EGS Collab Experiment 2 testbed on the 4100 level of SURF. The boreholes are labeled by name and the locations of the seismic sensors are indicated with red triangles. The fiber loop is installed in the four grouted boreholes (AMU, AML, DMU, and DML) shown in black. A string of hydrophones is installed in non-grouted borehole TS.

3.4 Recording systems

Two recording systems were used to digitize the data coming from the accelerometers and hydrophones; one in continous recording mode and the other in triggered recording mode. The continuous data recorder was a 64-channel VIBbox-64 manufactured by Data Translation. This system recorded each channel of the three-component accelerometers and half of the hydrophone channels at a sampling rate of 100 kHz. The triggered system was an interconnected series of Geometrics Geode seismographs, which were triggered to record based on the shot times of the CASSM sources. This system recorded each available channel from all sensors. The full CASSM system is explained in greater detail in a separate submission to the Geothermal Data Repository.

4 Data

This section describes the raw data and data products produced by the Data Translation VIBbox continuous recorder. The triggered recordings from the CASSM system are detailed in a separate report within the relevant GDR submission for the CASSM dataset.

4.1 Raw data

The data from the VIBbox-64 were saved as 32-bit binary files, each containing 32 seconds of data from 64 channels. Each file consists of header values (the first 148 bytes) followed by the data itself, which are stored as 32-bit unsigned integers. The gain of the system was set to x100, corresponding to ±0.1 V input.

We use the SEED convention in naming each channel coming in from the sensors. This consists of four fields: network, station, location, and channel, and is written like `NET.STA.LOC.CHAN`. We named the network CB (CollaB). The stations are named for the borehole that the sensor is installed in (up to 5 characters) and its relative depth in the borehole (1 to 4 for increasing depth). For example, the Z channel for station AMU1 would be written as `CB.AMU1..XNZ`. The location code is omitted as it is not useful in this case. Please refer to the SEED channel naming convention for information on channel naming. The order in which the data are stored to disk is indicated in Appendix Table 2. Note that not all of the hydrophone channels were recorded on the VIBbox because we had more than 64 channels available. Therefore we recorded only the even-numbered hydrophone channels. We also included three CASSM-specific channels in the data: CMon, CTrg, and CEnc. CTrg records the trigger signal sent to the CASSM source and CEnc encodes which source is being fired. These data were recorded to help remove active source shots from the processing of the VIBbox data, which was focused on passive-source seismicity. The final channel, CB.PPS.., is a time signal, one square wave per second from a Rubidium clock-backed PTP server installed with the rest of our monitoring equipment. The onset of the square wave corresponds to the start of a second.

Appendix 6.3 provides a Python function to read a single VIBbox binary file to an Obspy Stream object. For those unfamiliar with the Obspy Python package, it is an extremely useful tool for manipulating and processing seismic data in the Python ecosystem. Its documentation can be found here.

4.2 Realtime seismicity processing

During EGS Collab Experiment #2, we processed the VIBbox data in near realtime in order to use the location of seismic events to inform decision-making. To do this, we used a modified version of the software program DUGseis. Because we were unable to get the VIBbox to write to the HDF5-based format required by the software, many modifications

were necessary to the source code and some features (e.g. interactive phase picking and plotting) were eliminated. The final version of the code used on the 4100 level can be found in the `lbl_dev` branch of my fork of the DUGseis repository here. The realtime system worked well until early June 2022, when we filled our fast network attached storage (NAS) systems and needed to write VIBbox data to external hard drives while we sent the NAS drives back to LBL to be emptied and swapped. Writing to the external drives was too slow for the realtime system to keep pace effectively. Data following approximately June 5 were processed at LBNL after the experiment was demobilized (at the time of writing in March 2023, this effort was ongoing). The output from the system included automatic event detection, location, and magnitude estimation.

4.3 Noise sources and other data quality notes

With so much activity in the drift and so many different monitoring systems operating in the same boreholes, users are warned that the continuous VIBbox data have a number of data quality issues that are important to understand.

4.3.1 CASSM shots

The CASSM system ran nearly continuously from March 17 until September 12, 2022. The system cycled through each of the 20 sources in succession, firing 16 shots at one-second intervals, waiting a number of seconds to stack the signals, and then moving to the next source. These signals dominate the continuous seismic records and must be either removed or ignored to effectively identify any seismicity related to injection activities. As mentioned above, the CASSM signals are somewhat easy to remove once they are detected because the known source waveform is recorded in the CB.CTrg channel.

4.3.2 ERT cross-talk

Another system that was operating during the entirety of the experiment was the Electrical Resistivity Tomography (ERT) system. This system consisted of a number of electrodes, installed in the same boreholes as the seismic sensors, that both sent and received electrical signals across the testbed. As discussed in the installation section, an effort was made to electrically isolate the ERT and seismic instrumentation from each other using a schedule 40 PVC shroud. However, while this was effective in eliminating the effect of the TEC and metal sensor enclosures on the ERT system, the reverse was not true. ERT signals appear as large spikes in the continuous data, varying in shape depending on the location of the source electrode relative to the seismic sensor in question, but occurring at roughly the same time across all channels. These types of signals are difficult to remove, especially in a realtime application where speed is of the highest priority. The approach we settled on was to use matched filter detection techniques, in this case a Python pack-

age called EQcorrscan [1], to find occurrences of ERT cross-talk and remove them from the data. We manually selected ten ERT spikes for all 64-channels of data and scanned these template events through each 32-second chunk of data. Where any of the templates matched the continuous data, we removed that section of data and linearly interpolated over the gap. Finally, we overprinted the filled gap with artificial noise created by drawing from a random normal distribution scaled to the median absolute deviation of the entire 32-second trace. This technique proved capable of detecting and eliminating at least 95% of the ERT cross-talk spikes from the data.

4.3.3 Blast shots

Far less common, but important to note, were the occurrences of blasting shots conducted for the excavation of large caverns on the 4850 level. These occurred up to twice a day at recorded intervals. Because the site of the blasting is more than one kilometer from the EGS Collab site, the frequency of these waves recorded by the hydrophones and accelerometers in our boreholes is too low to adversely affect the detection of the small events of interest to us. But these blasts are visible in the data and could be made use of by other researchers with different aims. Please consult SURF directly for records of the timing and location of these blasts.

4.3.4 VIBbox hardware malfunction: 7-9-2022

At 14:03:50.412766 UTC on July 9, 2022, during the chilled water circulation test, the VIBbox interrogator suffered a hardware malfunction. The cause is unknown as of this writing, but the result was that eight channels swapped their write order in the raw data files. This was only discovered months after the experiment had been completely decommissioned, but the malfunction partly contributed to the failure of the realtime system during EGS Collab Experiment 2 (and 3). Table 1 describes which channels were affected and the channel they changed places with after the hardware issue. This issue is still under investigation the time of writing. If any user wants to analyze VIBbox data from after this malfunction, please reach out to chopp@lbl.gov to see if we've reached a resolution after this report's publication.

Original SEED ID	Original write position	New write position
CB.PPS..	64	8
CB.CEnc..	63	9
CB.CMon..	61	10
CB.Trig..	62	11
CB.TS16..XDH	8	64
CB.TS18..XDH	9	63
CB.TS20..XDH	10	61
CB.TS22..XDH	11	62

Table 1: Original and new channel ordering following the VIBbox malfunction on 7-9-2022.

4.4 Sensor calibration and frequency response information

As mentioned briefly above, we purchased calibration certificates for three of the 16 installed accelerometers. These certificates provide detailed information about the response of the sensors to excitation at known frequencies and can therefore be used to construct frequency response curves. These certificates are included in the GDR submission with the VIBbox dataset and Figure 3 shows the acceleration amplitude and phase response from these calibrations. The shake tests were only conducted up to 20 kHz, so users are cautioned against correcting for instrument response at frequencies higher than this. These results apply only to the bare accelerometers themselves and do not account for the effect of the enclosures or the grouting on the frequency response convolved into the data.

To help combat the unknowns mentioned above, we conducted a series of calibration shots along the rib of the main drift. We used an automatic, adjustable center punch tool with a known striking force of 250 N (Rennsteig model #430 231). 11 points were surveyed along the main drift rib starting north of the Site A alcove and running to south of the Site B excavation. Seven surveys were carried out during the duration of the experiment, with each survey consisting of a single sweep along all 11 shot points. At each shot point, we began with a single blow from a 5 lb sledgehammer, followed by 10 shots from the center punch. The locations of the 11 shot points are recorded in Appendix 4 and the approximate time and shot point for each hammer blow is shown in Appendix 5. Unfortunately, we were unable to trigger the Geodes in the CASSM system to record on the hammer or center punch shots as we did not have a trigger cable long enough to span the entire survey area. Analyses of these shots must therefore be conducted manually using the continuous VIBbox data.

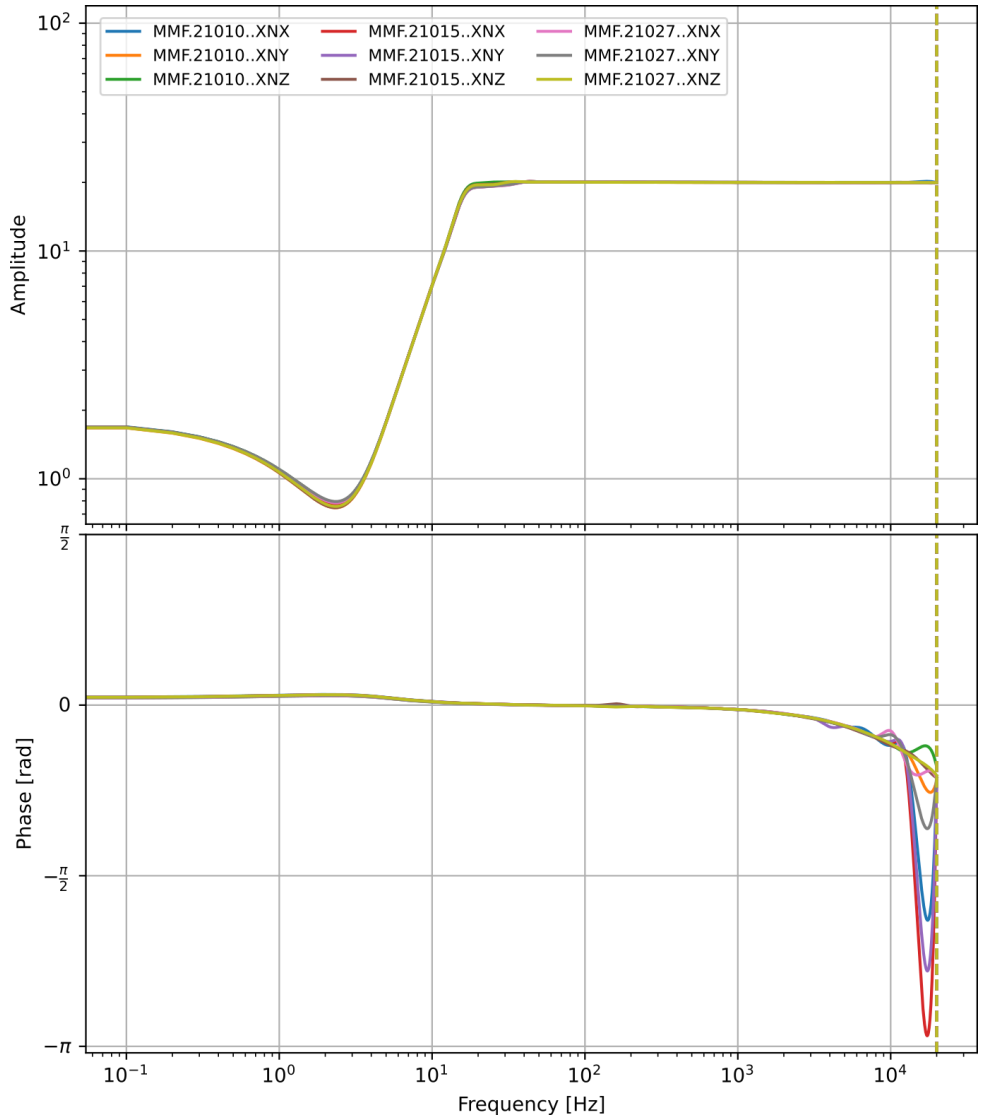

Figure 3: Acceleration amplitude (top) and phase (bottom) response for three of the 16 installed accelerometers. These results were obtained from a calibration certification process conducted by the sensor manufacturer MMF through a shake table test.

5 Results

When this report was written, results were only available through June 5, 2022. This was the date after which the realtime system stopped working and no further analysis of the continuous waveforms is possible until they are uploaded to servers at LBNL.

The final version of the catalog has been manually reviewed to both remove false detections and manually revise the phase arrival picks. This was necessary due to the low signal-to-noise ratio (SNR) of nearly all of the detected events, a consequence of the low sensitivity of the accelerometers (relative to those installed during the previous experiment). Following the revision of the events, we also relocated the seismicity with the NLLoc software (v6.0) using a homogenous velocity model ($V_p = 6900$ m/s, $V_s = 4100$ m/s, taken as an average from well logs).

Figure 4 shows the current final catalog from the start of the experiment until June 5, 2022. Figure **??** shows injection pressure and flow rate over the course of fracture creation and circulation testing. The seismicity detected on April 28 is actually the seismic manifestation of full waveform sonic logging of borehole TN and not seismicity in the usual sense.

The next obvious observation is that seismicity was not actually observed until May 6, which was one day after the start of injection into borehole TU. Injection had previously been into borehole TC from which a fracture had been driven all the way to the drift near the Site A alcove. It is safe to assume that the driving of a fracture many tens of meters from the point of injection was accompanied by seismicity, so the outstanding question is, “Why was seismicity detected once injection in TU exceeded 5000 psi at 5 L/min, and not during injection into TC?". There are three factors at play:

- The accelerometers installed in this testbed are one order of magnitude less sensitive than those installed in the previous testbed on the 4850 level.
- The period when seismicity began corresponds to the highest flow rates and injection pressures to that point in the experiment (5 L/min and 5000 psi)
- TU sits at the top of the injection well set (highest elevation), closer to sensors in AMU and DMU, but further from AML and DML.

While the decrease in sensor sensitivity certainly hampers our ability to detect smaller-magnitude seismicity (this is immediately obvious from the low SNR of the events we do detect), it doesn't explain the related inference that the seismicity associated with TU injection is therefore of a higher magnitude than the seismicity that, presumably, occurred during injection, and fracture creation, from TC. Partly, the larger magnitudes could be explained by the increase in pressure and flow rate, but we would still have expected to detect the seismicity associated with the fracture created from TC. It's possible that something about the rock mass in the upper portion of the testbed lends itself to larger

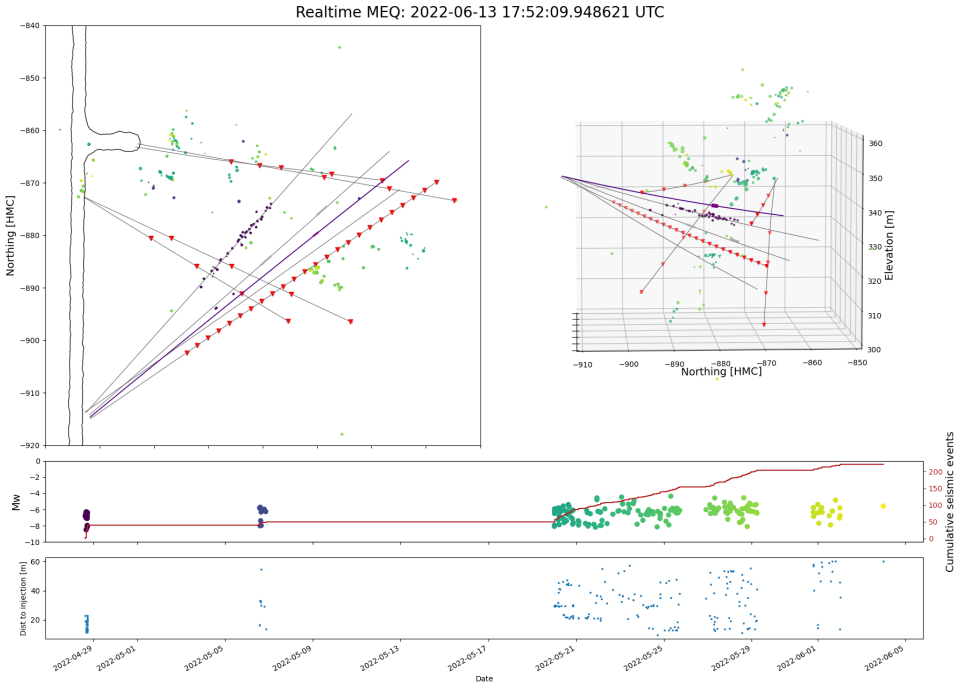

Figure 4: Acceleration amplitude (top) and phase (bottom) response for three of the 16 installed accelerometers. These results were obtained from a calibration certification process conducted by the sensor manufacturer MMF through a shake table test.

seismicity and/or more efficient propagation of seismic waves. The fact that we accurately detect and locate the FWS logging shots in TN, however, shows that we should have been able to detect seismicity along the fracture that passed directly through TN during injection into TC.

6 Appendices

6.1 VIBbox channel order

SEED id	Type of data
CB.TS02..XDH	Hydrophone
CB.TS04..XDH	Hydrophone
CB.TS06..XDH	Hydrophone
CB.TS08..XDH	Hydrophone
CB.TS10..XDH	Hydrophone
CB.TS12..XDH	Hydrophone
CB.TS14..XDH	Hydrophone
CB.TS16..XDH	Hydrophone
CB.TS18..XDH	Hydrophone
CB.TS20..XDH	Hydrophone
CB.TS22..XDH	Hydrophone
CB.TS24..XDH	Hydrophone
CB.AML1..XNX	Accelerometer
CB.AML1..XNY	Accelerometer
CB.AML1..XNZ	Accelerometer
CB.AML2..XNX	Accelerometer
CB.AML2..XNY	Accelerometer
CB.AML2..XNZ	Accelerometer
CB.AML3..XNX	Accelerometer
CB.AML3..XNY	Accelerometer
CB.AML3..XNZ	Accelerometer
CB.AML4..XNX	Accelerometer
CB.AML4..XNY	Accelerometer
CB.AML4..XNZ	Accelerometer
CB.AMU1..XNX	Accelerometer
CB.AMU1..XNY	Accelerometer
CB.AMU1..XNZ	Accelerometer
CB.AMU2..XNX	Accelerometer
CB.AMU2..XNY	Accelerometer
CB.AMU2..XNZ	Accelerometer
CB.AMU3..XNX	Accelerometer
CB.AMU3..XNY	Accelerometer
CB.AMU3..XNZ	Accelerometer
CB.AMU4..XNX	Accelerometer
CB.AMU4..XNY	Accelerometer
CB.AMU4..XNZ	Accelerometer
CB.DML1..XNX	Accelerometer
CB.DML1..XNY	Accelerometer

CB.DML1..XNZ	Accelerometer
CB.DML2..XNX	Accelerometer
CB.DML2..XNY	Accelerometer
CB.DML2..XNZ	Accelerometer
CB.DML3..XNX	Accelerometer
CB.DML3..XNY	Accelerometer
CB.DML3..XNZ	Accelerometer
CB.DML4..XNX	Accelerometer
CB.DML4..XNY	Accelerometer
CB.DML4..XNZ	Accelerometer
CB.DMU1..XNX	Accelerometer
CB.DMU1..XNY	Accelerometer
CB.DMU1..XNZ	Accelerometer
CB.DMU2..XNX	Accelerometer
CB.DMU2..XNY	Accelerometer
CB.DMU2..XNZ	Accelerometer
CB.DMU3..XNX	Accelerometer
CB.DMU3..XNY	Accelerometer
CB.DMU3..XNZ	Accelerometer
CB.DMU4..XNX	Accelerometer
CB.DMU4..XNY	Accelerometer
CB.DMU4..XNZ	Accelerometer
CB.CMon..	CASSM Monitor
CB.CTrig..	CASSM Trigger
CB.CEnc..	CASSM Source Encoder
CB.PPS..	Pulse per second time signal

Table 2: SEED names for each channel in the order stored in the VIBbox binary data files.

6.2 Seismic sensor locations

Station name	X [HMC ft]	Y [HMC ft]	Z [HMC ft]
TS01	4022.308614	-2960.480988	1105.456392
TS02	4028.730674	-2955.923056	1103.281251
TS03	4035.159656	-2951.361893	1101.133504
TS04	4041.658533	-2946.752842	1098.99255
TS05	4048.124287	-2942.168286	1096.891169
TS06	4054.603637	-2937.574515	1094.812869
TS07	4061.088634	-2932.977166	1092.76025
TS08	4067.579209	-2928.376291	1090.733326
TS09	4074.106998	-2923.750888	1088.719353
TS10	4080.624526	-2919.135762	1086.73056
TS11	4087.115853	-2914.542168	1084.771571
TS12	4093.604668	-2909.953319	1082.835051
TS13	4100.124222	-2905.347141	1080.916049
TS14	4106.699635	-2900.707122	1079.011584
TS15	4113.235412	-2896.100648	1077.149315
TS16	4119.779132	-2891.494103	1075.31533
TS17	4126.343224	-2886.87296	1073.501334
TS18	4132.87711	-2882.268382	1071.717443
TS19	4139.492447	-2877.601627	1069.933412
TS20	4146.045568	-2872.974048	1068.188082
TS21	4152.634164	-2868.32002	1066.45809
TS22	4159.187727	-2863.691775	1064.763952
TS23	4165.738106	-2859.066808	1063.097141
TS24	4173.156098	-2853.830083	1061.230863
AML1	4048.9701	-2841.082857	1076.228815
AML2	4079.264196	-2844.939494	1050.317648
AML3	4109.716412	-2848.916415	1024.377829
AML4	4140.207133	-2852.808518	998.5486472
AMU1	4066.106288	-2843.574918	1116.460595
AMU2	4105.277604	-2850.81498	1111.442245
AMU3	4144.562651	-2858.120697	1107.048016
AMU4	4183.847975	-2865.504628	1103.28804
DML1	4000.655148	-2889.068877	1092.552036
DML2	4028.111438	-2906.43786	1069.132752
DML3	4055.576022	-2923.61341	1045.66585
DML4	4083.337964	-2940.782028	1022.031092
DMU1	4013.037448	-2888.868988	1125.728398
DMU2	4049.216969	-2906.382033	1125.153255
DMU3	4085.221558	-2923.805786	1125.339731
DMU4	4121.212243	-2941.237009	1126.234317

Table 3: XYZ coordinates for each seismic sensor. The coordinates are in Homestake Mine Coordinates, which is a cartesian coordinate system used in the mine. Units are feet.

6.3 Python function to read raw, 32-bit VIBbox data to an Obspy Stream

```
import numpy as np

from scipy.stats import median_absolute_deviation
from obspy import Stream, Trace, UTCDateTime
from obspy.core.trace import Stats

import matplotlib.pyplot as plt


def vibbox_read(fname, seeds, debug=0):
    """
    Read function for raw VIBbox, 32-bit binary data files

    :param fname: Name of the file to read
    :param seeds: Iterable of the SEED ids in order stored on file
    :param debug: Debugging flag, basically to check time signal is
                                            being read
    :return:
    """
    network, stations, locations, channels = zip(*[s.split('.') for s in
                                            seeds])
    network = network[0]
    # Find channel PPS (pulse per second)
    try:
        clock_channel = np.where(np.array(stations) == 'PPS')[0][0]
    except IndexError:
        print('No PPS channel in file. Not reading')
        return
    # TODO Everything from here to file open should go in config?
    HEADER_SIZE=4
    HEADER_OFFSET=27
    DATA_OFFSET=148
    VOLTAGE_RANGE=10  # +/- Volts
    with open(fname, "rb") as f:
        f.seek(HEADER_OFFSET, os.SEEK_SET)
        # read header
        H = np.fromfile(f, dtype=np.uint32, count=HEADER_SIZE)
        BUFFER_SIZE=H[0]
        FREQUENCY=H[1]
        NUM_OF_BUFFERS=H[2]
        no_channels=H[3]
        # read data
        f.seek(DATA_OFFSET, os.SEEK_SET)
        A = np.fromfile(f, dtype=np.uint32,
                        count=BUFFER_SIZE * NUM_OF_BUFFERS)
        try:
            A = A.reshape(int(len(A) / no_channels), no_channels)
        except ValueError as e:
            print(e)
            # File was interrupted mid-write. Return empty stream
            return Stream()
```

```
    # Sanity check on number of channels provided in yaml
    if len(channels) != no_channels:
        print('Number of channels in config file not equal to number in
                                                data')
        return
    A = A / 2**32  # Norm to 32-bit
    A *= (2 * VOLTAGE_RANGE)
    A -= VOLTAGE_RANGE  # Demean
    path, fname = os.path.split(fname)
    try:
        # Use derivative of PPS signal to find pulse start
        dt = np.diff(A[:, clock_channel])
        # Use 70 * MAD threshold
        samp_to_first_full_second = np.where(
            dt > np.mean(dt) + 30 * median_absolute_deviation(dt))[0][0]
        # Condition where PPS not recorded properly
        if samp_to_first_full_second > 101000:
            print('Cannot read time signal')
            return
        # If we start during the time pulse, use end of pulse for timing
        if samp_to_first_full_second > 90000:
            print('Start of data is during time pulse. Using end of
                                                pulse.')
            # Negative dt
            samp_to_first_full_second = np.where(
                dt < np.mean(dt) - 30 *
                median_absolute_deviation(dt))[0][0] + 90000
        if debug > 0:
            fig, ax = plt.subplots()
            ax.plot(dt, color='r')
            ax.plot(A[:, clock_channel], color='k')
            ax.axhline(y=np.mean(dt) + 30 * median_absolute_deviation(dt
                                                ),
                       color='magenta', linestyle='--')
            ax.axvline(x=samp_to_first_full_second, color='magenta',
                       linestyle='--')
            fig.text(x=0.75, y=0.75, s=samp_to_first_full_second,
                     fontsize=14)
            plt.show()
        starttime = UTCDateTime(
            np.int(fname[5:9]), np.int(fname[9:11]), np.int(fname[11:13]
                                                ),
            np.int(fname[13:15]), np.int(fname[15:17]), np.int(fname[17:
                                                19]),
            np.int(1e6 * (1 - (np.float(samp_to_first_full_second) /
                               FREQUENCY))))
    except Exception as e:
        print(e)
        print('Cannot read exact time signal: ' + fname +
              '. Taking an approximate one instead')
        starttime = UTCDateTime(
            np.int(fname[5:9]), np.int(fname[9:11]), np.int(fname[11:13]
                                                ),
            np.int(fname[13:15]), np.int(fname[15:17]), np.int(fname[17:
                                                19]),
```

```
            np.int(1e2 * np.int(fname[19:23])))
    # arrange it in an obspy stream
    st = Stream()
    for i, sta in enumerate(stations):
        stats = Stats()
        # stats.sampling_rate = round(H[1], 1)
        stats.delta = 1. / H[1]
        stats.npts = A.shape[0]
        stats.network = network
        stats.station = sta
        stats.channel = channels[i]
        stats.location = locations[i]
        stats.starttime = starttime
        # Create new array to avoid non-contiguous warning in obspy.core
                                                .mseed
        st.traces.append(Trace(data=np.array(A[:, i]), header=stats))
    return st
```

6.4 Borehole design cross-sections

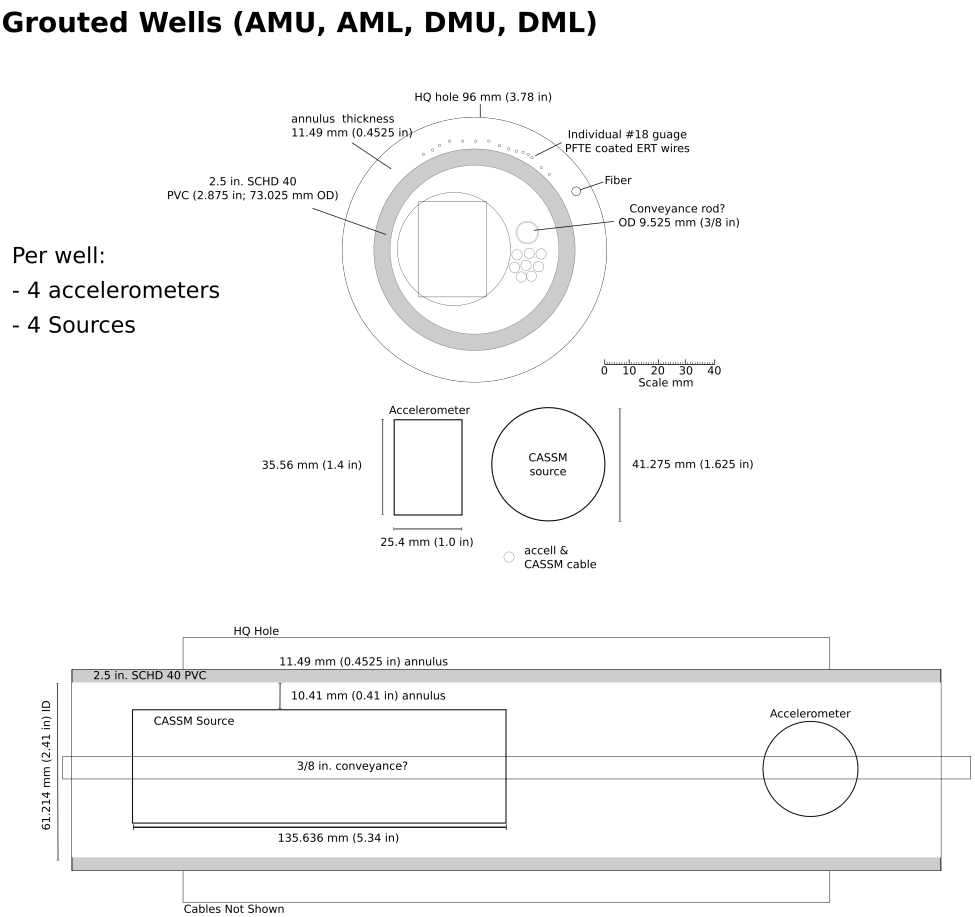

Figure 5: Scale cross-section of the grouted boreholes AMU, AML, DMU, DML showing all equipment installed in these boreholes.

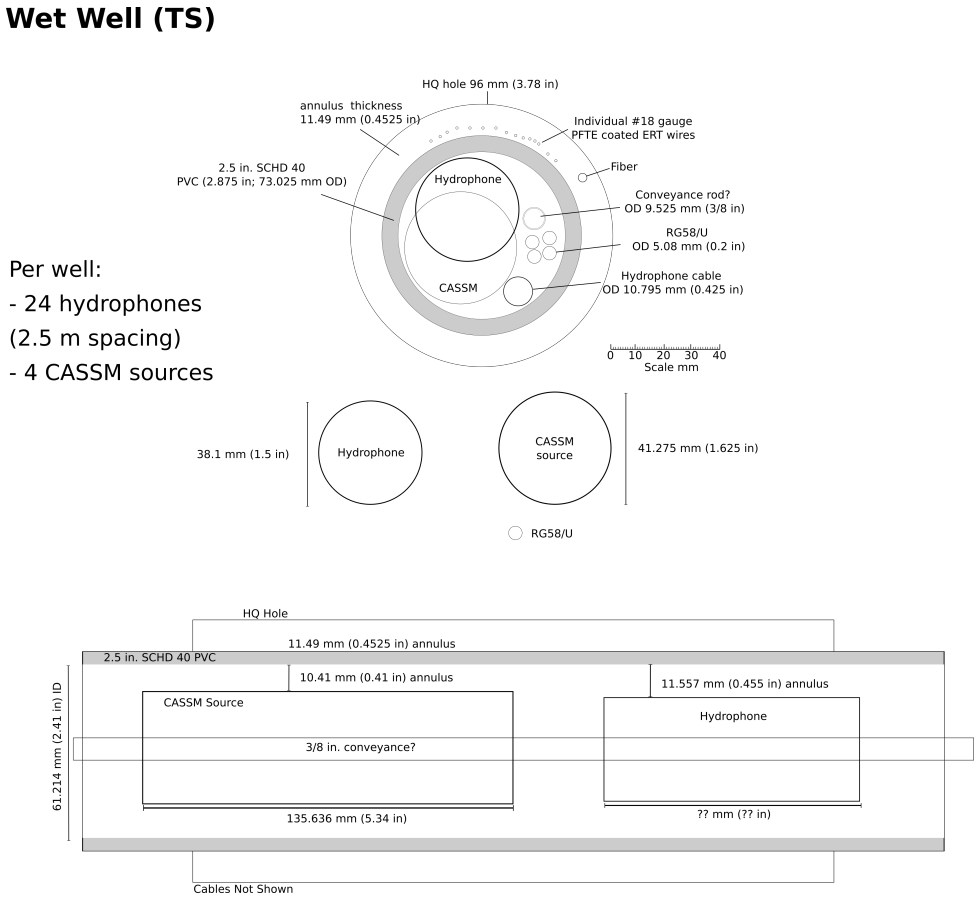

Figure 6: Scale cross-section of the non-grouted (i.e. wet) borehole, TS, showing all equipment installed.

6.5 Center punch calibration shot points

Shot pt name	X [HMC m]	Y [HMC m]	Z [HMC m]
S-1	3999.726	-2758.007	1126.956
S-2	3994.419	-2790.907	1126.421
S-3	3991.186	-2818.472	1125.364
S-4	3984.619	-2854.833	1126.722
S-5	3978.965	-2887.941	1125.982
S-6	3973.136	-2921.056	1126.629
S-7	3970.155	-2943.064	1126.278
S-8	3963.764	-2980.992	1127.543
S-9	3954.997	-3036.468	1126.018
S-10	3950.652	-3067.296	1126.359
S-11	3945.863	-3094.749	1125.745

Table 4: XYZ coordinates for each calibration shot point.

6.6 Center punch calibration shot times

Time of hammer (+/-0.5 sec UTC)	Shot point
3/8/2022 22:54:20	S-1
3/8/2022 22:55:30	S-2
3/8/2022 22:58:10	S-4
3/8/2022 22:59:20	S-5
3/8/2022 23:00:30	S-6
3/8/2022 23:01:30	S-7
3/8/2022 23:02:50	S-8
3/8/2022 23:05:30	S-10
3/8/2022 23:04:30	S-11
3/11/2022 19:00:00	S-1
3/11/2022 19:01:00	S-2
3/11/2022 19:02:20	S-4
3/11/2022 19:03:50	S-5
3/11/2022 19:04:50	S-6
3/11/2022 19:05:50	S-7
3/11/2022 19:06:50	S-8
3/11/2022 19:08:20	S-10
3/11/2022 19:09:20	S-11
3/11/2022 19:10:20	S-10
3/11/2022 19:11:30	S-8
3/11/2022 19:12:30	S-7
3/11/2022 19:13:20	S-6
3/11/2022 19:14:20	S-5
3/11/2022 19:15:20	S-4
3/11/2022 19:16:20	S-2
3/11/2022 19:17:20	S-1
3/11/2022 19:19:50	S-2
3/11/2022 19:26:00	S-4
3/11/2022 19:27:00	S-5
3/11/2022 19:28:00	S-6
3/11/2022 19:28:50	S-7
3/11/2022 19:29:40	S-8
3/11/2022 19:31:40	S-10
3/11/2022 19:32:30	S-11
3/11/2022 19:34:00	S-10
3/11/2022 19:35:10	S-8
3/11/2022 19:36:10	S-7
3/11/2022 19:37:00	S-6

3/11/2022 19:38:30	S-5
3/11/2022 19:39:30	S-4
3/11/2022 19:41:40	S-2
3/11/2022 19:42:30	S-1
4/13/2022 16:23:00 (Aprrox)	S-4
4/22/2022 19:26:00	S-1
4/22/2022 19:26:50	S-2
4/22/2022 19:27:40	S-3
4/22/2022 19:29:00	S-4
4/22/2022 19:30:00	S-5
4/22/2022 19:30:50	S-6
4/22/2022 19:32:00	S-8
4/22/2022 19:34:20	S-10
4/22/2022 19:35:10	S-11
4/22/2022 19:36:10	S-10
4/22/2022 19:37:40	S-6
4/22/2022 19:38:30	S-5
4/22/2022 19:39:20	S-4
4/22/2022 19:40:10	S-3
4/22/2022 19:41:00	S-2
4/22/2022 19:41:50	S-1

Table 5: Timing of the hammer shot preceding ten center punch shots at the specified shot point.

References

[1] Calum J. Chamberlain, Chet J. Hopp, Carolin M. Boese, Emily Warren-Smith, Derrick Chambers, Shanna X. Chu, Konstantinos Michailos, and John Townend. EQcorrscan: Repeating and Near-Repeating Earthquake Detection and Analysis in Python. *Seismological Research Letters*, 89(1):173–181, 12 2017.

[2] Thomas M. Daley, Ray D. Solbau, Jonathan B. Ajo-Franklin, and Sally M. Benson. Continuous active-source seismic monitoring of CO2 injection in a brine aquifer. *Geophysics*, 72(5):A57–A61, 07 2007.

BERKELEY LAB

EGS Collab Experiment 2

Distributed temperature (DTS) system

Technical report
LBNL EESA
September 2022

AUTHOR (Last, First):
Hopp, Chet
DATE:
11-8-2022
TITLE:
EGS Collab Experiment 2: Distributed fiber optic temperature system

Contents

1 Terminology

- **DTS**: Distributed Temperature Sensing. A form of Distributed Optical Fiber Sensing (DOFS) that uses the Raman component of backscattered light along the length of a fiber to measure temperature.
- **DFOS**: Distributed Fiber Optic Sensing. A family of methods used to interrogate lengths of fiber using backscattered light.
- **SURF**: Sanford Underground Research Facility. The old Homestake gold mine in Lead, SD, USA where the EGS Collab experiment has taken place.
- **OD**: Outer diameter
- **ID**: Inner diameter
- **ERT**: Electrical Resistivity Tomography
- **GDR**: Geothermal Data Repository.

2 Introduction

The EGS Collab Experiment #2 took place from approximately February–September 2022 at the Sanford Underground Research Facility in Lead, SD. The project was the continuation of a years-long experiment aiming to validate models of enhanced geothermal systems through a series of high-pressure injections into rock between 1200 and 1500 meters below the surface. These injection experiments were extensively monitored by a number of systems including seismic waveform recording, pressure and temperature probes, active source seismic tomography, electrical resistivity tomography, and a full suite of DFOS interrogators.

This report details the Distributed Temperature Sensing (DTS) system, which uses Raman back-scattered light from a forward-propagating laser pulse to measure the temperature along the length of a multi-mode fiber optic cable. For details on this method, the reader is referred to [1].

Figure 1: Silixa XT-DTS unit used to collect the measurements reported here.

3 Installation

The sensing fiber (manufactured by NBG of Germany) was installed as a continuous loop in four monitoring wells. The fiber package comprised six individual fibers, two multi-mode and four single-mode, encapsulated in a 2.2 mm OD stainless steel casing. The casing was coated in high-density polyethylene and the entire package had a manufacturer-reported minimum bend radius of 25 mm.

The entire ∼720 m continuous fiber loop was installed in four 96 mm ID boreholes behind 73 mm OD centralized PVC casing (Figure 4). The ∼11 mm annulus space was shared with electrodes used for electrical resistivity tomography (ERT). Additional instrumentation was installed inside the PVC casing and then each of the holes was filled with a specially formulated grout to couple all of the instrumentation to the rock.

Figure 5 shows a simplified schematic of the layout of the fiber loop, while Figure 2 shows the location of the boreholes and seismic sensors in the Experiment 2 testbed. The fiber package was installed as one continuous piece, meaning that there are no breaks or splices in the loop. The free ends of the loop returned to the same location at Site A (black boxes in Figure 2) of the experiment where the individual fibers were spliced to jumper cables that were then connected to the various interrogator units, all of which resided either in weather-tight steel enclosures or on tables near the intersection of the Site A and the main drift. Two water baths were also located at this location. One was maintained at roughly 40 degrees C, the other was left at ambient temperature. A length of the fiber package (between 15 and 30 m) was coiled and placed into each of these water baths. The package passed through each bath once on its way from the interrogator to borehole AMU and again on its way from borehole DML back to the interrogator (for a total of two coils of cable in each bath). See Figure 5 for an illustration of the installation.

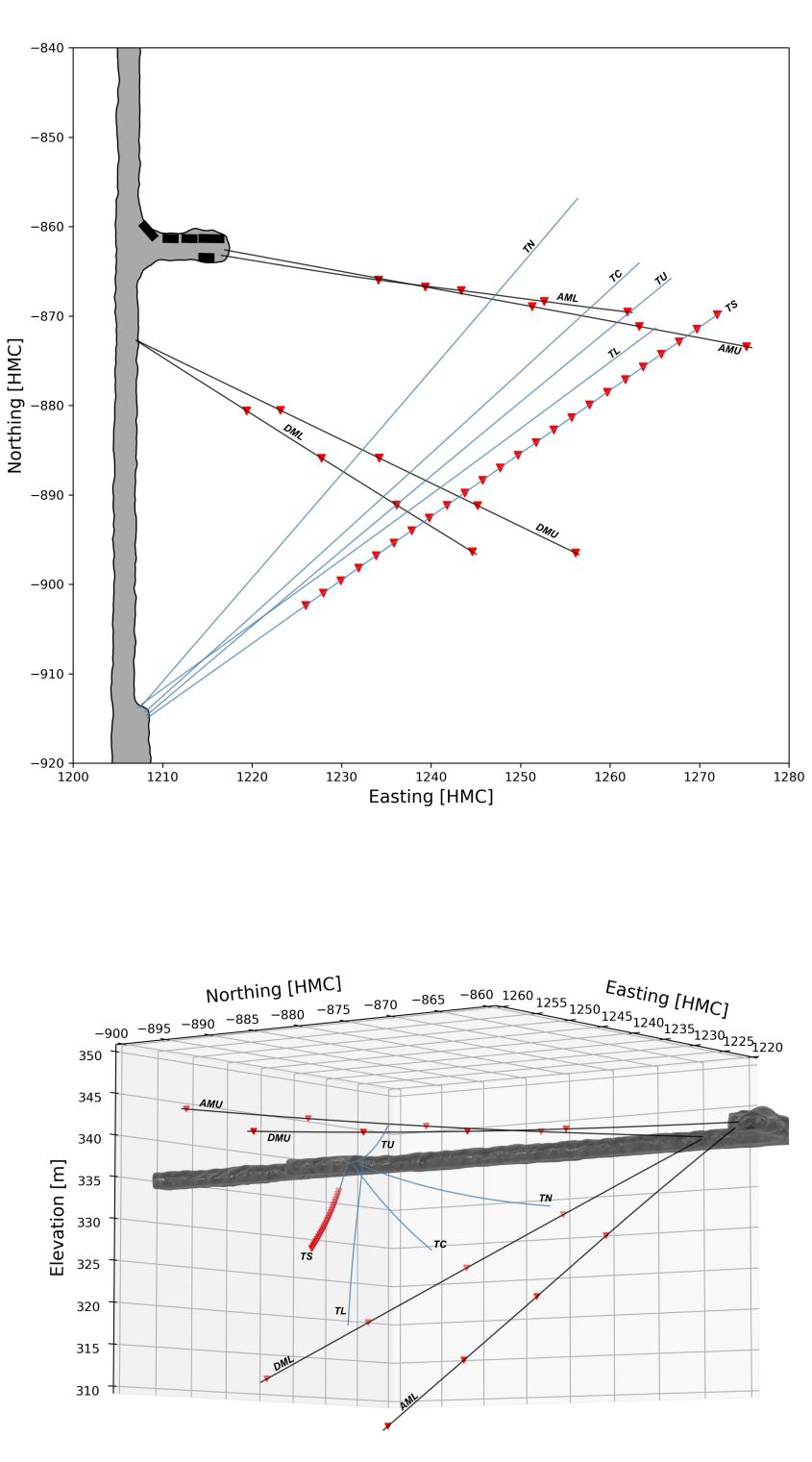

Figure 2: Overview of the EGS Collab Experiment 2 testbed on the 4100 level of SURF. The boreholes are labeled by name and the locations of the seismic sensors are indicated with red triangles. The fiber loop is installed in the four grouted boreholes (AMU, AML, DMU, and DML) shown in black. A string of hydrophones is installed in non-grouted borehole TS.

Figure 3: Interior of the hot water calibration bath showing the submersible heater (black) placed into the interior bath containing the fiber loop. This smaller bath was filled with water, capped, and then the entirety of the larger tub was filled with bubble wrap that acted as insulation.

The DTS interrogator used for EGS Collab (Experiments 1 and 2) was a Silixa XT-DTS system (Figure 1). Each end of one of the multi-mode fibers was connected to the XT-DTS. This so-called 'double-ended' (the fiber is interrogated in both directions) configuration takes longer to make a single measurement than a single-ended setup but results in a more accurate, stable data product. The two water baths were used for temperature calibration with one bath maintained at ~40 ^{o}C using an electric, submersible heating element (Figure 3) and the other bath remained at ambient mine temperature. The XT-DTS was connected to two thermistors that were used to continuously record the temperature in each bath and anchor the temperature sensed by the fiber in the baths to the temperature measured by the thermistors.

For the duration of the experiment, measurements were taken every 10 minutes with a spatial resolution (spacing of measurements along the fiber) of 0.254 m.

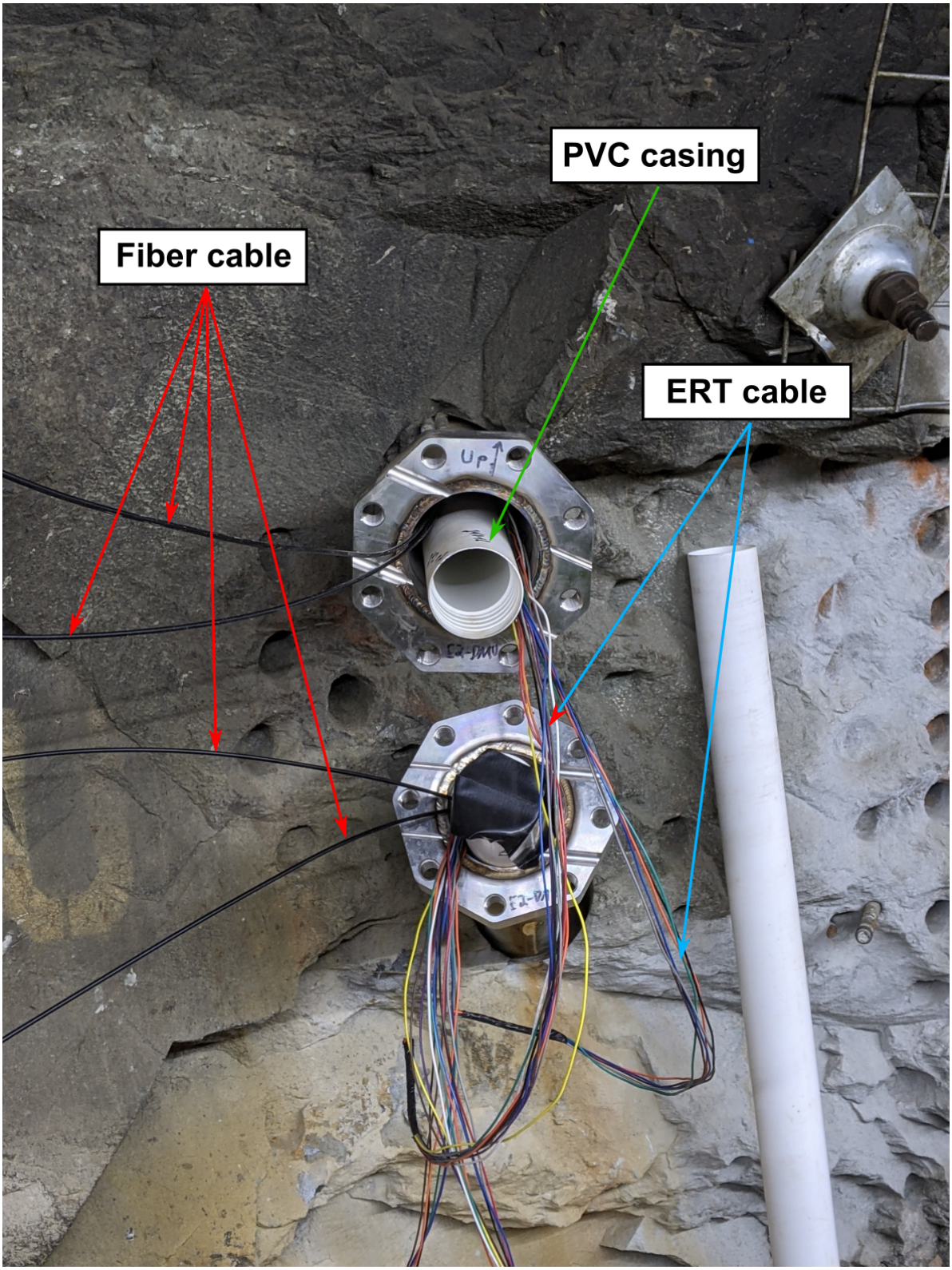

Figure 4: Two grouted monitoring wells (AMU and AML) after installation of the PVC casing, ERT electrodes, and fiber optic package. The wells were later capped and grouted.

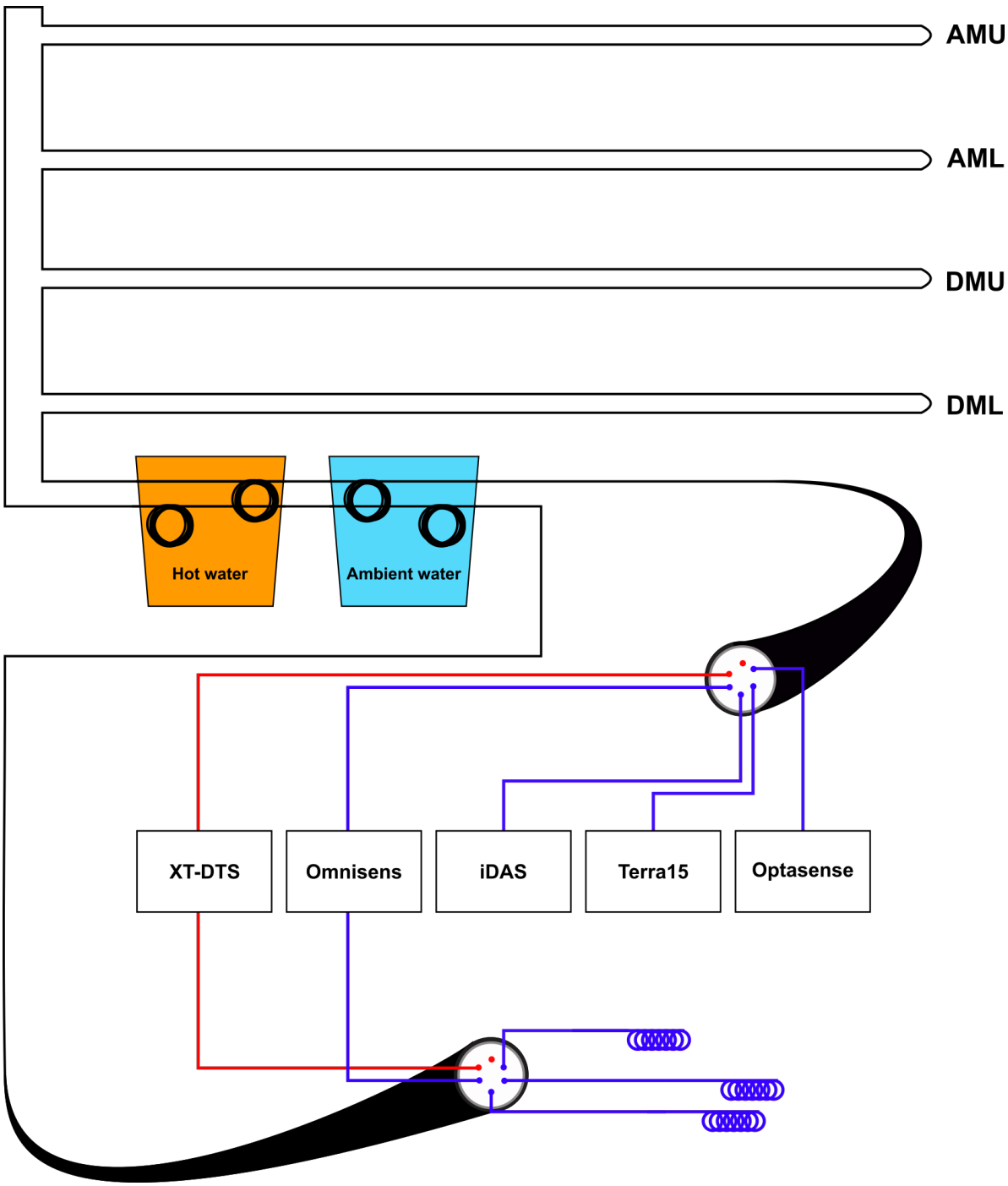

Figure 5: Generalized layout of the entire fiber optic sensing system. Each of the four single-mode fibers (blue) was connected to a different DAS or DSS interrogator, while only one of the multi-mode fibers (red) was connected to the XT-DTS temperature sensing unit. The final MMF was not used.

4 Data

This section describes the data products produced by the XT-DTS interrogator box and provides useful context for users.

4.1 Raw data

The data recorded by the XT-DTS is saved as single XML files. Each file contains the data for all points along the fiber for a single measurement in time. There are six columns of data in each of the files:

- Length along fiber (LAF) in meters
- Stokes intensity (ST)
- anti-Stokes intensity (AST)
- reverse Stokes intensity (REV-ST)
- reverse anti-Stokes intensity (REV-AST)
- DTS temperature (TMP) in degrees C

The four columns of Stokes intensity are measurements of the intensity of the Raman component of backscattered light at each point along the fiber and are used by the box to calculate the temperature at that point. This calculation makes a number of assumptions about the fiber itself and the relationship between Stokes intensity and temperature and is done internally. If the user wishes to apply a different algorithm to temperature calculation they may do so using these columns. In most cases, the user will be interested in only the distance along fiber and the temperature in degrees C columns (the first and last, respectively).

4.2 Location mapping

In order to turn the lengths along fiber recorded by the XT-DTS to meaningful coordinates relative to the boreholes in the experiment, an effort was made to "map" the points at which the fiber package entered and exited each borehole. To do this, we heated the entry and exit points with a heat gun for a period of roughly 1 minute. We did this in two steps, one for boreholes AMU and AML and the other for DMU and DML. The resulting spike in temperature is visible at 14:29 UTC for AMU/AML and at 14:09 UTC for DMU/DML, both on 2022-9-12. This corresponds to the filenames `channel 1_20220912141411046.xml` and `channel 1_20220912142413359.xml`, respectively, in the raw data. The mapping is shown in the table below:

Borehole	Entry point [m along fiber]	Exit point [m along fiber]
AMU	85.70	207.19
AML	221.67	343.69
DMU	384.37	495.44
DML	505.10	616.43

4.3 Processed dataset

We applied the mapping above to the raw data set to extract only the portions of the data pertaining to the boreholes, omitting any data from portions of the fiber package that were hanging in the drift, or spooled in the water baths. We refer to this as the 'processed' dataset.

The processed data come as four files, one for each monitoring borehole in the 4100 testbed. The data span the period of 3-14-2022 to 9-14-2022, including all of the stimulations and flow tests that took place throughout the course of EGS Collab Experiment 2.

Each file is formatted as NetCDF: https://www.unidata.ucar.edu/software/netcdf/ which is a self-describing binary file format. It originated in the geosciences and is used for array-based measurements, especially in atmospheric science.

Most major programming languages have an interface for NetCDF I/O, but the files here were written using the `xarray` Python package: https://xarray.pydata.org/en/stable/index.html

Therefore, if the user is working in Python, I recommend reading the files with `xarray` as follows (assuming `xarray` is installed in your path):

```
import xarray as xr
ds = xr.open_dataset('path-to-file')
```

This will read the data in as an `xarray Dataset`, which is a container for multidimensional, labeled data: https://xarray.pydata.org/en/stable/data-structures.html

As mentioned in the Installation section, each borehole contains a single loop of fiber optic cable. We have split each borehole into a 'downgoing' and an 'upgoing' section where the downgoing is the closest to the start of the cable and the upgoing the furthest (although the 'start' or 'end' of the cable is essentially arbitrary). The temperature data (in ^{o}C) are represented in the `Dataset` as two `DataArrays` named `down_data` and `up_data` respectively, where the 'values' attribute is a 2-dimensional `numpy` array of measurements. Each row corresponds to a single channel of data (i.e. a single point along the fiber) and each column corresponds to a single measurement in time.

If you've read in the data following the snippet above, you can plot them as follows:

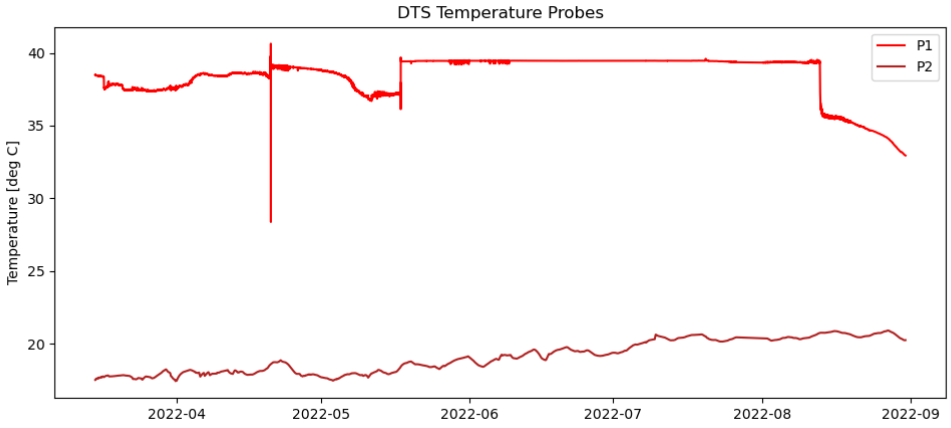

Figure 6: Time series plots of the two temperature probes in either of the water baths used for XT-DTS temperature calibration.

```
import matplotlib.pyplot as plt
ds["up_data"].plot()
plt.show()
```

4.4 Calibration bath issues

There is one important issue with these data that the user needs to be aware of before processing and interpreting results. As detailed in the Installation section above, the temperatures recorded in the raw and processed data are calculated by the XT-DTS using a calibration via two temperature probes placed in the two water baths. To reiterate, there is a length of fiber (>10 m) in each bath and this exact length is known to the XT-DTS. The XT-DTS then uses the known temperature of the water from the probe, which should be the same as the temperature of the fiber in the bath, to calibrate the temperature sensed along the entire fiber length. Unfortunately, the hot water bath (maintained at 40°C) slowly evaporated with time and needed to be refilled periodically. This meant that, at times, the temperature probe was measuring air temperature in the bath, while the fiber was still submerged. The exact effect of this discrepancy is unknown as oftentimes no one was underground to refill the bath or observe the position of the temperature probe relative to the water level. It is also difficult to know what the temperature of the water (and therefore fiber) was as the water level dropped because the circulation heater did not reach all the way to the bottom of the bath and was attempting to maintain 40°C even when not fully submerged.

Figure 6 shows the temperature measured by the XT-DTS temperature probes in the hot (P1) and ambient (P2) temperature water baths with time. The long period of stable temperature in the hot water bath corresponds to a period of stable water level. This also

coincides with the start of the circulation tests being conducted as part of EGS Collab Experiment 3. Deviations from this stable trend represent issues with the water level and probably a discrepancy between the temperature being measured by the probe (colder) and the temperature to which the fiber package in the bath was subjected (warmer). This would produce an apparent, and incorrect, cooling across the entire fiber. The ambient temperature water bath simply tracks the temperature in the drift that, in turn, is a damped measure of the air temperature at the surface, which is used to ventilate the mine. This trend is consistent with a general warming of the air in South Dakota from March until September.

We applied a simple correction for this bath-related apparent temperature variation, which we made available as a 'corrected' dataset on the GDR. The 'processed' and 'corrected' data are otherwise the same. To apply the correction, we assumed that each channel was affected equally by the calibration bias and attempted to remove this common trend. For each borehole, we selected a representative 'trend' channel near the toe where relatively little real temperature variation was expected. For the entire time series of measurements at this channel, we removed the absolute temperature offset (so that the first measurement was 0^oC). We then subtracted the trend from each channel in that borehole to get to the final 'corrected' result. Following this procedure, the channel selected as the 'trend' channel obviously becomes a flat line but we feel this is an acceptable trade given the relatively fine channel spacing (0.25 meters). The resulting, processed dataset shows the various signals much more clearly than the raw data (Figure 7). Users are encouraged to use these bath-calibration corrected data unless they are assessing the validity of our correction scheme.

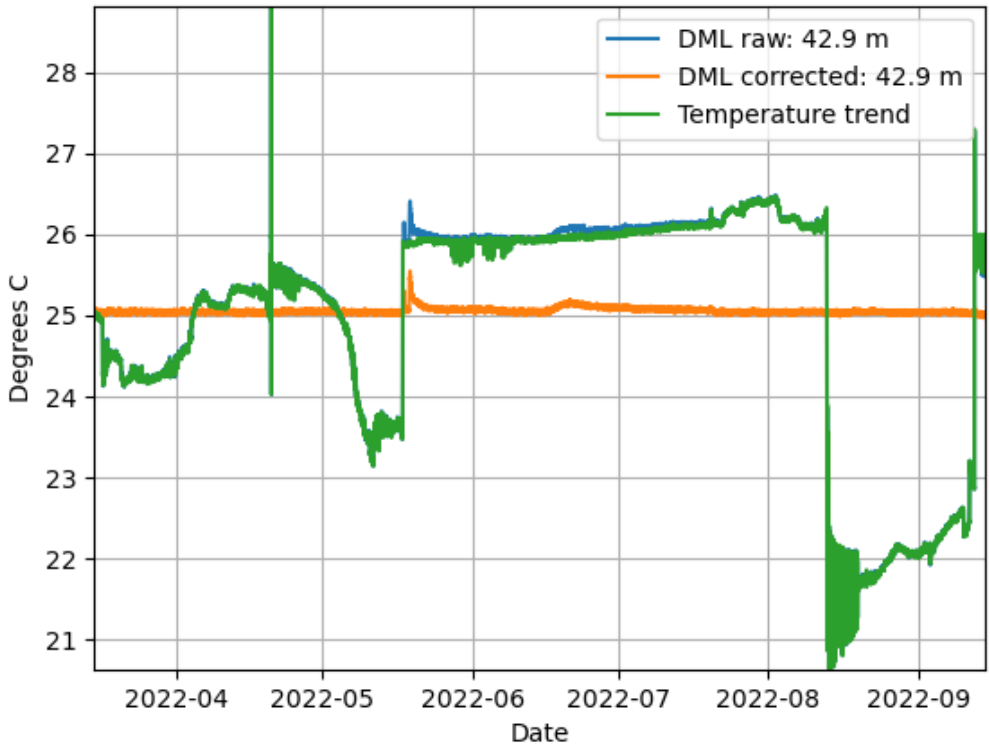

Figure 7: Demonstration of the calibration bath correction described above. Shown are the raw (blue), corrected (orange), and DML temperature trend (green) for the entire time series at a single channel. Green minus blue equals orange and this procedure was applied to each channel in each borehole.

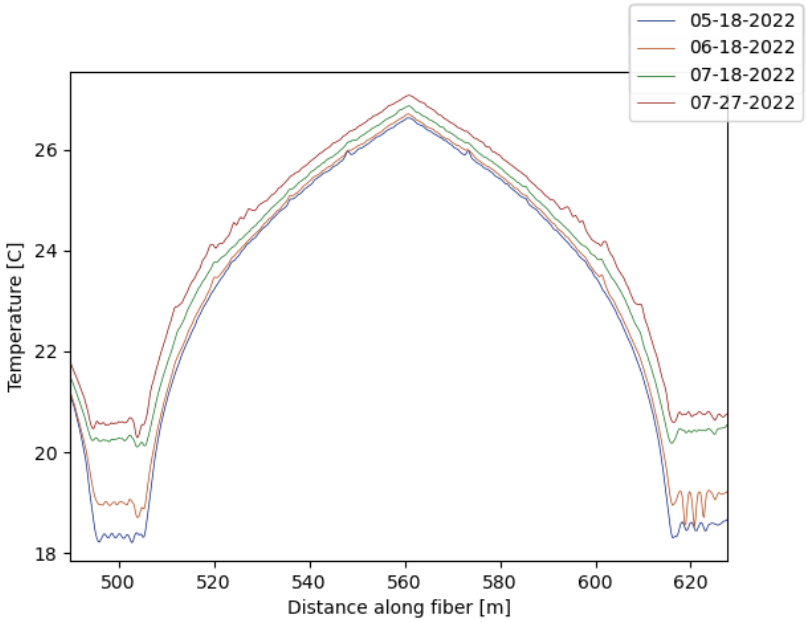

Figure 8: Comparison of the temperatures measured in borehole DML at various times during the circulation test of Experiment 3.

5 Results

The utility of the XT-DTS temperature dataset is twofold. First, it provides a means to locate points along the boreholes where the temperature rapidly changes. These ΔT data are most useful in identifying fracture intersections with the monitoring boreholes. Second, the absolute temperature can be used to calibrate thermo-hydro-mechanical models of the testbed.

5.1 Joule-Thomson effect at fracture intersection points

In the case of the EGS Collab experiments, rapid temperature change occurs most often when a flowing fracture (man-made or otherwise) intersects one of the monitoring boreholes. In this case, through what's known as the Joule-Thomson effect, water heats when depressurized and therefore the DTS system sees a positive change in temperature where pressurized fluid intersects the borehole.

Figure 8 shows this effect at four times during the flow tests of Experiment 3. Under static conditions, the boreholes exhibit a 'smooth' temperature profile, increasing with distance from the drift. The spikes observed at different depths for all time steps in Figure 8 indicate depths where a flowing fracture has intersected this borehole. These features are somewhat ephemeral, as indicated by their presence only during specific periods and not

Borehole	Intersection depth [m]	Start time	End time (approximate)
AMU	34.0	4-12-2022 5:23	4-13-2022 16:00
DML	42.9	5-17-2022 21:24	5-18-2022 5:50
DML	42.9	5-18-2022 22:39	5-22-2022 0:00
DML	43.9	5-18-2022 22:39	5-22-2022 0:00
AMU	54.9	5-24-2022 10:11	6-11-2022 0:00
DML	14.9	5-26-2022 2:13	5-28-2022 0:00
AMU	54.9	6-16-2022 6:00	Unclear
DML	14.9	6-16-2022 21:34	6-19-2022 0:00
DML	42.9	6-17-2022 11:01	Unclear
DML	6.7	7-20-2022 12:36	8-21-2022 12:00
DML	14.9	7-20-2022 12:36	8-21-2022 12:00
DML	22.3	7-20-2022 12:36	8-21-2022 12:00
AML	45.5	8-17-2022 7:16	8-23-2022 0:00
DMU	18.5	7-1-2022	Unclear
DMU	31.0	7-1-2022	Unclear
DMU	43.0	7-1-2022	Unclear

Table 1: Timing and depth of each heating signal observed in the grouted monitoring wells during the entire experiment.

during others. When compiled, these features give a good picture of the spatiotemporal evolution of the flowing fracture network.

Another effective way to visualize these data is to make a so-called 'waterfall' plot of the change in temperature relative to the start of data collection for each borehole. Figure 9 shows the change in temperature for each borehole during the chilled water injection tests of EGS Collab experiment 3. All of the Joule-Thomsen heating signatures as well as the three 'cooled' zones mentioned in the next section are easily identified.

The table below summarizes the location and timing of visually apparent fracture intersections during Experiments 2 and 3. This list is probably not exhaustive and users are encouraged to apply more quantitative methods to identifying temperature changes along these boreholes.

The table above was compiled by visually identifying anomalies in a movie comprised of 6-hourly frames showing the temperature along the entire fiber. Where large (>0.1 ^{o}C) temperature fluctuations were noted, we plotted them in more detail to try to determine the exact depth and onset time. Figure 10 shows one such detailed plot showing the first intersection, with borehole AMU, in the table. The arrival of the fracture and decay of the Joule-Thomson heating effect following injection shut-in is evident in the temperature time-series plot in the lower right.

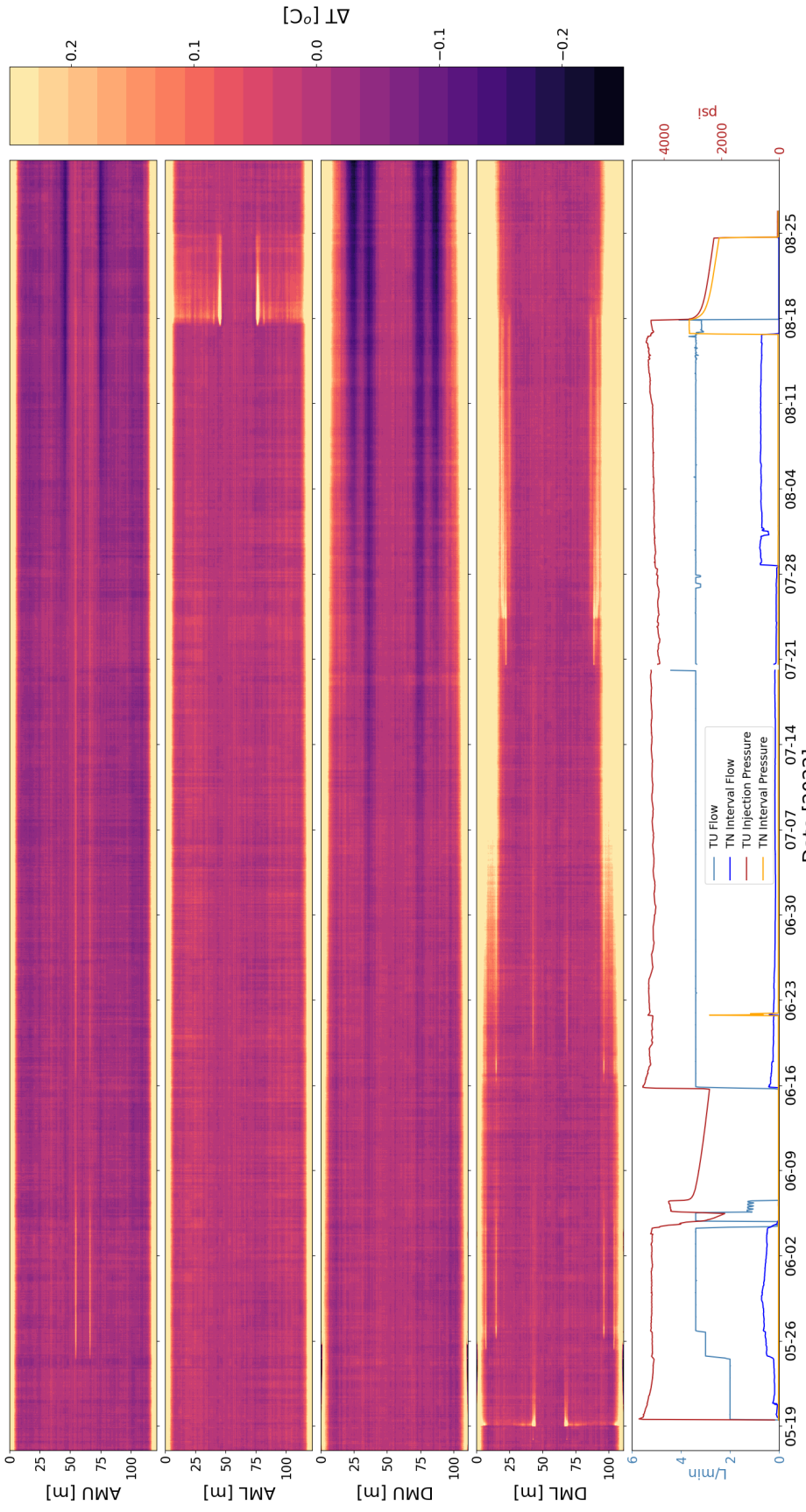

Figure 9: Change in temperature for each of the four grouted monitoring boreholes during the chilled water circulation test. Each panel shows the data for the entire fiber in each borehole (into and back out of the hole). The color scale is ±0.25 °C.

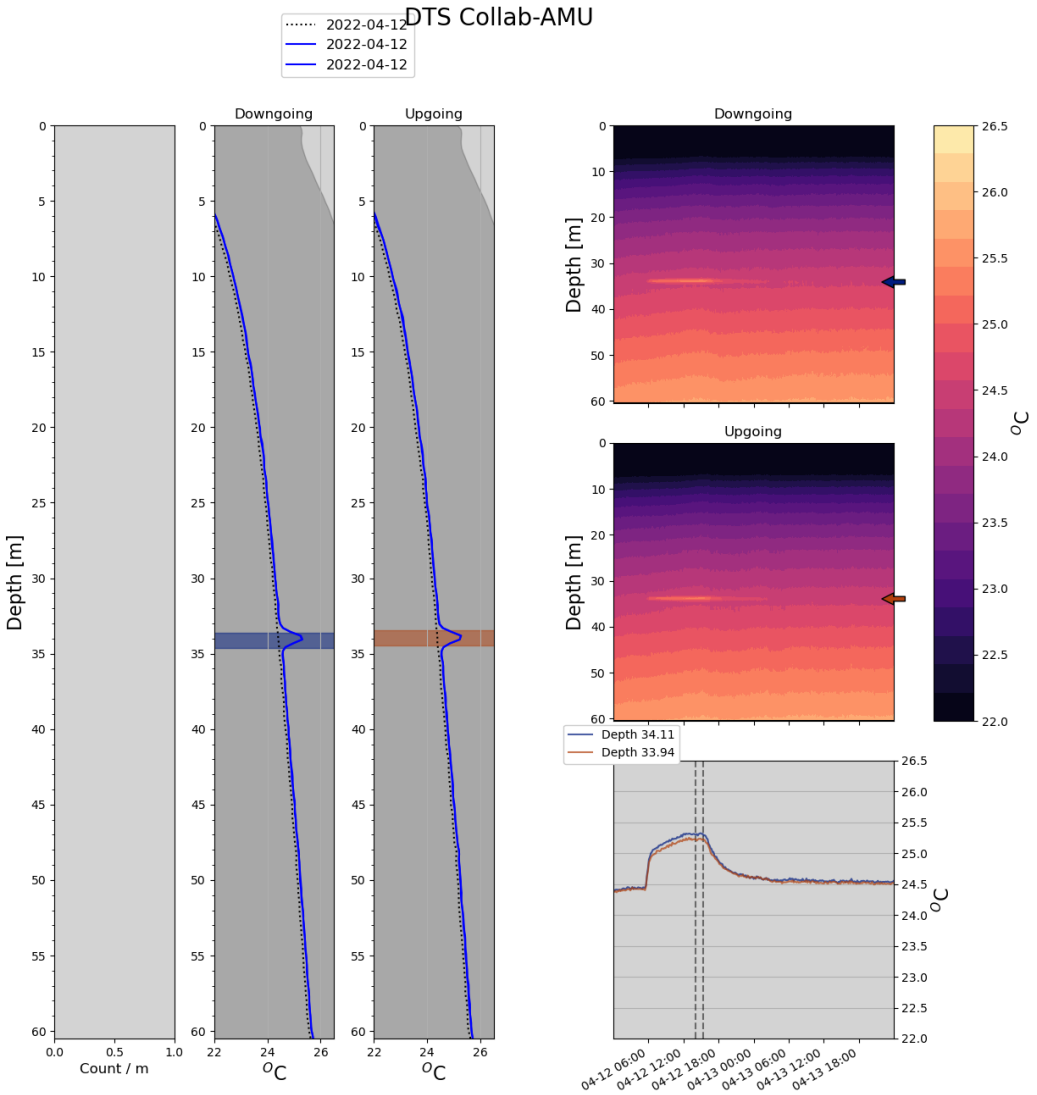

Figure 10: Plot showing the temperature profile along the borehole (left two traces), temperature with time (top right two plots), and the temperature time series at two selected depths (bottom right) for borehole AMU between 4-12-2022 and 4-14-2022.

Borehole	Center-of-interval depth [m]	Start time	Width [m; approx]
DMU	23.7	7-24-2022	10
DMU	36.2	7-7-2022	7
AMU	45.9	7-24-2022	5

Table 2: The table above indicates the depths, approximate onset date, and width of the intervals of cooling along boreholes AMU and DMU during the chilled water injection into TU.

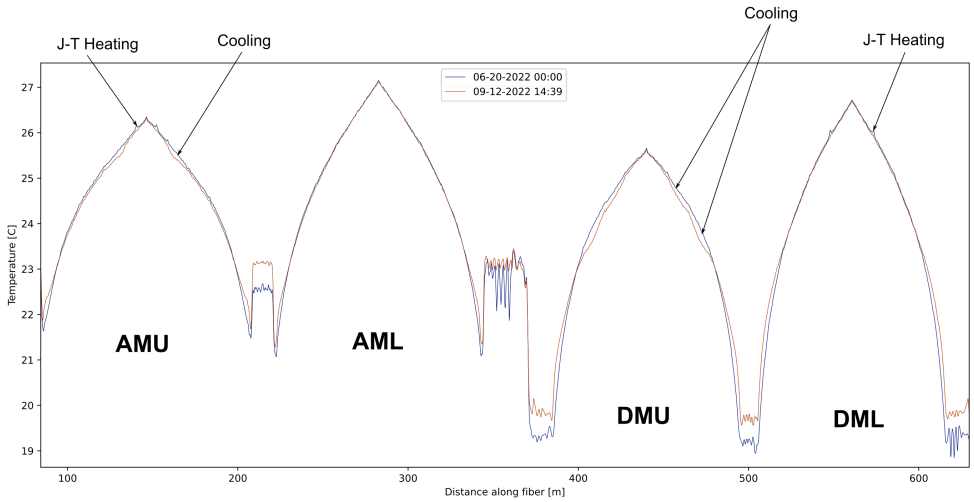

Figure 11: Temperature along fiber on 6-20-2022 (blue) and 9-12-2022 (orange) showing all four boreholes. Locations of Joule-Thomson heating anomalies on 6-20 and cooled zones on 9-12 are indicated.

5.2 Cooling of monitoring boreholes during chilled water circulation

Starting on May 19, 2022, and restarted on June 15, 2022 (following a pump failure), chilled water was injected into borehole TU as part of Experiment 3, aiming to observe a thermal breakthrough at any of the monitoring boreholes. Cooling of the upper, grouted monitoring boreholes (AMU and DMU) was observed starting in early June. The depths and onsets of these zones of cooling are shown in the table below. Figure 11 shows the temperature along fiber for two measurements; one on June 20, 2022, only five days after the restart of chilled water circulation (blue), and the other on September 12, 2022, roughly a month after shut-in of injection (orange). At the indicated sections of AMU and DMU, the orange curve exhibits depressed temperatures of approximately 0.1 ^{o}C relative to the blue. Figure 9 also clearly shows the onset and persistence of these features as dark streaks in AMU and DMU during the circulation tests. It is possible that this represents breakthrough of the chilled water with the monitoring boreholes.

5.3 Data access

The data referenced in this report are available on the GDR at this link: https://gdr.openei.org/submissions/1428

The repository contains three sets of data:

- Raw data records: Single XML files for each measurement as described above.
- Raw, processed data: Four NetCDF files, one per borehole. These have not been corrected for the calibration bath trend.
- Temperature corrected, processed data: Four NetCDF files, one per borehole. These *have* been corrected for the calibration bath trend (see details above)

References

[1] Arthur H. Hartog. *An Introduction to Distributed Optical Fibre Sensors*. CRC Press, may 2017.

Appendix J - Tracer Tests

Earl Mattson and Ghanashyam Neupane

Introduction

Fluorescein - a nonsorbing tracer, rhodamine B - a sorbing tracer, and sodium chloride - a nonsorbing electrical conductivity tracer were applied in these tetst. Tracers were detected at a number of locations within the production wells, two grouted monitoring wells, ceiling drips, wall weeps, and the floor. Based on the tracers and bulk water measurements, [*Mattson et al.*, 2023]conclude that most of the injected water was collected, however a large fraction of the water entered the drift through the floor, where the ability to collect, quantify, and analyze water was limited to crude bulk measurements. Water measurements over time from ceiling drips and wall weeps suggest a dynamic flow system where drift outflows shifted location with time. Fluorescein tracer breakthrough curves were used to determine travel time to the production wells and various parts of the drift. These results suggest a main fast flow pathway from the injection point in TU to the alcove/drift intersection with a series of secondary fractures with slower transport.

Fluorescein injection tests are listed in Table 1. In addition to these, the water injection system was configured such that the local mine water (~400 uS/cm) and mine water treated by reverse osmosis (~100 uS/cm) could be automatically switched to create a series of varying electrical conductivity pulses throughout the long-term constant injection. Two tracer tests were conducted to quantify the effects of the equipment (no flow in the rock) with fluorescein or sodium chloride. Additional tracer tests include two injections of rhodamine B, one sodium chloride injection for which the BTC was monitored using the inline electrical conductivity probes, and an 8-hour duration sodium chloride injection for electrical resistivity tomography analysis.

Initial Sodium Chloride Test

The first cross-well tracer test was conducted on May 31, 2022. This tracer test was to provide data for designing the subsequent fluorescein tracer tests. Three hundred mL of 105.5 mS/cm solution was injected at 50 mL/min into the main injection hose. Not accounting for dispersion in the injection/production hoses, this injection should have produced a peak concentration of ~1.5 mS/cm. The electrical conductivity from the interval of TN was measured at the well discharge. The dynamic background of the EC measurements from the square-wave ionic strength of the injection water was removed resulting in the salt water EC response shown in Figure 1. These BTC results suggest that there is a factor of 10 dilution of the injected peak concentration with a fairly rapid breakthrough. This information was used to design subsequent tracer tests.

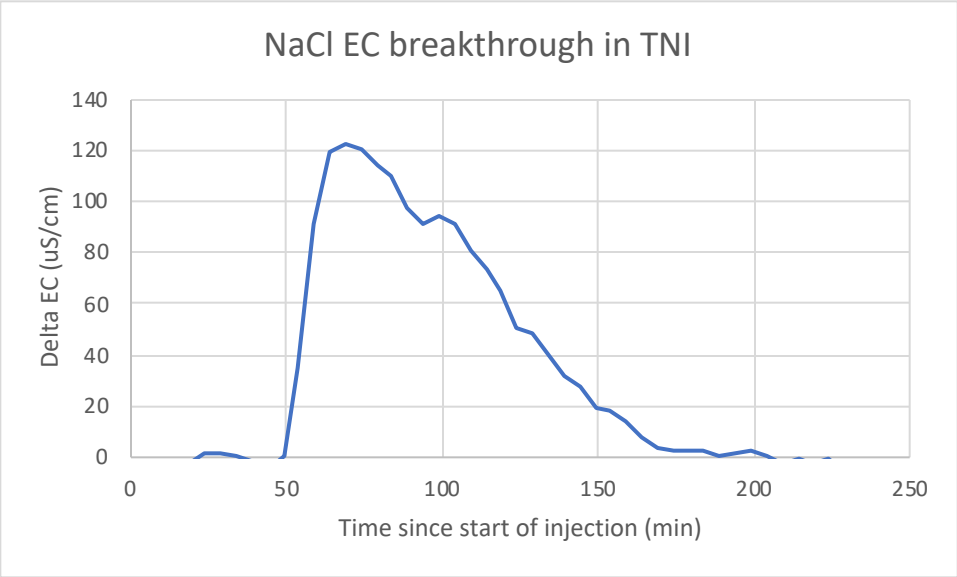

Figure 1 Initial NaCl injection test results for 05-31 EC measurements for TN Interval. Cyclic reverse osmosis injection EC responses were removed from the data. Time zero is at the beginning of the NaCl injection response at TNI. The ideal peak concentration was 1,500 uS/cm.

Fluorescein tracer

Four fluorescein tracer tests were performed during the circulation test (Table 1). All tests used the same injection point in TU located at 177.9 ft. Tracer was detected at numerous points in the production wells, in two of the grouted monitoring wells, and at ceiling drips, wall weeps, and the floor of the drift (Figure 2). Complete tracer breakthrough curves were determined for a number of tracer detection points enabled by the available fraction collectors and accessibility to the 4100 level during these tests.

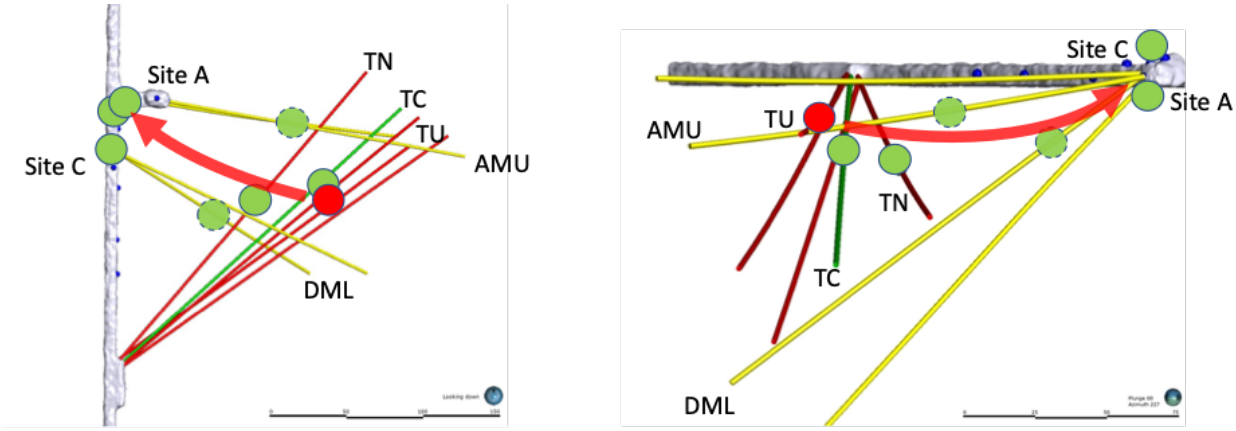

A) B)

Figure 2: Tracer detection locations from the 07/29/22 fluorescein injection. A) Plan view, B) vertical cross section looking to the southwest. Red dot is the approximate location of the TU injection site, green dots are known locations of detection, green dashed dots are approximate locations in wells, and the red arrow represents the general direction of the tracer-laden water. the scale bar lengths are 150 m.

Table 1: Fluorescein pulse injection tests and detection locations.

	Fluorescein Detection Location							
Injection Date	TNI	TCI	TCB	Site C Tarp	DML	AC Wall	TNC	Limited data for:
06/01/22	BTC	BTC	BTC	BTC	x		x	AMU, Site A ceiling, Corner Tarp
06/22/22	BTC	BTC*		BTC			x	
07/26/22	BTC	BTC*	x		x	x	BTC	TNC, A-C puddle
07/29/22**	BTC			BTC*	BTC*	BTC*	BTC*	A-C puddle

Notes:
* partial BTC (missing beginning, middle or end data)
x tracer detection
** New packer location for TNI and TNB (10.5 feet closer to drift in higher flow zone)

Tracer tests were accomplished by injecting approximately 300 mL of a concentrated tracer cocktail (10,000 mg/L) from one of the two Quizix pump cylinders and activating a pump inlet 3-way valve. The stock tracer solution consisted of four grams of reagent grade fluorescein mixed with 400 mL of nano-pure water in a bottle. The second cylinder was filled with the service water from the 4100 Level pressurized water supply line. Prior to injection, both cylinders were pressurized to match the injection pressure. The tracer cocktail was injected at 50 mL/min into the main injection hose through 25 feet of 5.9 mm ID SpirStar ® hose (blue line in Figure 3). At this point, the tracer cocktail mixed with the 3,400 mL/min injection water and was transported to the injection well packer interval (orange line in Figure 3). Then tracer was transported through the rock fractures to a production well (yellow lines in Figure 3), a monitoring well, or the drift. From the production wells, tracer was returned to the main instrument panel via 295 ft 12.8 mm ID SpirStar ® hose at the production well effluent flow rate (purple in Figure 3). Water samples were either manually collected and immediately analyzed or collected in a fraction collector overnight and analyzed the next morning.

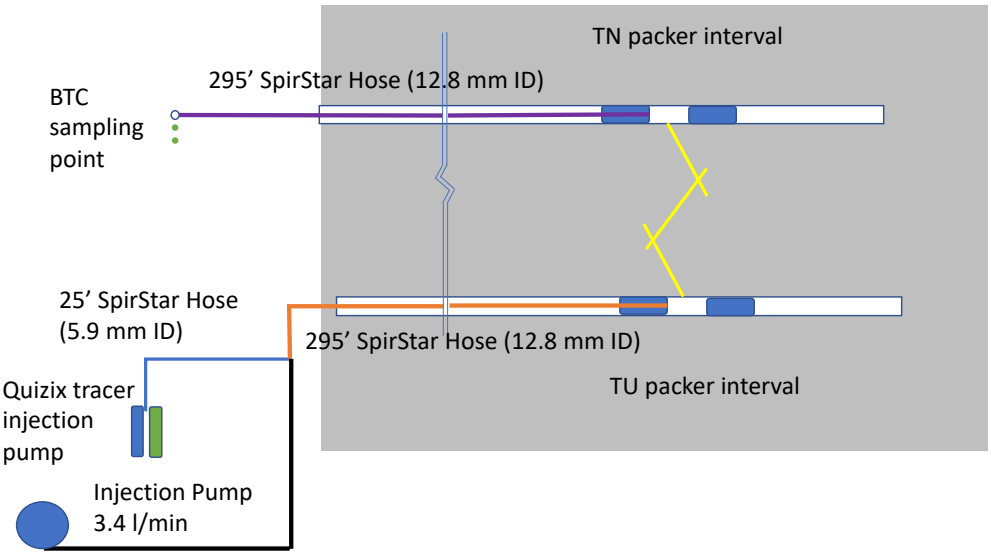

Figure 3: Tracer injection system for cross-well tracer testing.

Both the leftover mass of fluorescein in the stock solution and trapped mass of fluorescein in the Quizix pump and flow line were quantified to estimate the exact mass of fluorescein injected into the testbed. The trapped mass of fluorescein in the Quizix pump assembly and flow lines were obtained by back flowing and rinsing the Quizix pump cylinders, valves and flow lines.

All samples were analyzed at the test site for fluorescein using an Ocean Optic spectrophotometer system (Ocean optic FIA-SMA-FL-UTL cell, PX-2 pulsed xenon lamp, QEPRO spectrophotometer). For analysis of fluorescein, a beam of excitation radiation at 484.22 nm wavelength was used. The mean wavelength emission band was at 518 nm. For each sample, three scans average fluorescence count was recorded with 5 sec integration time for each scan. Background fluorescence values were established using the pre-tracer injection production water from each major producer and corrected either during analysis (for TN-interval samples) or subsequently during data processing (for other producers). Prior to each analysis, a series of fluorescein calibration standard solutions were prepared using the TN-interval background water for construction of calibration curve with $R^2 > 0.99$. Consequently, the recorded fluorescence count of each sample was converted to fluorescein concentration using the relationship between fluorescence counts and fluorescein concentration in the standards.

Analysis of the tracer breakthrough curves

Tracer tests conducted at various times and samples collected at different locations (Table 2) were used to test if measurable differences in velocity and dispersion could be detected over the two-month circulation test. To determine the velocity and dispersion of the tracer in the fracture segment from the tracer breakthrough curves, the tracer concentration input function at the packer interval in the TU injection well and the tracer breakthrough curve at the tracer discharge location must be known. The tracer injection/recovery system can be divided into four segments: 1) the tracer pump and initial injection hose, 2) a larger diameter main injection hose, 3) the rock fracture system, and 4) the return hose from the packer interval and bottom segments. These four segments are schematically represented in Figure 3 as the blue line, orange line, yellow line, and the purple line respectively. For production wells, the tracer discharge location would be the packer

interval. For ceiling drips and wall weeps in the drift there is no segment 4. Uncertainty in the location of fracture intersections with monitoring wells and production wells above and below the production well packers must be considered when viewing velocity and dispersion calculations for these locations.

Two tracer tests to examine the equipment only portion of the flow system were conducted to assess the amount of dispersion created by the Quizix injection pump and in the SpirStar ® injection hoses. These results indicated that there was significant dispersion of the tracer as it traveled from the injection pump to the TU injection interval in the borehole (Figure 4). The fluorescein tracer test was conducted using the TL packer interval. The TL interval had zero discharge making it an ideal equipment injection/discharge test. To measure discharge from the TL interval, 3.4 mm diameter SpirStar ® tubing that terminated at Site B in the drift was used. Tracer concentration as a function of time was measured. Figure 4 illustrates the calculated concentration results assuming plug flow occurs through the hoses and tubing (blue line) compared with the measured tracer concentrations. As shown in this figure, the measured tracer concentrations are about 1/10th of the value of the expected peak concentrations, which indicate the presence of Gaussian dispersion in the SpirStar ® hoses.

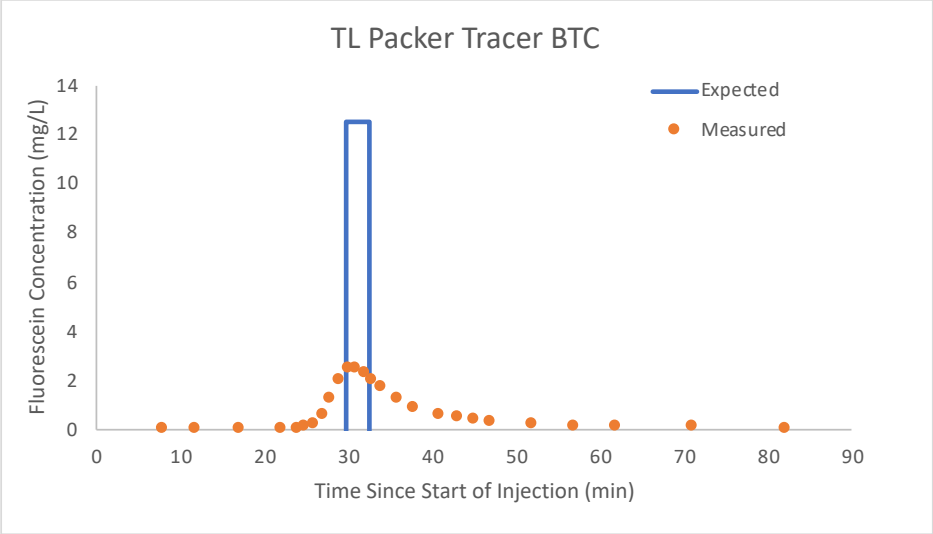

Figure 4: Expected and measured breakthrough curves at the packer interval

As part of this analysis, we sought to remove the effect of dispersion in the SpirStar ® hoses that carried fluid to and from the fracture system. To estimate dispersion in the hoses, the modeled tracer breakthrough curves were fitted to the two tracer tests aimed at measuring transport behavior in the hoses. Tests examined transport in the (1) 25-ft long hose that brings tracer to the primary fluid delivery hose (Figure 5A) and (2) the combination of hoses delivering and recovering injected fluids (Figure 5B). Both tests were conducted at fluid flow rates considerably less than that used in the actual tracer tests. Fitting these data via adjustment of velocity and dispersion indicated that the dispersion was considerably less than expected based on steady-state Taylor dispersion theory. Therefore, we attempted to fit the data to a model that used mathematical relationships describing pre-asymptotic Taylor dispersion [*Taghizadeh et al.*, 2020]. However, a simple dispersivity model (dispersivity = 0.9 m) provided a better estimate of the dependence of dispersion on velocity

(Figure 5), and the latter relationship was used to predict the effect of dispersion in the tubing in subsequent analyses, which were conducted at significantly higher fluid injection rates.

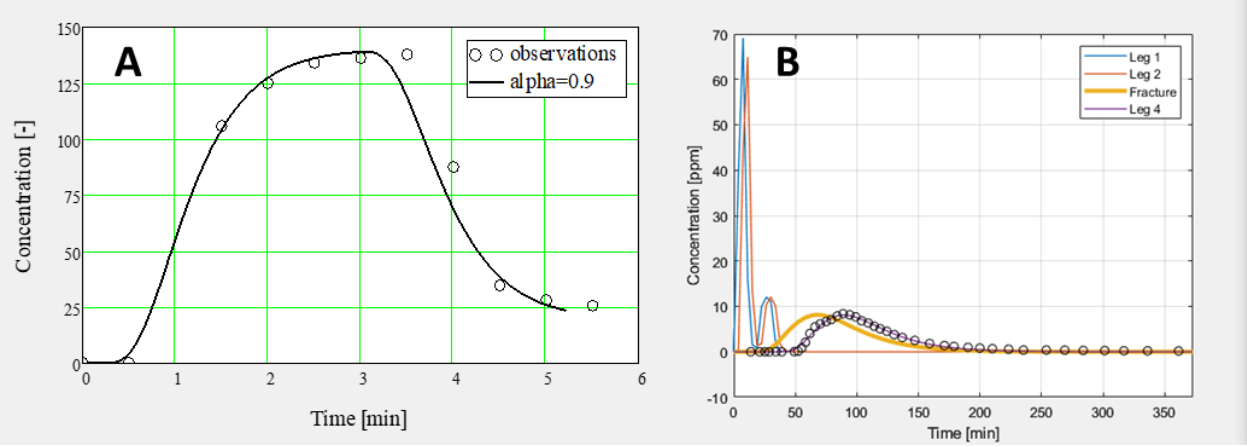

Figure 5. (A) Fluorescein tracer breakthrough curve (open circles) from flow through the 25-ft of tracer delivery tubing. Solid line illustrates model fit using a dispersivity of 0.9 m. (B) Breakthrough curves (open circles) from return flow of tracer injected into, and collected from, the TN interval June 1st injection by fitting the velocity, dispersion and mass fraction of the segment 3 fracture. Different segments (see color segment scheme in Figure 3) refer to the sequence of hoses and tubing, for which exit concentration is calculated. Solid lines illustrate model fit of the fracture using a dispersivity of 0.9 m for the other three segments.

To estimate velocity and dispersion from each of these curves, the tracer transport process was simulated using MATLAB-based solutions of the transport equations with a four-step injection input and a 1-D domain that accounted for the calculated velocity and estimated dispersion in each of the sections of tubing carrying fluid and tracer to the fracture zone. Fitted velocities, dispersion coefficients and calculated dispersivities for the fracture segment are provided in Table 2.

Table 2. Model fitted velocity, dispersion, and mass balance results for the fracture segment for the first three fluorescein tracer tests.

Date	Location	Qwell	M	V	D	Dispersivity
		mL/min	-	m/s	m^2/s	m
6/1/22	TNI	540	0.6908	0.0031	0.0059	2
6/22/22	TNI	195	0.7218	0.0007	0.0052	7
7/26/22	TNI	101	0.5541	0.0004	0.0068	17
6/1/22	TCI	120	0.6379	0.0009	0.0030	3
6/22/22	TCI	56	0.8382	0.0002	0.0010	5

6/1/22	Tarp	55	0.3220	0.0021	0.0016	1
6/22/22	Tarp	61	0.4720	0.0066	0.0145	2
7/29/22	Tarp	27	0.2695	0.0022	0.0041	2

Fluorescein Test Interpretations

Using water discharge measurements in the production wells and the drift ceiling/wall weeps, calculated water mass balance, and the first detection of tracer arrival during tracer tests, a conceptual model for water flow in the fractures was developed. This conceptual model was then used to interpret the role of production water discharge and its utility on predicting the water velocity in a fracture rock system.

Water and tracer conceptual model

During the 2.5-month flow test, water discharge varied from the production wells as a function of time suggesting a change in the flow dynamics within fractures at the 10-meter scale. In addition, these flow changes were also seen at the 50-meter scale (i.e., in the drift) as indicated by flow rate changes in ceiling and wall weeps. Variability in the discharge in both the production wells and the drift occurred despite attempts to maintain a constant injection rate.

The water mass balance calculations suggest the presence of major flowing fracture(s) from the TU injection location to the intersection at the alcove/drift intersection. This conceptual model is supported by the time of first detection of fluorescein tracer in the production wells and the drift. Figure 6A illustrates the spatial distribution of the time of first tracer detection (blue dots with time in hours) for the July 26-29 tracer tests. As seen in this figure, tracer is first detected in the two production wells (TC interval 0.3 hrs, TN interval 0.4 hrs) suggesting a fast flow pathway velocity of 34 and 40 m/hr (0.009 m/s and 0.011 m/s) for TC interval and TN interval respectively. The fastest tracer detection velocity, however, was located at the floor seep at the alcove/drift intersection (46 m/hr - 0.013 m/s) despite being about 3 times further from the TU injection point than the production wells. Other tracer detections in the drift (the Site C tarp and the Site A ceiling drip) took at least twice as long (i.e., ½ the velocity) compared to the alcove/drift detections even though the distance of all three tracer discharge points from TU interval are approximately the same.

The early detection of tracer at the alcove/drift floor is corroborated by the water mass balance analysis and suggests a major flow pathway has been developed from TU interval to the drift/Battery Alcove intersection location and is represented by the large red arrow in Figure 6A. This flow path appears to pass through/near the two production wells, the TC interval, and TN. The Site A and C detections suggest that there are secondary flow pathways that are either branching off from the main fracture near these detection locations, or the detections possibly represent long secondary flow pathways.

Although the water measurements and the tracer tests provide indications of the locations of travel pathways, the measurements do not provide quantitative information on the exact pathway the

water and tracer travel through the fracture rock. Figure 6B includes a preliminary tomographic representation of the change in electrical conductivity of the July 26 sodium chloride tracer injection presented above.

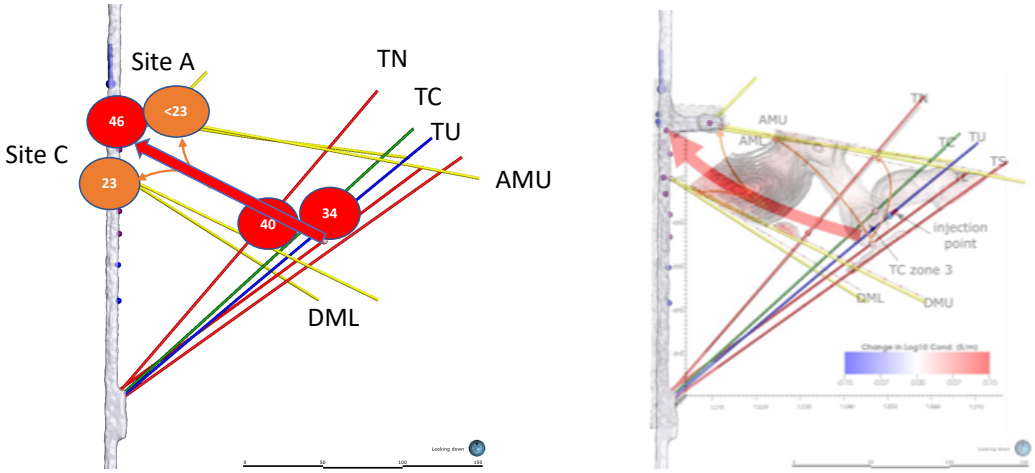

A) B)

Figure 6. A) Calculated tracer velocity of first detection of the July 26 – 29, 2023 fluorescein tracer test (in hours after injection) in the production wells and in the drift, B) conceptual model of tracer pathways from the injection well to discharge locations overlain with an electrical resistivity tomographic image from a salt water tracer injection on July 26.

Water discharge rate vs. flow velocity in fractures

The simplest conceptual model of water movement in a fracture from an injection well to a production well is a stream tube that connects the two points. In a model of the testbed, numerous stream tubes could exist from the injection location to the multiple discharge locations. In this case, the production well flow rate is considered to be the correct variable related to the tracer velocity in the stream tube. A second conceptual model of water flowing in a fracture could be described as a major flow pathway with points along the flow path where the water leaks into individual fracture pathways. Although a major fracture flow pathway could also be considered a stream tube, in this case the velocity in the main fracture is not controlled by individual discharge flows. Depending on the tracer residence time in the main fracture compared to the tracer residence time in the secondary fracture, the production well discharge rate may have a small influence on the calculated velocity of the tracer between the injection and production locations.

Figure 7 illustrates the calculated fluorescein fracture velocity from tracer tests conducted on June 1, 2022 and July 26, 2022 for the TN interval, TC interval and the Site C tarp plotted against the well discharge rate. Results from these limited data sets support the first conceptual model (simple flow through a stream tube) because the production well flow rates appear to be linearly related to the average tracer velocity to each discharge point. According to the water mass balance analyses, the majority of fracture flow is being discharged to the base of the drift near the alcove/main drift intersection. Despite the fact that both the drift and the TN interval and TC interval production wells intervals are approximately atmospheric pressure and the production well packed off intervals are located approximately 1/3rd of the distance from the injection well compared to the discharge locations in the drift, these wells only captured about 25% of the injected

water. Schwering et al. (2023) examined the pressure response of the production wells during shut-in tests conducted at the end of the flow experiment. The producing zones of these wells quickly reached a near-steady-state shut-in pressure, which indicates the near-wellbore fracture aperture was maintained while the injection at TU continued. After the TU injection was terminated, the producing zones slowly lost pressure which suggests closure of these near-wellbore fractures and no significant shear residual permeability (e.g., from shearing). This production well skin effect could explain the low production well recovery of the injected water.

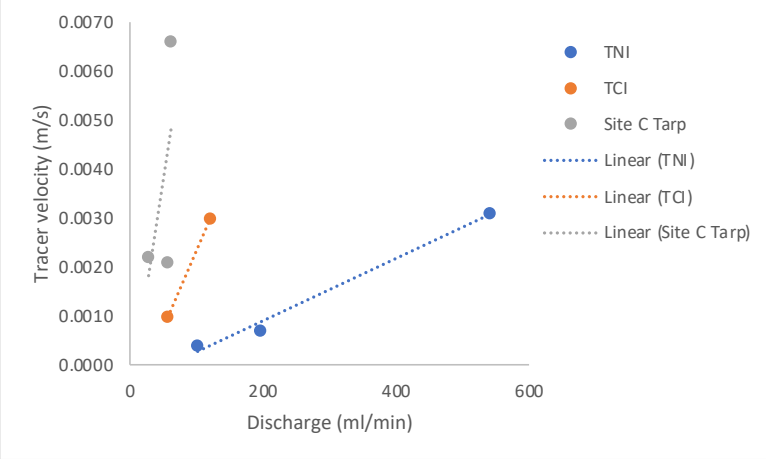

Figure 7. Relationship tracer velocity in the fracture and production wells TNI and TCI water discharge rates.

Rhodamine B tracer injections

Two Rhodamine B tracer injections were performed as part of the flow characterization task. Rhodamine was injected into the TU interval on June 2nd and again on June 23rd. Rhodamine injections were conducted a day after a Fluorescein injection to allow comparison of sorbing and non-sorbing tracers. Rhodamine injection protocols were similar to the Fluorescein injections except that the volume of the injected tracer was greater and its concentration was higher to account for sorption.

Figure 8 illustrates the fluorescein and rhodamine concentrations for the first pair of injections (June 1st and 2nd) from the TN interval discharge hoses as a function of time from the start of injection. The initial and peak arrival of rhodamine B was delayed as compared to the non-sorbing fluorescein dye. The magnitude of the rhodamine B peak is approximately 100 times less than the fluorescein peak and the rhodamine B breakthrough curve is more spread out compared to the fluorescein breakthrough curve. These observations are consistent with typical behavior of sorbing and non-sorbing tracers. The June 22nd fluorescein and June 23rd rhodamine B breakthrough curves exhibit similar behavior, albeit a full rhodamine breakthrough curve was not obtained due to SURF access restrictions.

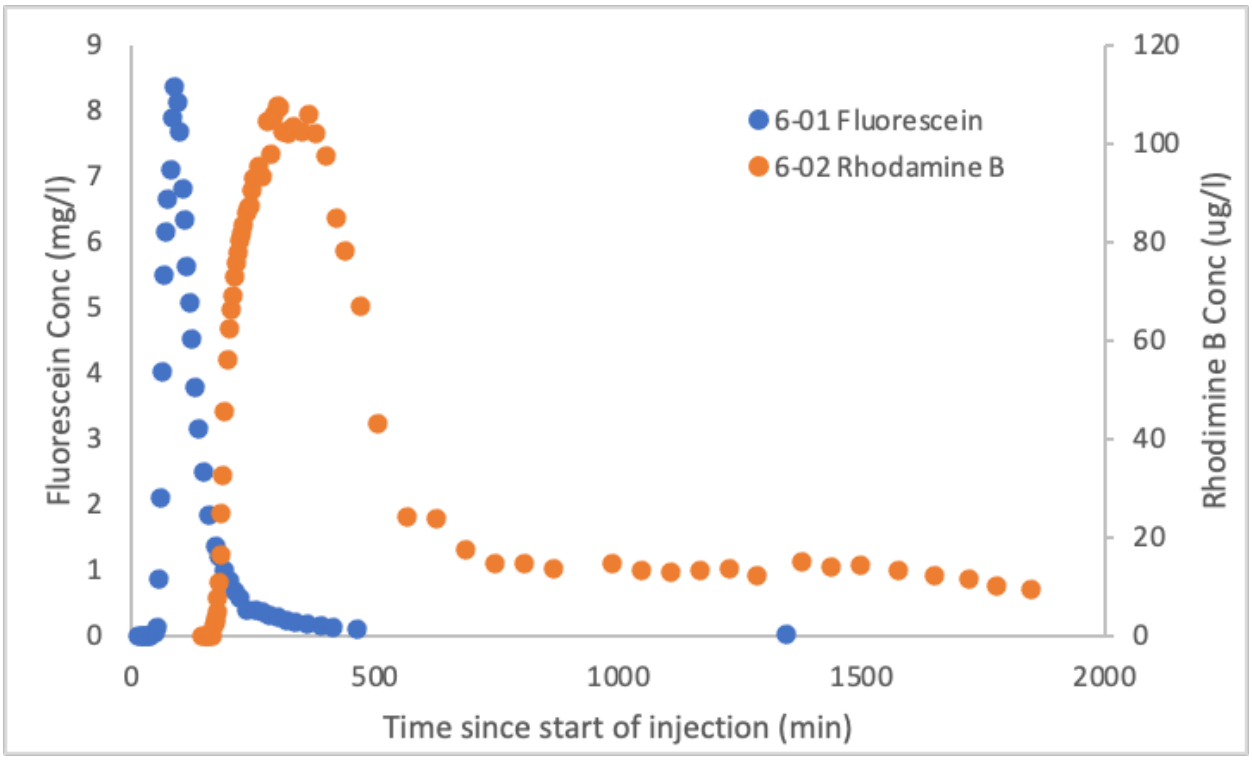

Figure 8. Comparison of the Fluorescein and Rhodamine B concentrations from TNI for the early June tracer characterization tests.

Rhodamine sorption analysis

A float Yates amphibolite sample collected from 4850 level near the Yates Shaft was crushed to grain size < 2mm for sorption experiments. A stock rhodamine-B (ACS grade) solution of 100 mg/L was prepared in nano-pure (>18.2 MW×cm) water, and further diluted to a series of rhodamine-B solutions with concentrations ranging from 0.5 m2/L to 25 mg/L. The crushed amphibolite was homogenized, and sequentially split using riffle splitter to obtain a series of masses of 2 g each. The sorption tests were conducted in a 50 mL centrifuge tube at solid-to-fluid ratio of 2 g: 10 mL. A blank (without rhodamine-B) experiment was also included for the sorption test.

The mixtures of 2 g crushed rock and 10 mL rhodamine-B solution were agitated at 200 rpm on a platform shaker for 24 hours. After 24 hours, the equilibrated solutions were separated by centrifugation. Supernatants after centrifugation were analyzed for their rhodamine-B content using an Ocean Optic spectrophotometer system (Ocean optic FIA-SMA-FL-UTL cell, PX-2 pulsed xenon lamp, QEPRO spectrophotometer). For analysis of rhodamine-B, a beam of excitation radiation at 509.9 nm wavelength was used. The mean wavelength emission band was at 578 nm. For each sample, three scans average fluorescence count was recorded with 5 sec as integration time for each scan. Background fluorescence values were established using the blank supernatant. A series of fluorescein calibration standard solutions were prepared for construction of calibration curve with $R^2 > 0.99$.

Rhodamine-B sorption data on crushed Yates amphibolite is given in Table 3. Both the Langmuir and Freundlich isotherm models were used to interpret the sorption data. The model fitting parameters for these to isotherms were obtained using the Solver module in the Microsoft® Excel.

A function of squared error [(modeled value – experimental value)^2] was minimized to obtain the optimized model fitting parameters. For the Langmuir isotherm, the values of model parameters S_{max} and b are 209.43 and 0.12, respectively. For the Freundlich isotherm, the values of model parameters K_f and n are 22.49 and 0.74, respectively Figure 9 shows the experimental and modeled isotherms plots.

Table 3. Rhodamine-B sorption on crushed Yates amphibolite

Equilibrium concentrations (mg/L)	Sorbed (mg/kg of crushed rock)
0	0
0.067	2.16
0.087	4.57
0.28	8.62
1.11	19.43
1.88	40.61
6.68	91.62

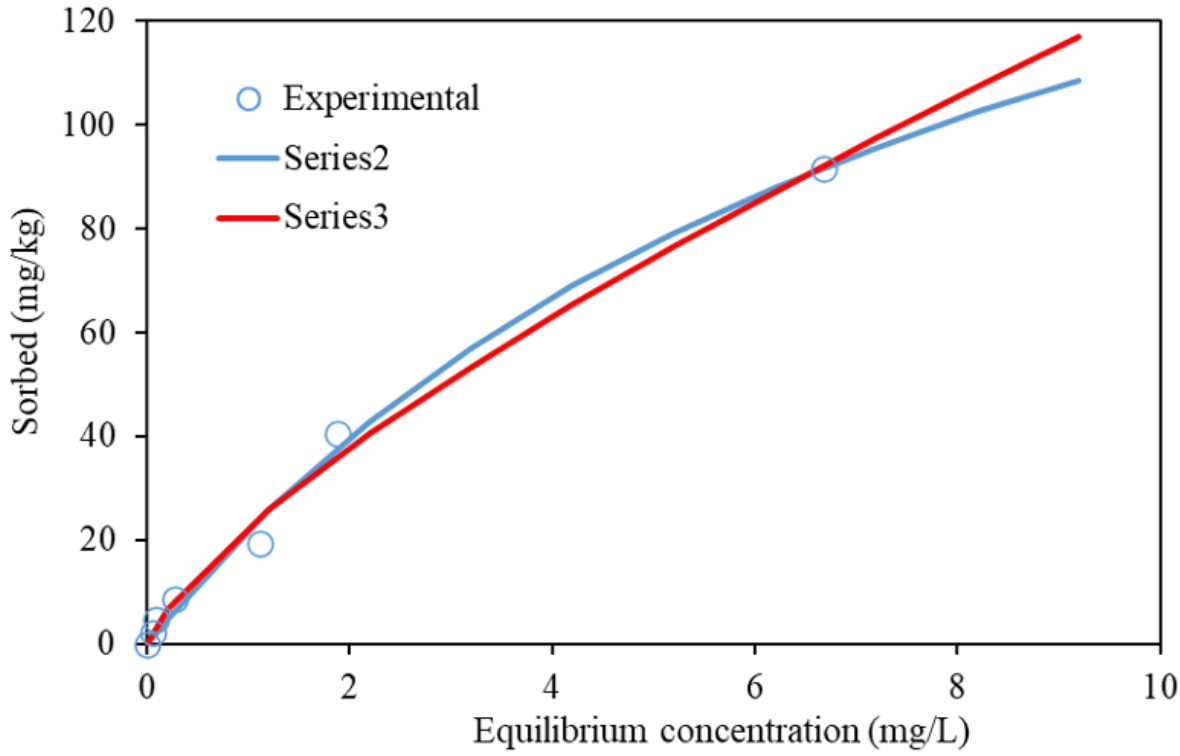

Figure 9. Isotherms of rhodamine-B on crushed <2 mm) Yates amphibolite.

References

1. Mattson, E., M. Plummer, H. Neupane, V. Vermeul, D. Sirota, M. Ingraham, . . . E. C. Team (2023), Fluorescein Tracer Testing on the 4100L – A Preliminary Examination of Initial Arrival in Wells and the Drift at the Second EGS Collab Testbed, paper presented at 48th Workshop on Geothermal Reservoir Engineering, Stanford University, Stanford, California, February 6-8, 2023.
2. Taghizadeh, E., F. Valdés-Parada, and B. Wood (2020), Preasymptotic Taylor dispersion: Evolution from the initial condition, *Journal of Fluid Mechanics*, *889*, doi:10.1017/jfm.2020.56 (2020).

Appendix K - Simulation of Chilled-water Injection at EGS Collab Testbed 2 using the GEOS simulation framework

LLNL team members: Matteo Cusini, Fan Fei, Joseph P. Morris

1. Context and objectives

This work seeks to model the chilled-water injection that occurred at EGS Collab Testbed 2 as part of Experiment 3, using the open-source GEOS simulation framework. Modeling of this process, previously conducted using STOMP-GT, confirmed that thermal breakthrough was expected to occur during the chilled water injection and may have been masked by strong Joule-Thompson effects induced by large pressure drops between the fractures and the production wells. Building a GEOS numerical model of this process will allow to include additional physics. In fact, GEOS can model fully coupled thermo-poromechanical processes in fractured porous media and can be employed to model the process of artificially enhancing rock permeability by hydraulically fracturing the rocks. For example, the GEOS model could help understanding the dynamic nature of the EGS Collab Experiment 3 flow system. Since the limited time and resources do not allow for an extensive study, the focus is on building a baseline model of this process. As such, the main outcomes of this modelling efforts are listed below.

1. A GEOS model of the EGS Collab Testbed 2 Experiment 3, and a comparison with the modeling results obtained with STOMP-GT and with the data collected at EGS Collab.
2. A validation of GEOS thermal single-phase flow modeling capabilities in fractured media. This is particularly valuable because analytical solutions to validate modeling of flow processes in fractured media are hard to find.
3. An open-source model of the EGS Collab Testbed 2. The model will be described in detail on GEOS' documentation page and made available through GEOS repository. As such, it will serve as a baseline for other researchers interested in studying the EGS Collab Experiment 3 through numerical studies.

2. Formulation and discretization method

The simulations are performed with GEOS' thermal single-phase flow solver. The mass and energy conservation equations are discretized using a finite-volume methods with using a two-point flux approximation and an upwinding scheme for all fluid properties. Fractures are modelled as a lower dimensional manifolds and governing equations describing flow within them and max and energy exchanges with the rock matrix are discretized according to the Embedded Discrete Fracture Method (EDFM) [1, 2].

3. Geometry, simulation parameters and boundary conditions

Figure 1 presents the geometry of the model of EGS Collab Testbed 2. We consider a $148.375\ m \times\ 75\ m \times 143.375\ m$ domain and we employ a system of coordinates with origin in $\{0,0,0\}$. The drift and battery alcove are represented by the two rectangular prismatic regions highlighted in blue in Figure 1. The locations of their vertices are provided in Table 1. A single embedded planar fracture is considered (i.e., shaded surface in Figure 1). The fracture unit normal vector is $\boldsymbol{n} = \{0.3569123763, 0.9123044601, 0.2007837838\}$ and its center is in $\{100,\ 37.5,\ 30\}$. The fracture location and orientation are consistent with the microseismic data collected during flow testing and qualitatively similar to the one employed in the STOMP-GT model. Finally, injection well TU, production

wells TC and TN and monitoring wells AMU, AML, DMU, DML are also shown. The domain is discretized, in space, using a $68 \times 30 \times 65$ structured mesh, for a total of 132600 elements in the rock matrix and 4284 elements in the embedded fracture, as shown in Figure.2.

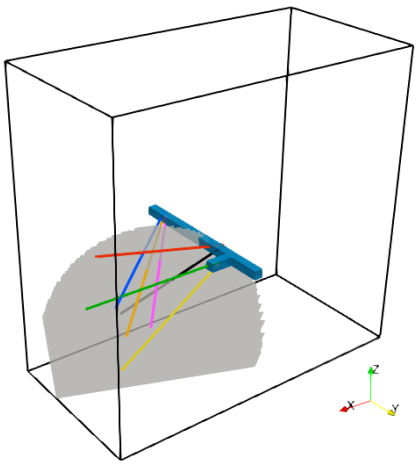

Figure 1: Model of the EGS Collab testbed 2 showing the drift, the battery alcove (blue box), injection well TU (blue), production wells TC (orange) and TN (pink), monitoring wells AMU (green), AML (yellow), DMU (red), and DML (black), and an hydraulic fracture.

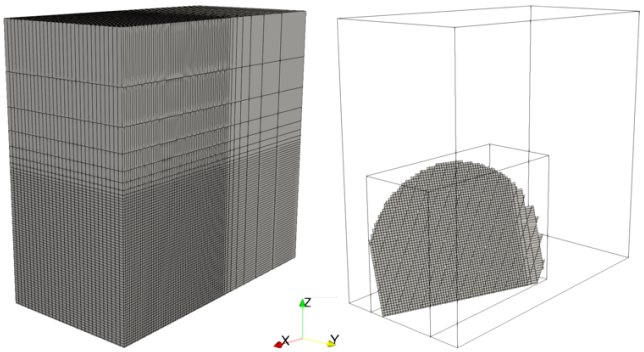

Figure 2: GEOS computational mesh.

Pressure and temperature Dirichlet boundary conditions are considered at the top boundary ($z = 143.375\ m$), i.e., $p_{top} = 2\ MPa$ and $T_{top} = 23.0153$ °C. The temperature gradient is $-0.0488\ °C/m$ whereas hydrostatic pore pressure distribution is assumed. The drift and the alcove are assumed to have constant pressure and temperature. Thus, Dirichlet boundary conditions are considered for both, i.e., $T_{drift} = 18.5\ °C$ and $T_{alcove} = 20.637\ °C$.

Table 1: Location of the vertices of the rectangular prisms defining the drift and the battery alcove.

Drift	{77.9,0.0,57.9}, {82.1,0.0,57.9}, {77.9,75.1,57.9}, {82.1,75.1,57.9} {77.9,0.0,63.1}, {82.1,0.0,63.1}, {77.9,75.1,63.1}, {82.1, 75.1, 63.1}
Alcove	{81.9, 53.9, 58.9}, {92.1, 53.9, 58.9}, {81.9, 58.1, 58.9}, {92.1, 58.1, 58.9}, {81.9, 53.9, 63.1}, {92.1, 53.9, 63.1}, {81.9, 58.1, 63.1}, {92.1, 58.1, 63.1}

Rock and fluid properties are presented in the Table 2. Here, the temperature dependency of fluid density and viscosity is neglected. The fluid enthalpy is assumed to be a linear function of the temperature. Additionally, constant fracture permeability and aperture are considered as reported in Table 2.

Table 2: Rock and fluid properties used in the GEOS model.

Rock porosity	0.01
Rock Permeability	$10^{-20}\ m^2$
Thermal conductivity	$3.81 \frac{W}{m \cdot K}$
Rock heat capacity	$2.3345 \cdot 10^6\ \frac{J}{m^3 \cdot K}$
Fluid density (@1 MPa)	$1000 \frac{kg}{m^3}$
Fluid viscosity	$0.001\ Pa \cdot s$
Fluid compressibility	$10^{-10} \frac{1}{Pa}$
Fluid heat capacity	$4.2 \cdot 10^6 \frac{J}{m^3 \cdot K}$
Fracture aperture	$0.001\ m$
Fracture permeability	$10^{-9}\ m^2$
Fracture-Matrix heat transfer coefficient	$150 \frac{W}{m\,K}$

4. Initial conditions before water injection

To compute the initial distribution of pressure and temperature prior to the chilled-water injection, we run a simulation for 200 years considering the Dirichlet boundary conditions described in the previous paragraph. Figure 3 shows the temperature distribution at the end of the simulation. Remark that the presence of the drift and the battery alcove has significantly impacted the temperature field.

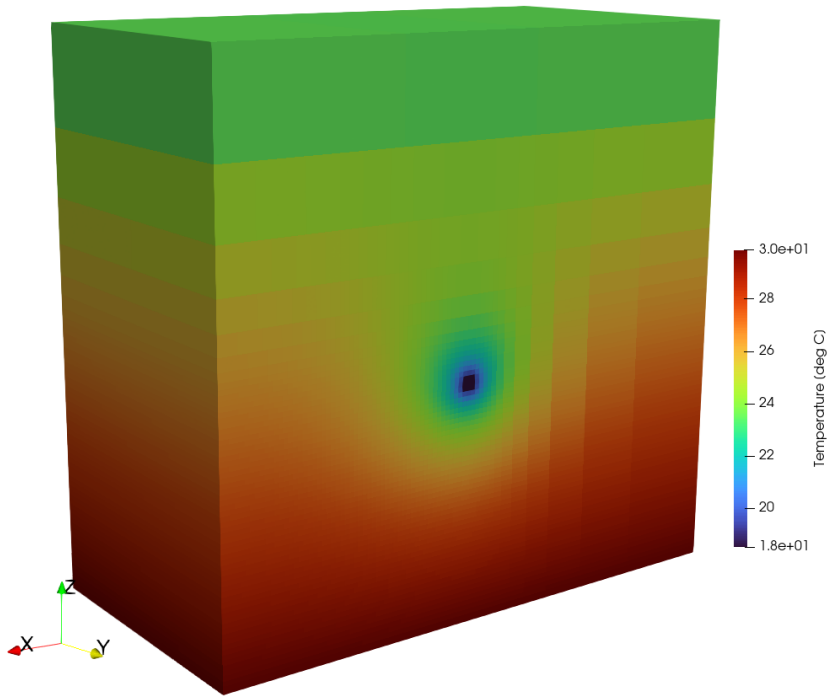

Figure 3: Initial temperature profile after 200 years simulation to equilibrate the imposed boundary conditions on the drift.

Figure 4 compares the temperature field computed by GEOS at the location of the monitoring wells against those measured using DTS throughout the experiment. Note that the numerically computed temperature field qualitatively matches the data collected during the experiment.

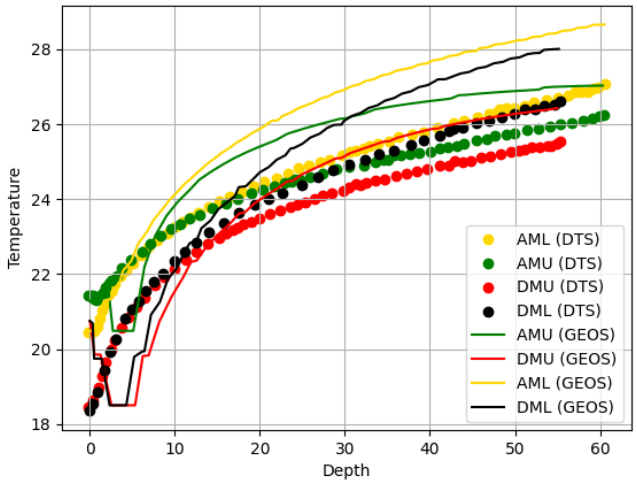

Figure 4: Initial temperature distribution along monitoring wells computed by GEOS and measured during the experiments prior to the onset of chilled-water injection.

5. Chilled-water Injection simulations

To simulate the chilled water injection, the flow rates recorded at injection well TU and at production wells, TC and TN, are approximated by stepwise constant functions of time and applied as flux boundary conditions in the fracture cells intersected by each well. Additionally, the injection temperature for well TU is also considered to be a stepwise constant function of time and prescribed as a Dirichlet boundary condition for fracture cells intersected by well TU. The time evolution of the fluid temperature at the injection temperature and of the volumetric flow rates is presented in Figure 5. Finally, since the fracture working fracture pressure was estimated to be 13.3 MPa, a sink term with a constant pressure $p_{fd} = 13\ MPa$ is considered for all fracture elements intersecting the drift. All fracture cells are also initialized at the working fracture pressure right before the beginning of injection.

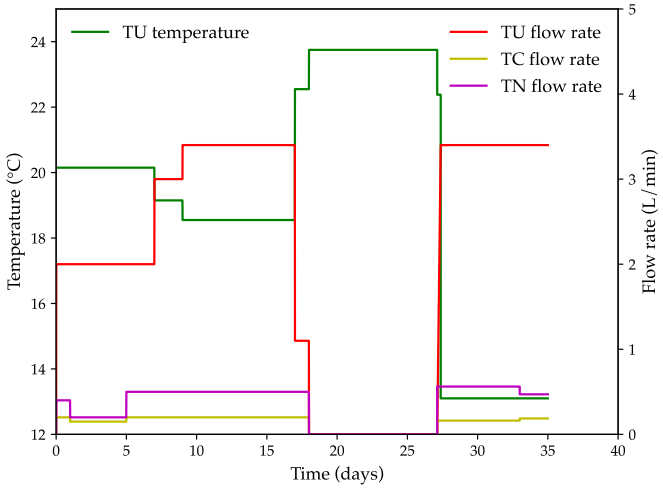

Figure 5: Fluid temperature at TU and volumetric flow rates at TU, TC, and TN as a function of time from onset of injection.

After having computed the initial condition as described in the previous paragraph, the chilled-water injection stage is simulated for 35 days. Figure 6 shows the temperature profile 35 days after the start of injection. Note that the GEOS model predicts a faster advancement of the cold temperature front compared to reference STOMP-GT model, and therefore an earlier thermal breakthrough. Additionally, differently from the results obtained with the STOMP-GT model, the cold waterfront reaches the drift.

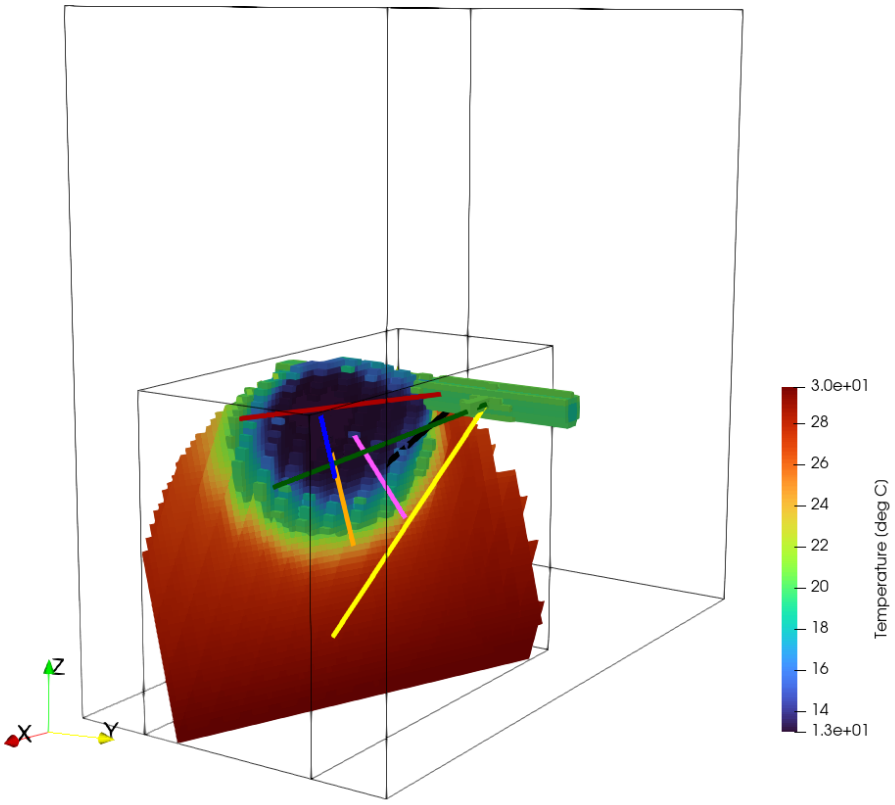

Figure 6: Temperature distribution in the fracture at simulation time 35 days after the start of the chilled water injection.

6. Conclusions

We have built a GEOS model of the chilled-water injection that took place at EGS Collab Testbed 2 as part of Experiment 3. GEOS results, despite showing considerable differences compared to the results obtained with STOMP-GT, confirm that thermal breakthrough is likely to have occurred and was probably masked due to strong Joule-Thompson effects. The discrepancies between the two numerical models are likely related to differences in constitutive models, boundary conditions and fracture geometry and location. If extra resources were to be available, we recommend to further investigate the source of such discrepancies. Additionally, even though the limited amount of time and resource has not allowed for it, it will be possible, with a relatively small effort, to extend the model to include additional physics such as poromechanical effects and coupling between the fracture's properties and the mechanical configuration. The model will be made public through GEOS documentation page.

Acknowledgements

We thank Dr. Mark White for sharing the STOMP results and helping us setting up the GEOS model and understand the source of some the discrepancies.

This work was performed under the auspices of the U.S. Department of Energy by Lawrence Livermore National Laboratory under Contract DE-AC52-07NA27344.

References

[1] L. M. J. C. Lee SH, "Hierarchical modeling of flow in naturally fractured formations with multiple length scales.," *Water Resour. Res.,* vol. 37, no. 3, pp. 443-455, 2001.

[2] K. D. J. P. Hajibeygi H, "A hierarchical fracture model for the iterative multiscale finite volume method," *J. Comput. Phys.,* vol. 230, no. 24, pp. 8729-8743, 2011.